GASIFICATION-BASED CLEAN CONVERSIONS AND UTILIZATIONS OF COAL, OIL SHALE AND BIOMASS

Peng Jiang, MEng, BEng

Thesis submitted to The University of Nottingham for the degree of

Doctor of Philosophy

July 2020

Abstract

Gasification-based conversion of solid fuels into syngas for power and chemical product generations is regarded as the cleanest and most efficient thermal process. The objectives of this study is to have an in depth understanding of gasification (and co-gasification) of coal, oil shale and biomass in terms of its kinetics, thermodynamics, economics and environmental impacts through the combination of lab experiments and simulations. To summarize, the work carried out in this study can be divided into the following three parts.

The first part focused on coal pyrolysis and gasification. Firstly, an isothermal CO_2 gasification of four coal chars prepared via two different heating regimes, i.e., conventional and microwave pyrolysis, was carried out by thermogravimetric analysis. Results showed that the microwave induced char had the superior thermodynamic performances due to the greater C/H mass ratio and more ordered carbon structure. Secondly, the gasification performances of coal and its corresponding macerals (i.e. vitrinite, liptinite and inertinite) as well as the interactions among macerals under typical gasification conditions were investigated. It was found the cold gas efficiency was changed in the order of liptinite > vitrinite > inertinite. The relationships between synergistic coefficients of gasification indicators were correlated well with maceral contents. The increase of gasification temperature was found promoting the synergistic coefficients slightly, whilst at an oxygen-to-coal mass ratio of 0.8 and a steam-to-coal mass ratio of 0.8, the highest synergistic coefficients were obtained. Thirdly, the distributions and speciation of nine hazardous heavy metals (i.e., Ba, Co, Cr, Cu, Mn, Ni, Pb, V, and Zn) in coal and gasification slags collected from two opposed multi-burners gasifiers were quantified. The morphology of fine slags appeared fragmentized, small spheres and covered with fine floccules, whilst coarse slags were vitreous, angular and less porous than that of fine slags. The elements of Cr, Cu, Ni, V and Zn were mainly in residual fractions (48.8 -82.6 wt%) of the coal samples, while almost all heavy metals were principally bonded with residual fractions (42.3 -94.8 wt%) in gasification slags.

The second part focused on thermal co-processing of coal and oil shale via combustion and gasification at laboratory scale. The thermal behaviours of co-combustion of Qinghai (QH) coal and Fushun (FS) oil shale were evaluated. The results indicated that the ignition index and burnout index of the blends reached maximum for 10% of FS. The increase of heating rates promoted the combustion performances. Significant synergistic interactions were observed in the temperature range of 410 - 480 °C. Besides, Flynn–Wall–Ozawa and Kissinger–Akahira–Sunose models were employed to derive the activation energy and the lowest apparent activation energy was found to be 64.1 kJ/mol at 10% blending of oil shale. Pre-exponential factors and reaction mechanism functions were investigated using an integral master-plots method. The slagging and fouling tendencies were alleviated with the addition of oil shale in combustion. On the other hand, a clean and effective utilization of inert oil shale semi-coke by co-gasification with coal was conducted under CO_2 atmosphere using a non-isothermal thermogravimetric analyser within the temperature range of 25 - 1050 °C. A back propagation neural network optimized by genetic algorithm (GA-BPNN) was applied to predict gasification mass loss curves at various heating rates, blending ratios and gasification temperatures. The GA-BPNN model was validated effectively using the experimental data, and the shrinking core kinetic model was found to be a better fit than the volumetric model.

The last part focused on process simulations of gasification plants for olefins production using renewable biomass. An indirect steam gasification of biomass to olefins (IDBTO) coupled with CO_2 utilization process was proposed. Comparisons of IDBTO and direct oxygen-steam gasification of biomass to olefins (DBTO) were performed in terms of their energy and exergy efficiencies, net CO_2 emissions, and economics. The results indicated that the olefins yield, energy and exergy efficiencies of IDBTO were about 19%, 49% and 44%, respectively, which were 2%, 8% and 7% higher than those of the DBTO process. Meanwhile, the quantitative economic performances (net present value and internal rate of return) of IDBTO were superior than that of the DBTO process.

Publications and awards

Journal publications

- **Peng Jiang**, Ashak Mahmud Parvez, Yang Meng, Mengxia Xu, Tianchi Shui, Tao Wu*. Exergetic, economic and carbon emission studies of bio-olefin production via indirect steam gasification process. Energy, volume 187, 15 November 2019, 115933.
- **Peng Jiang**, Dengting Guo, Xiang Luo, Mengxia Xu, Tao Wu*. Comparative study of coal and its macerals gasification and prediction of synergistic effects under entrained gasifier conditions. Journal of Energy Resources Technology, Volume 142, Issue 3, March 2020. DOI: 10.1115/1.4044552.
- **Peng Jiang**, Yang Meng, Ziyao Lu, Lan Xu, Gang Yang, Xiang Luo, Kaiqi Shi, Tao Wu*. Kinetics and thermodynamic investigations on CO_2 gasification of coal chars originated from conventional and microwave pyrolysis. International Journal of Coal Science & Technology. DOI: 10.1007/s40789-020-00358-5.
- **Peng Jiang**, Yang Meng, Ashak Mahmud Parvez, Xinyue Dong, Xinyun Wu, Mengxia Xu, Cheng Heng Pang, Chenggong Sun, Tao Wu*. Influence of oil shale blending on the combustion of coal and ash fusion behaviors. Energy, under first-round revision.

- Haitao Zhao#, **Peng Jiang#**, Zhe Chen, Collins I. Ezeh, Yuanda Hong, Yishan Guo, Chenghang Zheng, Hrvoje Džapo, Xiang Gao*, Tao Wu*. Improvement of fuel sources and energy products flexibility in coal power plants via energy-cyber-physical-systems approach. Applied Energy, Volume 254, 15 November 2019, 113554. (Co-first author)
- Yang Meng#, **Peng Jiang#**, Yuxin Yan, Yuxin Pan, Xinyun Wu, Haitao Zhao, Nusrat Sharmin, Edward Lester, Tao Wu, Cheng Heng Pang*. Fourth round review in the Chinese Journal of Chemical Engineering. Co-first author.
- Ashak Mahmud Parvez, Muhammad T. Afzal*, **Peng Jiang**, Tao Wu. Microwave-assisted biomass pyrolysis polygeneration process using a scaled-up reactor: Product characterization, thermodynamic assessment and bio-hydrogen production. Biomass and Bioenergy 139 (2020): 105651.
- Meng Yang, Yuxin Yan, **Peng Jiang**, Min Zhang, Jumoke Oladejo, Tao Wu, and Chengheng Pang*. Pre-treatment of Oil Shale: Microwave Processing and Effects on Milling Behaviour**.** Chemical Engineering and Processing-Process Intensification (2020): 107909.
- Meng Yang, Luyao Tang, Yuxin Yan, Jumoke Oladejo, **Peng Jiang**, Tao Wu, and Chengheng Pang*. Effects of Microwave-enhanced Pretreatment on Oil Shale Milling Performance. Energy Procedia 158 (2019): 1712-1717.
- Tang Luyao, Yuxin Yan, Yang Meng, Jiayu Wang, **Peng Jiang**, Cheng Heng Pang*, and Tao Wu. CO_2 gasification and pyrolysis reactivity evaluation of oil shale. Energy Procedia 158 (2019): 1694-1699.

Journal papers under preparation

- **Peng Jiang**, Yang Meng, Ruohang Wang, Mengxia Xu, Cheng Heng Pang, Tao Wu*. Utilization of an inert oil shale semi-coke in the coal gasification under CO_2 atmosphere: thermal, kinetics and artificial neutral network investigations. Energy & Fuel, prepared for submission.
- **Peng Jiang**, Ashak Mahmud Parvez, Yang Meng, Xinyue Dong, Mengxia Xu, Kaiqi Shi, Tao Wu*. Novel two-stage fluidized bed-plasma gasification based integration system for power generation from MSW: A thermodynamic investigation. Chemical Engineering and Processing-Process Intensification, prepared for submission.
- **Peng Jiang**, Xiang Luo, Gang Yang, Mengxia Xu, Tao Wu*. Distributions and modes of occurrence of heavy metals in opposed multi-burners (OMB) coal-water-slurry (CWS) gasification plants. Energy & Fuel, prepared for submission.
- **Peng Jiang**, Mengxia Xu, Xinyu Feng, Tao Wu*. Advanced exergy based evaluations of a MSW gasification to methanol process. Waste Management, prepared for submission.
- Meng Yang, **Peng Jiang**, Yuxin Yan, Xinyun Wu, Chenxi Fang, Yan Zhao, Edward Lester, Tao Wu, Chengheng Pang*. Co-pyrolysis behaviour, kinetics and product characteristics of four Chinese oil shales, prepared for submission.

Conference proceedings

- **Peng Jiang**, Yang Meng, Chengheng Pang, Tao Wu*. Thermal characteristics and ash fusion behaviours of co-combustion of coal and oil shale. Oral Presentation in the Annual Meeting of CIESC, October 17-19, Qingdao, China.
- **Peng Jiang**, Kaiqi Shi, Mengxia Xu, Tao Wu*. Process evaluation of an integrated SOFC and CLC with bubbling fluidized bed-plasma gasification of municipal solid waste system for power production with CO_2 capture. Oral Presentation in the International conference of applied energy in March 14-16, 2019, Oxford, United Kingdom.
- **Peng Jiang**, Kaiqi Shi, Xinyue Dong, Mengxia Xu, Tao Wu*. Thermodynamic analysis of air gasification of sewage sludge integrated with internal combustion engine for combined heat and power co-production. Oral Presentation in the 12th National Conference of Environmental Doctoral Students in Oct.18-20, 2018, Tsinghua University, Beijing, China.
- **Peng Jiang**, Kaiqi Shi, Xinyue Dong, Mengxia Xu, Tao Wu*. Thermodynamic evaluation of a SOFC coupling with CLC system to electricity fuelled by municipal solid waste. Oral Presentation in 2018 Ningbo Postgraduate Academic Festival: Doctoral Session in November, 2018, CNITECH, Ningbo, China.
- **Peng Jiang**, Dengting Guo, Mengxia Xu, Tao Wu*. Synergistic effect of coal and biomass co-gasification based on Aspen Plus. The third energy conversion conference, April 20-22, 2018, Xiamen, China.

Patent

- Tao Wu, Haitao Zhao, Gang Yang, Xueliang Mu, **Peng Jiang**, Shuai Liu, Chengheng Pang, Mengxia Xu. A test method for heavy metal adsorption capacity of mussel shell material. Application number: CN108828141A. November 16, 2018.

Awards

- “Doctoral Innovation Bronze Medal” in Ningbo Postgraduate Academic Festival, October 2018, Ningbo, China.
- “Academic Excellence Award in CPC party members” in the Party Branch of University of Nottingham Ningbo China, December 2019, Ningbo, China.

Acknowledgements

I would like to give my sincere appreciation to the following people:

Prof. Tao Wu, my principal supervisor, for his constructive guidance and financial supports throughout the duration of PhD study.

Dr. Mengxia Xu, my second supervisor, for his contributions in recruiting summer research interns and his assistance in revising manuscripts.

Dr. Chenggong Sun, my third supervisor, for his enthusiasm during my visit to the University of Nottingham, University park campus, UK.

Dr. Cheng Heng Pang, Dr. Haitao Zhao, Dr. Kaiqi Shi, Dr. Xiang Luo, Dr. Yipei Chen, Dr. Xueliang Mu, Dr. Shu Liu, Mr. Yang Meng, Mr. Gang Yang, Mr. Shuai Liu, Ms. Jiahui Yu and Mr. Chengrui Xie, for their helps and supports during my research work.

My family members and friends, for their love and unconditional supports and encouragements all through my studies.

The following funding bodies are acknowledged for partially sponsoring the research:

- National Key Research and Development Program of China: Large-scale coal-water-slurry gasification and its demonstration (2017YFB0602601).
- Key Research and Development Program of Ningxia Hui Autonomous Region: Study on high temperature thermal behaviours and corrosion

damage characteristics of impinging entrained bed gasifier (2019BCH01001).

- Ningbo “2025 S&T Innovation Megaproject”: Research and demonstration project of a complete set of equipment for pyrolysis and gasification of municipal solid waste (2018B10027).
- Key Laboratory for Carbonaceous Wastes Processing and Process Intensification Research of Zhejiang Province in the New Materials Institute for providing experimental equipment and facilities.
- University of Nottingham Ningbo China for providing scholarship.

Finally, during the preparation of this thesis, COVID-19 pandemic broke out unexpectedly worldwide. I am very grateful for all workers in the front line of anti-epidemic, especially for doctor and nurses in the hospitals, for without their consistent dedications, the thesis can’t be completed in time. Wish them all the best.

Table of contents

List of figures

List of tables

Chapter 1 Introduction

1.1 Background

1.1.1 Coal gasification

The resource endowment distribution in China is rich in coal but poor in oil and gas, which determines that coal is the dominated energy supplier [1-3]. Figure 1.1 shows the changes in energy consumption rate and its prediction conducted by BP energy outlook from 1990 to 2040 [4]. As can be seen from this figure that coal shares about 61.84% of the total primary energy consumption, compared to that of oil and gas which take up 18.89% and 6.19% in 2016, respectively. Besides, although the energy consumption share of coal will drop to about 35.93% in 2040 according the prediction with the addition of renewable energy, coal is still the primary energy.

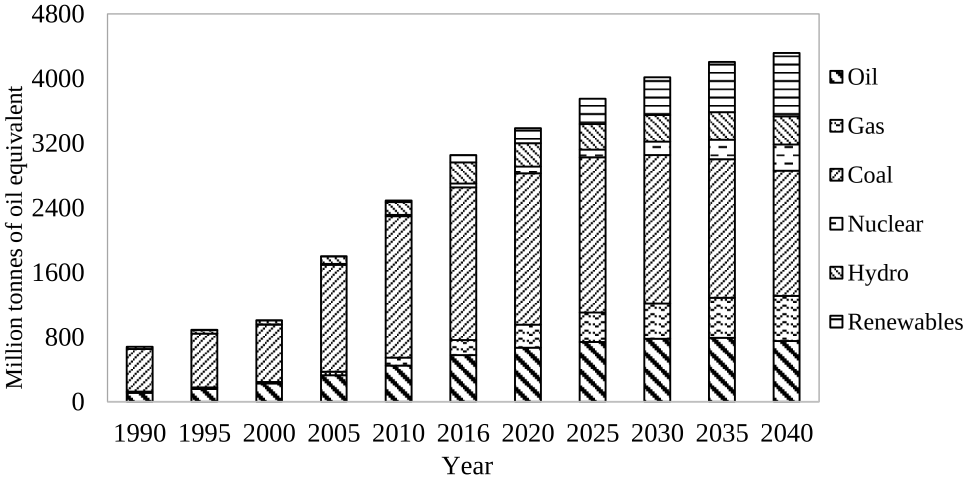

Figure 1. 1 Changes in energy consumption and prediction in China

There are mainly four types of thermochemical conversion of coal, namely pyrolysis, liquefaction, gasification and combustion for the produce of char, oil, syngas and heat respectively. Among these alternatives, coal gasification converting solid coal into syngas at high temperature is considered the cleanest utilization approach due to the near-zero sulphur and particulate emissions, high energy efficiency and flexible chemical productions [5-7]. In the coal gasification process, char gasification with gasifying agents is regarded as the rate-controlling step because of its lower reacting rate compared with water evaporation, pyrolysis and combustion. Therefore, studies on the kinetics and performances of char gasification are essential for the reactor design, control and efficiency.

Char reactivity is greatly affected by the char characteristics which are mainly decided by coal pyrolysis conditions, in which pyrolysis temperature is the most significant decisive parameter [8]. Microwave heating can realize rapid, volumetric, selective and non-contact heating for a coal by directly converting electromagnetic energy into thermal energy [9], and it is very different from the conventional heating mechanism that the heat transfer is from coal surface to inside by conduction. The microwave-induced char has different characteristics, which lead to different gasification reactivity, kinetics and thermodynamic performances. However, far too little attention has been paid to these aspects.

From the perspective of coal composition, macerals are the smallest and microscopically recognizable components of the organic constituent in coal [10]. Macerals are generally classified into three groups, namely vitrinite, liptinite and inertinite based on their physical appearances according to the classification of International Commission for Coal Petrology (ICCP) [11]. Besides, maceral groups also differ in their chemical compositions, which bring distinct technical performances. Therefore, an insight into macerals is the most fundamental step to understand the properties of the parent coal and subsequently, the efficiency of maceral-enriched feedstock [12].

Based on different gas-solid flow scheme, coal gasifiers are classified into fixed-bed gasifier such as Lurgi gasifier, fluidized bed gasifier such as U-gas gasifier and entrained bed gasifier such as Shell and opposed multi-burner gasifiers. The entrained gasifiers possess tar-free syngas, high carbon reaction conversion rates and low methane content rendering it becomes a superior candidate for large-scale gasification application [13]. The gasification behaviours of coal macerals and interactions among macerals in the typical entrained gasifiers have rarely been investigated.

On the other hand, coal also consists of different types of inorganic constitutes. During gasification at high temperature and pressure, a large part of the mineral and non-mineral inorganic elements are melt and reacted to formulate liquid phases [14]. The liquid slags are then solidified in a water quenching system. Coal slags consist of complex mineral species such as silicates, carbonates, sulfides, and amorphous inorganic components as well as unconverted char. The physical and chemical properties of coal gasification slags are dependent on feeding coal type, pre-treatment method and gasification conditions [15]. Generally, the gasification slags are classified as coarse slag and fine slag. Fine slag comprises fine particles entrained in the syngas, which are captured by the cyclone and water scrubber. However, coarse slag is from the bottom of gasifiers and has relatively low carbon content [16]. To safely dispose fine and coarse slags, it is imperative to investigate the characteristics, heavy metals concentrations and speciation features of coarse and fine slags.

As a large-scale gasification technology, the opposed multi-burner gasifier developing by East China University of Science and Technology (ECUST), has been applied over 50 companies worldwide [17], not much research has been conducted to gain an insight in the modes of occurrence, migration and leaching characteristics of heavy metals in coal and slags.

1.1.2 Thermal co-processing of coal and oil shale

Oil shale (OS) consists of organic material of kerogen distributed dispersedly within the sedimentary rock [18, 19]. It is estimated that China has 7.2×10^{11} tons of reserve OS [20]. Currently, the primary utilization strategy of OS is the retorting process for the productions of shale oil and fuel gas based on Fushun-type retorting technology [21, 22]. However, the abandoned fine OS particles, discarded semi-coke and tail gas, low-quality shale oil, complicated process and high cost lead to the OS retorting less competitive or even unprofitable especially under the low crude oil price condition [22, 23]. Compared with pyrolysis, direct combustion of OS for power generation is shown to be the most direct and straightforward technology [24] and has been employed in a commercial power plant using circulating fluidized-bed (CFB) technology in Estonia [25, 26]. Nevertheless, for few OS basins, such as Fushun Basin which is the largest oil shale mine in Asia [20], produce OS with low calorific value, high ash content and low shale oil yield [21] rendering it unsuitable for large scale mono-combustion.

As a conventional fossil fuel, coal will dominate in power generation [27]. The co-combustion of OS and coal for energy production offers a promising practical alternative for the utilization of OS, reduction of the pollutant emissions, enhancement of the coal combustion performances with an appropriate addition of OS [28, 29].

However, the blending of coal with OS can increase combustion complexities, including different combustion behaviours, ash fusion, slagging and fouling characteristics [30]. Besides, the un-additive synergistic interaction between coal and OS during co-combustion could improve the overall combustion performances. These properties have a significant impact on subsequent boiler efficiency and auxiliary equipment utilization [31]. Thus, it is of great importance to perform researches on the co-combustion of coal and OS to determine the stable combustion conditions and optimise blending ratio. Nevertheless, systematic investigations on co-combustion characteristics and interactions, kinetics, and ash fusion and mineral transformations of coal and Funshun oil shale have not been comprehensively explored.

Apart from co-combustion of coal and oil shale, how to utilization of the oil shale semi-coke generated from oil shale retorting processes deserve significant attention. It is estimated that the production of one ton shale oil produced 20-30 tons semi-coke [32]. Semi-coke has disadvantages being high ash, low energy density and heavy contaminations which cause environmental damage with direct landfill disposal [33]. Nevertheless, semi-coke contains organic compounds which can be considered as a fuel. Hence, development of sustainable, effective and environmental utilization of such semi-coke should be implemented. Similarly, thermal co-processing of coal and semi-coke is regarded as an efficient method to eliminate semi-coke as well as recover energy from the inert semi-coke [34-36]. Gasification is superior than combustion, as it involves a cleaner processing, low flue gas treatment, higher temperature, easy transport control and operation [37]. Investigations on co-gasification thermal behaviours and kinetics are required since they have significant influences on the modelling of gasification at industrial scale. However, far too little attention has been paid to the co-gasification of coal and oil shale semi-coke.

1.1.3 Olefins production from biomass gasification: process design and systematic evaluations

Light olefins including ethylene and propylene are the most important petrochemicals [38], and have been widely used in the production of plastics, elastomers and rubbers [39]. At present, the production of olefins relies on the thermal steam cracking of naphtha. However, the growing demand in olefins and the depletion and unsustainable nature of petroleum supply [40] have made the development of alternative routes to synthesize olefins very essential.

Methanol to olefins (MTO) technology offers a financially feasible pathway to utilize other types of fossil fuels, such as coal and natural gas for the production of olefins [41]. Because of the energy structure of China, many attempts have been made to develop coal to olefins (CTO) process. In 2010, the world first commercial MTO plant with an olefin production rate of 600 kt/y was launched in Shenhua, China. It is projected that the production of olefins from methanol would reach 15 Mt/y in 2020 [42], which accounts for about 20% of the total olefin production capacity in China. However, a well-to-wheel analysis found that the greenhouse gas emissions (GHG) from CTO was 2.6 times higher than that from oil to olefins (OTO) process even after carbon capture unit was added, the GHG emission would still be 1.7 times of OTO process [43]. Beside GHG emission, H_2/CO molar ratio in syngas from coal gasification is usually in the range of 0.2 to 1, which is not appropriate for the methanol synthesis [44]. Thus, CTO process requires large quantity of steam in order to adjust the H_2/CO ratio to be around 2.05 to 2.1.

Biomass is considered as an inherently carbon-neutral renewable solid waste, which contains higher hydrogen than coal [45]. Therefore, the employment of biomass instead of coal as the raw material to olefins production can be regarded as a sustainable decarbonization strategy. This scheme can be implemented through biomass gasification to methanol followed by methanol to olefins synthesis. Basically, there are two types of gasification options: indirect gasification and direct gasification [46]. Indirect gasification uses steam as the gasifying medium and the heat is provided by a combustor while both oxygen and steam are employed for direct gasification. Concerning biomass to olefins, most studies focused on the use of direct biomass gasification as the syngas production unit [39, 47-49]. Studies on utilize biomass indirect steam gasification as a source of syngas to olefins through methanol as the intermediate is limited. The energy, economic and environmental performances of the indirect biomass gasification to olefins are unclear.

1.2 Aims and objectives

1.2.1 Aims

The aim of this research was to investigate some fundamental and applied fields of clean conversions and utilizations of a suite of diverse solid fuels, i.e., coal, oil shale and biomass, through gasification approaches. The specific aims were : 1) to investigate the characteristics of coal chars prepared via both microwave-assisted and conventional pyrolysis from proximate and ultimate, XRD and SEM image perspectives; 2) to reveal process mechanisms and heavy metals distributions during coal gasification, co-combustion and co-gasification with oil shales through kinetics analyses, artificial neural networks, ash fusion behaviours and heavy metals characterizations; 3) to demonstrate the applications of gasification-based technology for chemical production (olefins) through novel process designs and evaluations with biomass as raw materials. Figure 1.2 presents the aims and contents of this research.

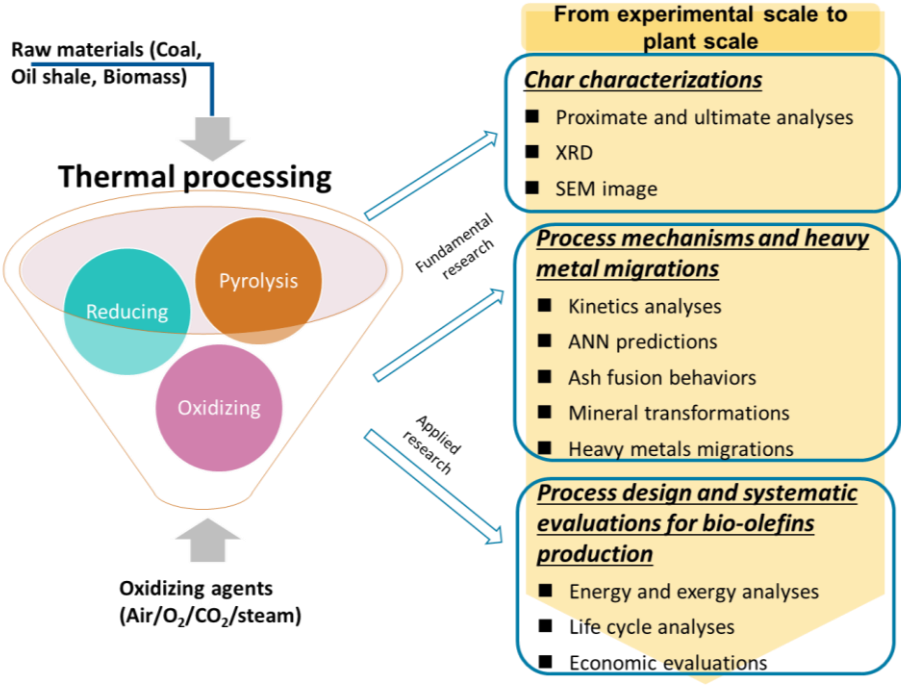

Figure 1. 2 Research aims and contents

1.2.2 Objectives

To achieve the above aims, both experimental and simulation methods were employed. The research objectives were divided into three parts including: 1) coal pyrolysis and gasification, 2) co-combustion and co-gasification of coal and oil shale, and 3) plant-scale simulations and evaluations of olefins production from biomass gasification. The objectives of each part are as follows:

(1) Coal pyrolysis and gasification

- ➢ Preparations and characterizations of coal chars via microwave-insisted pyrolysis and conventional pyrolysis at different temperatures.
- ➢ Comparisons between the CO_2 gasification of the microwave-induced char and the conventional chars from the perspectives of

gasification reactivity, kinetics parameters using shrinking un-reacted core model and random pore model, syngas compositions and cold gas efficiencies.

- Gasification behaviors of coal and its macerals under entrained gasifier conditions.
- Quantitation and effect of operating parameters on the interactions among macerals during gasification.
- Distributions and speciation of nine heavy metals in coals and gasification slags from two OMB's gasification plants.

(2) Co-processing of coal and oil shale (semi-coke)

- Evaluations of combustions characteristics, interactions and ash fusion behaviors of coal and oil shale co-combustion.
- Estimations of activation energies, mechanism functions and pre-exponential factors using varies FWO and KAS kinetic modes and master-plots methods for comprehensive understanding the co-combustion process.
- Kinetic calculations for non-isothermal CO_2-gasications of coal and oil shale semi-coke.
- Genetic algorithm combined with artificial neural networks to predict the TGA mass loss curves.
- Investigations the impact of heating rate on the behaviors of co-gasification.

(3) Biomass gasification for olefins production

- Design a biomass indirect steam gasification to olefins via methanol with CO_2 utilization process.
- Evaluations of the 3E (exergy, economic and environmental) performances of the proposed olefins process and comparison with the direct biomass gasification to olefins system.
- Explorations of the influence of some parameters on the thermodynamic and economic behaviors.

1.3 Structure of the thesis

The thesis is structured into 10 chapters and a brief outline is presented as follows.

Chapter 1 introduces the background of coal and macerals gasification as well as heavy metals distributions, thermal co-processing of coal and oil shales, and the gasification based technology for olefins production from biomass. It also conveys the research gaps, motivations, aims and objectives of this study.

Chapter 2 presents the literature review on origin and properties of coal, coal gasification, oil shale conversion, thermal co-processing of coal and oil shale, as well as biomass gasification for olefins production.

Chapter 3 shows the descriptions of experimental equipment and methods used in this thesis. The mathematic principles in the analysis of kinetics are also included.

Chapter 4, 5 and 6 are concerned with coal gasification. Chapter 4 presents the kinetics and thermodynamic investigations on CO_2 gasification of coal chars prepared via conventional and microwave pyrolysis. Chapter 5 shows the comparative study of coal and its macerals gasification and prediction of synergistic effects under entrained gasifier conditions. Chapter 6 illustrates the distributions and modes of occurrence of heavy metals in opposed multi-burners coal-water-slurry gasification plants.

Chapter 7 and 8 are devoted to the thermal co-processing of coal and oil shale. The former covers the influence of oil shale blending on the combustion of coal and ash fusion behaviours, while the latter demonstrates the utilization of an inert oil shale semi-coke in the coal gasification under CO_2 atmosphere through thermal, kinetics and artificial neutral network investigations.

Chapter 9 is related to the exergetic, economic and carbon emission studies of bio-olefin production via indirect steam gasification process.

The last chapter provides the conclusions to the present study and gives suggestions for possible future work.

Chapter 2 Literature review

2.1 Origin and composition of coal

2.1.1 Coal formation and classification

Coal is an organic and combustible biological rock appearing as brownish-black or black colour. The formation of coal begins at dead plant debris followed by the deposition of mud and water and after which, through diagenesis and metamorphic processes at several kilometres depths and hundred million years, transitions to a solid material which exhibits different physical and chemical properties from the original plants [50]. The coalification process takes place from peat to lignite, subbituminous coal, bituminous coal and anthracite in that order by the accumulation of time and mature transformation. The typical properties of the different rank coal are listed as Table 2.1 [50, 51].

Table 2. 1 Comparison of typical properties of lignite, bituminous and anthracite coal

Coal type	Lignite	Bituminous	Anthracite
Colour	Brown and blackish brown	Black	Greyish black
Hardness	Low	Relatively high	high
Agglomerating	Non-agglomerating	Agglomerating	Commonly agglomerating

Bulk density/(kg/m^3)	641-865	673-913	800-929
Moisture content/(w%)	39	2.2-15.9	2.8-16.3
Fixed carbon content/(w%)	31.4	44.9-78.2	80.5-85.7
Sulphur content/(w%)	0.4	0.7-4	0.6-0.77
Mineral matter/(w%)	4.2	3.3-11.7	9.7-20.2
Volatile matter [a] /(w%)		14-31%	2-14%
Gross calorific value [a] /(MJ/kg)	14.7-19.3	19.3-32.6	

[a] it is based on dry and mineral matter–free basis.

2.1.2 Coal macerals

Under incident light, organic macerals can be identified according to their colour, morphological feature, cellular structure and protuberances using a microscopy. Figure 2.1 shows some pictures of the different macerals observed under oil-immersion microscope.

Vitrinite, as displayed in Figure 2.1a and b, is the most abundant group and usually shares about 60-80% of the total coal constituent in many Chinese coalfields. The original formation entities of the vitrinite are mainly lignin and cellulose. Besides, proteins and lipid substances may also be included in this group. Vitrinite is typically shiny and glass-like in appearance and under an oil-immersion reflector, it is presented to be grey to light grey colour while no presence of protrusions. The reflectance of vitrinite depends on the maturity of coal, for the low rank to medium or high rank bituminous coal, the reflectance value is 0.5-1.6%, while for the anthracite coal, the reflectance is in the range of 2.0-10% [52].

Inertinite, as shown in Figure 2.1c and d, is the second abundant maceral group in coal and it accounts for 10-20% in many Chinese coal fields [50]. The original sources of the inertinite group are mainly from plant tissues and fine detrital fragments, which are similar with the vitrinite group. However, inertinite has undergone strong transformation under oxygen conditions during the first stage of deposition. According to the different coalification route and extent of tissue degradation, the intrinite group can be further divided into the following seven macerals including fusinite, semifusinite, funginite, secretinite, macrinite, micrinite and inertodetrinite, while the former two are the most abundant components in the inertinite group. Except for the white and structural appearances and a higher reflectivity compared with vitrinite group, a stronger aromatization as well as higher carbon and low hydrogen contents than the other maceral groups are also the unique behaviours possessed by inertinite group [11, 53].

Liptinite group, as seen in Figure 2e and f, shares a small portion in the coal fields and originates from spores, cuticles, resins, and algae species. Liptinite maceral contains high content of hydrogen and high percentages of aliphatic substances and has recognizable morphological features. Hence, it is regarded as the most reactive macerals. Besides, it shows black to grey colours under reflected light using oil-immersion microscopy and therefore the liptinite usually has lowest reflectance among all the maceral groups. Another distinguishable feature of liptinite is the fluorescent phenomenon varied from greenish-yellow colour when it is illuminated with violet or blue light [54, 55].The liptinite group can includes several submacerals, such as sporinite, cutinite , resinite and alginate.

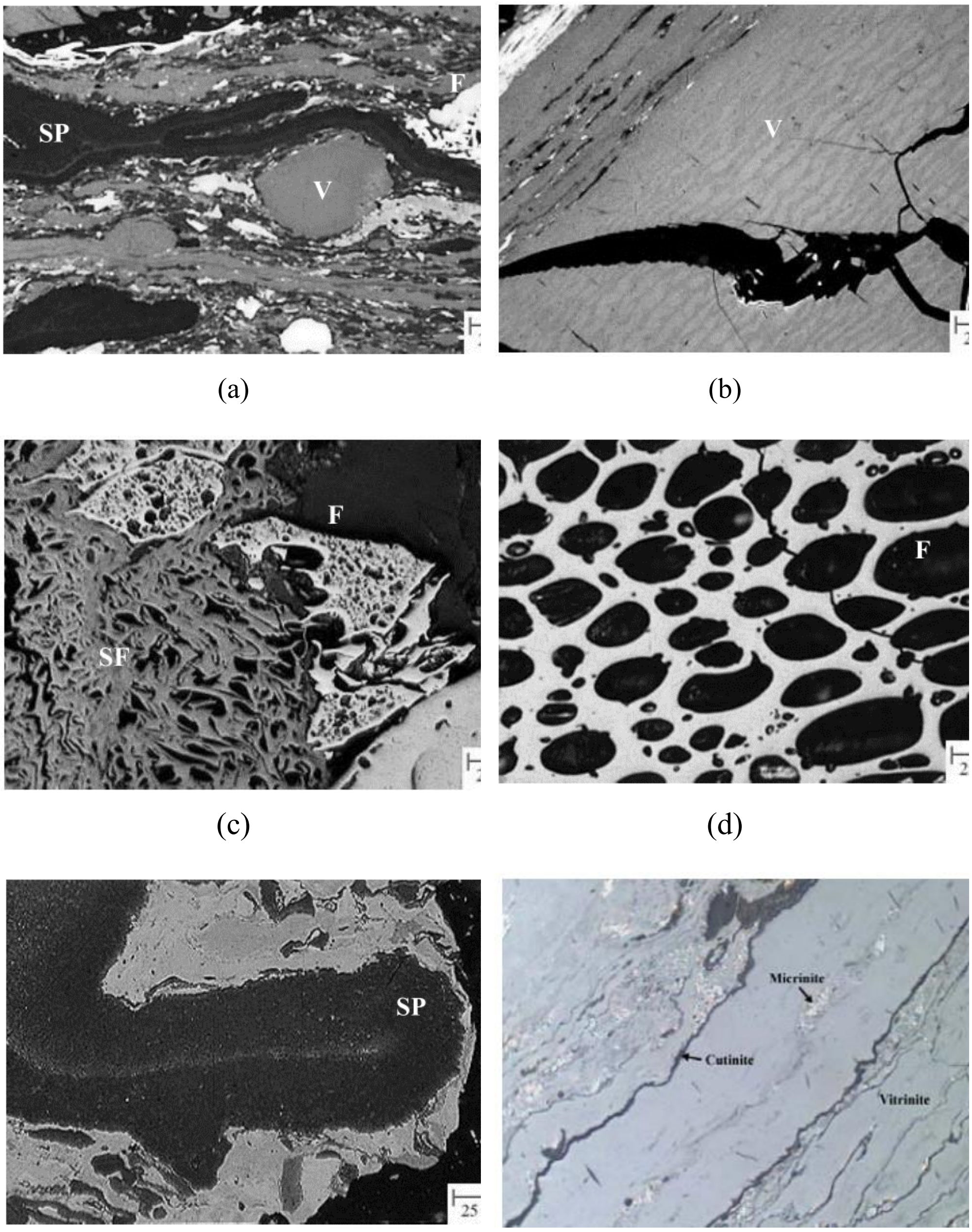

(a) (b)

(c) (d)

(e) (f)

Figure 2. 1 Photomicrograph of different macerals. Here V: vitrinite; SP: sporinite (liptinite); F: fusinite (inertinite); SF: semifusinite (inertinite)

2.1.3 Mineral matter

Mineral matter in coal contains all the minerals and other inorganic elements. Minerals originate from three sources including inherent minerals, secondary minerals and extraneous minerals. The inherent minerals mean the minerals such as alkali, which are intimately associated with macerals and reserved in the coal-forming plants. The content of inherent minerals is less than 10 wt% [56]. The secondary minerals are the external minerals such as kaolin, calcite and pyrite, which are blended with coal during coalification. Besides, the extraneous minerals refer to the mixed discrete rock fragments in the crushing and exploitation [57]. The determination of mineral contents can be achieved by testing the low temperature ash using X-ray diffraction techniques [58]. Table 2.2 shows some principal minerals found in coal [59].

Table 2. 2 Principal minerals in coal

Mineral	Formula	Mineral	Formula
Clay minerals		***Carbonate minerals***	
Kaolinite	$Al_2Si_2O_5(OH)_4$	Calcite	$CaCO_3$
Illite	$KAl_2(AlSi_3O_{10})(OH)_2$	Dolomite	$CaMg(CO_3)_2$
Chlorite	$Mg_5Al(AlSi_3O_{10})(OH)$	Siderite	$FeCO_3$
Muscovite	$KAl_2(OH,F)_2(AlSi_3O_{10})$	***Sulfate minerals***	
Montmorillonite	$Al_2Si_4O_{10}(OH)_2 \cdot H_2O$	Anhydrite	$CaSO_4$
Sulfide minerals		Gypsum	$CaSO_4 \cdot 2H_2O$
Pyrite	FeS_2 (cubic)	***Chloride minerals***	
Marcasite	FeS_2 (orthorhombic)	Halite	NaCl

Silicate minerals		Sylvite	KCl
Quartz	SiO_2	***Phosphate mineral***	
Oxide minerals		Apatite	$Ca_5(PO_4)_3(F,Cl,OH)$
Hematite	Fe_2O_3	***Others***	
Magnetite	Fe_3O_4	Goethite	$Fe(OH)_3$
Rutite	TiO_2	Rutile	TiO_2

2.2 Coal gasification

2.2.1 Coal pyrolysis

Coal pyrolysis is defined as the decomposition of organic substances through a series of physical and chemical reactions upon heating in the absence of air without catalyst [60]. Pyrolysis is the initial step in the coal gasification and accounts for almost 70 wt% weight loss of coal [61]. The products of coal pyrolysis are pyrolytic gas, liquid tar and solid char. The changes of coal during pyrolysis involve three steps, namely drying and degassing, depolymerisation and decomposition, and semi-coke to coke conversion [62]. Figure 2.2 shows a typical coal pyrolysis process.

The first step is the coal drying and degassing, which takes place from room temperature to 300 ºC. In this stage, coal properties and shapes are nearly unchanged. Before 120 ºC, coal is dehydrated and later the absorbed light gases such as CH_4, N_2 and CO_2 are removed from 120 to 200 ºC. Lignite begins to decarboxylate and slightly release CO_2.

The second step is the decomposition of volatiles beginning from 300 to 600 ºC. Coal experiences softening, melting and cohering with the increase of temperature. Simultaneously, a large amount of fuel gases containing CO, H_2, CO_2 and hydrocarbons are released and tars including complex aromatic are generated. At the high temperature above 500 ºC, coal continues to expanding and solidifying to form semi-coke.

The third step is the polycondensation reactions occurring at 600-1000 ºC. Semi-coke is further converted to coke with the releases of light fuel gas (mainly H_2) and little tar.

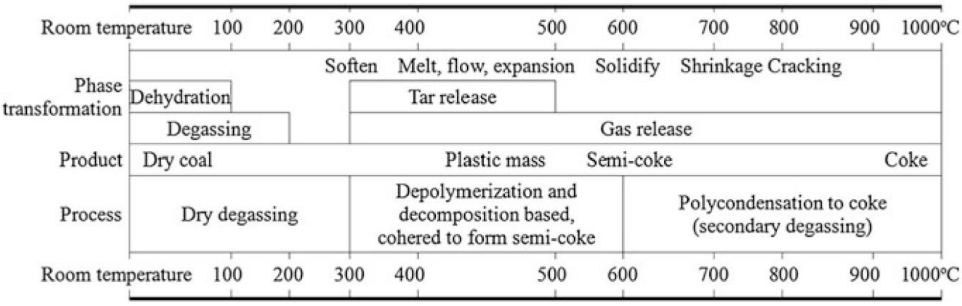

Figure 2. 2 Typical coal pyrolysis process

From the above steps, it can be clearly seen that the pyrolysis controls softening, swelling and particle agglomeration [63], and subsequently has a significant impact on char structure and reactivity.

2.2.2 Char gasification

Compared with pyrolysis, char gasification is relatively slow. The char gasification reactivity can be used as a representative of coal gasification. There are two types of reactions during char gasification, i.e., heterogeneous reactions (Eqs.(2.1)-(2.5)) and homogeneous reactions (Eqs.(2.6)-(2.7)), which are listed as follows [64]:

$$C + CO_2 = 2CO, \Delta H = +160 \text{ kJ/mol} \tag{2.1}$$

$$C + H_2O = CO + H_2, \Delta H = +119 \text{ kJ/mol} \tag{2.2}$$

$$C + O_2 = CO_2, \Delta H = -405.9 \text{ kJ/mol} \tag{2.3}$$

$$C + \frac{1}{2} O_2 = CO, \Delta H = -123 \text{ kJ/mol} \tag{2.4}$$

$$C + H_2 = CH_4, \Delta H = -87 \text{ kJ/mol} \tag{2.5}$$

$$CO + H_2O = H_2 + CO_2, \Delta H = -41 \text{ kJ/mol} \tag{2.6}$$

$$CO + 3H_2 = CH_4 + H_2O, \Delta H = -206 \text{ kJ/mol} \tag{2.7}$$

Reactions (2.1) and (2.2) are the core reactions in the gasification process and the required heat is provided by the combustion heat from Eq. (2.3). Besides, the syngas composition can be adjusted using the Reaction (2.6).

The char-CO_2 reaction of Eq. (2.1) is generally employed to test the reactivities of various chars at laboratory level using different contacting equipment such as thermogravimetric analysis and fixed bed furnace. The char-CO_2 mechanism can be interpreted using the widely accepted oxygen-exchange mechanism proposed by Gadsby et al. [65], as follows:

$$CO_2 \rightarrow CO + (O) \tag{2.8}$$

$$C + (O) \rightarrow CO \tag{2.9}$$

In the first stage, CO_2 breaks down at the char surface to produce CO and an atom of absorbed oxygen. Then, the absorbed oxygen is reacted with carbon and then evaporated as the form of CO. To reveal the retarding effect of CO, the following reaction is suggested as,

$$CO \leftrightarrow (CO) \tag{2.10}$$

It shows that produced CO can be absorbed in the active site and compete with oxygen.

Later, another combined oxidation/gasification mechanism describing the char oxidation and gasification under CO_2 and steam atmospheres is assembled by Hurt [66]. The exact expressions are shown as below.

Oxidation:

$$2C + O_2 \rightarrow CO + C(O) \tag{2.11}$$

$$C + C(O) \rightarrow (CO) + CO_2 \tag{2.12}$$

$$C(O) \rightarrow CO \tag{2.13}$$

Gasification:

$$C + CO_2 \leftrightarrow CO + C(O) \tag{2.14}$$

$$C(O) \rightarrow CO \tag{2.15}$$

$$C + H_2O \leftrightarrow C(O) + H_2 \tag{2.16}$$

$$C(O) \rightarrow CO \tag{2.17}$$

$$C + H_2 \rightarrow CH_4 \tag{2.18}$$

It should be noted that the expression of C(O) stands for the oxide complex on the char surface.

The heterogeneous reactions generally take place at the char active sites and can be described by Langmuir-Hinshelwood kinetic model [67, 68]. The gas-solid reaction path presents as follows:

- Gas reactant diffuses to the active site region;
- Gas absorbs onto the active site of char;
- Intrinsic chemical reaction is ignited;
- Product gases desorb from the reactive sites;
- Product gases diffuse away from the active site region.

Figure 2.3 depicts the above-mentioned gas-solid reaction regimes including chemical reaction controlled regime (Regime 1), internal diffusion controlled regime (Regime 2) and external diffusion controlled regime (Regime 3) [69]. At low temperature (Regime 1), concentrations of the reactant gases and product gases inside and outside of the char particles are the same. The active energy is the true active energy and bulk reaction order is the true order (m) [69]. As the temperature increases to around 1000 ºC, the reactivity is controlled by the internal diffusion (Regime 2). Reactant gas concentration at the active site of char is zero [70]. The apparent active energy at this regime is approximately half of the true active energy. Under regime 3, reactant gases are only reacted on the external surface. The apparent active energy tends to be 0 and reaction order is considered as the first order [71]. This phenomenon can be described by a shrinking core model.

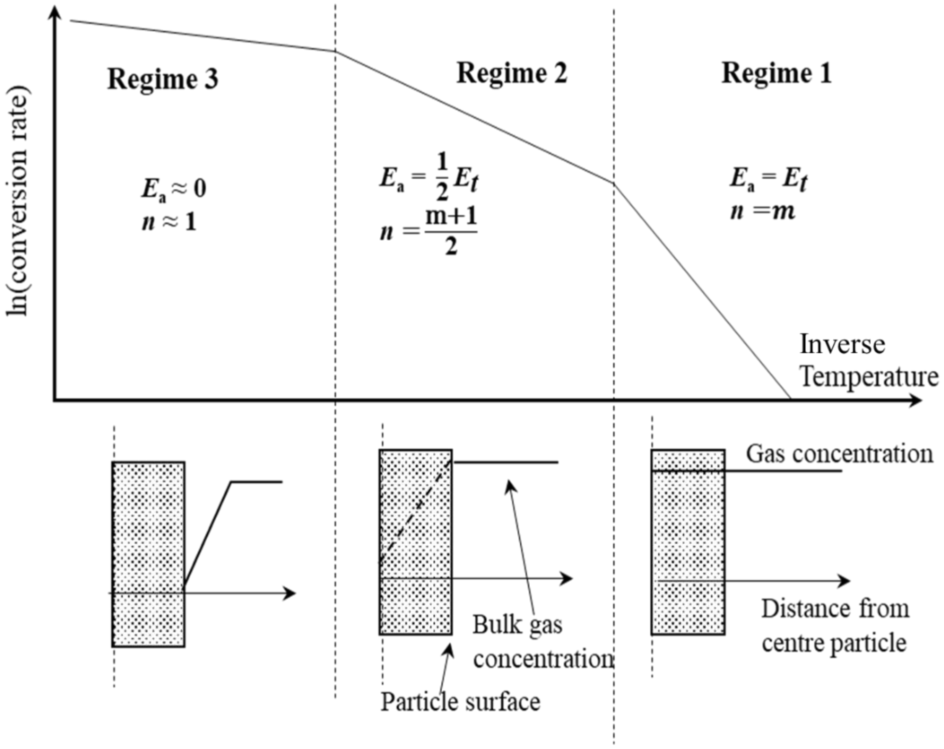

Figure 2. 3 Gas-solid reaction regimes. Regime 1,2 and 3 stand for chemical reaction control, internal diffusion control and external diffusion control zone, respectively. Here *n*,*m* are the reaction order, E_a is activation energy and E_t is the true activation energy.

It is therefore that the bulk reactivity of char not only depends on coal properties, char structures and morphology, but also relies on diffusivity affecting by operating conditions such as temperature, pressure, heating rate and reaction atmospheres [64]. Besides, other factors such as catalysts and reactor regimes can also impact reactivity [69, 72].

2.2.3 Effect of coal properties on char gasification

2.2.3.1 Rank

The effect of coal rank on char reactivity has been intensively investigated by [73-75]. It can be concluded that low rank coals are generally more reactive than high rank coals. However, Miura et al. [76] found that the reactivity of low rank coals was not always higher than those of high rank coals, as displayed in Figure 2.4. When the carbon content was less than 75%, the reactivity data were scattered, the reactivity showed a well decreasing trend when carbon content was beyond than 75%. Takayuki et al. [75] demonstrated that the char reactivity was also firmly associated with coal oxygen functional group and inorganic matters.

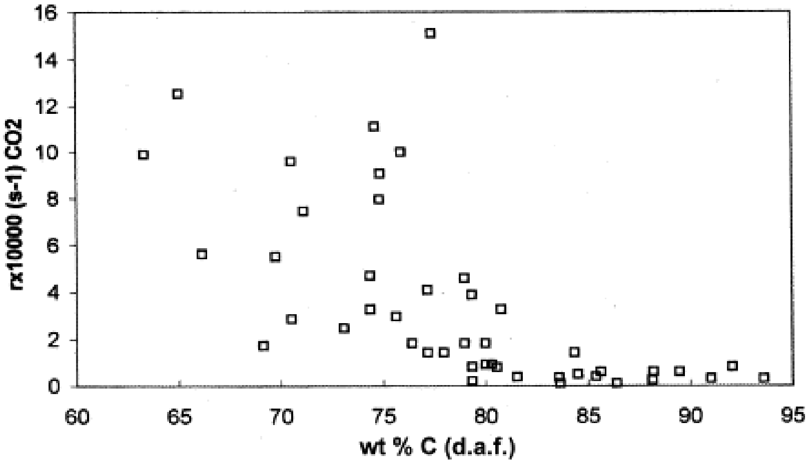

Figure 2. 4 Variation of char-CO_2 reactivity with carbon content

2.2.3.2 Macerals

Maceral components have a significant influence on the char morphology and structure, which lead to the impact on char gasification reactivity. Table 2.3 presents a summary of char reactivity of different macerals. Huang et al. [77] found that the inertinite char was more reactive than vitrinite char while the difference was rather small. Conversely, Megritis et al. [78], Sun et al. [79], and Wang et al. [80] reported that vitrinite char had a higher reactivity than inertinite. This was attributed to the vitrinite generated more thin wall char with high porosity while inertinite gave thick wall and poor porosity [81, 82]. Xie et al. [62] studied the gasification reactivity of different macerals from Pingshuo coal under CO_2 atmosphere and suggested that the liptinite was the most reactive, followed by vitrinite and inertinite. This was mainly because that the inertinite had a high aromatic condensation, which led to low active sites after pyrolysis. It can be found that macerals have significant on gasification reactivity while their impacts are complex.

Table 2. 3 Summary of char reactivity of different macerals

Author	Gasification condition	Main conclusion
Huang et al. [77]	Char was prepared by a fluidized bed reactor in N_2 atmosphere and gasification was conducted in CO_2 atmosphere, 0.1MPa, 850 °C	Reactivity: inertinite char > virtrinite char
Megaritis et al. [78]	Char was pyrolyzed in pure He atmosphere and gasification in CO_2, 1 and 20 bar, and at 1000 °C	CO_2 –gasification conversion: vitrinites > liptinites > inertinites
Sun et al. [79]	CO_2 gasification of maceral chars using CAHN TG-151 pressurized TG at 0.1 or 3 MPa	Gasification reactivity of maceral chars: vitrinite > inertinite chars
Wang et al. [80]	Pyrolysis and CO_2 -gasification reactivity in a STA409C TG	Reactivity: vitrinites> inertinites
Xie et al .[62]	CO_2 -gasification reactivity in a TGA at atmospheric pressure	Reactivity: liptinites > vitrinites> inertinites

2.2.3.3 Minerals

Numerous researches have stated that the alkali, alkaline earth and transition metals contained in the minerals have catalytic effects on char gasification. Xie et al. [62] compared the gasification conversion of one char containing ash with the char without ash, as presented in Figure 2.5. Clearly, the curve one of ash containing char had a shorter time to gasify completely. However, the catalytic effects were effective up to 1060 °C, and it showed less pronounced when gasification temperature was beyond than 1060 °C [83]. Ye et al. [83] examined the catalytic char CO_2 gasification and reported that Na had highest catalytic effect, followed by K, Ca and Ni.

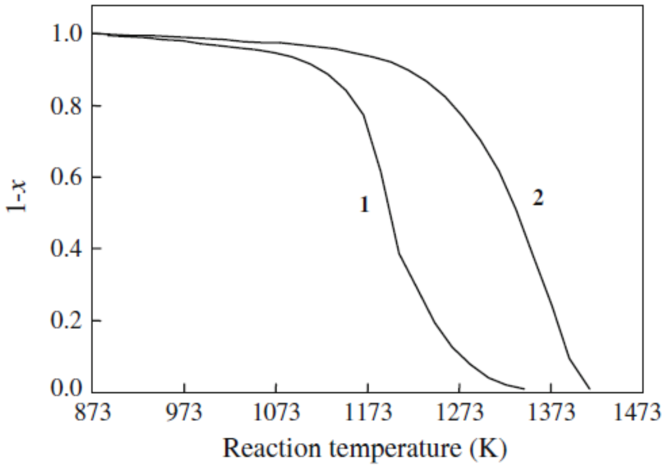

Figure 2. 5 Influence of ash on char conversion. 1-char containing ash; 2-char without ash

2.2.3.4 Particle size

Particle size is a decisive parameter on gas diffusion. Kovacik et al. [84] found that when particle size was larger than -105 + 74 μm, the CO_2 diffusion could affect the gasification rate. Kajitani et al. [85] investigated the char gasification rate using different particle size at various temperatures. It was concluded that smaller char had a high gasification reactivity at high temperature while the reactivity had no different for different size char particles at low gasification temperature. The quantitative trend for reactivity versus temperature at different particle sizes are exhibited in Figure 2.6 [85]. This showed that pore diffusion played a more important role at high temperature for large particle size. However, Chin et al. [86] reported no diffusion effect even through the char particle size was up to 1000 µm. Hanson et al. [87] also concluded that the coal particle size ranging from 0.5-2.8 mm was insensitive to char reactivity.

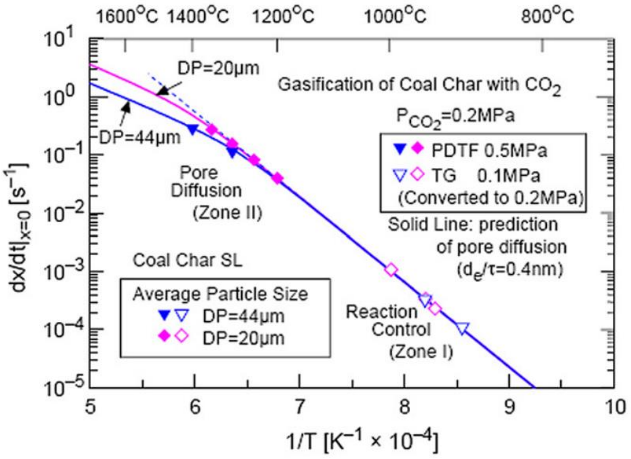

Figure 2. 6 Influence of particle size on char gasification rate

2.2.3.5 Pyrolysis processes

Pyrolysis induced char has some very different properties with the original coal. For example, for a typical coal, the porosity and surface area can increase from 2% to 20% and from 10-20 m^2/g to 200-400 m^2/g, respectively, after pyrolysis [88]. Because char structures have a dominated influence on char gasification stage, investigations on the effect of operating parameters on pyrolysis are required.

Effect of coal rank on char properties can be found in the literatures of [89-92]. Anthracite coal char has highest value of dielectric constant due to a higher aromatic carbon structure concentration. Besides, an increase of coal particle size resulted in the addition of char yield whist the crystallinity of char was observed to be independent to particle size [93].

Pyrolysis temperature has a positive impact on the char surface area and volatile content. Ludvig et al. [94] conducted an experiment of coal pyrolysis at the temperature from 350 ºC to 600 ºC. It was showed that N_2 physisorption was almost unchanged while CO_2 physisorption changed greatly indicating the increase of microporous in the char. Besides, the pore volume and area of char increased firstly before 700ºC, while when temperature was higher than that value, the pore volume decreased due to the block of the pore [95]. Recently, Xiao et al. [96] studied the effect of high-temperature pyrolysis on the char structure, their results found as the addition of pyrolysis temperature from 1000-1600 ºC, four indicators including BET surface area and char reactivity, power resistivity and real density exhibited a decrease trend. With respect to operating pressure, the increase of pyrolysis pressure up to 40 bar, char reactivity exhibited an addition trend [97].

Microwave heating can realize rapid, volumetric, selective and non-contact heating of coal by directly converting electromagnetic energy into thermal energy [9], and it is very different from the conventional heating mechanism that the heat is transferred from the coal surface to the centre via conduction driven by temperature gradients [98]. Figure 2.7 shows the difference between microwave and conventional heating [99, 100].

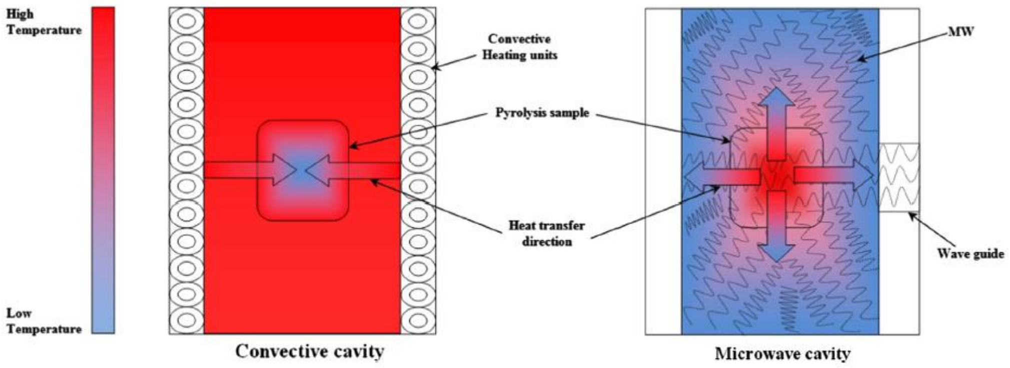

Figure 2. 7 Schematic diagram of microwave and conventional heating

Microwave absorption ability depends on dielectric properties. However, it is demonstrated that coal has low dielectric loss and is transparent to microwave at low temperature [101]. To aid microwave pyrolysis of coal at the initial stage, solid microwave absorbers with high dielectric loss materials, such as activated carbon, biomass char and SiC, can be added to coal to increase microwave assimilation capacity. The dielectric loss ability of coal is firmly associated with temperature, the relative dielectric constant increases sharply when pyrolysis temperature is above 500 ºC [101]. Subsequently, the microwave absorption ability of coal improves significantly and can be heated rapidly.

Previous investigations on microwave pyrolysis of coal were mainly concentrated on three areas, including: (i) effect of microwave pyrolysis on the physicochemical properties such as grindability and drying of coal [102-104]; (ii) dielectric properties, interaction mechanism and enhancement pyrolysis of coal by microwave absorbers [101, 105-107]; and (iii) properties of pyrolysis products of gaseous, tar and char [108-110] as well as microwave reactor and its scale up [111, 112]. It was demonstrated that microwave pyrolysis showed more gaseous and less tar, high quality liquid fuels and more energy efficient than conventional pyrolysis [108, 109]. Abdelsayed et al. [108] investigated the effects of pyrolysis temperatures and microwave heating on product distributions and char structure changes of Mississippi coal char and tested the combustion reactivity using a non-isothermal thermogravimetric analysis (TGA). Studies on the structures, gasification reactivity and kinetics of pyrolysis-assisted coal char are rarely reported.

2.2.4 Effect of operating conditions on char gasification

2.2.4.1 Temperature

Both of the carbon water gas reaction and carbon CO_2 reaction are endothermic, the increase of temperature is beneficial for gasification. This statement was validated by the experiment carried out by Liu et al. [113], who found that carbon conversion increased with temperature at the same gasification time. Everson et al. [114] investigated the influence of temperature on gasification rate at 100% CO_2 condition and they observed that higher temperature could shorten the reaction completion time. Besides, Ye et al. [73] concluded that the gasification rate was strongly dependent on the temperature.

2.2.4.2 Pressure

Regarding the effect of gasification pressure, Schmal et al. [115] carried out char-steam gasification experiment and found that high pressure did not change the H_2 concentration, while methane concentration increased and prohibited CO/CO_2 ratio. For CO_2 char gasification, Adanez et al. [116] reported that char reaction rate exhibited a decreasing sensitivity to the variation of pressure as shown in Figure 2.8 [116, 117]. With the increase of pressure, the reaction rate increased dramatically then it levelled off when pressure beyond 1.5 MPa. This feature was also supported by the experiment investigated by Sha et al. [117].

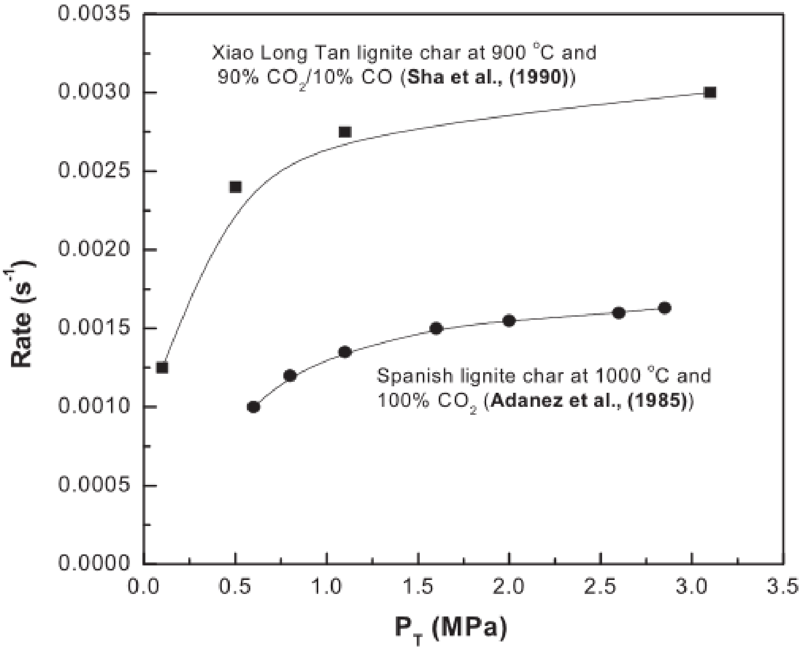

Figure 2. 8 Effect of gasification pressure on the char CO_2 gasification rate

2.2.4.3 Heating rates

Heating rates have significant influences on the char conversion and gasification reactivity, which have been studied by different researchers [118-120]. Figure 2.9 shows a char conversion versus temperature at different heating rates [118]. With the increase of hearing rate, the char conversion curve moved to a higher temperature zone. This was due to the fact that at the lower heating rate, the time to reach a certain conversion was longer, so the diffusion effect was less than that of higher heating rates, which leading to a relatively lower temperature.

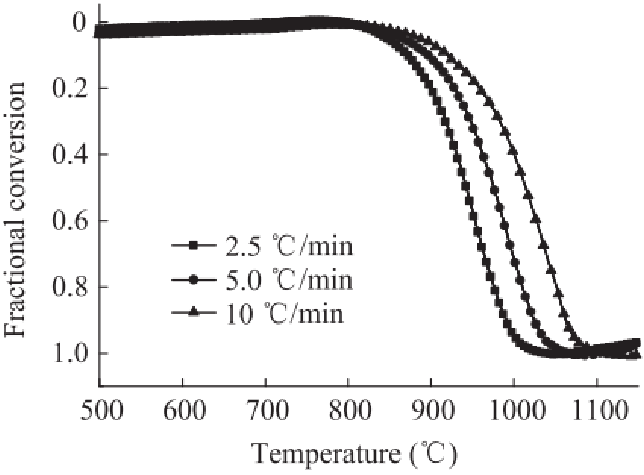

Figure 2. 9 Variation of CO_2-char conversion versus heating rates

2.2.4.4 Atmosphere

Generally, the participated gasifying agents are oxygen or air, steam, carbon dioxide and hydrogen in a typical gasifier. There are numerous studies focusing on the effect of different agents on the char reactivity and mechanism [119, 121-126]. Roberts et al. [125] carried out the gasification of coal char with O_2, CO_2, and H_2O using a pressurized thermogravimetric analyser. They concluded that the order of char relative reaction rate for different agents was: $O_2 > H_2O > CO_2$. Besides, the reports from Zhang et al. [126] also confirmed the reactivity of char steam gasification was about 10 times high than those of the char CO_2 gasification. To describe the competition of CO_2 and H_2O co-gasification of coal chars, a modified Langmuir–Hinshelwood (L–H) gasification model was proposed by assuming that the two agents share partially active sites [127]. However, Zhang et al. [128] confirmed the common active site mechanism stating that H_2O and CO_2 shared common active sites in char gasification and they pointed out that the char–H_2O reaction was inhibited by the char–CO_2 reaction.

2.2.5 Gasifiers

2.2.5.1 Different types of gasifiers

Based on different gas-solid flow scheme, coal gasifier can be generally classified into moving/fixed bed gasifier, fluidized bed gasifier and entrained bed gasifier. The comparisons with respect to typical gasifier appearances and technological characteristics are presented in Table 2.4 [129, 130]. The entrained gasifier possesses tar-free syngas, high carbon reaction conversion rates and low methane content rendering it becomes a superior candidate for large-scale gasification applications [13].

Table 2. 4 Comparison of different gasifiers and their technological performances

Gasifier type	Moving/Fixed bed	Fluidized bed	Entrained bed
Depiction	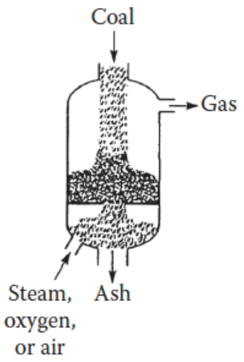	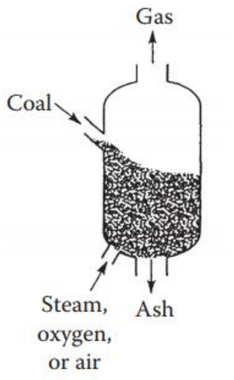	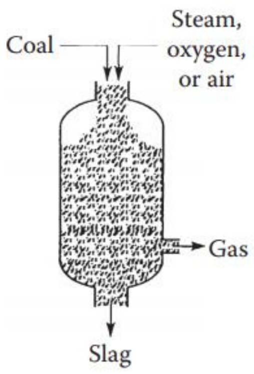
Temperature profile	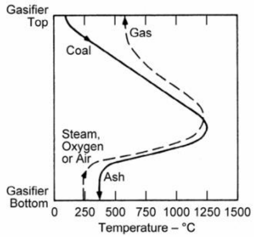	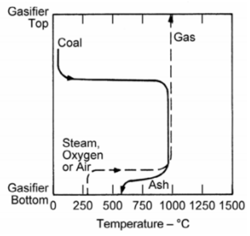	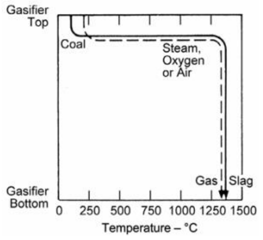
Outlet temperature/	425-700	900-1050	1250-1600

°C			
Oxidant demand	low	moderate	high
Steam demand	low	moderate	low
Ash condition	dry ash or slagging	dry ash or slagging	slagging
Size of coal feed/mm	6-50	6-10	<0.1
Heating rates/ (°C/s)	< 50	<200	>10000
Average residence time/s	~ 3600	>100	0.5-10
Acceptability of fines	limited	good	unlimited
CO_2 in raw gas/vol%	26-29	18	6-16
Tar produced	moderate to high	intermediate	absent
CH_4 in raw gas/vol%	8-10	6	<0.3
CO/H_2	1.7-2.0	0.7	0.7-0.9
Typical processes	Lurgi	KBR Transport Gasifiers	Shell, GE, OMB

2.2.5.2 Typical large scale entrained gasifiers

GE Texaco gasifier

The Texaco gasification technology was previously developed by Cheveron corporation in the 1950s and then it was purchased by General Electric in 2004. The process employs an entrained flow, downward feed, refractory lined gasifier, which is used to generate syngas from a coal-water slurry (about 65 wt%) and oxygen (> 95%). Figure 2.10 shows a schematic diagram of Texaco gasifier with radiant cooling mode [131]. The slurry feedstock and pure oxygen from air separation plant are pumped and compressed into the injectors mounted at the top of the gasifier. In the gasifier, coal is reacted with oxygen and steam to form syngas and slag. The operating temperature and pressure are 1300-1700 ºC and 4.0-8.7 MPa, respectively.

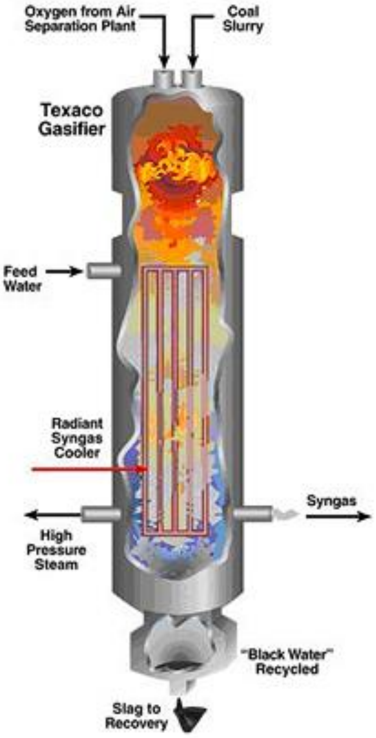

Figure 2. 10 Schematic diagram of Texaco gasifier with radiant cooling mode

The raw syngas from the gasifier is cooled by a radiant cooler, where water is injected to absorb the sensible heat in the syngas and slag and then generates high-pressure steam. At the bottom of gasifier, both syngas and slag are quenched with water. Subsequently, slag is discharged by a lock hopper. The unit capacity can be up to 4000 tons coal per day. The advantages of Texaco gasifier include: 1) wide adaptability for coal type; 2) high carbon conversion ratio (97-98%); 3) high syngas yield. Therefore, it is one of the most widely applied gasification technologies in China with over 40 gasification facilities.

OMB gasifier

The Opposed Multi-Burner Gasifier (OMB) was developed by East China University of Science and Technology in 1990s. The OMB gasifier includes four evenly-distributed opposed nozzles where coal water slurry (CWS) and oxygen are injected into the top of gasifier, as shown in Figure 2.11. This configuration allows equal and flexible control of coal water slurry. The raw syngas generated in the gasifier together with the melting slag are cooled in the multi-layer quench chamber. The coarse slag can be collected at the bottom of the gasifier. The main parameters of the OMB technology are presented in Table 2.5 [132]. Compared with other Texaco gasifiers, OMB gasifier has superior properties in system performances, stability and reliability [133].Currently, the unit operating capacity ranges from 500 to 3000 tons per day of coal and an ultra-large scale gasifier of processing 4000 tons per day of coal is under construction in Inner Mongolia, China [134]. Besides, OMB gasification process has been applied over 58 projects with near 160 gasifiers.

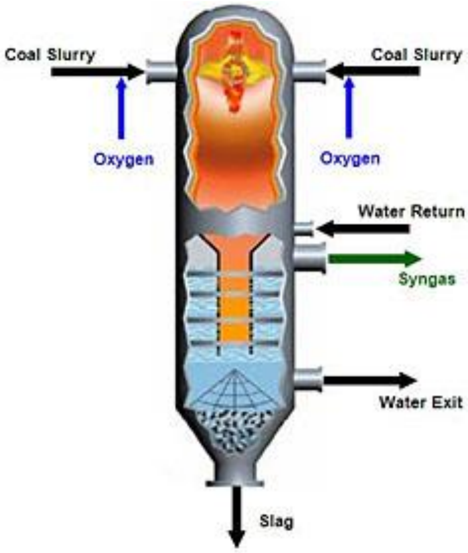

Figure 2. 11 Schematic diagram of OMB gasifier with CWS

Table 2. 5 Main parameters of OMB gasifier

Item	Value
Pressure /MPa	1.5-8.5
Temperature/°C	1300
Specific oxygen consumption/ (Nm^3 O_2/($CO+H_2$) Nm^3)	0.41
Specific coal consumption/ kg coal/($CO+H_2$) Nm^3	≤0.55
Carbon conversion ratio/%	>98
Effective syngas content/%	>81

Shell gasifier

The Shell coal gasification began in 1972 and it fits a wide variety of feedstocks such as refinery residual oil and pet coke [135]. Shell gasifier is a dry-feed, pressurized, entrained flow and slagging reactor. Figure 2.12 shows a simplified diagram of Shell coal gasification process [136]. The feeding coal is dried and pulverized before is pressurized to the gasifier via lockhoppers. Simultaneously, pure oxygen and steam are also mixed and injected to gasifier to react with coal char. The high temperature raw syngas exits to the gasifier and then is firstly quenched by the recycled cooling syngas at the top of gasifier. Subsequently, raw syngas goes through a syngas cooler, which is designated to produce high pressure steam and low pressure steam. The entrained fly slag contained in the syngas is separated with cyclones. Besides, the molten slag is cooled by the membrane wall and the released heat is recovered by water for medium pressure steam production. Shell gasifier operates at 1400- 1700 °C and pressures of 3-4 MPa. The dominant advantages of Shell gasifier are feed flexibility and low specific oxygen consumption of 0.35 Nm^3 $O_2/(CO+H_2)$ Nm^3, making it a good candidate for wide application with over 50 Shell gasifiers in operation worldwide [137, 138].

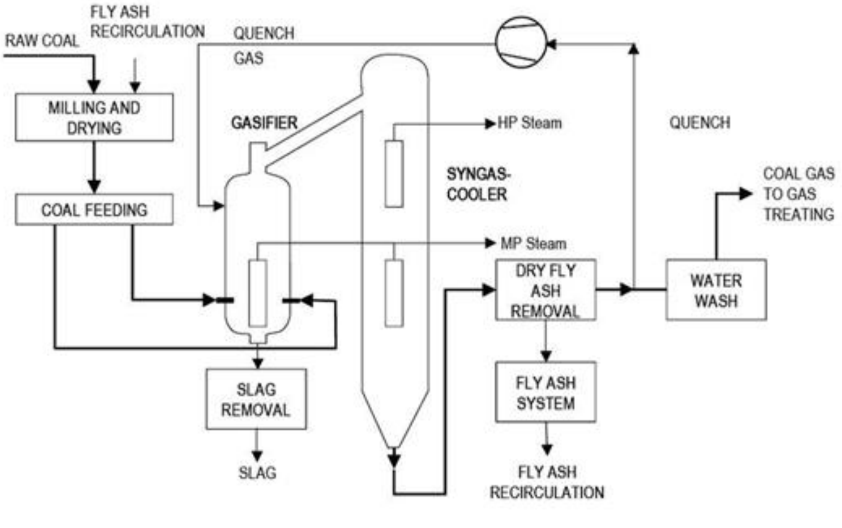

Figure 2. 12 Simplified diagram of Shell coal gasification process

2.2.6 Heavy metals in gasification slags

In the entrained gasifier, mineral matters are discharged in the form of coarse and fine slags. Coarse slag is the vitreous solid at the bottom of gasifier, while the fine slag is the fine ash particle entrained in the syngas and collected at the downstream of gasifier. Figure 2.13 presents a typical route of mineral matter transformation of coal in entrained gasifiers [56, 139]. Different size of slags are possibly formulated through char fragmentation, ash coalescence, and heterogeneous and homogeneous condensation of inorganic species [140]. When unconverted carbon particles contact with slag surface, they might deposit on the surface [139]. Therefore, the collected slags have organic matters.

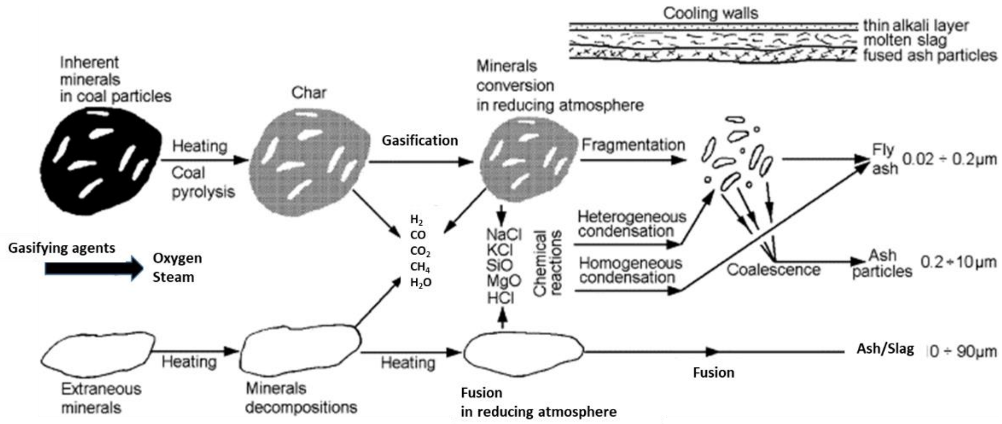

Figure 2. 13 A typical route of mineral transformation in entrained gasifiers

Recently, studies on gasification slags have been concentrated on the morphology, mineralogical compositions, and combustion and gasification reactivity, etc. [15, 141-145]. Besides, the impact of particle size of slags on gasification activities were also reported [144]. With respect to the thermal behaviour and fate of heavy metals during coal gasification, there are some experimental and thermodynamic calculations being carried out [146-152], which are mainly focused on the underground coal gasification or gasification process in fixed-bed dry-bottom gasifiers. Only a few attempts have been made to evaluate the leachability, enrichment and speciation performances during entrained-flow gasification [153-155]. For example, the concentration and enrichment characteristics of 21 hazardous trace elements under three different types of entrained flow gasification processes, i.e., Opposed Multi-burners and Texaco gasification technologies, were studied [154]. The modes of occurrence of 17 trace elements were determined using a five-step sequential extraction [155]. However, for the large-scale gasification technology, the OMB gasifier, not much research has been conducted to gain an insight in the modes of occurrence, migration and leaching characteristics of heavy metals in coal and slags.

2.3 Oil shale conversion

2.3.1 Oil shale retorting and semi-coke utilization

Oil shale is an ash-rich petroleum source rock with high contents of organic matter [156]. The main organic matter contained in oil shale is kerogen and a typical molecular structure of kerogen in Huadian oil shale is shown in Figure 2.14 [157]. As can be seen from this figure that oil shale is mainly composed of carbon, hydrogen and oxygen with little nitrogen and sulphur. Compared with other solid fuels such as coal and biomass, oil shale is rich in H/C, as presented in Figure 2.15 [158]. High H/C indicates that oil shale can generate a lot of hydrogen free radical, which act as a hydrogen donor [159]. Currently, it is estimated that the world oil shale resources are about 689 billion tons of shale oil, which is about four times of crude oil resources [160]. Despite its abundance, only few countries including China, Estonia and Brazil have developed commercial scale facilities for shale oil production through retorting or pyrolysis method. Figure 2.16 shows a schematic diagram of oil shale retorting process [159]. As indicated in the figure, the organic part of oil shale of kerogen and bitumen is firstly converted into bitumen upon heating before 300 °C in the absence of air. Simultaneously, the contained moisture is vaporized while minerals are kept unchanged. As the temperature increases to 500 °C, the bitumen is further decomposed into shale oil, gas, pyrolytic water and carbonaceous residues. Together with the minerals, the residues are known as semi-coke [161].

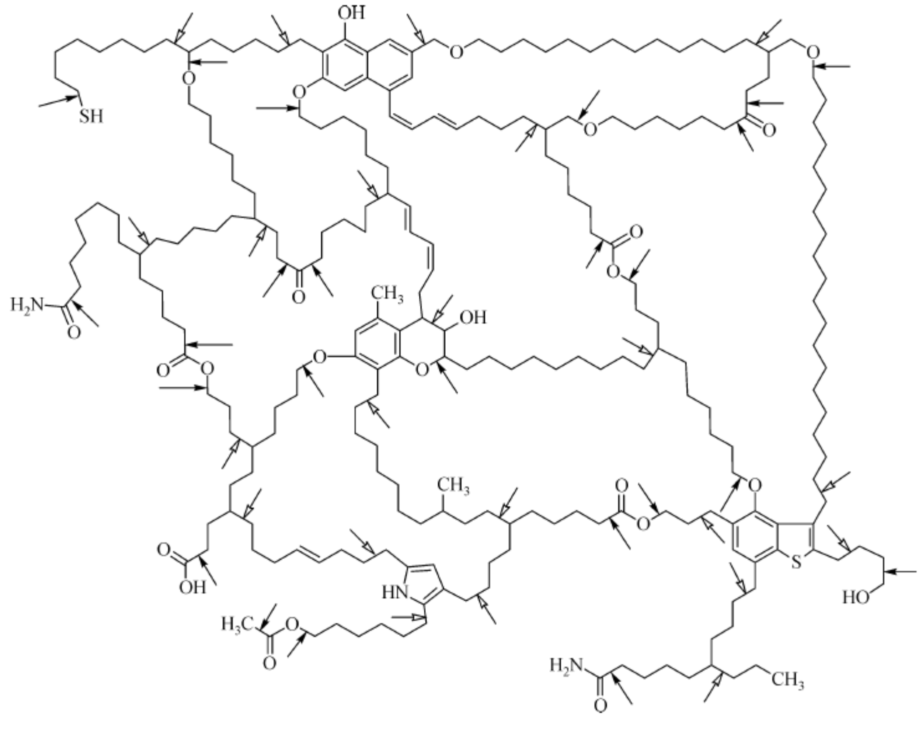

Figure 2. 14 Average molecular model of kerogen from Huadian oil shale

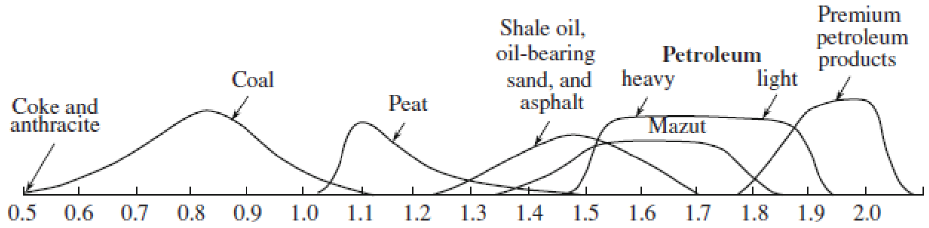

Figure 2. 15 H/C ratio distributions among different fuels

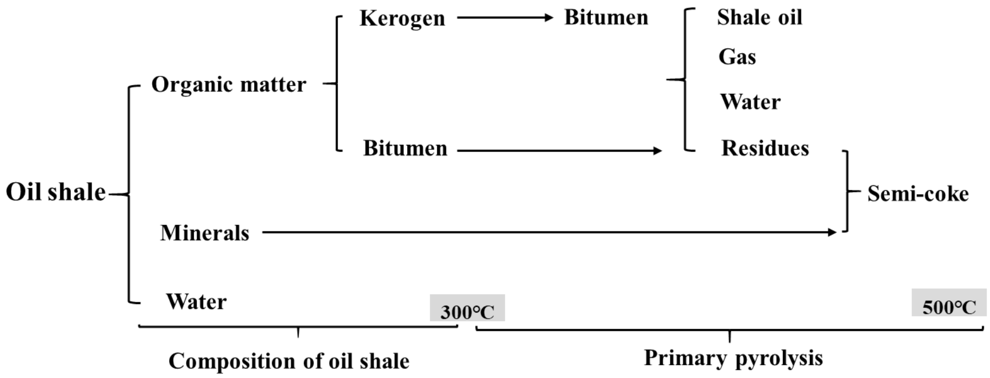

Figure 2. 16 Schematic diagram of oil shale retorting/pyrolysis process

Oil shale semi-coke is characterized as low carbon and high ash energy source [162]. At present, the majority of semi-coke is disposed in landfills. However, semi-coke is classified as a dangerous waste as it contains phenols, polycyclic aromatic hydrocarbon (PAH) and heavy metals, which cause groundwater pollution [161]. The other alternative utilizations of semi-coke residues include cement and binding agent productions [163, 164], pyrolysis and co-pyrolysis [165, 166], combustion and co-combustion with other high calorific fuels [35, 167-172], sorbent materials [162, 173], and activated carbon production [172]. Among them, semi-coke combustion is the most straightforward and efficient manner to recover the energetic potential for it does not require complex separation, leaching or activation processes. Han et al. [174] proposed two technical routes for large scale semi-coke utilization through combustion. One was integrated with oil shale retorting, where semi-coke was burned in a circulating fluidised bed (CFB) boiler for heat supplement for the retorting reactor. The other was to realize semi-coke combustion in a CFB, and this technology had been achieved in Estonian retorting plants [175].

2.3.2 Oil shale combustion

Except for retorting, direct combustion of oil shale for power production is another conventional method for the utilization of oil shale. Due to the high hydrogen content, the thermal stability of oil shale is lower than coal upon heating. Hence, oil shale is easy to ignite. It was demonstrated that the ignition behaviour of oil shale was homogeneous [176]. Thermal analysis was applied to oil shale combustion and it was found that oil shale combustion existed two distinguishable mass loss stages. One was low-temperature stage, in which volatile was burnt between 280 – 500 °C, whilst at high-temperature stage, the heterogeneous reactions of fixed carbon and residual volatile with air were taken place and the mass loss was about 10% from 620-730 °C [176]. Besides, it was reported that the activation energy of the low-temperature stage was lower than that of high-temperature stage based on the method of Freeman-Caroll. Increasing heating rates led to a higher activation energy [177].

Currently, several countries as Estonia, China, Israel, and Germany have commercial oil shale combustion technologies such as pulverized furnaces (PF), bubbling fluidized bed, and circulating fluidized bed [178, 179]. Because PF operates at high temperature and has low thermal efficiency of 30%, which makes PF unfavourable for oil shale combustion[180]. On the other side, CFB has a higher combustion efficiency of 36%, low SO_x and NO_x emissions, making it gradually becomes the leading technology for oil shale combustion [179, 181].

2.4 Coal and oil shale thermal co-processing

2.4.1 Coal and oil shale co-combustion

Oil shale properties is determined by its formation and some oil shales (such as Funshun oil shale) with high ash content up to 80-90% and low heating value and shale oil yield, which are unsuitable for directly combustion [179]. Due to the richness of coal in China, co-processing of oil shale and coal is emerged as an attractive option to utilize oil shales. On the one hand, oil shale has high H/C ratio, which can improve the ignition characteristic of blending fuel [181]. On the other hand, oil shale contains rich carbonates, which is expected to act as a desulfurizer [182]. As a result, thermal co-processing of coal and oil shale can reduce the environmental impacts such as SO_2 emission as well as promote combustion performances.

Combustion can be regarded as a complete gasification process when the flow rate of oxidants is larger than the theoretical requirement. In recent years, there has been an increasing amount of literature on the co-combustion of oil shales with its semi-coke [21, 169], biomass [183-185], hydrochar [186], municipal solid waste [187] and sewage sludge [19] to investigate the co-combustion behaviours, kinetics and reduction of pollutant gas emissions. However, to date, only few studies have been reported the co-combustion behaviours of coal and oil shale. Jiang et al. [182] and Yu et al. [188] employed a thermal analyser to study the co-combustion characteristics of Huadian oil shale and Heshan coal and calculate the kinetic parameters using Freeman-Carroll method. It was demonstrated that the ignition temperature was lowered and 20% oil shale was feasible for Heshan coal desulfurization. Nevertheless, model-fitting methods usually lead to “kinetic compensation effect”, the employment of iso-conversional approaches can eliminate such effect since they do not assume the reaction models during the determination of activation energy [189]. With respect to ash fusion and slagging performances of coal and OS co-firing, only recently, Lu et al. [190] reported the mineralogy, morphology and sintering characteristics of the addition of Changji OS to the high-sodium Zhundong coal combustion with an emphasis on sodium migration. Systematic investigations on co-combustion characteristics and interactions, kinetic triplets with iso-conversional methods, and ash fusion and mineral transformations of coal and Funshun low calorific oil shale are vital for the subsequent industrial application. However, previous results may not be completely appropriate and hence there is a need to perform studies on co-combustion of the coal and oil shale comprehensively.

2.4.2 Coal and oil shale semi-coke co-gasification

Oil shale semi-coke is characterized as high ash, low fixed carbon content and low calorific value[169], which leads to a low reactivity. The co-processing of coal and oil shale semi-coke benefits both resources. It not only increases the energy density of oil shale, but also offers a practical way for sulphur fixation. Gasification is an effective method to convert solid fuels to gaseous fuels, which can be utilized for producing various liquid fuels [129].

At present, the co-gasification of coal and other materials such as biomass, sewage sludge, plastics and petroleum coke using thermogravimetric analysis (TGA), pilot-scale and processing simulation techniques have been reported intensively and widely [191-198]. For example, Masnadi et al. [193] investigated the co-gasification of coal and biomass under CO_2 atmosphere from kinetics interactions perspective using TGA and found that inhibitory effect was observed in low potassium contents while gasification reactivity was enhanced when K/Al > 1 M ratios. García et al. [191] studied the effect of feedstock compositions on the performances such as gas heating values and cold gas efficiencies of coal and sewage sludge co-gasification under a laboratory-scale fluidized-bed reactor, and reported that tar yield decreased while H_2 and CO increased due to the synergistic effects. Aznar et al. [192] performed an plastic co-gasification with coal and biomass with air in a fluidized-bed pilot plant to generate syngas. The results showed that a syngas containing a medium hydrogen content and low tar was obtained. Besides, Fan et al. [198] conducted a thermodynamic investigation on coal and biomass co-gasification to synthesis natural gas and power polygeneration process based on Aspen Plus. Nevertheless, the researches on coal and oil shale semi-coke co-gasification are rarely reported. Li et al. [199] tested the CO_2 gasification behaviours and kinetics of coal and oil shale pyrolyzed residues in a TGA with an emphasis on the continuous co-gasification after pyrolysis without char or semi-coke cooling stage. They had concluded that minerals in ash had a catalytic effect on the co-gasification. However, far too little attention has been paid to the co-gasification of coal and oil shale semi-coke deriving from retorting process. It is imperative to investigate the co-gasification thermal behaviours and kinetics since they have significant influences on the modelling of gasification at industrial scale.

Artificial neural network (ANN) is a powerful artificial intelligence (AI) strategy, which can deal with non-linear and complex systems speedily by a learning algorithm between input and output data [200, 201]. The applications of ANN in gasification modelling for the predictions of gasification performances such as syngas yield and composition had been evaluated in several literatures [201-205]. It was found that the ANN predicted values had better accuracy than the conventional methods irrespective of the approaches of data regression, thermodynamic, kinetics and fluid-dynamics results [202]. In the modelling of co-processing thermogravimetric curves, Xie et al. [206], Buyukada et al. [207-209] and Chen et al.[210] developed ANN models for the prediction of combustion mass loss with three inputs namely temperature, heating rate, and blending ratio. Among ANN models, back-propagation neural network (BPNN) is the most classical and popular in industrial applications [211]. Nevertheless, the training results in BPNN often falls into local optimum hindering the convergence rate and the predicting accuracy [212]. Essentially, the genetic algorithm (GA) is a global optimization method and can be integrated with BPNN effectively to optimize the initial weights and thresholds in BPNN and thus the above limitations can be overcome and a better forecasting performance can be expected [212, 213]. So far, no study has been attempted to implement a BPNN combined GA for the prediction of co-gasification properties.

2.5 Biomass gasification to olefins

2.5.1 Gasification processes and reactions

Biomass is a non-fossilized organic material mainly originating from plants. Due to the climate change and global warming, the renewable and carbon-neutral biomass has great potential for producing modern energy carriers, such as power, gas and liquid fuels, through biochemical routs (i.e., digestion and fermentation) and/or thermochemical routes (pyrolysis, gasification, liquefaction and combustion) [214]. Thermal conversions of biomass are faster and higher efficiency than that of biological processes [215]. Compared with direct combustion, gasification of biomass has less pollutants including flue gas, SO_2 and NO_x emissions [216]. Besides, the desired syngas from the gasification can be used as the intermediate bridges for various chemical and power productions. Therefore, gasification alternative is showed to be the most efficient ways for biomass utilization.

Biomass gasification is a complex process involving many heterogeneous and homogeneous reactions and producing a variety of gaseous products including CO, H_2, CO_2, CH_4, H_2O, C_2+, tar and solid products of char and ash [216]. Figure 2.17 presents a schematic diagram of biomass gasification, and the main reactions involved in this process are tabulated in Table 2.6 [216]. As indicated, biomass is firstly devolatized into light gas, char and tar upon heating. After initial decomposition, biomass undergoes a secondary pyrolysis including tar reforming, oxidation and thermal cracking to smaller gases. Simultaneously, the permanent gases react with oxygen and steam and result in CO_2 and H_2O as

Eqs.(2.25-2.28) and generate a large amount of heat which is used for the endothermic char boudouard and steam reactions. In addition, char may also react with oxygen to full combustion as displayed in Eqs.(2.20)-(2.21). The ash is discharged at the bottom of gasifier.

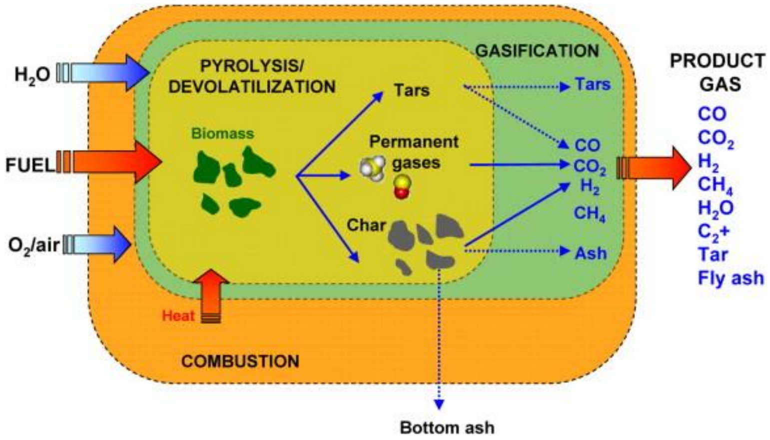

Figure 2. 17 Schematic diagram of biomass gasification

Table 2. 6 Main reactions involved in biomass gasification

Name	Reaction	Number
Pyrolysis	Biomass → char + tar + H_2O + light gas ($CO + CO_2 + H_2 + CH_4 + C_2 + N_2 + \ldots$), $\Delta H > 0$	(2.19)
Partial combustion	$C + ½O_2 \rightarrow CO$, $\Delta H = -111$ kJ/mol	(2.20)
Complete combustion	$C + O_2 \rightarrow CO_2$, $\Delta H = -394$ kJ/mol	(2.21)
Boudouard reaction	$C + CO_2 \rightarrow 2CO$, $\Delta H = 173$ kJ/mol	(2.22)
Steam gasification	$C + H_2O \rightarrow CO + H_2$, $\Delta H = 131$ kJ/mol	(2.23)
Hydrogen gasification	$C + 2H_2 \rightarrow CH_4$, $\Delta H = -75$ kJ/mol	(2.24)
Carbon monoxide oxidation	$CO + ½O_2 \rightarrow CO_2$, $\Delta H = -283$ kJ/mol	(2.25)

Hydrogen oxidation	$H_2 + ½O_2 \rightarrow H_2O$, $\Delta H = -242$ kJ/mol	(2.26)
Methane oxidation	$CH_4 + 2O_2 \rightarrow CO_2 + 2 H_2O$, $\Delta H = -283$ kJ/mol	(2.27)
Water–gas shift reaction	$CO + H_2O \leftrightarrow CO_2 + H_2$, $\Delta H = -41$ kJ/mol	(2.28)
Partial oxidation	$C_nH_m + (n/2) O_2 \rightarrow nCO + (m/2) H_2$, $\Delta H>0$	(2.29)
Dry reforming	$C_nH_m + n CO_2 \rightarrow (m/2) H_2 + (2n) CO_2$, $\Delta H>0$	(2.30)
Steam reforming	$C_nH_m + nHO_2 \rightarrow (m/2 + n) H_2 + nCO_2$, $\Delta H>0$	(2.31)
Hydrogenation	$C_nH_m + (2n - m/2) H_2 \rightarrow n CH_4$, $\Delta H>0$	(2.32)
Thermal cracking	$C_nH_m \rightarrow (m/4) CH_4 + (n - m/4) C$, $\Delta H>0$	(2.33)

2.5.2 Direct and indirect fluidized-bed biomass gasifiers

Similar to coal gasification, biomass gasifier can be generally divided into three types: fix-bed, fluidized bed, and entrained bed gasifier. The fixed bed has the biomass moving down through the gasifier while the gasifying media and gas either move up or down [216]. The fixed bed gasifier is the simplest, inexpensive and small type of gasifier, while the mixing and heat transfer in the gasifier are inefficient, while lead to agglomeration. For fluidized bed gasifier, the biomass particles are kept in a state of suspension by the gasifying agents. It has excellent mixing and temperature uniformity, which decrease the agglomeration significantly. Besides, the tar production is less than that of fixed bed gasification due to a higher operating gasification temperature. The fluidized bed gasifier can be designed from medium-size scale to a large-size scale up to 100 MW_{th}. With respect to entrained flow gasifier, it operates above 1200 ^{o}C and hence the ash is removed in a liquid state and the syngas is free of tar [217]. However, the entrained gasifier has several drawbacks including: 1) the difficulties of biomass particle reduction; 2) the corrosions of reactor lining; 3) the three times investment in comparison with fluidized bed gasifier; 4) the availability of biomass; and 5) high oxygen consumption [218]. Those characteristics have prevented the utilization of entrained bed gasifier in biomass gasification. Therefore, the fluidized bed gasifier is the best option for biomass gasification.

According to the different heat supplement scheme, the fluidized bed gasifier can be designed in two principals: direct gasification and indirect gasification, as illustrated in Figure 2.18 [216]. In direct gasification, biomass is gasified by oxygen and steam and the required heat is provided autothemally. The indirect gasification consists in two fluidized bed gasifiers, biomass gasification with steam takes place in a bubbling fluidizing bed reactor, and the char is combusted in a circulating fluidized bed combustion chamber, which is used for heat supplement for the gasifier. The heat transfer between the two reactors is achieved by the recirculation of bed particles [219]. The indirect gasification has some advantages over direct gasification. The indirect gasification uses air as the oxidant in a separate combustor, thus the energy intensive air separation unit is avoided and simultaneously, the product gas contains high hydrogen content being benefit to liquid fuel synthesis. Besides, steam gasification enhances gasification yield while decreases tar content, and has been applied commercially [220].

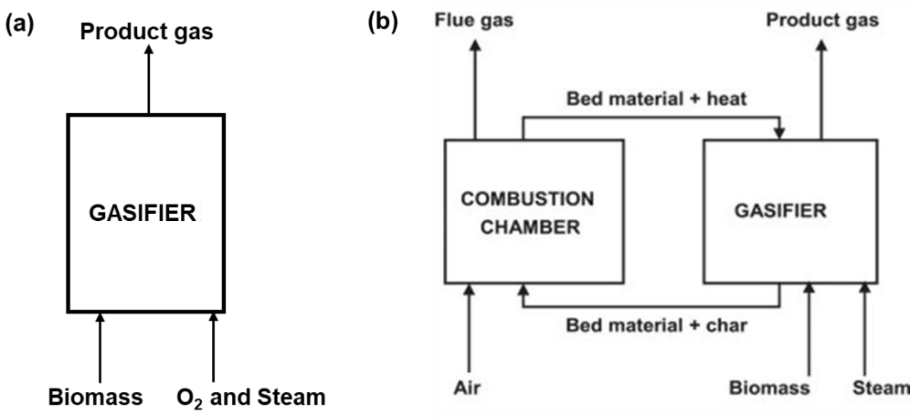

Figure 2. 18 Direct and indirect fluidized bed gasification

2.5.3 Bio-olefins production

Light olefins including ethylene and propylene are the most important building blocks for various plastics, such as polyethylene and polypropylene [221]. The global demands of ethylene and propylene are around 150 and 80 million tons per year and are expect to grow by 1.5% to 4.1% per year [222]. Most light olefins are currently produced by steam cracking of hydrocarbons such as naphtha, whilst they can also be produced through coal, natural gas and shale gas via methanol to olefins (MTO) process [223-225]. However, the depletion of fossil fuels and increase of greenhouse gases emissions force to seek sustainable methods to achieve olefins production. Biomass gasification to syngas is a renewable and promising way to synthesize value-added products [226]. Methanol synthesis based on biomass gasification has been intensively studied and implemented in the industries [227, 228]. The integration of syngas to methanol and methanol to olefins (MTO) process enables to produce olefins from biomass.

Several studies have analyzed the biomass gasification to olefins process from energy and economic performances. Johansson [229] presented an energy analysis of biomass to olefins process via methanol as the intermediate. The investigated system used a O_2/steam-blown fluidized-bed gasifier to generate the syngas. The results indicated that the energy yield of biomass to methanol was 0.51. Besides, Hannula et al. [39] also employed the fluidized-bed steam/O_2 gasifier to convert biomass to syngas and subsequently for methanol synthesis and ultimately for light olefins production. Energy analysis presented that the olefins yield was 169-203 kg per one tone of biomass depending on whether using the olefins cracking process. Onel et al. [230] introduced a process integrating biomass and natural gas to liquid fuels and olefins process and found the proposed process were economically viable because of high net present values. In addition, Xiang et al. [48] evaluated a biomass to light olefins process adopting an entrained-flow gasifier from the exergetic point. It was revealed that the energetic and exergetic efficiencies of this system were 54.66% and 47.65%. Recently, Liptow et al. [47] explored the environment impacts of biomass to olefins through gasification and fermentation routes, respectively, and demonstrated that the gasification route had lower impact to the environment. The gasification agents of the above studies are both oxygen and steam, while the air separation unit is energy-intensive and hence, a preferred indirect biomass gasification technology is expected to employed in the renewable olefins production. Under this circumstances, a systematic energy, economic and environmental investigations are imperative. To the best knowledge, studies that utilize biomass indirect steam gasification as a source of syngas to olefins through methanol as the intermediate in the open literature are limited. Besides, the consideration of CO_2 as a gasification agent for the enhancement of olefins production has not been reported. The quantitative evaluation of life cycle CO_2 emission and economic analysis from biomass to olefins are also scarce. Therefore, the present study is expected to fill those gaps.

Chapter 3 Materials and methods

In this chapter, the materials and experimental techniques used in this thesis are described. Descriptions of raw materials collection, preparation, coal char preparation through microwave and conventional pyrolysis are detailed in Section 3.1 to 3.3. Section 3.4 presents the employment of thermogravimetric analysis to investigate the proximate compositions, gasification and combustion tests. Characterization equipment and procedures are presented in Section 3.5 and the heavy metal analysis is shown in Section 3.6. Section 3.7 concerns the ash slagging characteristics and simulation methods using Factsage to reveal the mineral transformation mechanism. Finally, the artificial neural network for the prediction of mass loss curves in the co-gasification experiment is presented in Section 3.8.

3.1 Sample collection and preparation

3.1.1 Coal

The coal used in the experiment was the bituminous Qinghai coal (QH), which was collected from a domestic power plant in China. The sample was dried in an oven at 105 ºC for 24 h to remove water. Approximate 500 g sample was grounded by a ball mill and then sieved by vibrating screens. To avoid heat- and mass-transfer limitations during heating experiments, only particles smaller than 0.106 mm were collected.

3.1.2 Coal gasification slags

The desired slags were collected from two OMB coal gasification plants. The first gasification plant has a capacity of 1000 tons per day (TPD) and is operated at 6.5 MPa and 1250 °C, while the second plant has a capacity of 2500 TPD and is operated under the same operating pressure and temperature as the first gasifier. Besides, the coal slurry concentrations of the first and second gasifiers are about 62.5% and 58%, respectively. Figure 3.1 shows the schematic process diagram of the OMB gasification process. As can be seen from this figure that the whole process includes coal-water slurry preparation, coal gasification, syngas purification with water scrubber and slag-containing water treatment and recycle [231]. Firstly, the prepare CWS together with oxygen are introduced into the gasifier via four burners. In the gasifier, coal is converted into crude syngas and molten ash which then proceeds to quench chamber and coarse slag is obtained. The washed syngas is subsequently forward to a cyclone and a water scrubber for the removal of unconverted particles and fine ash. On the other hand, all wastewater streams pass to a hot-water tower to realize the dissolved acid gas separation. After series flash units including a low pressure and a vacuum flash, the waste water is sent to a sedimentation pool, in which the fine slag is precipitated with the help of flocculants. The fine slag is obtained after filtration and the remaining clarified water undergoes to the grey water tank, where part of water is recycled to the gasification and hot-water tower. The syngas after water scrubber continues to downstream for acid gas removal.

In this work, the feeding coal was sampled from the CWS tank. The coarse slag was collected from the lock hopper, while the fine slag was taken from the filtration facility after the sedimentation pool. The coal and slag samples corresponding from the two gasification plants (Plant-1 and Plant -2) were noted as Coal-1, Coal-2, CS-1, CS-2 and FS-1, FS-2, respectively. About 500 g collected samples were dried at 105 °C for 24 hours to eliminate the moistures in a vacuum dry oven, and then milled and sieved to a size smaller than 0.106 mm.

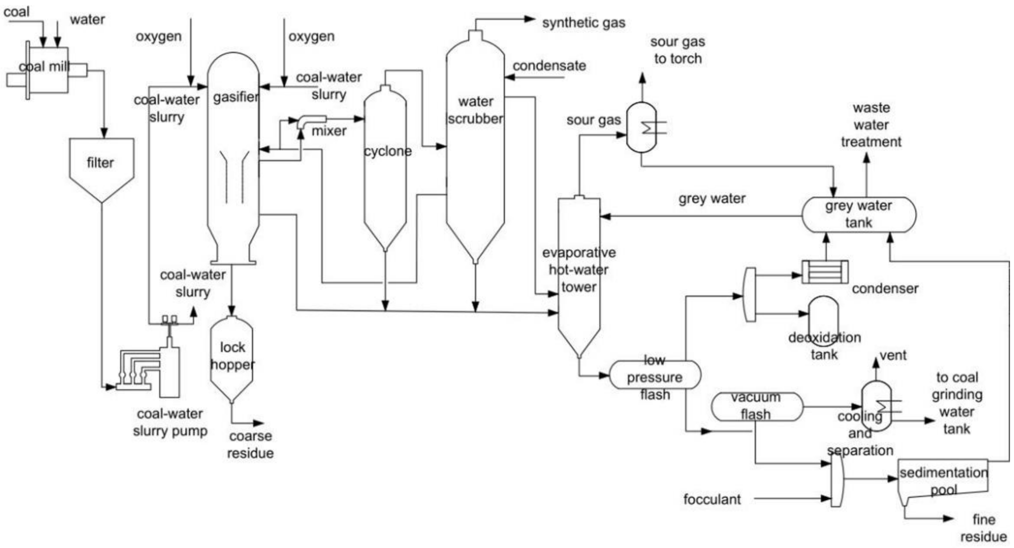

Figure 3. 1 Flow diagram of OMB gasification process

3.1.3 Oil shale and oil shale semi-coke

Fresh Funshun oil shale sample (FS) used in the co-combustion was obtained from an oil shale chemical plant in Fushun, Liaoning province, China. However, the oil shale semi-cokes (SC) sample for the co-gasification experiment was collected from an oil shale pyrolysis experiment which was conducted at 520°C. Similarly, both samples were dried and milled to less than 0.106 mm in particle size prior to experiments.

3.1.4 Sample blends

During the co-combustion experiment, the QH coal and FS oil shale blends were prepared using 0, 10, 20, 30, 40 and 100 wt% of FS and denoted as QH, 90QH10FS, 80QH20FS, 70QH30FS, 60QH40FS and FS, respectively. The blends were carried out in a 500 ml ball mill jar for 3 minutes to mix fully. For the co-gasification case, the blending mass ratios of SC: coal were set as 1:0, 1:9, 3:7, 0:1, respectively.

3.2 Microwave-assisted coal pyrolysis

The microwave-derived QH coal char was prepared in a 2.45 GHz multi-mode microwave-cavity manufactured by Nanjing Jiequan Microwave Co., Ltd [232]. Figure 3.2 shows the schematic diagram of experimental rig. The pyrolysis temperature was detected by a K-type thermocouple (with thermometric range from 0 to 1600 K) injected in the quartz reactor. The inner diameter of the quartz reactor was about 30 mm and the length was 60 mm. It is noteworthy that the organic part of coal is essentially transparent to microwave and the dielectric loss tangent (tan δ) of coal is about 0.02-0.08 [233], while the increase of pyrolysis temperature leads to the dramatic improvement of dielectric loss to a level of tan δ equalling to 0.29 [234], which can absorb microwave efficiently. In order to improve the heating rate of coal at the initial stage of microwave pyrolysis, microwave absorbers with high dielectric loss are suggested to mix with the coal sample. Therefore, approximately 2.0 g of the prepared QH coal sample was blended with 20.0 g of silicon carbide (used as a microwave absorbent to assist in coal pyrolysis) and pyrolyzed at 1173 K for 30 minutes under nitrogen atmosphere of 100 mL/min at 0.1 MPa pressure. After pyrolysis, the char was separated from SiC by sieving. The exhaust gas from the pyrolysis passed through the gas washing bottle before it discharged to ventilation system. Char derived from microwave pyrolysis was noted as MW.

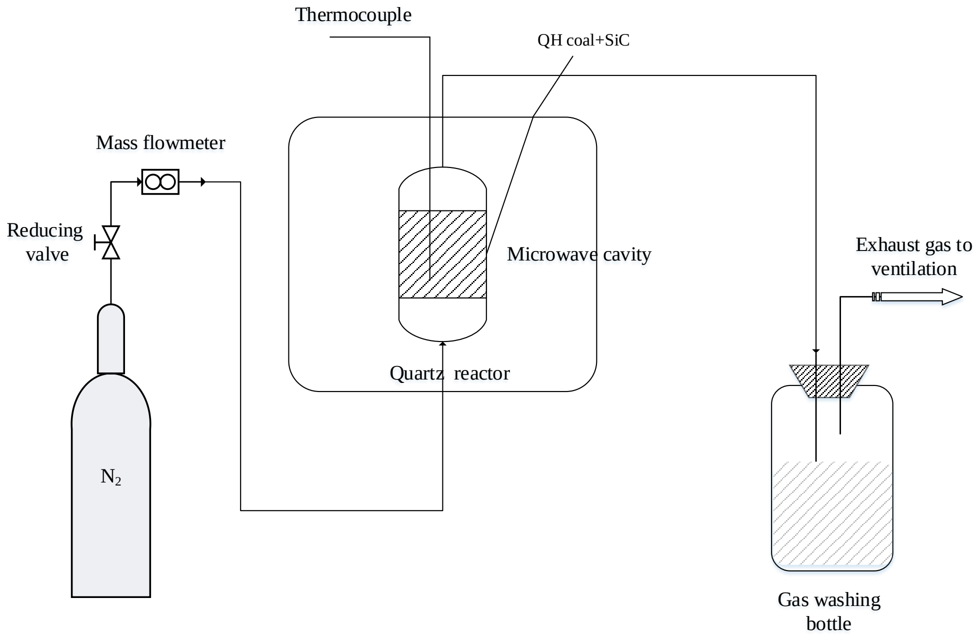

Figure 3. 2 Schematic diagram of microwave-assisted coal pyrolysis

3.3 Conventional coal pyrolysis

Conventional pyrolysis was performed in a laboratory-scale tube furnace, which is displayed in Figure 3.3. The inner diameter of the tube and the constant temperature zone were 40mm and 250 mm. The coal pyrolysis temperatures were set at 1073, 1173 and 1273 K. In the experiments, the tube furnace was heated to the designated temperature from the room temperature at the heating rate of 10 °C/min. Then the corundum boat loaded with 2.0 g sample was pushed into the middle of the furnace and pyrolyzed about 30 min in 300ml/min N_2 atmosphere. Similarly, the flue gas was passed to a gas-washing bottom containing 5% HNO_3 before it discharged to the ventilation system. The collected chars were stored separately in a dryer and labelled Py1073, Py1173, and Py1273, respectively.

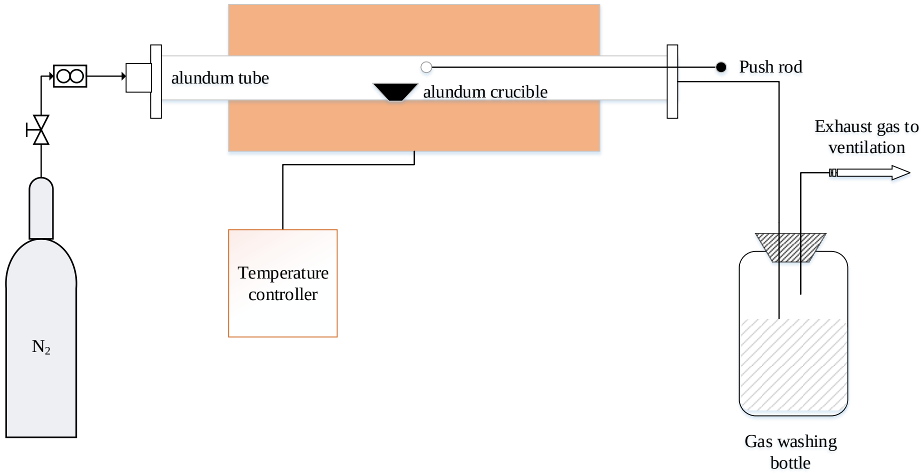

Figure 3. 3 Schematic diagram of conventional coal pyrolysis

3.4 Thermogravimetric analysis

Thermogravimetric analysis (TGA) measuring the weight changes as the function of increasing temperature has been widely used for coal characterizations [235]. In this thesis, a thermal analyser device of Netzsch STA 449 F3 Jupiter was employed to perform thermogravimetric analysis including proximate analysis, isothermal and non-isothermal gasifications, and combustion test. Figure 3.4 shows the picture of Netzsch STA 449 F3 Jupiter instrument and the data processing unit.

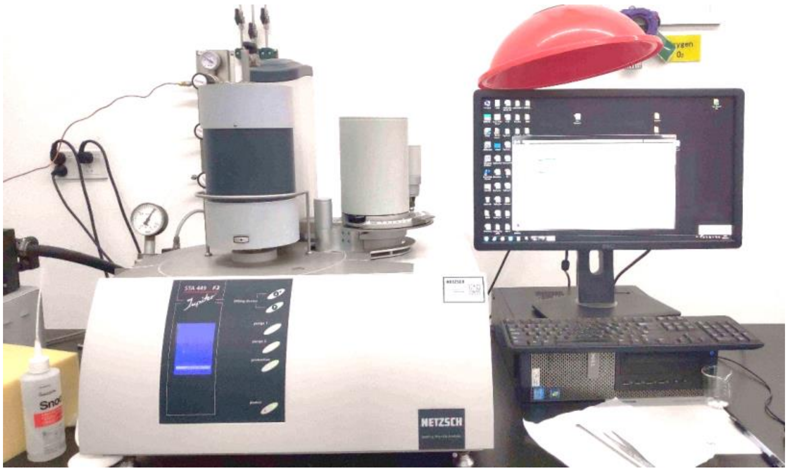

Figure 3. 4 Netzsch STA 449 F3 Jupiter

3.4.1 Proximate analysis

Proximate analysis of the investigated samples was conducted to determine the contents of moisture, volatile matter, fixed carbon and ash. About 10 mg sample was put in the corundum crucible and then heated to 105 ºC at 10 ºC/min under the N_2 flow rate of 20 mL/min. The temperature was kept at 105 ºC for 5 minutes to allow the complete removal of moisture. Then, the sample was heated to 920 ºC under 10 ºC/min in nitrogen and held for 10 min to ensure the complete release of volatile matter. Subsequently, the sample was slowly cooled down to 820 ºC and kept for 40 min under the air atmosphere to realize the combustion of fixed carbon. Figure 3.5 shows the proximate analysis from the obtained TGA curve.

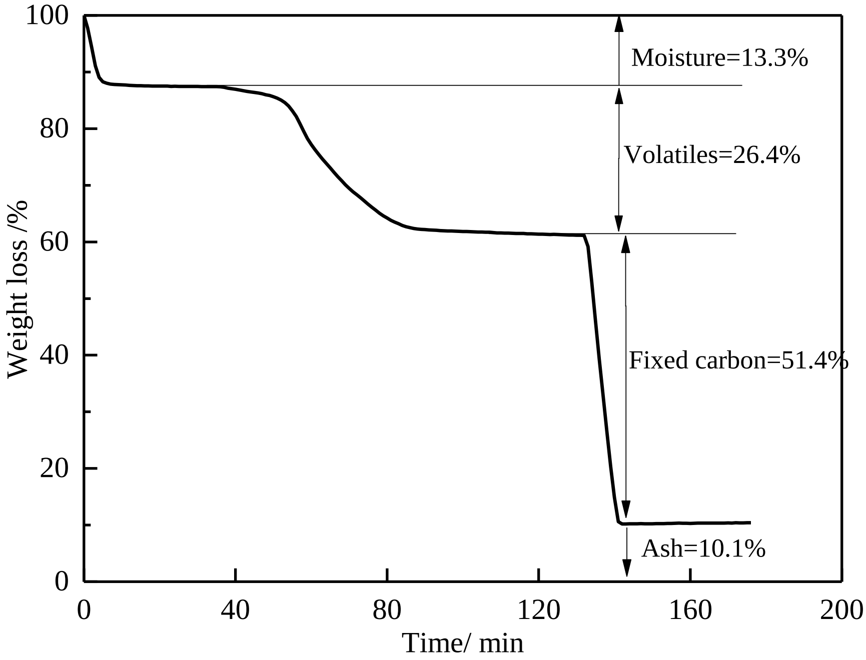

Figure 3. 5 Proximate analysis from TGA curve

3.4.2 Gasification test

3.4.2.1 Isothermal gasification

In isothermal char gasification experiments, each char sample (10 mg ± 0.5 mg) was heated to the gasification temperature at 25 °C /min under a pure N_2 flow of 50 mL/min. When the gasification temperatures (900, 950, and 1000 °C) were reached, the N_2 flow was replaced by a CO_2 flow (50 mL/min). Subsequently, the gasification temperature was kept constant for approximately 60 min under CO_2 atmosphere. The weight loss curve was recorded from room temperature to the end of gasification. Each experiment was replicated three times to ensure reproducibility. The experimental errors were within ± 2%.

The evaluation of reactivity of different chars at various gasification temperatures was based on the reactivity index, $R_{0.5}$, which is expressed as:

$$R_{0.5}=\frac{0.5}{t_{0.5}} \tag{3.1}$$

where $t_{0.5}$ represents the time required for the char conversion of 50%. It is noted that a higher reactivity means a better gasification performance.

Gasification conversion (x) is calculated as [236]:

$$x=\frac{m_0-m_t}{m_0-m_{ash}} \tag{3.2}$$

where m_0 means the char mass at the initial time of gasification, m_t is the char mass at time t, and m_{ash} represents the ash mass in char.

In general, the gasification rate for a heterogeneous reaction can be described as:

$$r=\frac{dx}{dt}=k(T)f(x) \tag{3.3}$$

$$k(T)=Aexp\left(-\frac{E_a}{RT}\right) \tag{3.4}$$

where A is the pre-exponential factor; E_a is the activation energy; and R is the universal gas constant, R=8.314 J/(K·mol). Here, $f(x)$ is the gasification mechanism function.

For the isothermal gasification, the SCM and RPM were adopted as the mechanism functions to fit the experimental data due to their widely application in simulation of char gasification process [237]. The SCM considers that the gasification takes place at the char surface and moves inside. The expression for the SCM model is described as follows:

$$r=\frac{dx}{dt}=k_{SCM}(1-x)^{2/3} \tag{3.5}$$

The RPM assumes overlapping of pore surfaces. The gasification rate is shown as:

$$r = \frac{dx}{dt} = k_{RPM}(1-x)\sqrt{1-\psi\ln(1-x)} \tag{3.6}$$

where ψ is a structural parameter that is calculated using a regression method as follows:

$$\frac{t_x}{t_{0.8}} = \frac{\sqrt{1-\psi\ln(1-x)}-1}{\sqrt{1-\psi\ln(1-0.8)}-1} \tag{3.7}$$

The apparent rate constants of k_{SCM} and k_{RPM} can be obtained from the linear fit of the experimental data with the following expressions of SCM and RPM, respectively.

$$3\left[1-(1-x)^{1/3}\right] = k_{SCM}t \tag{3.8}$$

$$(2/\psi)\left[\sqrt{1-\psi\ln(1-x)}-1\right] = k_{RPM}t \tag{3.9}$$

After determination of the reaction rate constant, the activation energy and pre-exponential factor are determined by plotting $\ln k$ and $1/T$ via the following equation:

$$\ln k = -\frac{E_a}{RT} + lnA \tag{3.10}$$

3.4.2.2 Non-isothermal gasification

Non-isothermal gasification experiments were used for the investigation of co-gasification of coal and oil shale semi-coke. Each sample (10 ± 0.5 mg) was heated under CO_2 flow rate of 50 ml/min. The weight loss curves were recorded simultaneously from ambient temperature to 1050 ºC at 5, 10, 15 °C/min, respectively.

The gasification rate for a heterogeneous reaction is showed in Eqs. (3.3) and

(3.4), which can be further deduced to be:

$$\frac{dx}{dT} = \frac{A}{\beta} exp\left(-\frac{E_a}{RT}\right) f(x) \tag{3.11}$$

where A is the pre-exponential factor; E_a is the activation energy; R is the universal gas constant, R=8.314 J/(K·mol). Here, f(x) is the gasification mechanism function.

By applying Coats-Redfern method, the above equation is integrated as:

$$ln\left[\frac{g(x)}{T^2}\right] = ln\left[\frac{AR}{\beta E_a}\left(1 - \frac{2RT}{E_a}\right)\right] - \frac{E_a}{RT} \tag{3.12}$$

where β is the constant heating rate, E_a represents the activation energy; T is the absolute temperature and t is the reaction time; g(x) is the integral conversion function. In this study, the volumetric model (VM) and shrinking core model (SCM) are employed for solid-state reactions due to their widely used in the CO_2-gasification process [238, 239]. The expressions of $g(x)$ for the VM and SCM are respectively shown as:

$$g(x) = -\ln(1 - x) \tag{3.13}$$

$$g(x) = 1 - (1 - x)^{1/3} \tag{3.14}$$

Subsequently, the value of E_a at different conversion rate can be obtained from the slope by the plot of $ln\left[\frac{g(x)}{T^2}\right]$ versus $1/T$. Besides, the pre-exponential factor A can also by determined using the intercept of the previous fitting-line.

3.4.2.3 Co-gasification indices

The evaluation of co-gasification includes characteristic temperatures and comprehensive gasification characteristic index. The characteristic temperatures are initial gasification temperature (T_i) determined use tangent method, and the final gasification temperature (T_b) which is defined as the mass loss of 95%. Besides, the comprehensive gasification characteristic index (S) is defined as:

$$S = \frac{(dw/dt)_{max}(dw/dt)_{mean}}{T_i^2 T_f} \tag{3.15}$$

where $(d\alpha/dt)_{max}$ and $(d\alpha/dt)_{mean}$ are the maximum and average gasification rates.

3.4.2.4 Co-gasification interaction

The obtained TG/DTG profiles during co-gasification experiments were used to study the interaction between Qinghai coal and oil shale semi-coke. The theoretical TG curves of the blend were calculated as the adding up the weight loss rates of each individual component and compared with the experimental TG curves in order to determine if synergistic interactions occurred between among the components of the blends during this process [240, 241]. Therefore, the chemical synergistic interactions between the QH coal and semi-coke samples during the co-gasification can be modelled as follows:

$$TG_{cal} = (1 - x_{SC})\ TG_{QH} + x_{SC} TG_{SC} \tag{3.16}$$

$$\Delta W = \mathrm{TG_{EX}} \text{-} \mathrm{TG_{cal}} \tag{3.17}$$

where TG_{WL}, TG_{QH} are the corresponding weight loss (%) of the individual materials, while the x_{SC} is the mass fraction of SC in the blends.

3.4.3 Combustion test

3.4.3.1 Coal and oil shale co-combustion

In the TG analyser, about 10 mg sample was heated under an air flow rate of 50 ml/min. The weight loss curve was recorded from room temperature to 950 ºC at three different heating rates (10, 20 and 30 ºC/min). Each experiment was repeated three times to ensure reproducibility, and the errors of experimental results were within ± 2%.

3.4.3.2 Combustion parameters

The combustion performances of all samples could be obtained by using the characterized temperatures directly from TGA-DTG curves. These parameters included ignition temperature (T_i), burnout temperature (T_b) and peak temperature (T_{max}) [242]. Among them, T_i was determined by using the tangent method, while T_b and T_{max} represented the temperature at the maximum weight loss rate point and at the fuel conversion of 98% point, respectively [243].

Besides, the ignition index (C_i, %/min^3), burnout index (C_b, %/min^4) and comprehensive combustibility index (CCI, %^{3}/ºC^{3}min^2) were applied to evaluate the combustion performance of blended samples [244]. The ignition index is determined as follows:

$$C_i = \frac{(dw/dt)_{max}}{t_i t_{max}} \tag{3.18}$$

Where $(dw/dt)_{max}$ is the maximum mass combustion rate. t_i and t_{max} stand for the corresponding ignition and maximum mass loss time, respectively.

The burnout index is calculated as:

$$C_b = \frac{(dw/dt)_{max}}{\Delta t_{1/2} t_{max} t_b} \tag{3.19}$$

where $\Delta t_{1/2}$ is the time span of $(dw/dt)/(dw/dt)_{max} = 1/2$ [244]. Here, t_b is burnout time.

The comprehensive combustibility index (*CCI*) included both ignition and burnout and reflected the difficulty of combustion completion [245]. A higher comprehensive combustibility index suggests a better combustion performance of a sample. This index is expressed as:

$$CCI = \frac{(dw/dt)_{max}(dw/dt)_{mean}}{T_i^2 T_b} \tag{3.20}$$

Where $(dw/dt)_{mean}$ is the average combustion rate.

3.4.3.3 Synergy indices

Similar to the definition given in the co-gasification, the synergy index ($\triangle$W) in the co-combustion is defined as Eq.(3.21). If $\triangle W < 0$, then it indicated that there was a promoting interaction during co-combustion.

$$\triangle W = TG_{EX} - TG_{TH} \tag{3.21}$$

The calculation of TG_{th} assuming no interaction effect is expressed as:

$$TG_{TH} = (1 - x_{FS})\ TG_{QH} + x_{FS} TG_{FS} \tag{3.22}$$

where TG_{FS} and TG_{QH} represent the experimental TG curves of FS and QH samples respectively. The x_{FS} is the FS weight percentage of the mixed sample.

3.4.3.4 Kinetics

The heterogeneous solid-state combustion reaction kinetics are described as [246]:

$$\frac{d\alpha}{dT}=\frac{A}{\beta}exp\left(-\frac{E_a}{RT}\right)f(\alpha) \tag{3.23}$$

where T is the reaction temperature, α is the conversion ratio. Here, A represents the pre-exponential factor, E_a stands for the apparent activation energy and R is the gas constant. β is the heating rate, $\beta = dT/dt$.

By integrating Eq.(3.23) gives [247],

$$G(\alpha)=\int_0^{\alpha}\frac{d\alpha}{f(\alpha)}=\frac{A}{\beta}\int_{T_0}^{T}exp\left(-\frac{E_a}{RT}\right)dT\approx\frac{A}{\beta}\int_0^{T}exp\left(-\frac{E_a}{RT}\right)dT=\frac{AE_a}{\beta R}P(u) \tag{3.24}$$

where $u=\frac{E_a}{RT}$, the function of $P(u)$ does not have an exact analytical solution. However, it can be derived from numerical methods.

The two most common integral iso-conversional methods, *i.e.*, Flynn–Wall–Ozawa method and Kissinger–Akahira–Sunose, were used to determine the kinetic parameters in combustion. The Doyle's approximation of $P(u) = 0.0048e^{-1.0516u}$ is used for the FWO method and hence, Eq.(3.24) can be expressed as [210],

$$ln\beta = ln\left(\frac{AE_a}{G(\alpha)R}\right)-5.331-1.052\frac{E_a}{RT} \tag{3.25}$$

Subsequently, the value of E_a at different conversion rate could be obtained from the slope by the plot of lnβ versus 1/T under conversion of α.

In terms of KAS method, the approximation of $P(u) = u^{-2}e^{-u}$ expression was employed [248]. Then, the Eq. (3.24) can be rearranged as [247],

$$ln\left(\frac{\beta}{T^2}\right) = ln\left(\frac{AE_a}{G(\alpha)R}\right) - \frac{E_a}{RT} \tag{3.26}$$

Similarly, the value of E_a is provided by the slope from the plot of $ln\left(\frac{\beta}{T^2}\right)$ against $1/T$ for constant conversion.

After determination of apparent activation, the integral mater plot method was employed to estimate the most probable mechanism function of $G(\alpha)$ and the pre-exponential factor A. The basic idea for the determination of combustion reaction mechanism was to compare the experimental master plots, which was calculated based on experimental TG data, with the listed theoretical master plots as referred in [245, 249]. When α =0.5 is taken as the reference point, the Eq. (3.24) becomes:

$$G(0.5) = \frac{AE_a}{\beta R}P(u_{0.5}) \tag{3.27}$$

where $u_{0.5} = \frac{E_a}{RT_{0.5}}$ and $T_{0.5}$ represent the temperature required to realize a 50% conversion [250]. Here $G(0.5)$ is the integral reaction model at the conversion of 0.5.

Then, the following integral master plot equation is developed as:

$$\frac{G(\alpha)}{G(0.5)} = \frac{P(u)}{P(u_{0.5})} \tag{3.28}$$

where the left term of $\frac{G(\alpha)}{G(0.5)}$ versus α stands for the theoretical master plots of various G(α) as shown in Table 3.1 [249], while the $\frac{P(u)}{P(u_{0.5})}$ is the experimental master plots, which is generated by plotting $\frac{P(u)}{P(u_{0.5})}$ against α at different heating rates. When the best matching mechanism model is found, equivalent experimental values and theoretical values can be achieved.

Subsequently, once the mechanism model of $G(\alpha)$ was found out, the pre-exponential factor of A could be derived by plotting $G(\alpha)$ versus $\frac{E_a}{\beta R}P(u)$ for a constant heating rate.

Table 3. 1 Common reaction mechanisms of solid reactions

Mechanisms	Symbol	$f(\alpha)$	$G(\alpha)$
Order of reaction			
First-order	F_1	$1-\alpha$	$-\ln(1-\alpha)$
Second-order	F_2	$(1-\alpha)^2$	$(1-\alpha)^{-1}-1$
Third-order	F_3	$(1-\alpha)^3$	$[(1-\alpha)^{-2}-1]/2$
Diffusion			
One-way transport	D_1	0.5α	α^2
Two-way transport	D_2	$[-\ln(1-\alpha)]^{-1}$	$\alpha+(1-\alpha)\ln(1-\alpha)$
Three-way transport	D_3	$1.5(1-\alpha)^{2/3}[1-(1-\alpha)^{1/3}]^{-1}$	$[1-(1-\alpha)^{1/3}]^2$
Ginstling-Brounshtein equation	D_4	$1.5[(1-\alpha)^{1/3}-1]^{-1}$	$(1-2\alpha/3)-(1-\alpha)^{2/3}$
Limiting surface reaction between both phases			
One dimension	R_1	1	α
Two dimensions	R_2	$2(1-\alpha)^{1/2}$	$1-(1-\alpha)^{1/2}$
Three dimensions	R_3	$3(1-\alpha)^{2/3}$	$1-(1-\alpha)^{1/3}$
Random nucleation and nuclei growth			

Two-dimensional	A_2	$2(1-\alpha)[-\ln(1-\alpha)]^{1/2}$	$[-\ln(1-\alpha)]^{1/2}$
Three-dimensional	A_3	$3(1-\alpha)[-\ln(1-\alpha)]^{2/3}$	$[-\ln(1-\alpha)]^{1/3}$

3.5 Sample characterization

3.5.1 Elemental analysis

The ultimate analyses (hydrogen, nitrogen, sulphur and carbon) of all samples were tested by a Elementar vario EL III Analyser (GmbH) to identify the element contents including carbon, hydrogen, nitrogen and sulphur in the samples.

3.5.2 X-ray fluorescence spectroscopy

X-ray fluorescence (XRF) is a rapid, simple and accurate approach to determine the chemical composition of the solid samples. In this work, measurements of major elements in coal, gasification slags and oil shales were carried out using a Malvern PANalytical Epsilon4, as displayed in Figure 3.6. Approximate 5.0 g fine ash powder was compressed under 10 MPa into a homogenous sample pellet to ensure a perfectly flat surface. Then the prepared pellet was put into the sample holder for test. The secondary x-rays emitted from the sample after excited by primary x-rays was directed into a solid-state detector and followed by composition interpretations in the computer [251]. Finally, the element contents in the sample could be obtained. It should be noted that XRF only quantifies the element concentration in a sample and can’t distinguish between different oxides for an element. However, the elements contents can be converted to the corresponding oxides in the XRF report.

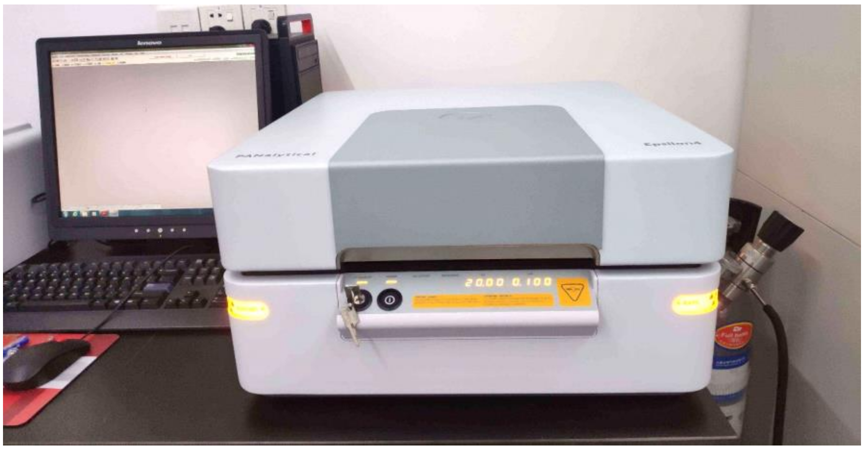

Figure 3. 6 Photograph of the PANalytical Epsilon4

3.5.3 X-ray diffraction

Char crystal structures and mineral phases were identified using a powder x-ray diffraction (XRD) method. Measurements were performed on a Bruker D8 advanced A25 diffractometer with Cu K_α radiation operated at 40 kV and 40 mA, as presented in Figure 3.7. The fine coal chars and slags samples were packed into a sample container and then flat upper surfaces were created for each sample. During test, the diffracted rays were detected when x-rays were directed to the sample. The diffraction pattern was scanned from 10° to 80° to ensure that all the major peaks were recorded. The crystals of coal chars were characterised quantitatively via their inter-layer spacings (d_{002}), stacking heights (L_c), and average number of crystallites in a stack (N_{mean}). Their expressions are illustrated as [252],

$$d_{002} = \frac{\lambda}{2\sin\theta_{002}} \tag{3.29}$$

$$L_c = \frac{0.89\lambda}{\beta_{002}\cos\theta_{002}} \tag{3.30}$$

$$N_{mean} = \frac{L_c}{d_{002}} + 1 \tag{3.31}$$

where λ is the wavelength (λ=1.5406 Å) of X-ray and β is the peak width at half maximum intensity.

Figure 3. 7 Photography of the Bruker D8 advanced A25 diffractometer

3.5.4 Scanning electron microscopy

The morphologies of coal chars and gasification slags were examined using a field emission scanning electron microscope (SEM, Zeiss, Sigma VP Germany), which employed an electron beam to illuminate a specimen to produce a magnified image [251]. In the SEM test, powder samples were spread and fixed over an aluminium stub using sticky carbon tape. Subsequently, the surface of the mount was coated with a gold layer. The prepared mount was transferred into the SEM instrument and exposed directly to the electron beam under a low vacuum mode. Figure 2.8 shows the photograph of the SEM equipment.

Figure 3. 8 Photography of the Zeiss Sigma VP scanning electron microscope

3.6 Heavy metal analysis

3.6.1 Microwave digestion

In order to determine the heavy metal contents in the coal gasification slags, ICP-OES analysis was required. Due to the solid state of the gasification slags, the samples should be dissolved before introduced to the ICP-OES instrument. In this work, a microwave digester (CEM-MARS 6, USA) was employed to accelerate solid dissolution process. Approximately 0.1 g of sample was placed in the Teflon HotBlock digestion vessel and dissolved in the mixture acids of 6 mL of 68% HNO_3 and 2 mL of 36% HCl, and then the vessel was heated simultaneously in the microwave digester. The digestion temperature was heated to 180 ℃ at 10 ℃/min and kept 20 min to allow the complete dissolution. Then, the digestion was cooled down to room temperature within 40 min. The solution after digestion was filtered and diluted to 50 mL using ultrapure water for the ICP-OES test. Figure 3.9 presents the used microwave digester of CEM-MARS 6.

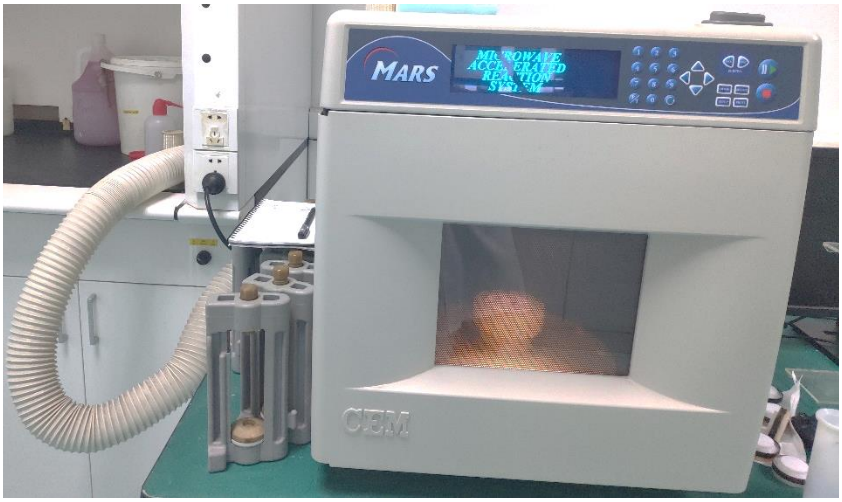

Figure 3. 9 Photograph of the microwave digester of CEM-MARS 6

3.6.2 Inductively coupled plasma optical emission spectroscopy

The prepared solution from the microwave digestion was directed to the inductively coupled plasma optical emission spectroscopy (ICP-OES, SPECTROBLUE FMS36) for the determination of concentrations of 9 heavy metals including Ba, Co, Cr, Cu, Mn, Ni, Pb, V and Zn. The instrument uses argon as the working gas with a pressure of 0.7 MPa. The argon flow rates of cooling, auxiliary, and atomizing were set to 12, 0.8, and 0.8 L/min, respectively. After spectra calibration using ICAL solution, five standard solutions were prepared and tested from low to high concentrations. Subsequently, choosing the built standard method and then the sample to be measured was fed to the introduction system by the peristaltic pump. When the measurement was complete, the results could be obtained accordingly. Each solution sample was detected in triplicate to eliminate the experimental error. The photograph of the ICP-OES equipment used in this study is shown in Figure 3.10.

Figure 3. 10 Photograph of the SPECTROBLUE FMS36

3.6.3 Determination of mode of occurrences

To determine the mode of occurrence of heavy metals in each sample, a modified four-step sequential extraction method were adopted [253, 254]. As can be seen from Figure 3.11, the content of a heavy metal was divided into four fractions including acid soluble fraction (F1), reducible fraction (F2), oxidizable fraction (F3) and residual fraction (F4). In the first step, approximately 1 g sample was mixed with 30 mL of 0.1 mol/L acetic acid in a centrifuge tube and oscillated for 16 h at room temperature. The supernatant was then filtered and diluted to 50 mL for ICP-OES analysis. The fraction 1 contains interchangeable HMs, which are associated with carbonates and those that are soluble in water or under slight acidic conditions.

The residue remaining from the first step was mixed with 30 mL of 0.1 mol/L $NH_2OH{\cdot}HCl$ in the centrifuge tube and oscillated for 16 h before centrifugation and filtration of supernatant. The prepared extracted solution was diluted using ultrawater for ICP-OES test. The fraction 2 is composed of metals, which bound to Fe and Mn oxides and hydroxides.

The solid remaining from the second step was transfer into a 50 mL beaker. Then, 10 mL H_2O_2 buffered by HNO_3 to PH=2 was added to the beaker for digestion at room temperature. After 1 hour, the beaker was put into a water bath for digestion at 85 ºC for another 1 hour with occasional manual shaking. After the volume of solution reduced to about 2 mL in the beaker, a second 10 mL H_2O_2 was added to the beaker, followed by digestion and heating at 85 ºC for one hour until the volume decreased to about 2 mL. After the solution was cooled down to conventional temperature, 30 mL NH_4AC was poured to the beaker and the resulting solution was transferred to a centrifuge tube. Finally, the supernatant solution was obtained after 16 hours oscillation and centrifugation. The extracted solution was filtered and diluted to 50 mL in a volumetric flask for ICP-OES test. The fraction 3 is for the HMs associated with organic matters and sulphides.

The residue from the last step was digested using the microwave digester involving the use of a mixture of 6 mL HNO_3 and 2 mL HCl. Then, the final extraction was filtered and diluted to 50 mL for ICP-OES analysis. The fraction 4 is the HMs that are strongly bounded to the structure of amorphous and crystalline phase and it is regarded as the most stable phase under the environment [255].

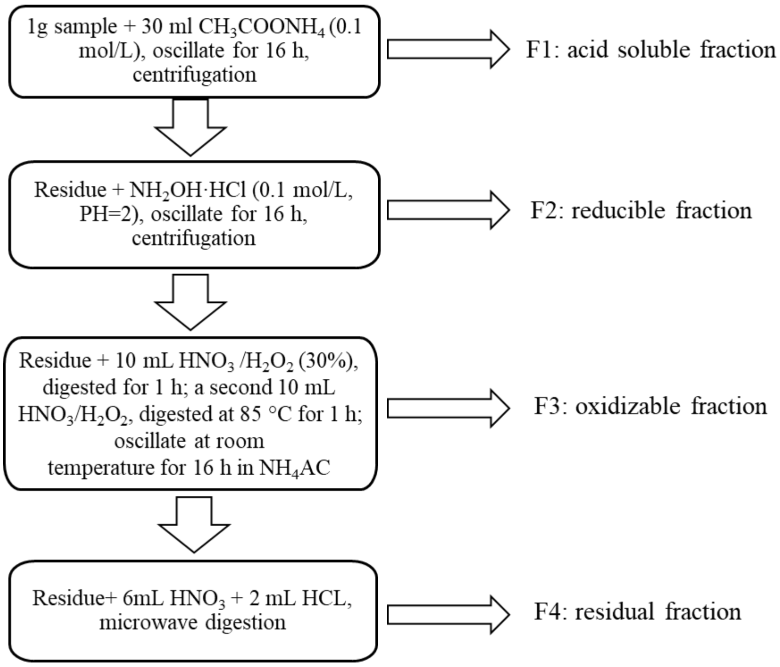

Figure 3. 11 Diagram of the four-step sequential extraction method

The recovery percentage of each heavy metal by the four steps sequential extraction was calculated in order to reflect the correctness of this method. The equation is formulated as:

$$\text{Recovery} = \frac{F_1+F_2+F_3+F_4}{HM_{total}} \times 100\% \tag{3.32}$$

where F_1, F_2, F_3, F_4 represent the concentration of heavy metals in each fraction. HM_{total} stands for the total content of the corresponding heavy metal.

3.7 Ash slagging characteristics and FactSage modelling

3.7.1 Ash slagging characteristics

In order to demonstrate the effect of oil shale addition on the ash slagging and fouling potential during co-combustion in the boiler, two widely used numerical indices were employed in this study, namely base to an acid ratio ($R_{B/A}$) and fouling index (F_U) [30, 256, 257]. Their expressions are demonstrated as follows:

$$R_{B/A} = \frac{Fe_2O_3+CaO+MgO+Na_2O+K_2O}{SiO_2+Al_2O_3+TiO_2} \quad (3.33)$$

$$F_U = R_{B/A} \times (Na_2O+K_2O) \quad (3.34)$$

where Fe_2O_3, CaO, MgO, N_2O, K_2O, SiO_2, Al_2O_3 and TiO_2 represent the mass fraction (%) of the corresponding chemical compounds in the ash. If $R_{B/A} \leq 0.5$, a blended sample has a low slagging propensity, if $0.5 < R_{B/A} \leq 1$, then a sample has an average slagging propensity, if $R_{B/A} > 1$, a sample has a very high slagging propensity. Similarly, when $F_u \leq 0.6$, a sample has low fouling inclination, medium for $0.6 < F_u \leq 1.6$, and high for $F_u > 1.6$ [258].

3.7.2 Factsage modelling

The above-mentioned correlations only gave a general justification of the ash slagging and fouling of the blended samples. To gain further insights of ash fusion behaviours and mineral transformation during combustions, thermodynamic equilibrium calculations of the ashes for all samples were performed using FactSage 6.3 due to its well predicting accuracy [259-262]. In this work, the FToxid and FactPS databases were selected to represent the phase formation, combination and transformation of metal oxides. Besides, the 'Equilib' module was employed to perform phase and chemical equilibrium calculation of the ashes based on Gibbs' energy minimization principle. The input data in the reactant window included C, H, O, N, S and ash contents such as SiO_2, Al_2O_3, CaO, Na_2O, MgO, K_2O, Fe_2O_3, SO_3, TiO_2, and P_2O_5. The reactions took place at atmospheric pressure, and the temperature ranges were set between 800 to 1500 °C with an interval of 100 °C. In addition, the air was also added as the reactant, and the air equivalent ratio was set at 1.15 [30].

3.8 Artificial neural network prediction

Artificial neural network (ANN) is an effective, efficient and reliable tool to correlate input and output data with a non-physical modelling manner, and has the capacity to construct a complex and nonlinear prediction model [263, 264]. A neural network includes three types of layers, namely, input layer, hidden layer and output layer. Generally, one hidden layer with suitable number of neurons can implement approximating any nonlinear function with acceptable accuracy [265]. Although the increase of hidden layer can improve the predictive accuracy, it also increases the training time and convergence difficulty. However, the number of neurons in hidden layers are usually determined by trial and error method [266]. In this study, a back propagation neural network (BPNN) with three layers were employed to simulate the weight loss curves in the co-gasification, as schematically shown in Figure 3.12. The input layer comprises SC to coal ratio, heating rate and temperature, while the output layer corresponds to the mass loss percent. Levenberg-Marquardt (LM) training function was selected to update the weight and bias values due to its superior prediction performance. The transfer functions for the input to hidden layer and the hidden to output layer were tansig and purelin, respectively. Before entering the hidden layer, the input data should be scaled in the range of -1 to 1 to avoid falling into the saturation region of the activation function, which might lead to the gradient disappearance. The operating parameter for the BPNN model is listed in Table 6.2. About 80% experimental data (approximately 1200 subsets) were selected randomly for training purpose, whilst the remaining data were employed for test. The predicted accuracies of the built BPNN were appraised by the following indices, mean square error (MSE), root MSE (RMSE), mean absolute error (MAE), mean absolute predictive error (MAPE) and correlation coefficient (R^2), which are mathematically expressed as:

$$MSE = \frac{1}{m}\sum_{i=1}^{m}(e_i - y_i)^2 \tag{3.35}$$

$$RMSE = \sqrt{\frac{1}{m}\sum_{i=1}^{m}(e_i - y_i)^2} \tag{3.36}$$

$$MAE = \frac{1}{m}\sum_{i=1}^{m}|e_i - y_i| \tag{3.37}$$

$$MAPE = \frac{100}{m}\sum_{i=1}^{m}\left|\frac{e_i - y_i}{e_i}\right| \tag{3.38}$$

$$R^2 = 1 - \frac{\sum_{i=1}^{m}(e_i - y_i)^2}{\sum_{i=1}^{m}(e_i - \bar{e})^2} \tag{3.39}$$

where e_i is the experimental value, y_i is the predicted value from network, and the $\bar{e}$ is the mean value of the experimental data.

In BP neural network, the weights and biases are generated randomly firstly, then BPNN uses the error gradient descent algorithm to correct the weight and threshold in order to minimise MSE. Nevertheless, there may be multiple local minima on the error surface, which makes the iterative process fall into local minima easily, leading to small adjustment range of weights and thresholds. Thus the convergences become slow. However, the implementation of genetic algorithm to optimize the weights and thresholds enable BPNN reach the global optimum results and enhance network performances and convergence speed. The integration of GA with BPNN is also presented in Figure 3.12. Firstly, the input data and operating parameters of GA (seeing Table 3.2) are initialized, while the initial weights and thresholds from BPNN are encoded, followed by the calculation of fitness. Secondly, selection the populations according to the individual fitness value, and then crossover and mutate the selected population based on the assigned cross and mutation probability. Thirdly, calculate of the new fitness value based on the updated individuals and evaluate whether the fitness values fulfil the terminal criteria. After that, the optimal weights and thresholds are input to the BPNN to train and predict the output data. The GA-BPNN modelling was realized based on MATLAB 2018 with ANN and GA Toolboxes.

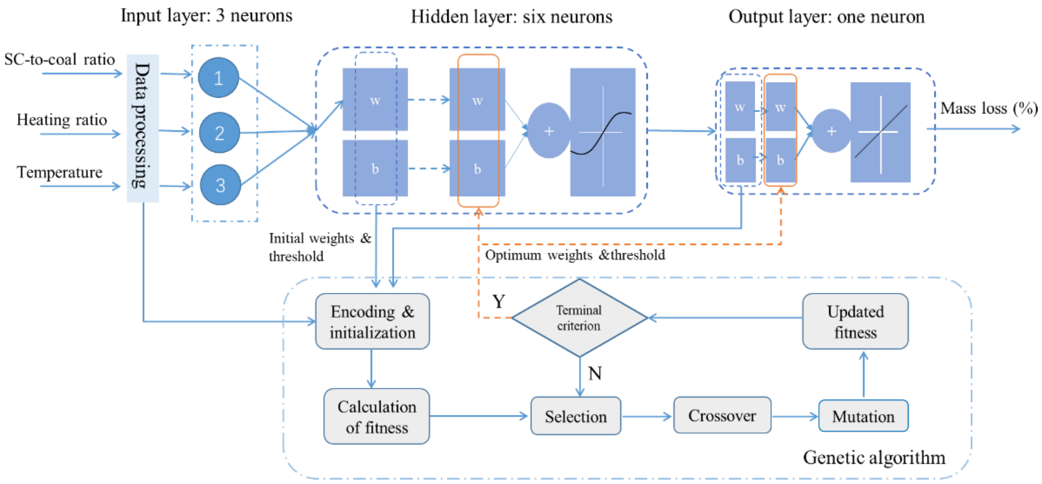

Figure 3. 12 GA-BPNN predictive structure diagram

Table 3. 2 Operating parameters for the GA-BPNN network

Parameter	Value
Number of hidden neurons	2-9
Transfer function of input to hidden layer	Tansig
Transfer function of hidden layer to output	Purelin
Performance function	MSE

Training algorithm	Levenberg Marquardt
Adaption learning function	Learndm
No. of Epochs	100
No. of lr	0.05
No. of goal	0.00001
Population size of GA	10
Maximum number of generation	100
Crossover rate	0.4
Mutation probability	0.2

Chapter 4 Kinetics and thermodynamic investigations on CO_2 gasification of coal chars prepared via conventional and microwave pyrolysis*

4.1 Introduction

Coal gasification involves two steps including pyrolysis and char gasification, of which the latter is considered as the rate-controlling step [267]. As a greenhouse gas, the accumulation of CO_2 contributes most to the global warming [268]. Hence, it is imperative to implement CO_2 mitigating strategies to alleviate climate changes. Fortunately, the employment of CO_2 to gasify coal char for valuable syngas production emerges as a promising alternative to reduce CO_2 pollution. Therefore, studies on the kinetics and performances of char-CO_2 gasification are essential for the reactor design, control and efficiency [269].

Pyrolysis conditions, especially pyrolysis temperature, have a significant effect on the char structure and reactivity. Microwave heating can realize rapid, volumetric, selective and non-contact heating of coal by directly converting electromagnetic energy into thermal energy [9]. Nevertheless, little research has been performed on gasification reactivity and kinetics of CO_2 iso-thermal

---

* This chapter has been published in the Journal of Coal Science and Technology.

gasification of coal chars prepared via microwave pyrolysis.

To ensure the implementation of CO_2 gasification, the prediction of thermodynamic performances for char-CO_2 gasification is of importance [270]. Process simulations of biomass gasification using pure or mixer CO_2 have been carried out broadly [270-273]. As far as we acknowledged, no study has been conducted in detailed thermodynamic performances of coal char gasification with pure CO_2 as a gasifying medium.

In this chapter, the kinetic behaviours and thermodynamic performances of char-CO_2 isothermal gasification were investigated using thermogravimetric analysis and Aspen Plus, respectively. One char was derived from microwave pyrolysis, while the other three char samples were produced under different temperatures using conventional pyrolysis for the purpose of comparison. Besides, chemical compositions, structures and morphologies of chars were analysed. Moreover, SCM and RPM methods were employed to calculate the kinetic parameters for all chars. Furthermore, thermodynamic performances including syngas compositions and cold gas efficiency (CGE) of char-CO_2 gasification were assessed.

4.2 Char characterizations

Table 4.1 shows the proximate and ultimate analysis of the coal and prepared chars. As indicated, both the volatile and moisture contents of the conventional chars decrease as the pyrolysis temperature increases. In contrast, fixed carbon is observed to have a positive relation with the pyrolysis temperature. As the temperature varies from 1073 to 1273 K, the carbon content and C/H mass ratio increase from 75.2 to 76.5% and from 29.1 to 62.0, respectively. This is expected since high temperatures favoured hydrocarbon cracking, which led to more complete devolatilization. The MW char exhibits the lowest volatile, moisture, and hydrogen contents, but the highest fixed carbon content and C/H ratio. This was mainly determined by the nature of microwave, which directly converted the electromagnetic energy into thermal energy from the centre area of char resulting in a faster heating rate than conventional heating [98]. Consequently, inside volatile in the char was further released at high temperature and therefore, more fixed carbon and C/H are obtained.

Table 4. 1 Ultimate and proximate analysis for the samples

		Coal	Py1073	Py1173	Py1273	MW
Ultimate analysis (w_{ad}%)	C	67.8	75.2	75.9	76.5	77.1
	H	3.7	1.7	1.5	1.3	1.2
	N	0.7	0.8	0.6	0.6	0.6
	S	0.3	0.9	0.9	0.9	0.9
	C/H	18.3	29.1	48.3	62.0	64.2
Proximate analysis (w_{ad}%)	Ash	14.9	16.7	19.5	19.8	19.8
	V	25.6	5.3	2.4	0.6	0.5
	M	5.9	3.5	2.1	2.0	1.8
	FC	53.5	74.6	76.0	77.6	77.9

The crystallinities and structural parameters of the raw coal and pyrolyzed chars were investigated via XRD. The results are displayed in Figure 4.1 and Table

4.2, respectively. Several sharp crystalline diffraction peaks are observed, such as those at 20.8° and 26.6°, which represent the inorganic mineral SiO_2. Besides, a broad diffraction peak is noted at the 2θ angle from 20 to 30°, corresponding to the (0 0 2) carbon crystallite band. Chars prepared at different pyrolysis temperatures exhibit similar diffraction peaks, but the intensity of the (0 0 2) diffraction peak increases slightly with the pyrolysis temperature. These phenomena indicate that the microcrystalline structure is prone to become ordered. The structure parameters of $d_{(0\ 0\ 2)}$, L_c and N_{mean} were employed to quantify the crystal characteristics of the all samples. As depicted in Table 4.2, MW char exhibits the smallest $d_{(0\ 0\ 2)}$ of 3.47 Å, which is similar to that of the well-ordered graphite (3.354 Å). Increasing the pyrolysis temperature reduces the $d_{(0\ 0\ 2)}$ of conventional chars from 3.72 to 3.65 Å. The L_c and N_{mean} increase from 13.8 to 17.43 Å and from 4.71 to 5.77, respectively, with the pyrolysis temperature from 1073 to 1273 K. In addition, the MW char exhibits the highest L_c and N_{mean}, suggesting greater crystallinity. Increasing the pyrolysis temperature could enhance cross-linking via dehydration and decarboxylation and even the dehydrogenation and aromatization reactions, resulting in the increasing ordered structures and also creating new ordered carbons [108]. Coal comprises minerals (such as pyrite) and polar organic compounds, which have higher dielectric loss than the organic part of char. Consequently, hot spots are expected to be formed under microwave heating and can result in temperatures that were far higher than those in bulk char [274]. Therefore, MW char is more ordered and has a higher thermal stability.

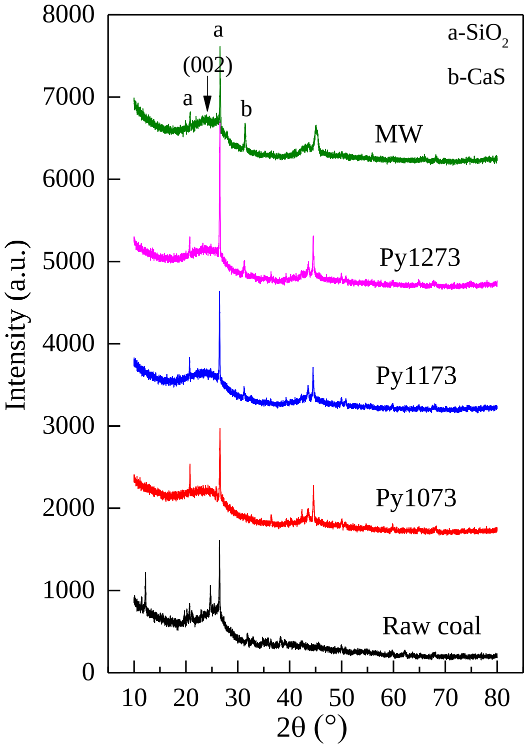

Figure 4. 1 XRD patterns for raw coal and pyrolyzed char after conventional and microwave processing

Table 4. 2 Structure parameters of coal and chars

Sample	$d_{(0\,0\,2)}$ (Å)	L_c (Å)	N_{mean}
Py1073	3.72	13.80	4.71
Py1173	3.69	15.60	5.22
Py1273	3.65	17.43	5.77
MW	3.47	20.30	6.83

The morphological characteristics of the raw coal and its derived four chars are revealed by the SEM images presented in Figure 4.2. Obviously, the raw coal clearly exhibits a non-porous, blocky shape with a rough surface. The char samples produced via conventional pyrolysis are similar, but more pores and cavities are detected as the pyrolysis temperature increases, as shown in Figure 4.2 (b) to (d). Besides, the surfaces are prone to be smooth and some microspheres appear as the pyrolysis temperature increases. Due to the release of volatile, some pores were formed on the surfaces and the addition of pyrolysis temperature led particles to fuse and minerals to melt, resulting in the formation of smooth surface and microspheres.

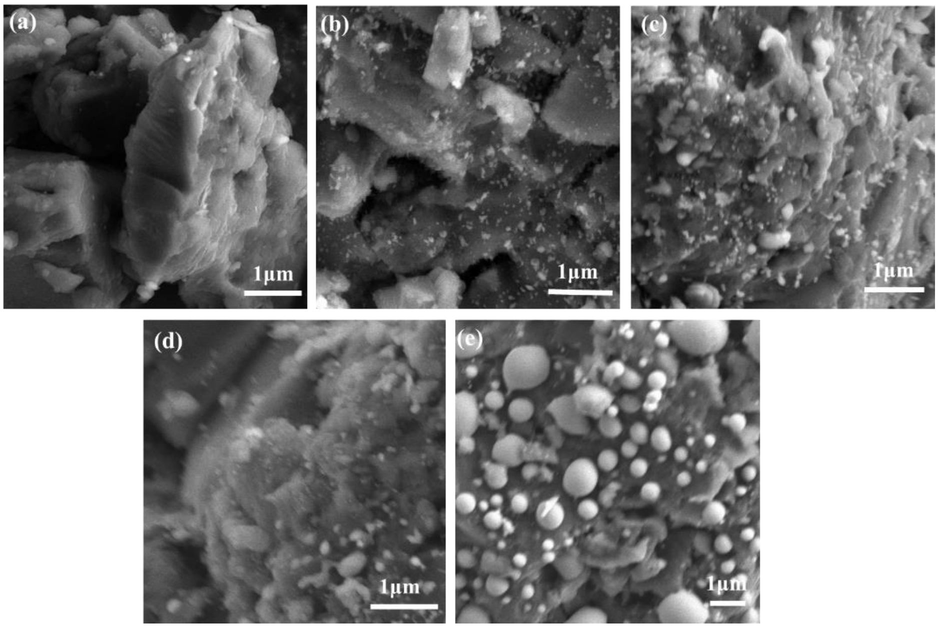

Figure 4. 2 SEM images of five samples: (a) raw coal; (b) Py1073 char; (c) Py1173 char; (d) Py1273 char; (e) MW char

In terms of MW char in Figure 4.2(e), its surface presents a more open structure due to the crack of internal small pores caused by rapid heating expansion. Besides, different size of microspheres with diameter varying from 0.2 to 1μm are exhibited. This was mainly contributed to the highly localized temperature in the hot spots induced by microwave heating [108]. As a consequence, minerals are melted at high temperature and shrunk to form such spherical droplets due to the surface tension.

4.3 Kinetic parameters

The reactivity of chars was quantified using the reactivity index, $R_{0.5}$, as detailed in Table 4.3. As the pyrolysis temperature increases from 1073 to 1273 K at a gasification temperature of 1173 K, $R_{0.5}$ decreases from 1.35 to 0.68. This indicates that the Py1073 char has better gasification reactivity. Similar results can be found at different gasification temperatures. Meanwhile, $R_{0.5}$ has a positive relationship with the gasification temperature. As the conventional char pyrolysis temperature increases from 1173 to 1273 K, the reactivity index increases by 0.75–1.86 times. This suggests that higher gasification temperatures help char gasification. Microwave induced char has a smaller $R_{0.5}$ than conventional chars formed at the same gasification temperature. Increasing the char preparation temperature not only decreases the quantity of volatile matter, but also increases the extent of cross-linking. The increase of char preparation temperature could not only decrease the volatile matters but also increase the cross-linking reactions. As a result, the C/H ratio decreases and the carbon structure becomes more ordered, as seen in Table 4.1 and Figure 4.1, respectively. Hence, the gasification reactivity of chars is ranked as: Py1073 > Py1173 > Py1273 > MW.

Table 4. 3 Summary of reactivity index ($R_{0.5}$)

Char type	$R_{0.5} \times 10^3$ (s^{-1})		
	1173 K	1223 K	1273 K
Py1073	1.35	1.74	2.37
Py1173	1.07	1.51	2.26

Py1273	0.68	1.48	1.95
MW	0.39	1.08	1.92

The determination of kinetic parameters include reaction constant, pre-exponential factor and activation energy. By plotting $3[1-(1-x)^{1/3}]$ and $(2/\psi)\left[\sqrt{1-\psi\ln(1-x)}-1\right]$ versus time (t), the reaction constant of k_{SCM} and k_{RPM} for the SCM and RPM were obtained as the slopes of the linearized curves at different gasification temperatures. Figure 4.3 presents a calculating example for the determination of k_{SCM} and k_{RPM} for the Py1073 char. It is worth noting that the value of structural constant φ was determined by plotting of ($t_x/t_{0.8}$) as a function of conversion as displayed in Eq.(3.7). The φ values are regressed to be 8.2, 7.5 2.8 and 2 for the chars of Py1073, Py1173, Py1273 and MW, respectively, which indicates that the MW undergoes less pore development during gasification. This result is accordance with the finding by Liu et al. [275] that conventional pyrolysis was more conducive to pore development than microwave treatment. Table 4.4 summaries the rate constants for the two kinetics models. The coefficients of determination (R^2) are also listed to show the effectiveness of fitting. As shown, the R^2 exceeds 0.99 in all cases suggesting excellent correlation. The resulting values of k_{SCM} and k_{RPM} are different for the same char under the same gasification temperature. As the gasification temperature increases, both k_{SCM} and k_{RPM} increase by about 1.86–4.88 times. Nevertheless, given a particular gasification temperature, both k_{SCM} and k_{RPM} decrease with the pyrolysis temperature, indicating the reduction of reactivity. Based on the calculated k values, the activation energy and pre-exponential factor were determined using the Arrhenius plot as displayed in Eq. (3.10). Figure 4.4 shows plots of ln$k$ as a function of $1/T$ with different models. Clearly, a good linear is achieved.

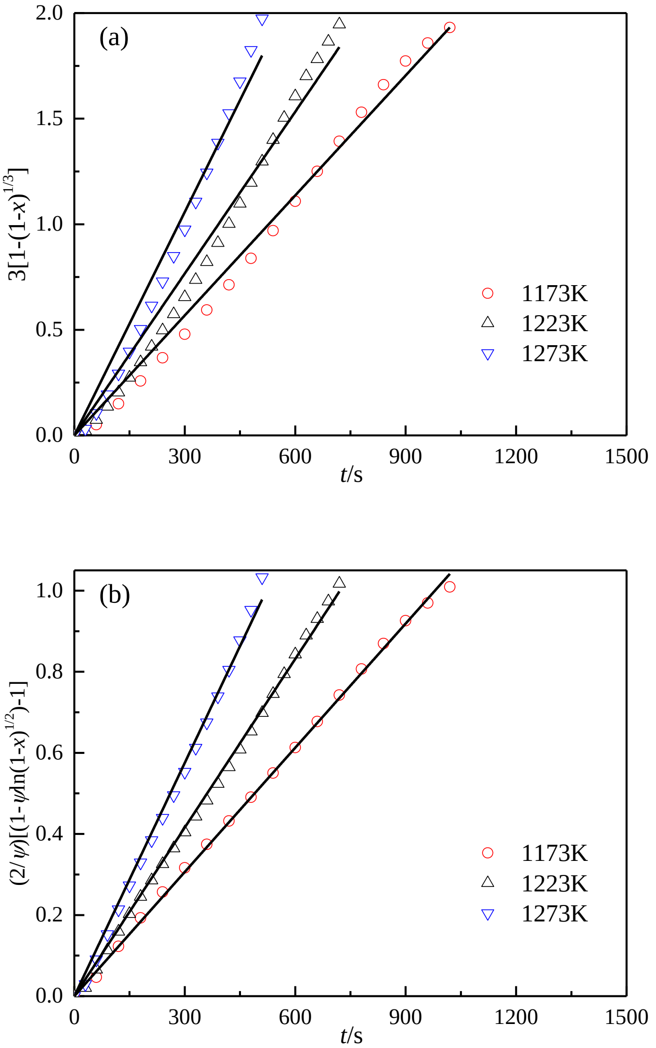

Figure 4. 3 Determination of rate constant for the char sample of Py1073: (a) k_{SCM} and (b) k_{RPM}

Table 4. 4 k values obtained from the linear fit of experimental data

Char sample	Model	Reaction rate constant, k ($\times10^{-4}$/s)					
		1173 K	R^2	1223 K	R^2	1273 K	R^2

Py1073	SCM	18.9	0.9984	25.5	0.9967	35.3	0.9952
	RPM	10.2	0.9998	13.9	0.9997	19.2	0.9984
Py1173	SCM	15.1	0.9975	22.1	0.9941	35.9	0.9883
	RPM	8.4	0.9996	12.3	0.9995	19.8	0.9976
Py1273	SCM	8.2	0.9985	19.1	0.9992	27.6	0.9946
	RPM	6.73	0.9991	15.1	0.9994	20.6	0.9974
MW	SCM	2.40	0.9987	6.14	0.9985	11.7	0.9982
	RPM	2.11	0.9988	5.26	0.9985	10.1	0.9985

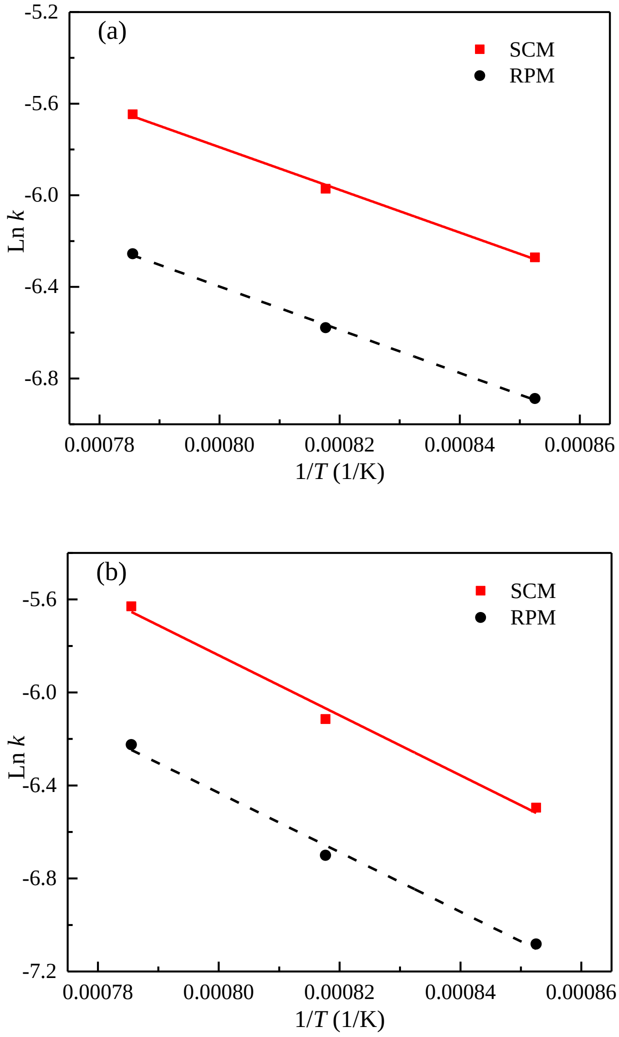

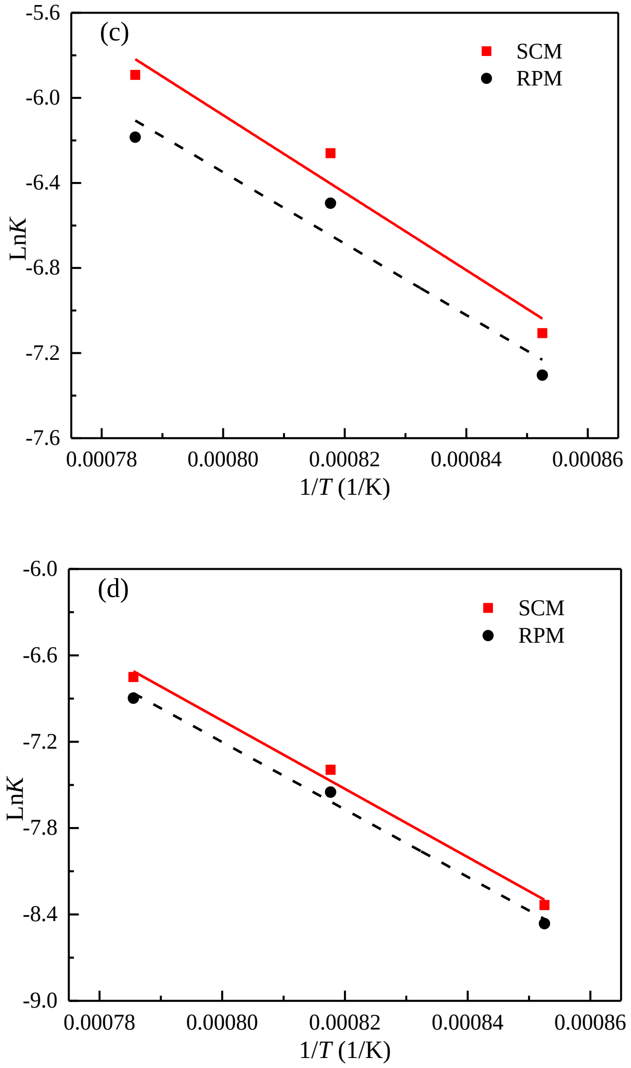

Figure 4. 4 Determination of the kinetic parameters A and E_a from the SCM and RPM models: (a) Py1073 char; (b) Py1173 char; (c) Py1273 char; and (d) MW char

Table 4.5 summarizes the kinetic parameters (E_a and A) calculated using the slopes and intercepts in Figure 4.4. There are slight differences between the E_a and A values obtained via the SCM and RPM methods. In addition, the pyrolysis temperature and use of microwave heating for char preparation have significant effects on the E_a and A, which vary from 78.45 to 194.72 kJ/mol and from 3.15 to 102231.99 s^{-1}, respectively, using the RPM approach. It is also noticeable that there exists a “compensation effect”, which is a kind of linear relationship between the logarithm of the frequency factor and the activation energy [276], as the increase of A when E_a increases from Table 4.5.

Table 4. 5 Intrinsic SCM and RPM model kinetic parameters of materials made using various pyrolysis temperatures

Char samples	SCM		RPM	
	A (1/s)	E_a (kJ/mol)	A (1/s)	E_a (kJ/mol)
Py1073	5.25	77.47	3.15	78.45
Py1173	88.49	107.28	44.25	106.23
Py1273	4817.45	151.39	1187.97	139.65
MW	148301.11	197.05	102231.99	194.72

To find the best imitative gasification reaction model, the carbon conversion was calculated for all chars as a function of the gasification time at various gasification temperatures. Figure 4. 5 compares the conversions predicted using the SCM and RPM methods to the experimental values. Visually, both models fit the conversion well. However, the RPM prediction is better than the SCM prediction, as the latter exhibits a relatively large discrepancy at times shorter than 800 s, as shown clearly in Figure 4. 5 (a) and (b). To quantify the fittings, both of R^2 and root mean square error (RMSE) were calculated for all chars and the results are detailed in Table 4.6. The R^2 of SCM conversion prediction varies from 0.955 to 0.994, while R^2 for RPM prediction ranges from 0.992 to 0.999.

In addition, the RMSE values for RPM are between 0.0084 and 0.0251, but the RMSE varies from 0.016 to 0.067 for the SCM. This means that the RPM is the model most suitable for describing gasification conversion.

On the other side, the variation of *r* along with *x* was also calculated using both SCM and RPM. The predictions are compared to experimental data in Fig. 6. The reaction rate increases until it reaches its maximum at approximately 0.15–0.4. This is followed by a decrease as conversion continues. The decrease of reaction rate was mainly attributed to overlapping of inner pores, which led to the reduction of reaction surface area and active points [237, 276]. The RPM fits the reaction rate data better than the SCM. Table 4.6 also shows the R^2 and RMSE values used to quantify reaction rate prediction effectiveness. For a given case, the RPM offers a higher R^2 and lower RMSE than its counterpart. Hence, the RPM approach is best for capturing the reaction rate.

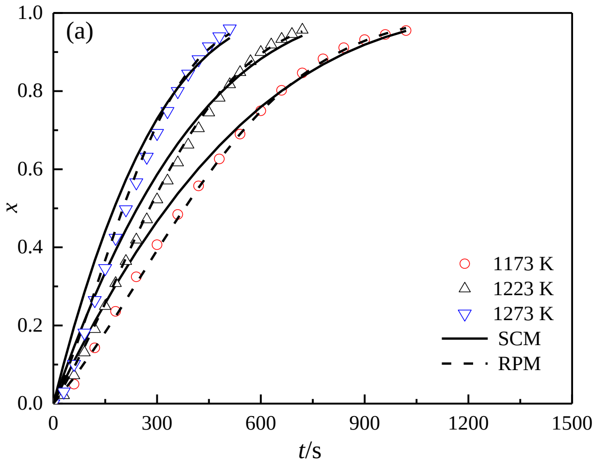

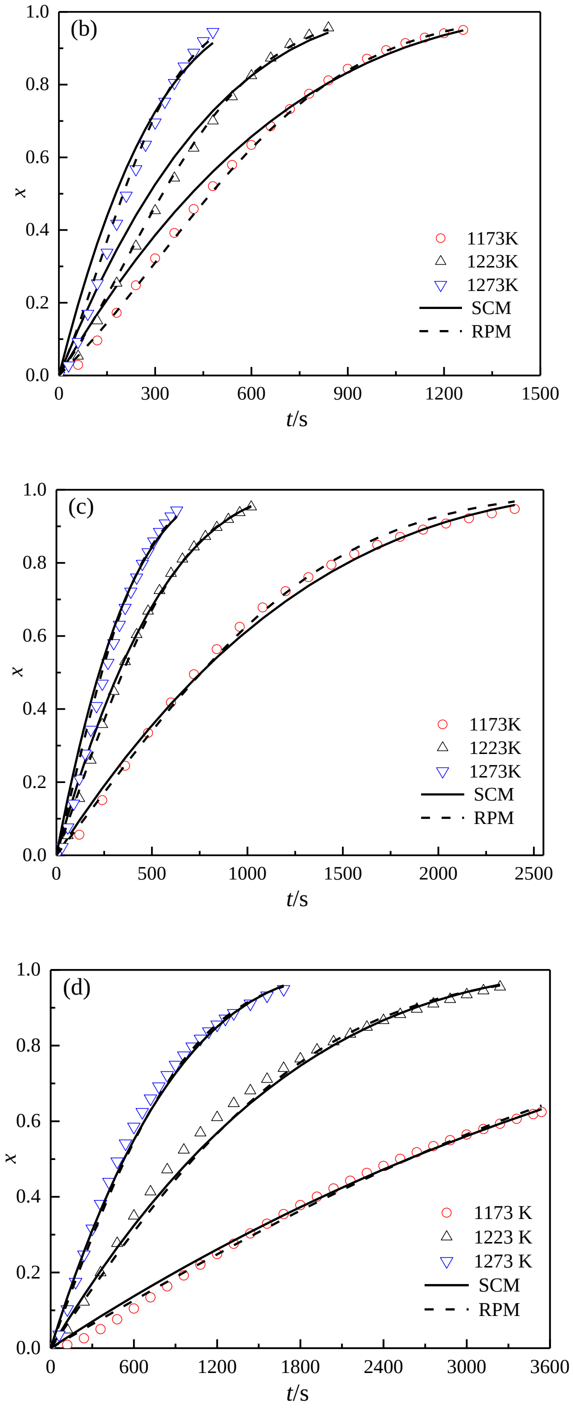

Figure 4. 5 Comparison of RPM- and SCM-predicted conversions to experimental values: (a) Py1073 char; (b) Py1173 char; (c) Py1273 char; and (d) MW char

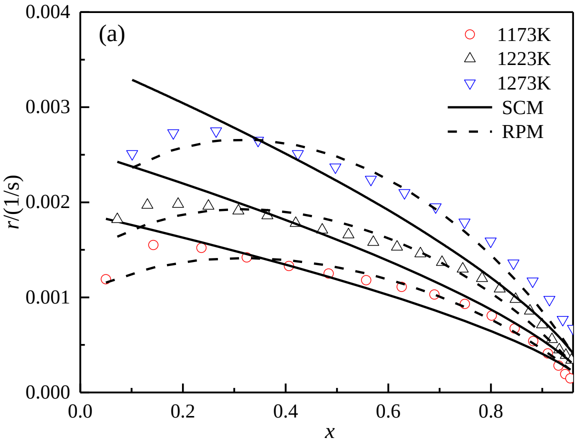
(a)
1173K
1223K
1273K
SCM
RPM
0.004
0.003
0.002
0.001
0.000
r/(1/s)
0.0
0.2
0.4
0.6
0.8
x

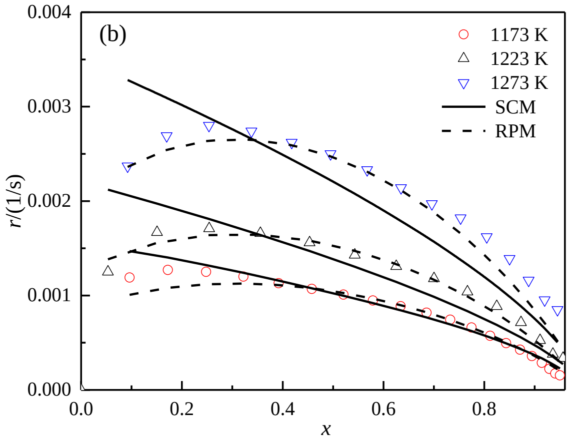
(b)
1173 K
1223 K
1273 K
SCM
RPM
0.004
0.003
0.002
0.001
0.000
r/(1/s)
0.0
0.2
0.4
0.6
0.8
x

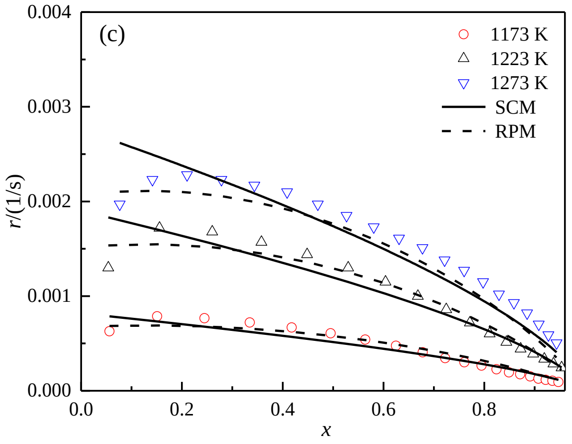
(c)
1173 K
1223 K
1273 K
SCM
RPM
0.004
0.003
0.002
0.001
0.000
r/(1/s)
0.0
0.2
0.4
0.6
0.8
x

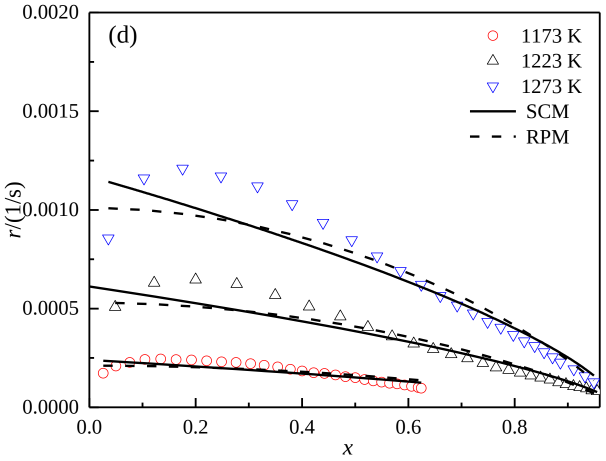

Figure 4. 6 Comparison of SCM- and RPM-predicted reaction rates to experimental values: (a) Py1073; (b) Py1173; (c) Py1273; and (d) MW char

Table 4. 6 Comparison of evaluation indexes based on SCM and RPM models

Char type	Variable	SCM_1173 K		SCM_1223 K		SCM_1273 K		RPM_1173 K		RPM_1223 K		RPM_1273 K	
		R^2	RMSE	R^2	RMSE	R^2	RMSE	R^2	RMSE	R^2	RMSE	R^2	RMSE
Py1073	x	0.981	0.04	0.963	0.0396	0.955	0.062	0.999	0.0084	0.998	0.0089	0.997	0.023
	r	0.831	0.0002	0.832	0.00009	0.776	0.0003	0.967	0.00008	0.969	0.00007	0.942	0.0001
Py1173	x	0.981	0.052	0.993	0.054	0.948	0.067	0.999	0.0122	0.998	0.012	0.992	0.025
	r	0.946	0.0002	0.647	0.00027	0.618	0.0004	0.970	0.00009	0.985	0.00006	0.961	0.0002
Py1273	x	0.994	0.0615	0.992	0.067	0.971	0.049	0.996	0.0226	0.997	0.024	0.991	0.026
	r	0.928	0.00053	0.905	0.0004	0.859	0.003	0.955	0.00017	0.963	0.00016	0.943	0.002
MW	x	0.992	0.016	0.992	0.022	0.994	0.021	0.996	0.0135	0.992	0.0251	0.995	0.021
	r	0.731	0.00004	0.920	0.00005	0.922	0.0002	0.751	0.00003	0.921	0.00005	0.932	0.0001

4.4 Thermodynamic analysis

Considering the experimental char-CO_2 gasification temperature are varied from 1173 to 1273 K, which are quite suitable for the operating temperature of a typical fluidized-bed gasifier. To evaluate the syngas composition and cold gas efficiency under char-CO_2 gasification conditions, thermodynamic modelling of char gasification using CO_2 was carried out using Aspen Plus based on the Gibbs minimization approach with fairly accurate [277]. Detailed simulation descriptions can be found in [278, 279]. The CGE represented the conversion of the energy content in the char to the lower heating value of syngas, as defined by Eqs.(4.1) and (4.2) [270].

$$\text{CGE} = \frac{LHV_{syg}}{LHV_{char}} \tag{4.1}$$

$$LHV_{syg} = n_{H_2}LHV_{H_2} + n_{CO}LHV_{CO} \tag{4.2}$$

where n and LHV refer to mole flow rate and lower heating value, respectively. The subscript H_2, CO and char represent the corresponding species.

The simulation result showing the gasification performances is depicted in Figure 4. 7 (a). The simulation conditions are: gasification temperature of 1273 K and CO_2 to carbon molar ratio (CO_2/C, which is defined as the molar ratio between CO_2 fed to gasifier and carbon content in the char) of 1. As presented in this figure, the molar concentration of CO exceeds 82% and the molar concentrations of CO_2 and H_2 are approximately 8% and 4%, respectively, in the syngas. When the pyrolysis temperature increases from 1073 to 1273 K, the CO fraction gradually increases from 82.09 to 85.58%, while both the CO_2 and H_2 fractions decrease moderately. The microwave-induced char produces the highest CO concentration of 86.18% and smallest quantities of CO_2 and H_2. This was mainly because that the MW had the most C/H ratio, followed by Py1273, Py1173 and Py1073. Given fixed gasification conditions, the higher carbon content in the char generated more CO specie and thus produced a larger CO fraction. The CGE has the similar change tendency as the CO concentration, changing slightly from 1.27 to 1.30. The reason was mainly due to the addition of CO concentration and the LHV of CO was larger than that of H_2. Consequently, according to Eqs. (4.1) and (4.2), increment in CGE is expected. It is clear that the CGE value exceeds 1 owing to the larger LHV of syngas than that of original char caused by the conversion of CO_2 to CO.

Figure 4.7(b) presents the influence of gasification temperature on gasification performances for the char of Py1073 and $CO_2/C=1$. The CO molar fraction increase slightly from 88.69 to 88.81%, whilst H_2 concentration exhibits a moderate decreasing trend. The increase of gasification temperature inhabited the exothermic water gas shift reaction ($CO + H_2O \rightarrow H_2 + CO_2$). Hence, CO concentration increases and H_2 reduces. Due to the near unchangeable of the syngas, CGE is presented to be invariant.

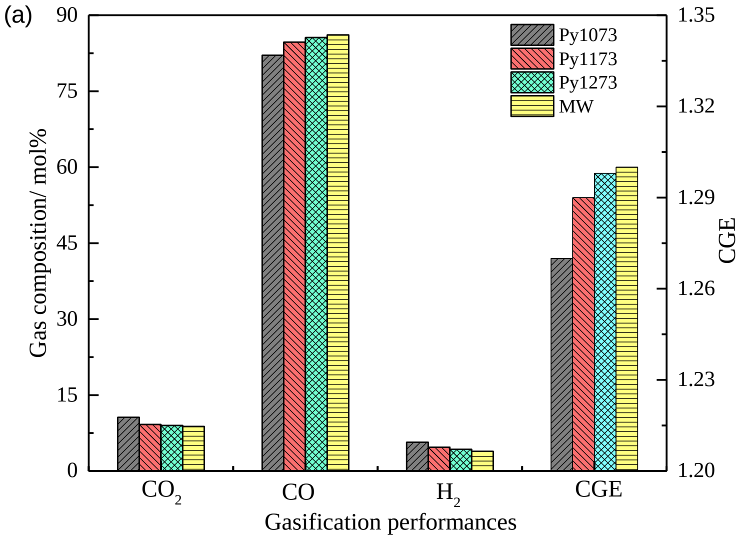

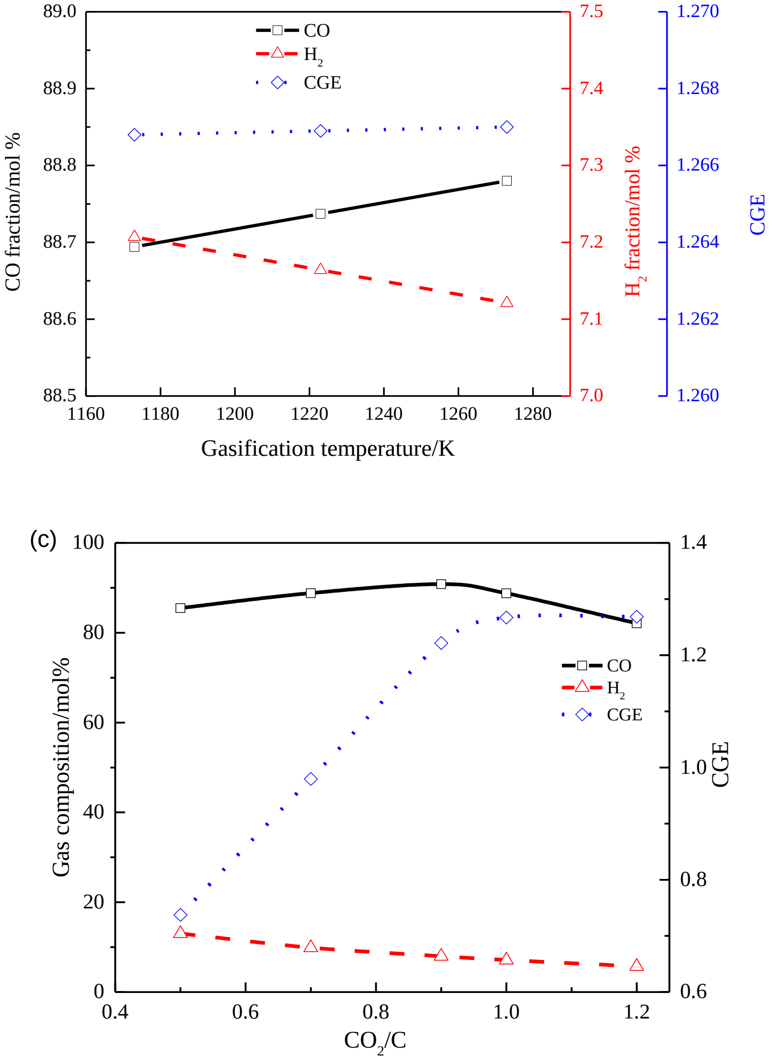

Figure 4. 7 Gasification performance of char-CO_2 system: (a) Effect of pyrolysis temperature; (b) Effect of gasification temperature and (c) Effect of CO_2/C molar ratio

The CO_2/C is another decisive parameter for it directly determined the char conversion ratio and syngas compositions. Figure 4.7(c) shows the effect of CO_2/C changing from 0.5 to 1.2 at the gasification temperature of 1273 K for the char of Py1073. Upon increasing CO_2/C, the CO concentration initially increases and then decreases moderately. Its maximum fraction is 93.8% at $CO_2/C = 0.94$. Nevertheless, increasing CO_2/C from 0.5 to 1.2 reduces the H_2

concentration from 13.0 to 5.7%. With respect to CGE, it firstly increases from 0.74 to 1.22 and then is constant at 1.26 when $CO_2/C = 0.94$. When $CO_2/C < 0.94$, the carbon in the char had not been fully gasified, the increase CO_2 flow rate contributed to the enhancement of CO through the Boudouard reaction ($C + CO_2 \rightarrow CO$). Meanwhile, H_2 presents a reducing trend because of the back-forward shift of WGS reaction. When $CO_2/C > 0.94$, the molar flowrate of CO remained unchanged, while continuous addition of CO_2 lowered both the CO and H_2 molar fraction after all carbon in the char was gasified with CO_2. As a consequence of that, CGE increases firstly and then levels off.

4.5 Conclusions

This study investigated the char structure, morphological evolution, kinetics, and thermodynamics of coal char-CO_2 gasification using XRD, SEM, TGA, and Aspen Plus. Three chars were prepared using conventional heating conditions at 1073, 1173 and 1273 K, while one char was derived via microwave pyrolysis at 1173 K. The main conclusions are as follows.

(1) Increasing the pyrolysis temperature enhanced the C/H mass ratio and crystallinity in the char. The microwave-induced char had the highest C/H ratio and most ordered carbon structure. Clear microspheres were observed in the MW char due to hot-spot formation.

(2) During gasification, the MW char was less reactive than conventional chars.

(3) The kinetic parameters were determined using the SCM and RPM methods. Comparison of R^2 values indicated that the RPM was better at

fitting the gasification conversion and reaction rate experimental data than the SCM. The activation energy and pre-exponential factor were in the range of 78.45- 194.72 kJ/mol and 3.15 - 102231.99 s^{-1}, respectively. A compensation effect was also noted during the gasification process.

(4) The MW char had the best thermodynamic performance, with the highest cold gas efficiency of 1.3 and CO molar concentration of 86.18%. Increasing the pyrolysis temperature, gasification temperature, and CO_2-to-carbon molar ratio could enhance the cold gas efficiency.

Chapter 5 Comparative study of coal and its macerals gasification and prediction of synergistic effects under entrained gasifier conditions*

5.1 Introduction

Macerals are the smallest and microscopically recognizable components of the organic constituent in coal [10]. Except for the differences in appearances, maceral groups differ in their chemical composition, which brings distinct technical performances. Therefore, an insight into macerals is the most fundamental step to understand the properties of the parent coal and subsequently, the efficiency of maceral-enriched feedstock [12].

In the past few decades, experimental studies on the structural transformation of macerals and the change in chemical reactivity during pyrolysis/gasification have attracted significant attention [12, 77-80, 280]. For example, Sun et al. [280] compared the structural variations of the macerals before and after pyrolysis and found that vitrinite led to the yield of more aliphatic C-H and lowered aromaticity than inertinite. It is reported [12, 78] that at a short gasification residence time (10 s), the conversion is in the order of liptinite > vitrinite > inertinite, while at a long residence time (200 s), the extent of

---

* This chapter has been published in the Journal of Energy Resources.

gasification was found to be inertinite > vitrinite > liptinite. Moreover, Sun et al. [79] conducted CO_2 gasification of vitrinite char and inertinite char in a pressurized thermobalance at a temperature up to 950 ºC and reported that the vitrinite char was more reactive than the inertinite char with or without a catalyst. However, more recently, Wang et al. [80] stated that the gasification reactivity of vitrinite was lower than that of inertinite under CO_2 gasification atmosphere.

The interaction among macerals during thermal processing is of significance for the basic understanding of the coal chemistry, developing new coal utilization technology and improving thermal efficiency. Sun et al. [281] compared the volatile yield of the pyrolysis of parent coal and its macerals and concluded the existence of synergism among macerals. Chang et al. [282] also studied the interaction during the pyrolysis of inertinite and vitrinite using FTIR, TG and fixed bed reactor and gave a thorough explanation of the interaction mechanisms at molecule levels. Later, the synergistic effect of macerals during hydropyrolysis was also reported by Sun et al. [283], whereas the maximum synergism reached 14.1% at 500 ºC and 3 MPa. Zubkova et al. [284] also explored the interactions of macerals during carbonization and obtained a denser coke than theoretical expectation.

To date, researchers have conducted a significant amount of work on the understanding of the reactivity of macerals during pyrolysis and gasification as well as on the determination of the interactions between macerals during pyrolysis, but few of them have paid attention to the differences of gasification products, cold gas efficiency, syngas content, specific oxygen consumption and specific coal consumption among macerals and parent coal. Besides, the synergistic effects of macerals during gasification have rarely been investigated.

Moreover, the influence of process operating parameters on the synergistic effect has not been discussed although Aspen Plus has been widely applied in the study of solid fuel gasification systems [285-288].

In this chapter, the comparative study of the gasification behaviours of the parent coal and its maceral components under actual entrained-bed gasification conditions was carried out by Aspen Plus. The quantitative evaluations of the interactions between macerals as well as sensitivity analyses were performed. In addition, the relationship between the synergistic coefficient and maceral contents was investigated. Moreover, impacts of typical operating parameters on the interactions among macerals were revealed.

5.2 Process description and simulation

Shell coal gasification technology is a commercial technology that is capable of dealing with a large range of coals at a high energy conversion efficiency [289, 290]. The Aspen Plus diagram of a Shell gasification process is illustrated in Figure 5.1. Milled coal is dried to 5% moisture content and mixed with N_2 in lock-hopper before being fed into the gasifier. The coal is gasified under the conditions of medium pressure using 95 vol% oxygen derived from a stand-alone air separation unit [289]. The commercial operating pressure is around 4.0 MPa, and the gasification temperature is in the range of 1350 to 1550 ºC. The steam to coal mass ratio varies from 0.01 to 0.16 and the feed oxygen to coal mass ratio is in the range of 0.5 to 1.1. The reactions considered in this study are the ones being employed in the literature [291]. The gas product from the gasifier is quenched by recirculated cold syngas to a temperature of 900 ºC [292]. After quench, the heat of the raw gas is recovered by a syngas cooler generating steam for power generation. The syngas is sent to a candle filter to remove particulate matters.

The gasification process was mainly simulated by using a combination of RYIELD and RGIBBS modules in Aspen Plus. The function of RYIELD model was to convert the unconventional coal into standard components such as H_2, N_2, O_2, S, H_2O, Cl_2 and ash, and their yield distribution was programmed using FORTRAN codes according to the ultimate analysis of coal [293-295]. The RGIBBS is a phase and chemical equilibrium model based on Gibbs free energy minimization and was commonly employed to model coal pyrolysis and gasification in the Shell gasifier [296]. In addition, the PR-BM method was used to calculate the thermodynamic properties of materials stream [297].

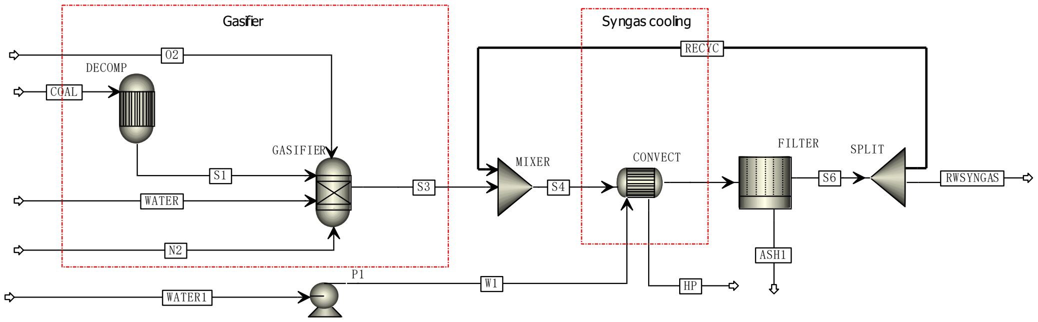

Figure 5. 1 Aspen plus flow sheet of Shell coal gasification process

In order to understand the gasification behaviours of the parent coal and its corresponding macerals, the existing analytical data of Pingshuo bituminous coal and its macerals were taken as the feedstock for this study. Maceral groups were separated based on their density difference using $ZnCl_2$ liquid [298]. The composition, together with the petrographic analysis of the feed coal and maceral groups, are listed in Table 5.1 [298]. The study of interaction among macerals was based on the petrological features of the Pingshuo Bituminous coal, which is shown in Table 5.2 [298]. The main process parameters and conditions of the gasification of the coal and its macerals are shown in Table 5.3 [299, 300].

Table 5. 1 Ultimate and petrographic analyses of Pingshuo Bituminous coal

	Coal	Vitrinite sample	Inertinite Sample	Liptinite Sample
Ultimate analysis/(d, wt%)				
C	62.003	78.322	83.077	70.912
H	4.093	5.311	3.883	7.269
O	10.119	13.406	9.697	16.600
N	1.111	1.218	0.647	0.819
S	0.334	0.569	0.745	0.800
Ash	22.341	1.174	1.951	3.600
Petrographic analysis/(daf,wt%)				
Vitrinite	69.8	95.2	2.3	2.3
Inertinite	23.1	3	96.7	1.4
Liptinite	7.1	1.8	1	96.3

Table 5. 2 Mass composition of simulated coal (wt%)

Simulated coal no.	Vitrinite	Inertinite	Liptinite
1	26.67	6.67	66.66
2	17.29	21.74	60.87

3	12.95	29.08	57.97
4	34.84	4.34	60.82
5	25.79	16.11	58.09
6	29.63	33.37	30
7	38.75	3.22	58.03
8	44.45	18.53	37.03
9	34.28	25.72	40

Table 5. 3 Main conditions for the gasification simulation

Item	Values
The feed flow rate for Coal and macerals, kg/s	10
N_2 flow rate, kg/s	0.717
Gasification pressure, MPa	4.0
Temperature range, °C	1350-1550
Steam to coal (STC) mass ratio:	0.01-0.16
Oxygen to coal (OTC) mass ratio:	0.5-1.1
Oxygen feed composition (vol%):	
O_2	95.0
N_2	1.0
Ar	4.0

5.3 Process evaluation

The evaluation indicators for the gasification of coal and its macerals mainly included specific oxygen consumption, specific coal consumption, syngas lower heating value (LHV), cold gas efficiency and the content of effective syngas ($CO+ H_2$) in the product gas.

Cold gas efficiency (CGE,%) is defined as [301],

$$\text{CGE (\%)}=\frac{\text{LHV of the syngas} \times \text{syngas flow rate}}{\text{LHV of feedstock} \times \text{ flow rate}} \times 100 \tag{5.1}$$

The LHV (MJ/Nm^3) of the syngas is calculated as [302],

$$\text{LHV}=\frac{(CO\times 126.36+H_2\times 107.98+CH_4\times 358.18)}{1000} \tag{5.2}$$

where CO, H_2, CH_4 is the volume fraction in the production of gas from the gasification.

The higher heating value (HHV) of coal/macerals is obtained by the correlation proposed by Channiwala et al.[303],

$$HHV_{coal}=349.1\ Zc+1178.3\ Z_H-103.4\ Z_O-15.1\ Z_N+100.5\ Z_S \tag{5.3}$$

The LHV of the coal is predicted using the following equation [304],

$$LHV_{coal} = HHV_{coal}-21.978\ Z_H \tag{5.4}$$

where Z_C, Z_H, Z_O, Z_N and Z_S are the mass concentration of the carbon, hydrogen, oxygen, nitrogen and sulfur in the feedstock, respectively, as shown in Table 5.1.

The specific oxygen consumption (SOC) is defined as the amount of oxygen consumed per volume of effective syngas production.

$$SOC= Nm^3\ O_2/(CO+H_2)\ kNm^3 \tag{5.5}$$

The specific coal consumption (SCC) represents the ratio of coal consumption or macerals consumption to the volume of effective syngas generated in the gasification.

$$\mathrm{SCC} = \mathrm{kg\ coal}/(\mathrm{CO}+\mathrm{H_2})\ \mathrm{kNm^3} \tag{5.6}$$

Synergetic coefficient (a_{ij}) accounts for the interactions among macerals is determined as following [298]:

$$a_{ij} = \frac{x_{ij}}{y_{ij}} \tag{5.7}$$

where *i* is the number of simulated coals, *i* =1 to 9; *j* stands for the gasification products and evaluation parameters, for example, *j* can be the mole fraction of CO, H_2 and the value CGE, etc. *x* is the numerical value of gasification products and the evaluation indicators calculated from Aspen plus. The physical meaning of *y* stands for theoretical values without considering interaction, which is obtained by the addition algorithm taking into account the mass weight fraction of each maceral in the simulated coal as tabulated in Table 5.2.

$$y_{ij} = \sum_{k=1}^{3} z_{ik} y_{kj} \tag{5.8}$$

$$\sum_{k=1}^{3} z_k = 1 \tag{5.9}$$

where *z* is the mass concentration of the *k*th independent macerals in the *i*th simulated coal.

5.4 Results and Discussion

Based on the basic data shown in Table 5.1 and Table 5.2, together with the simulation conditions indicated in Table 5.3, the gasification performance of each type of feedstock was calculated and compared under the same operating conditions. For comparison, the benchmark operating parameters were as follows: gasification temperature was at 1450 °C, the mass ratios of oxygen to coal and steam to coal were 0.8 and 0.08, respectively.

5.4.1 Simulation results

To validate the simulation, the comparison of the syngas composition from the gasifier between the simulation results and industrial data described in the reference [299] is shown in Table 5.4. As shown in Table 5.4, the simulation values are agreeable well with the industrial data [299], which demonstrates the reliability of this model.

Table 5. 4 Comparison of the simulation values and industrial data

Syngas Composition/vol%	Industrial Data	Simulation Value
H_2	30.0	29.9
CO	60.3	60.9
CO_2	1.6	1.3
H_2S	1.2	1.2
COS	0.1	0.1
N_2	3.6	3.6
Ar	1.1	1.1
H_2O	2.0	1.8
Others	0.1	0.1
Sum	100	100

The syngas composition and performance indicators for coal and its macerals are summarized in Table 5.5. It can be seen that H_2 and CO are the two main gases taking up most volume fractions up to 95 vol% of the gas product. The

($CO+H_2$) content varies in the order of vitrinite (94.98%) ≈ inertinite (94.67 vol%) > liptinite (93.87 vol%) > parent coal (89.52 vol%). As for the CO volume fraction, inertinite possesses the highest volume fraction of 67.36 vol%, followed by vitrinite of 63.20 vol% and liptinite of 56.71 vol%. However, for H_2, the order is changed to liptinite > vitrinite > inertinite. This was expected because based on ultimate analysis, liptinite and inertinite had the highest hydrogen and carbon content, which was higher than that of the parent coal. The indicators of SOC and SCC illustrate that the parent coal consumes the most amount of oxygen and fuel to produce the same amount of syngas, while the pure liptinite and vitrinite require the least amount of oxygen and fuel to produce the same amount of syngas. This was mainly because the feedstock of parent coal contained a considerable amount of ash (22.24 wt%) as compared with a small portion (less than 3.6 w%) of minerals in their respective maceral components. In addition, due to the less containment of hydrogen and carbon in the ultimate analysis of liptinite, the need for oxygen and coal to generate the same amount of effective syngas shows a corresponding reduction trend. With regard to CGE, the liptinite (84.27%) is superior to vitrinite (82.12%), parent coal (75.61%) and inertinite (71.48%). The reason for this order could be attributed to a higher syngas LHV value calculating from Eq.(5.2) of the liptinite than other components. Subsequently, the CGE of liptinite achieved a better performance based on Eq. (5.1). Although the LHV value of the syngas derived from the inertinite is greater than that of syngas derived from parent coal from Table 5.5, the LHV value of inertinite feedstock is greater than that of the parent coal resulting in a relatively smaller CGE of the inertinite.

Table 5. 5 Syngas composition (dry basis) and performance evaluation indicators for coal and its macerals

Composition	Coal /Vol%	Vitrinite /Vol%	Inertinite /Vol%	Liptinite /Vol%
CH_4	0.00563	0.196	0.145	0.026
H_2	26.81	31.78	27.31	37.16
CO	62.71	63.20	67.36	56.71
CO_2	4.73	0.22	0.25	1.7
H_2S	0.12	0.166	0.236	0.23
COS	0.012	0.014	0.025	0.015
N_2	5.27	4.15	4.37	3.88
Ar	0.33	0.26	0.29	0.25
Others	0.02	0.014	0.014	0.029
Sum	100	100	100	100
Performance evaluation				
Syngas flow rate, Nm^3/h	60507.9	77632.2	69908.3	79877.7
SOC	373.03	274.03	305.31	269.48
SCC	651.32	478.47	533.07	470.52
Syngas LHV, MJ/h	651799.91	887633.22	801249.79	889109.73
CGE,%	75.61	82.12	71.78	84.27
$(CO+H_2)$, vol%	89.52	94.98	94.67	93.87

Table 5.6 presents the summary of Aspen plus simulation and performance indicators of the simulated coal (as shown in Table 5.2). The input data of ultimate and proximate analysis to Aspen Plus for the simulated coals were

calculated using simple addition algorithm according to the mass percentage of macerals (as shown in Table 5.1). It can be seen from Table 5.6 that the mixed simulated coals have better thermodynamic performances concerning SOC, SCC, effective syngas and CGE than those from the parent coal and each maceral group.

Table 5. 6 Summary of simulation results and performance indicators for the simulated coals

	Simulated Coal No.								
Composition/vol%	1	2	3	4	5	6	7	8	9
CH_4	0.057	0.121	0.223	0.065	0.110	0.200	0.069	0.214	0.212
H_2	35.38	34.50	33.94	35.14	34.56	32.23	35.03	33.18	33.08
CO	59.38	60.64	61.28	59.71	60.55	62.83	59.86	61.95	62.05
CO_2	0.806	0.384	0.206	0.708	0.420	0.217	0.660	0.211	0.212
H_2S	0.209	0.212	0.214	0.204	0.207	0.2065	0.201	0.197	0.203
COS	0.0150	0.0165	0.0171	0.0153	0.0161	0.0170	0.0152	0.0163	0.0169
N_2	3.89	3.86	3.86	3.90	3.88	4.02	3.90	3.97	3.96
Ar	0.25	0.251	0.251	0.251	0.251	0.26	0.25	0.255	0.255
Others	0.013	0.0115	0.0069	0.0097	0.0079	0.0195	0.0148	0.0097	0.0141
Sum	100	100	100	100	100	100	100	100	100
Performance evaluation									
Syngas flow rate, Nm^3/h	81239	81276	80414	80566	80603	77577	80598	79302	79030
SOC	262.47	261.30	263.88	264.42	263.57	273.99	264.19	267.83	268.77
SCC	458.29	456.24	460.75	461.69	460.20	478.40	461.30	467.65	469.28
Syngas LHV, MJ/h	917018	924557	919349	910915	916181	887235	911988	906627	903572

CGE, %	87.56	88.69	87.85	87.52	87.74	89.57	87.49	85.69	85.47
(CO+H_2) vol%	94.76	95.14	95.22	94.85	95.11	95.06	94.89	95.13	95.126

5.4.2 Synergistic effects

Synergistic effect indicates that the products and performances arising from the simulated coals are higher or lower than the sum of their individual maceral. When the synergistic coefficient is not equal to 1, it indicates the interactions among macerals showing an influence on the gasification performance. Table 5.7 shows a summary of the matrix of the synergistic coefficients calculated by Eq. (5.7). It can be seen that interactions among macerals during gasification exist. The synergistic coefficients of H_2 and CO contents are higher than 1, while those of the other gases such as CO_2 and N_2 are less than 1. Looking at the performance indicators, the synergistic coefficients of SOC and SCC are in the range of 0.94 to 0.97 deviating from 1.0. However, the synergistic coefficient of both the effective syngas and CGE are slightly greater than 1.0 and most of the values are centralized distribution around 1.005, indicating that the synergistic effect is not apparent.

Table 5. 7 Summary of the matrix elements for the synergistic coefficients

Composition, vol%	Simulated Coal. No								
	1	2	3	4	5	6	7	8	9
CH_4	0.7324	1.5320	2.7934	0.7300	1.2634	1.6512	0.7310	1.7519	1.8751
H_2	1.0063	1.0051	1.0028	1.0059	1.0062	1.0031	1.0060	1.0026	1.0030
CO	1.0056	1.0108	1.0148	1.0060	1.0104	1.0074	1.0061	1.0088	1.0095
CO_2	0.6584	0.3312	0.1837	0.6237	0.3789	0.2954	0.6040	0.2660	0.2509

H_2S	0.9789	0.9623	0.9588	0.9797	0.9656	0.9784	0.9771	0.9736	0.9706
COS	0.9785	0.9816	0.9760	1.0172	0.9943	0.9449	1.0199	1.0041	0.9940
N2	0.9773	0.9594	0.9547	0.9768	0.9645	0.9731	0.9757	0.9715	0.9687
Ar	0.9804	0.9659	0.9583	0.9844	0.9715	0.9754	0.9805	0.9762	0.9701
Others	0.5381	0.4899	0.2993	0.4170	0.3441	1.0202	0.6481	0.4909	0.6959
Performance evaluation									
Syngas flow rate, Nm^3/h	1.0334	1.0511	1.0486	1.0242	1.0376	1.0264	1.0243	1.0294	1.0325
SOC	0.9621	0.9431	0.9437	0.9706	0.9553	0.9686	0.9704	0.9651	0.9616
SCC	0.9612	0.9431	0.9437	0.9706	0.9553	0.9686	0.9704	0.9651	0.9616
Syngas LHV, MJ/h	1.0387	1.0630	1.0648	1.0295	1.0477	1.0351	1.0297	1.0394	1.0434
CGE, %	1.0573	1.0941	1.0952	1.0552	1.0751	1.1342	1.0541	1.0591	1.0657
(CO+H_2), vol%	1.0058	1.0087	1.0105	1.0060	1.0089	1.0059	1.0061	1.0066	1.0072

The relationships between synergistic coefficient and maceral contents for various performance indicators were investigated by using a direct three-order polynomial correlation method based on the data shown in Table 5.7. Figure 5.2 correlates the relations of synergistic coefficient with maceral contents for SOC and SCC respectively. Figure 5.3 illustrates the influence of maceral content on synergistic coefficients of CGE and effective syngas respectively. From Figure 5.2, it is clear that vitrinite content correlates well with the synergistic coefficients of SOC and SCC respectively as their R-squares are 0.88 and 0.89, whereas inertinite content and liptinite content display poor correlation with synergistic coefficients of SOC and SCC. It is noted that with the increase in vitrinite, the synergistic coefficients of SOC and SCC exhibit an increase first then a decrease trend and the synergistic coefficients reach the maximum of 0.97 at a vitrinite content of 40%. In Figure 5.3, the change in intrinite content shows a promising correlation with synergistic coefficient of CGE. However, the synergistic coefficient of effective syngas exhibits significantly better correlations with vitrinite (R-square= 0.736) than initrinite (R-square= 0.508) and liptinite (R-square= 0.115). It can be observed from Figure 5.3 that CGE increases first and then reaches a plateau followed by an increase again at the inertinite content of 27%, while the synergistic coefficient of effective syngas decreases first to 1.006 and then slightly increases. Based on these correlations, we can quantitatively adjust or predict the synergistic coefficients when coal blends are used.

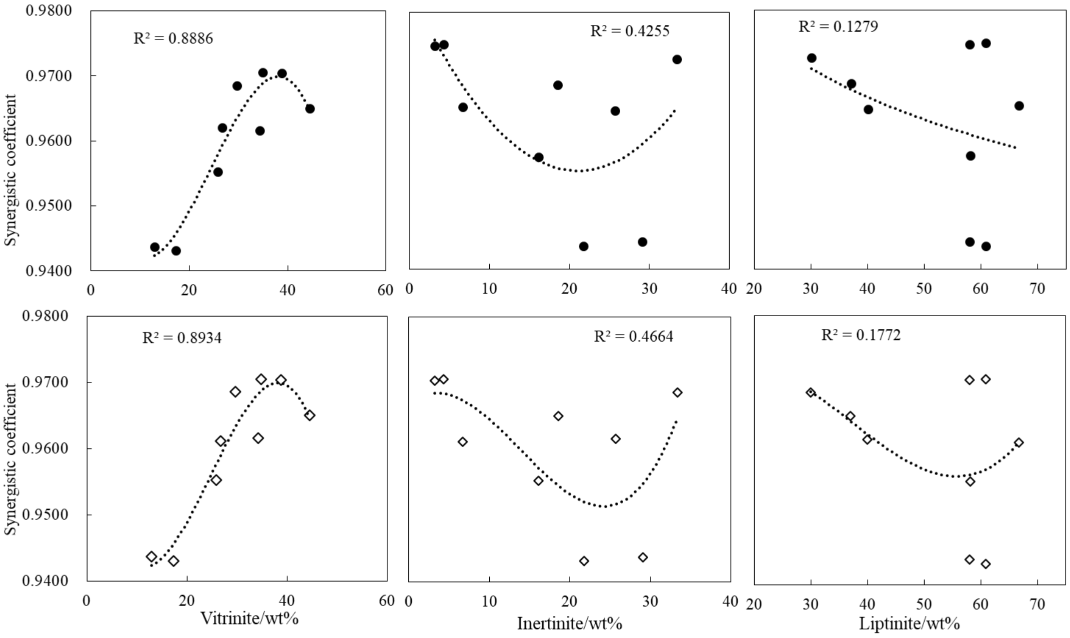

Figure 5. 2 Relationship between the synergistic coefficient and the maceral contents for the gasification performance indicators of SOC ("●") and SCC("◇")

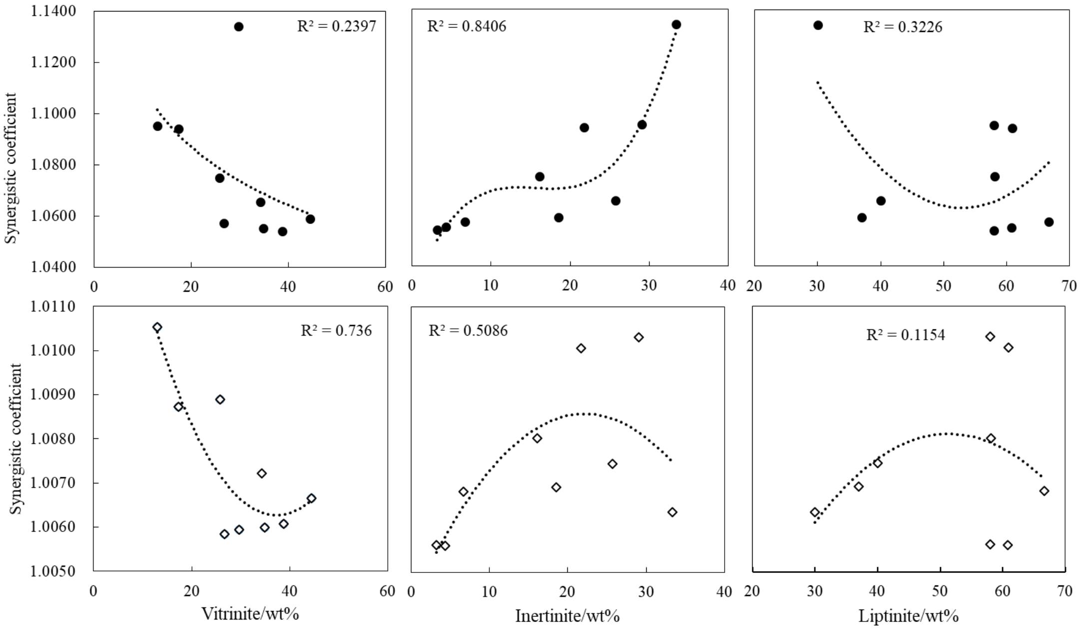

Figure 5. 3 Relationship between the synergy effect and the maceral contents for the gasification indicators of CGE (“●”) and effective syngas (“◇”)

5.4.3 Effect of gasification temperature

In order to track the different gasification behaviours of parent coal and macerals under different gasification temperatures, the plot of gasification performance indicators versus temperature varied from 1350 to 1550 °C is displayed in Figure 5.4. The gasification temperature has a slightly negative influence on SOC and SCC of the coal and its macerals. However, from Figure 5.4(b), with the increase in gasification temperature, the indicators of both CGE and (CO+H$_2$) % show a small addition. In addition, it can be observed that the liptinite has the highest CGE behaviour followed by vitrinite and inertinite in that order. As for the effective syngas, vitrinite has the highest effective syngas content up to 95. vol% at 1550°C. The reasons behind these phenomena were mainly attributed to the endothermic reactions, such as Boudouard reaction and carbon water gas reaction, being promoted and the exothermic reaction water gas reaction being restrained at high temperature, which resulted in the increase in ($CO+H_2$) %. The relative larger amount of effective syngas led to the increase in syngas LHV and according to Eq.(5.1), the CGE also shows an uptrend. In accordance with Eqs.(5.5) and (5.6), the indicators SOC and SCC decrease as the effective syngas content increased.

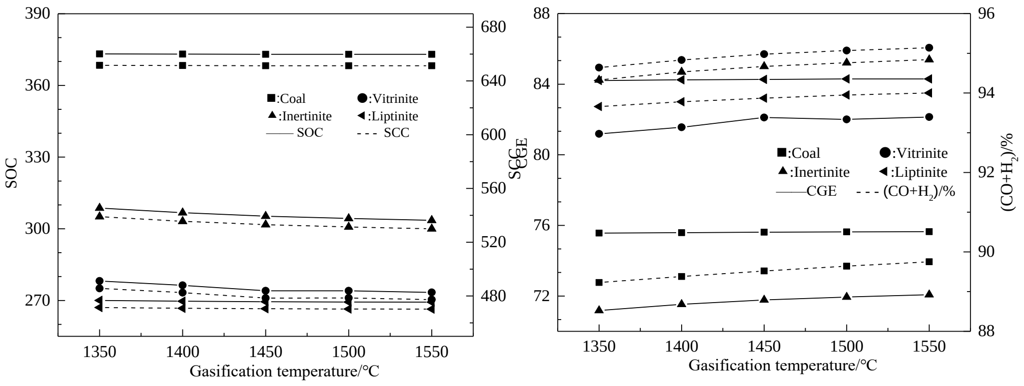

(a) (b)

Figure 5. 4 Effect of gasification temperature on the gasification performance parameters: (a) SOC and SCC, (b) CGE and ($CO+H_2$)%

The effect of temperature on the synergistic coefficients of SOC, SCC, effective syngas and CGE with the variation of maceral contents is shown in Figure 5.5. In order to have a better quantitative comparison of the synergistic coefficients at different temperatures, three fitting curves (denoted as “FC”) are presented at the temperatures of 1350, 1450 and 1550 °C as shown in Figure 5.5. It can be observed in Figure 5.5 (a) and (b) that the synergistic coefficients of SOC and SCC exhibit similar properties. When gasification temperature is below 1450 °C, the impact of temperature is not obvious, whereas when gasification temperature is higher than 1450 °C, the synergistic coefficient detrimental value is about 0.005. This suggests that higher gasification temperature is favourable to the maceral interactions and leads to the decrease in oxygen and coal consumptions. It can be seen from Figure 5.5(c) that the gasification temperature does not significantly affect the synergistic coefficient of CGE. Figure 5.5(d) depicts a slightly fluctuating phenomenon regarding the synergistic coefficient curves at 1350, 1450 and 1550 ℃. Nevertheless, the fluctuation range is limited to 0.05% demonstrating that temperature has little impact on the effective syngas content.

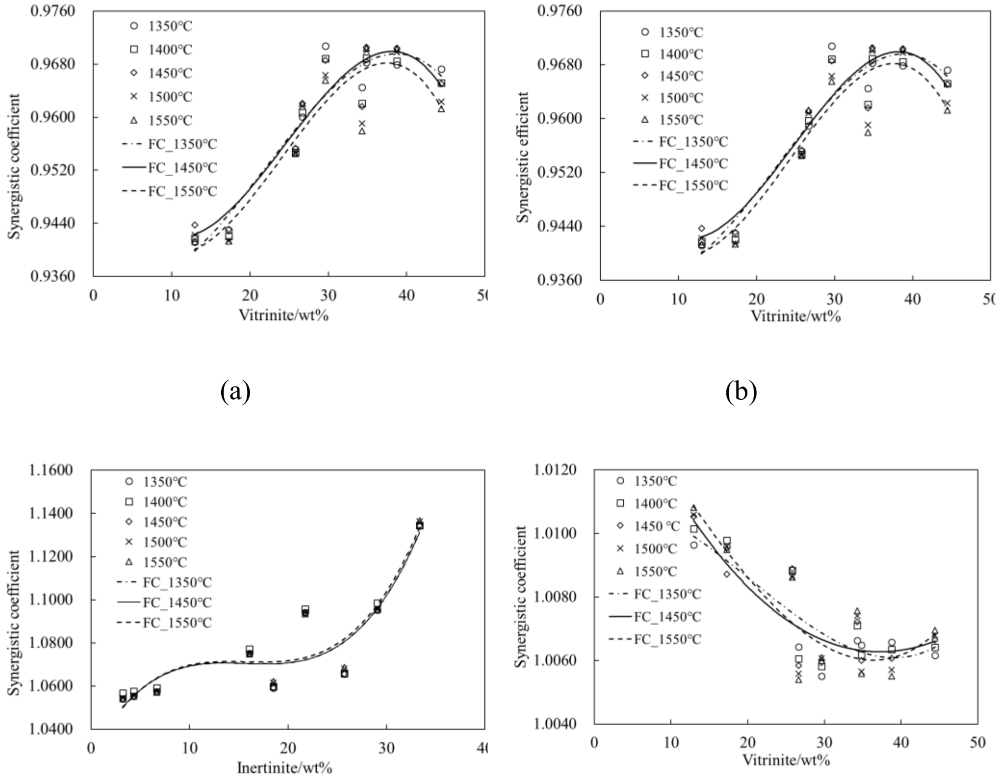

(a) (b)

(c) (d)

Figure 5. 5 Effect of vitrinite content on the synergy coefficients of (a) SOC, (b) SCC, (d) (CO+H_2)% and effect of inertinite on synergy coefficient of CGE (c) and at different gasification temperatures

5.4.4 Effect of oxygen to coal (OTC) mass ratio

The effects of oxygen to coal mass ratio on SCC, SOC, CGE and effective syngas content of parent coal and its macerals are shown in Figure 5.6. At low OTC, all the SOC values increase slightly and then increases sharply to a value of 700 when the OTC is greater than 0.65, while the SOC values of macerals still show a relatively tiny addition increment and their maximum SOC values are from 415 to 480 at the OTC=1.1. The SCC values of macerals show a decline at first and then increase for different macerals, but their variation patterns are not synchronous. The minimal SCC value of coal and its macerals are found to be 586.53 kg/kNm^3, 478.47 kg/kNm^3 (vitrinite), 468.63 kg/kNm^3(liptinite) and 481.21 kg/kNm^3 (inertinite) at the OTC of 0.65, 0.8, 0.65 and 0.95 respectively. Figure 5.6 (b) presents the results of oxygen addition in the gasifier on CGE and effective syngas content. The CGE values of parent coal, vitrinite, inertinite and liptinite vary from 55% to 84% and reach their corresponding peaks at the OTC=0.65, 0.8, 0.95 and 0.65. Besides, the mole fractions of ($CO+H_2$) go up slightly, which is illustrated by a sharp decrease at OTC of 0.65, 0.8, 0.95 and 0.65 for coal, vitrinite, inertinite and liptinite, respectively. The ($CO+H_2$) % is changed from 95 vol% to 74 vol%. Before the turning points of all the indicators for each feedstock, the flow rates of oxygen that was fed into the gasifier could not fully covert carbon into syngas, thus the increase of oxygen enhanced the increase of effective syngas, CGE and SOC. After the turning points, the oxygen flow rate exceeded the stoichiometric requirements of gasification, thus the addition of oxygen led to the combustion of syngas and resulted in the drop of the effective syngas and CGE. Besides, the reason for different turning point values of coal and its macerals was mainly attributed to the discrepancies of the elementary composition of macerals and coal.

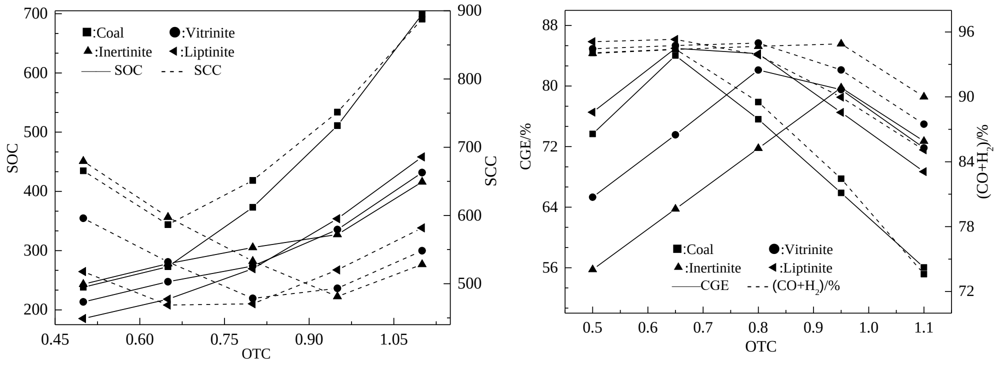

(a)

(b)

Figure 5. 6 Effect of oxygen to coal mass fraction on the gasification performance parameters: (a) SOC and SCC, (b) CGE and $(CO+H_2)$% for coal and its maceral components of vitrinite, inertinite and liptinite

Figure 5.7 reveals the effect of maceral contents on the synergistic coefficients of SOC, SCC, CGE and effective syngas at various OTC varying from 0.5 to 1.1. Besides, the correlation lines at the OTC of 0.5, 0.8 and 1.1 are also shown in those figures for better comparisons. From Figure 5.7 (a) and (b), the synergistic coefficients of SCC and SOC exist a minimum value which is found to be varied from 0.94 to 0.97 when OTC equals to 0.8. However, when OTC changes from 0.5 to 1.1, the synergistic coefficients of SCC and SOC increase initially and decrease afterwards. From Figure 5.7(c), it can be clearly seen that the synergistic coefficient of CGE maintains the highest at OTC=0.8 than that at any other OTC values in the whole range of Inertinite variation. Figure 5.7(d) shows that the synergistic coefficient is enhanced at the OTC of 0.8. However, the coefficient is lower than 1 at OTC>0.8, which indicates that interactions among macerals exist a slightly mutual inhibition effect. It can be concluded from Figure 5.7 that OTC is greater than 0.8, the interactions among macerals are no longer in existence or even existing inhibition effect and at the OTC=0.8, the synergistic coefficients of SOC, SCC, CGE and effective syngas achieve maximum efficiencies.

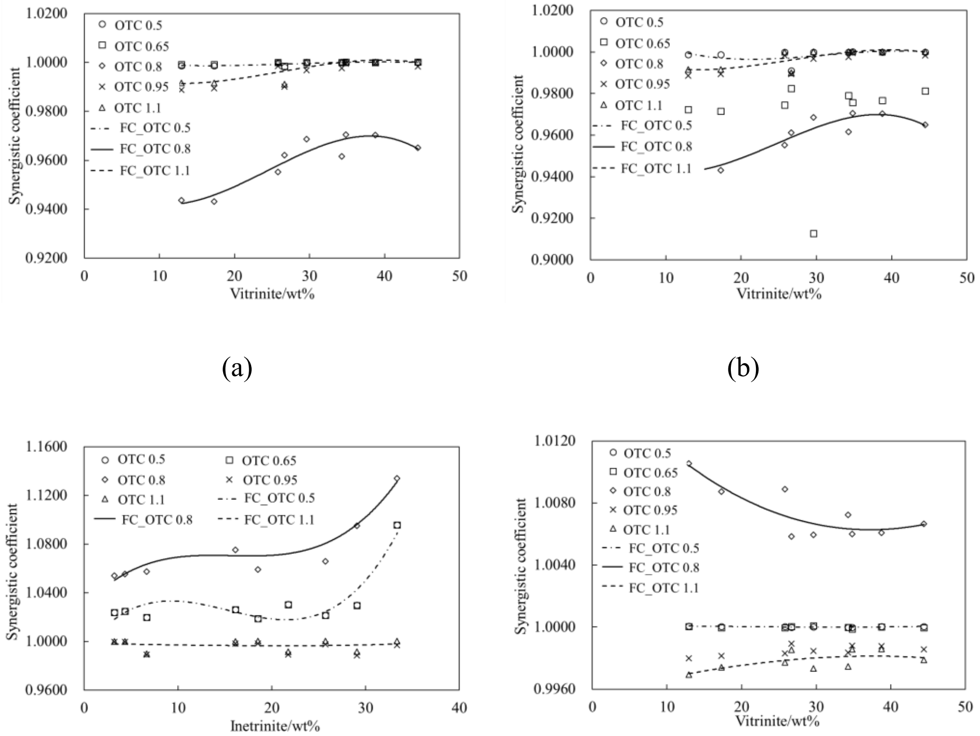

(a)

(b)

(c)

(d)

Figure 5. 7 Effect of vitrinite content on the synergistic coefficients of (a) SOC, (b) SCC , (d) (CO+H_2)% and effect of inertinite on the synergistic coefficient of CGE (c) and at different OTC

5.4.5 Effect of steam to coal (STC) mass fraction.

Figure 5.8 shows how the variation in performance indicators, such as SOC, SCC, CGE and effective syngas content of parent coal and its macerals with the increase of STC in the range of 0.01 to 0.16. As can be observed from Figure 5.8(a), both the SOC and SCC of coal and liptinite are not sensitive to the addition of steam, while both the SOC and SCC regarding vitrinite and inertinite decrease. Figure 5.8(b) describes that the CGE values of both coal and liptinite remain level, whereas the CGE values of both vitrinite and inertinite go up steadily. The $(CO+H_2)$ contents of both coal and liptinite shows a gradual decline while both vitrinite and inertinite show a moderate increase. The injection of steam in the gasifier favoured the reactions, such as $C+H_2O=CO+H_2$ and $CO + H_2O = CO_2 + H_2$, which enhanced the formation of CO and H_2. Therefore, the effective syngas content and CGE of vitrinite and inertinite increased. However, the behaviours of Coal and liptinite do not comply with this explanation, this was mainly because of the composition differences between parent coal and its macerals. Specifically, the carbon content of both coal and liptinite was lower than that of vitrinite and inertintie, by the addition of steam had little positive impact on the carbon water reaction for carbon had already been reacted completely with oxygen and with the moisture water in coal. Although the effective syngas of coal and liptinite showed a declining trend, the total flow rates of syngas for those feedstocks exhibited a slightly increasing trend, which resulted in the constant properties of SOC, SCC and CGE.

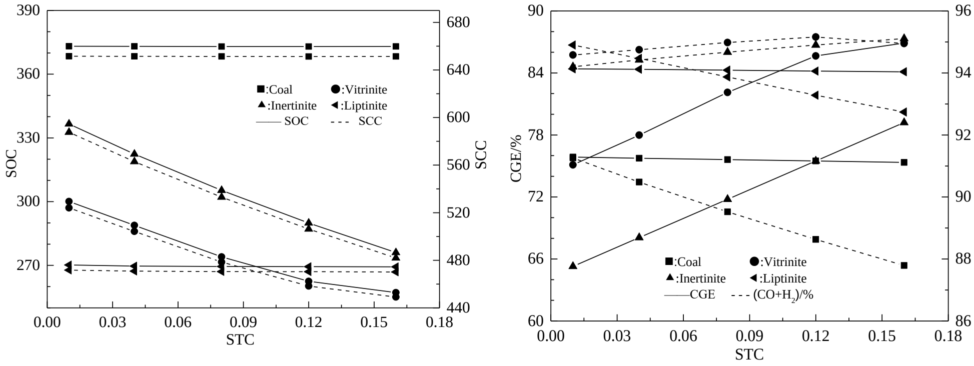

(a)

(b)

Figure 5. 8 Effect of steam to coal mass fraction on the gasification performance parameters: (a) SOC and SCC, (b) CGE and $(CO+H_2)$% for coal and its maceral components of vitrinite, inertinite and liptinite

The variations of synergistic coefficients of SOC, SCC, CGE and effective syngas at different STC values in the range of 0.01 to 0.16 are plotted in Figure 5.9. The fitting curves at the STC of 0.01, 0.08 and 0.16 are presented in this figure. It can be observed from Figure 5.9 that the synergistic coefficients achieve their extremums at STC=0.8, which indicates that the promoted interactions among macerals realize the maximum function.

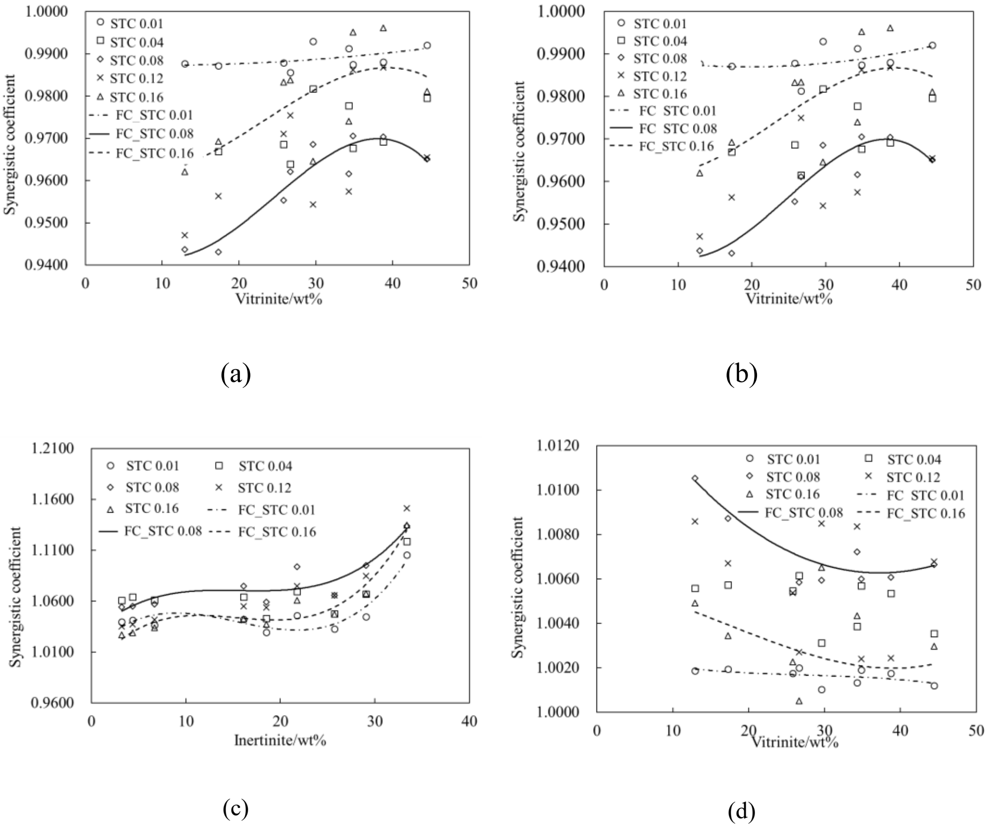

(a)

(b)

(c)

(d)

Figure 5. 9 Effect of vitrinite content on the synergy coefficients of : (a) SCC, (b) SOC , (d) (CO+H_2)% and effect of inertinite on synergy coefficient of CGE (c) and at different STC

Due to the complex physical and chemical properties of coal, it is hard to prove the existence of synergistic effect between macerals gasification directly. The present work is to compare the performance indicators from simulated coals and the calculated values based on the weight of the macerals assuming additive properties apply. According to the previous studies [239, 281, 283, 305, 306], the reasons for synergistic effect among macerals might be concluded as below. Liptinite holds the highest H/C followed by vitrinite and inertinite, when macerals are blended in gasifier, a large amount of hydrogen donors (H and OH radicals) produced from liptinite involve in the decomposition of the remained macerals and suppress re-polymerization and crosslinking reactions of free radicals during gasification [239, 306]. On the other hand, based on the works of [281, 283, 305], because liptinite and vitrinite occupy more hydrocarbon aliphatic and lower aliphatic, they are prone to produce more metaplast, which acts as the hydrogen donor solvent and stabilize more rupture fragments and free radicals produced by the inertinite, resulting in enhancement of gasification performances.

5.5 Conclusions

This study revealed the gasification performance of a coal and its corresponding macerals and the interactions among macerals based on Aspen Plus process modelling. For the first time, the synergistic coefficient was quantified to show the extent of the interactions among macerals during gasification. Sensitivity analyses were conducted to demonstrate the effects of gasification temperature, oxygen to coal mass ratio and steam to coal mass ratio on the gasification performance of coal and individual macerals and also on the synergistic coefficients. The main conclusions are:

(1) The synergistic coefficients of SOC and SCC of the simulated coals were in the range of 0.94 to 0.97 whereas the synergistic coefficient of

CGE was from 1.05 to 1.13 and that of the (CO+H2) % varied from 1.005 to 1.01.

(2) The synergistic coefficients of SOC, SCC and ($CO+H_2$) % had a very strong correlation with vitrinite contents while the CGE showed a good correlation with inertinite.

(3) The synergistic coefficient increases slightly with the increase in gasification temperature. The optimal synergistic coefficient was found out to be at OTC=0.8 and STC = 0.8.

Chapter 6 Distributions and modes of occurrence of heavy metals in opposed multi-burners (OMB) coal-water-slurry (CWS) gasification plants

6.1 Introduction

During coal gasification, the organic part is gasified into syngas, while the inorganic part is transferred into liquid slags at high temperature, and then is solidified into coarse and fine slags. The compositions of coal gasification slags depend on coal types and gasification conditions and generally, slags contain complex mineral species such as silicates, carbonates, sulfides, and amorphous inorganic components as well as unconverted char. In order to evaluate the contamination of gasification slags over environment and utilization, it is imperative to thoroughly investigate the characteristics, heavy metals concentrations and speciation features of coarse and fine slags.

Previous studies of characteristics of gasification slags have focused on the morphology, mineralogical and structural behaviours, and combustion and gasification reactivities [15, 141-145]. Studies on the leachability, enrichment and speciation performances of gasification slags are limited [153-155]. Wang et al. [154] reported the concentration and enrichment characteristics of 21 hazardous trace elements based on the gasification residues collected from three different entrained – flow gasification plants using opposed multi-burners

(OMB) and GE technologies, respectively. Tang et al. [155] then determined the modes of occurrence of 17 trace elements by five-step sequential extraction to detect the contents of water-soluble, carbonates, iron and manganese oxidation, sulphides, organic, and alumonosilicate fractions in coarse and fine slags sampled from GE and GSP gasifiers in Ningxia, China. As a most advanced gasification technology, the OMB gasifier has been applied over 50 companies in domestic and abroad [17]. Nevertheless, detailed investigations on the modes of occurrence, mobility and leaching characteristics of heavy metals in gasification solid residues from OMB's entrained-flow gasifiers are still blank.

In this chapter, the characteristics of the feeding coals, coarse and fine slags collected from two OMB gasifiers were investigated firstly with XRF, XRD and SEM. The concentrations and enrichment behaviours of heavy metals including Ba, Co, Cr, Cu, Mn, Ni, Pb, V, and Zn were subsequently determined using an ICP-OES. Besides, the modes of occurrence of the heavy metals in the samples were fully quantified. Finally, the mobility and leaching ability of heavy metals in the coarse and fine slags were evaluated.

6.2 Characterization of materials

The proximate and ultimate analyses are presented in Table 6.1. It can be seen from the table that both feeding coals are bituminous coal and have similar compositions (GB/T 5751-2009). Besides, the fixed carbon contents in the fine slags (5.22 wt% in FS-1 and 12.06 wt% in FS-2) are higher than that in the coarse slags (0.82 wt% in CS-1 and 7.72 wt% in CS-2). This could be attributed to that char particles wrapped by molten ash experienced much longer residual time, leading to lower carbon content in the coarse slags, whilst the char particle taken out by the syngas had relatively shorter reacting time and consequently, fine slags contained low carbon content. On the other hand, it is obvious that the carbon contents in the gasification slags from Plant-2 are much higher than that corresponding slags from Plant-1. Besides, the loss on ignition (LOI, defined as the ratio of mass difference between the unburned and burned samples to the initial mass weight of unburned samples [197]) test shows that the CS-1 has lowest value of 0.06% in comparison with LOI of 10.03% in CS-2. In addition, the LOI of FS-1 is 11.23%, which is lower than the FS-2 of 17.71%. The reason for the larger LOI and carbon content in the slags of Plant-2 is that, the coal water slurry concentration of Plant-1 was higher than that of Plant-2 and at the same oxygen to coal ratio, the gasification rates in the first gasifier was faster than that of the second gasifier due to the increase of gasification temperature as the reduction of water entering the first gasifier. As a result, the Coal-1 converted more thoroughly and less combustible substance was contained in the both fine and coarse slags. Additionally, a slightly higher fixed carbon and less volatile in Coal-2 also contributed to a larger LOI in the gasification slags of Plant-2.

Table 6. 1 Proximate and ultimate analyses of samples

	Coal-1	CS-1	FS-1	Coal-2	CS-2	FS-2
Proximate analysis wt.% (ad)						
Moisture	7.12	1.32	3.3	8.68	2.94	3.56
Volatiles	26.24	0.01	0.01	22.34	0.85	1.17
Fixed carbon	54.17	0.82	5.22	57.22	7.72	12.06

Ash	12.17	97.85	91.49	11.76	88.51	83.21
Ultimate analysis wt.% (d)						
C	68.76	1.15	6.88	70.32	9.74	14.28
H	4.238	0.402	0.89	3.95	0.55	1.23
N	1.01	0	0.4	0.99	0.26	0.43
S	0.41	0.246	0.271	0.322	0.28	0.76
O (by difference)	13.412	0.352	0.069	12.658	0.66	0.09
LOI/%	88.81	0.06	11.23	89.65	10.03	17.71

Table 6.2 shows ash compostition of the feeding coals and gasification slags. Besides, the loss on ignition is also listed. As indicated, all samples are mainly composed of SiO_2, Al_2O_3 and CaO. For the feeding coals, the SO_3 content are about 11.1 and 8.28 wt% for the Plant-1 and Plant-2, respectively. However, the SO_3 contents in the gasification slags were less than 3 wt%. In addtion, the Na_2O and Fe_2O_3 content in slags is higher than that in the corresponding feeding coals.

Table 6. 2 Ash chemical composition (wt%)

Sample	SiO_2	Al_2O_3	CaO	Na_2O	MgO	K_2O	Fe_2O_3	SO_3	TiO_2
Coal-1	36.412	19.84	16.93	4.84	3.36	0.55	5.9	11.1	0.46
Coal-2	39.47	25.23	10.29	9.05	2.14	0.41	4.22	8.28	0.44
FS-1	41.10	21.79	14.73	8.46	2.89	0.89	7.44	1.29	0.58
FS-2	39.57	23.37	11.71	9.59	2.34	0.75	8.62	2.6	0.62
CS-1	38.13	18.62	21.88	6.89	3.04	0.69	8.88	0.37	0.5

CS-2	39.11	20.34	15.41	10.35	2.38	0.75	9.62	0.79	0.50

In order to gain the differences among the samples, the morphological characteristics are shown in the SEM images as displayed in Figure 6.3. As can be seen from this figure, the morphologies of the feeding coals, CS and FS are similar for samples of Plant-1 and Plant-2. Coal particles are of angular and irregular shapes. Coarse slags are in a bulk state and appear to be vitreous and angular, which are similar with the feeding coal particles with more smoothness on the surface. Besides, a relative large spheric shape and porous structures exist as shown in Figure 6.3 (b). The fine slags, as shown in Figure 6.3 (c) and (f), are fragmentized and significantly more porous than the CSs. In addition, there are small spheres that are closed and/or covered with fine floccules. The coarse slags were produced from molten and liquid slag through cooling and breaking and finally collected from lock hopper [307]. However, the fine slags mainly came from the syngas washing tower. Hence, the coarse slags are found to be in a bulk and broad state and fine slags are appeared to be small spheres. Compared with the CS-1, CS-2 shows more floccules, which contains more carbon than that of CS-1 [141]. As a result, the floccule distributions are more widely and continuously in CS-2.

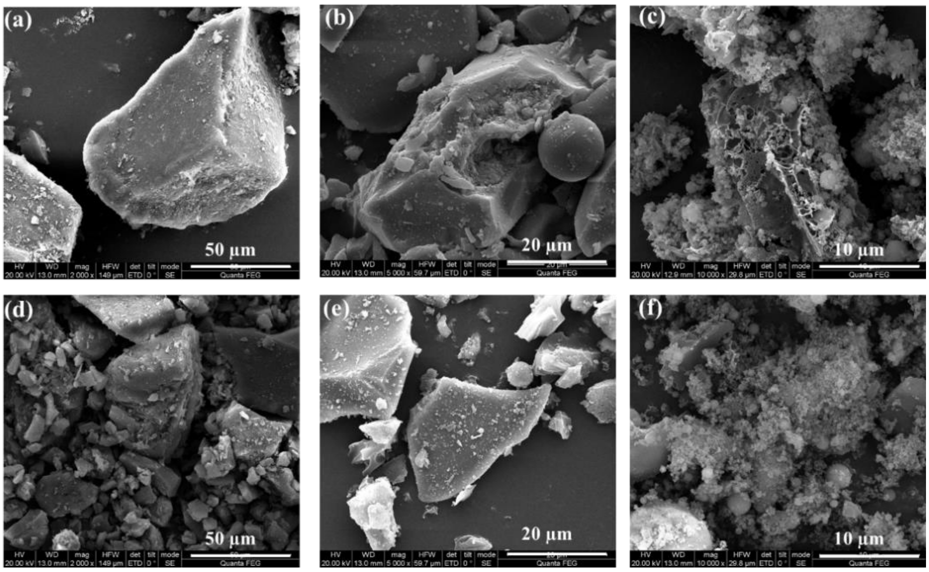

Figure 6. 1 SEM images of the samples: (a) Coal-1; (b) CS-1; (c) FS-1; (d) Coal-2; (e) CS-2; (f) FS-2

The mineralogical characteristics of the samples were determined by XRD and the results are shown in Figure 6.4. The minerals in feeding coals are mainly composed of quartz, kaolinite and calcite, while the CS and FS consist of a large amount of glass and amorphous phase and the crystal phase is mainly quartz. In addition, little barium lead and barium dithiodiargentate in Plant 1 as well as calcite and chalcopyrite in Plant-2 is also observed in the XRD patterns. The presence of quartz in the gasification slags are mainly derived from two sources, i.e., quartz from the original feeding coal and those derived from the recrystallization during slags cooling process [308].

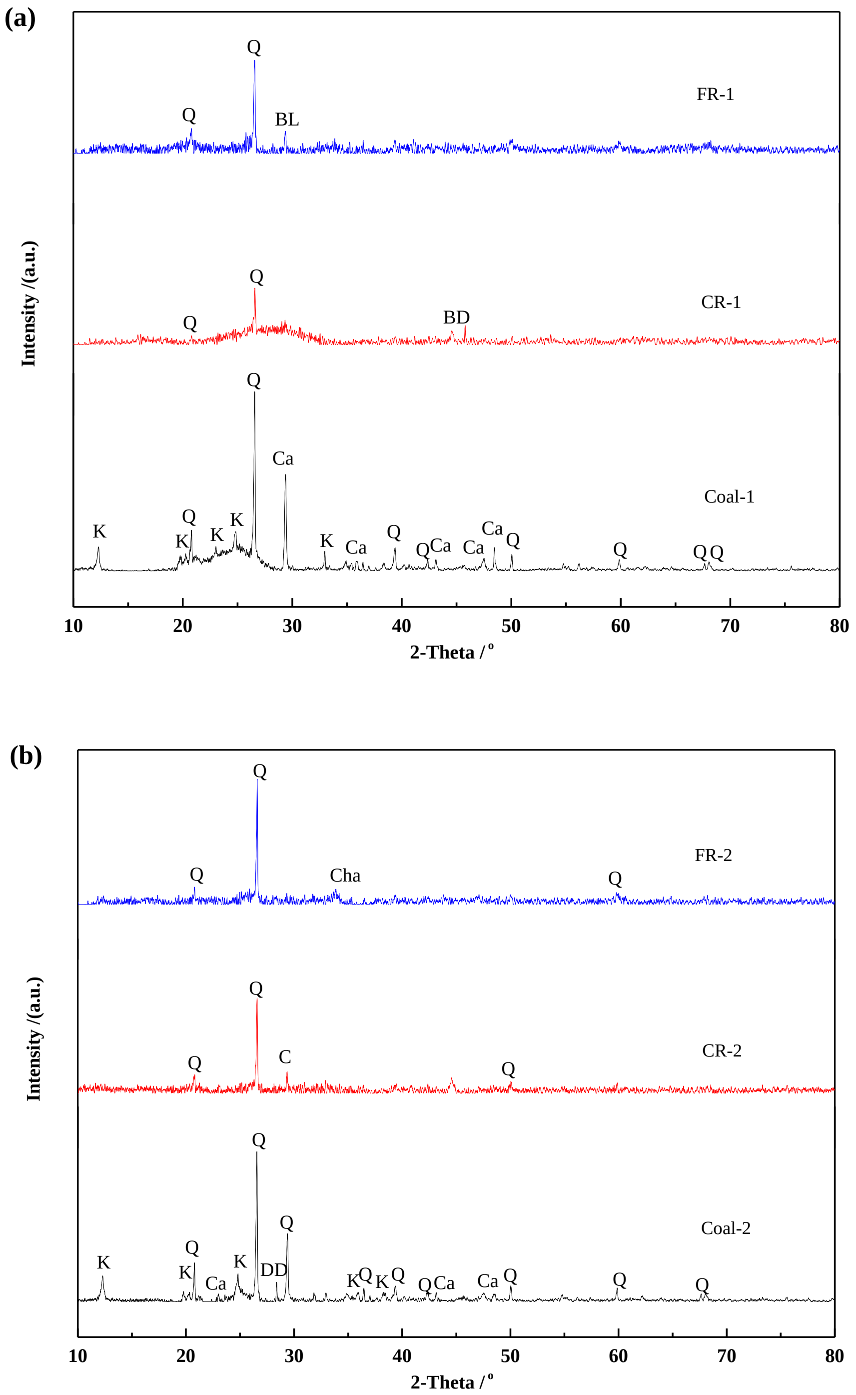

Figure 6. 2 XRD patterns of the feeding coals and gasification slags. (a) Samples from Plant-1; and (b) samples from Plant-2. K-kaolinite; Q-quartz; Ca-calcite; BD-barium dithiodiargentate; BL-barium lead; Cha-chalcopyrite; DD-distrontium dioxocuprate bromide

The concentrations of 9 selected heavy metals in coal and gasification slags are presented in Table 6.3. Generally, heavy metals content is similar for both coals, the average of which is in the order of Ba (215.5 mg/kg) > Mn (149.0 mg/kg) > Zn (52.0 mg/kg) > Cr (23.3 mg/kg) > Ni (21.2 mg/kg) > Cu (17.3 mg/kg) > V (9.3 mg/kg) > Co (5.2 mg/kg) > Pb (3.4 mg/kg). The content of Ba, Mn, Zn, Cu and Ni is higher in coal-1 than in coal-2, as shown in Figure 6.5. To further reveal the concentration levels of feeding coals, the parameter of concentration coefficient (CC) [309] is employed, which is defined as the ratio of heavy metal concentration in the selected coal to the average heavy metal concentration in a series of Chinese coals [310]. In general, a heavy metal can be classified into enriched, normal and depleted categories if CC > 2, 0.5 < CC < 2 and CC < 0.5, respectively. As shown in Figure 6.5, except for V and Pb, which are in the depleted zone, CC of the other heavy metals are all in the normal zone in comparison with normal Chinese coals.

As presented in Table 6.3, the concentrations of heavy metals in CS and FS after gasification are significantly higher than that in the feeding coals except for the Pb in the coarse slag (0.01 mg/kg). Both of Ba and Mn are the most abundant in fine and coarse slags. The contents of heavy metals of Cr, Cu, Ba and Mn in CS-1 are relatively higher than that in CS-2. For the gasification slags derived from a same plant, most of heavy metals are relatively enriched in fine slags, for example, Cu, Ba, Ni, Pb, V, Co and Zn in FS-2 are accumulated more. This could be attributed to that fine particles had a greater surface area and hence most of heavy metals were enriched in higher concentrations [154].

Table 6. 3 Heavy mental concentrations of the coal and slags / (mg/kg)

Elements	Cr	Cu	Ba	Mn	Ni	Pb	V	Co	Zn
Coal-1	24.05	27.85	314	158	25.85	5.15	9.55	5.08	71
CS-1	1286	71	1238.5	2030	87	0.01	114	79.5	30.6
FS-1	156	121.5	1149.5	1704.5	127	294	152	133	900
Coal-2	22.5	6.7	117	140	16.55	1.74	9.05	5.35	33.05
CS-2	409.5	66	977	1471	116	0.01	116	95.5	40.6
FS-2	138.5	114	1287.5	1323.5	139	297	155	186.5	269.5
Chinese coal*	15.4	17.5	159	117.5	13.7	15.1	35.1	7.08	41.4

* The normal heavy metal content of Chinese coals [310].

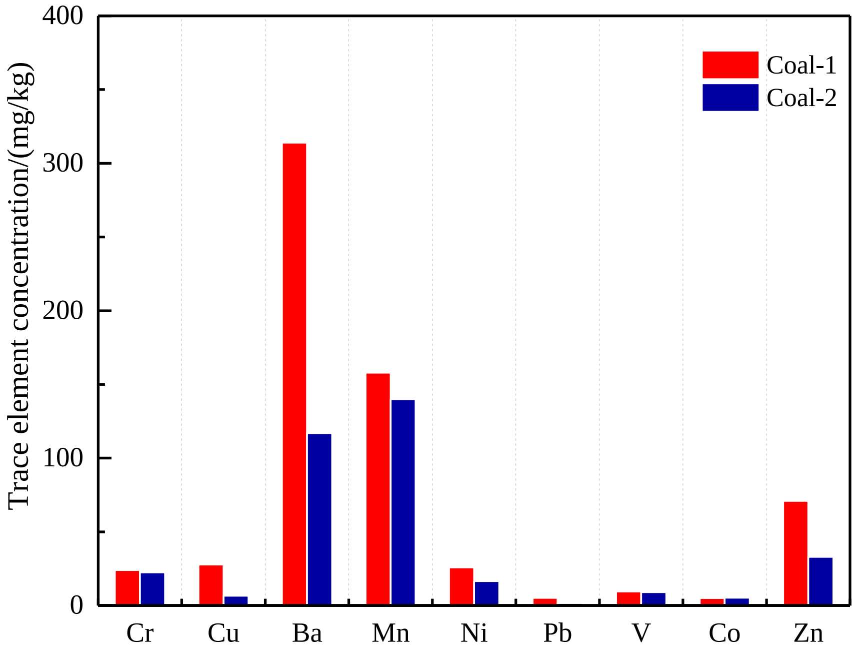

Figure 6. 3 Concentration of the trace elements in the feeding coals

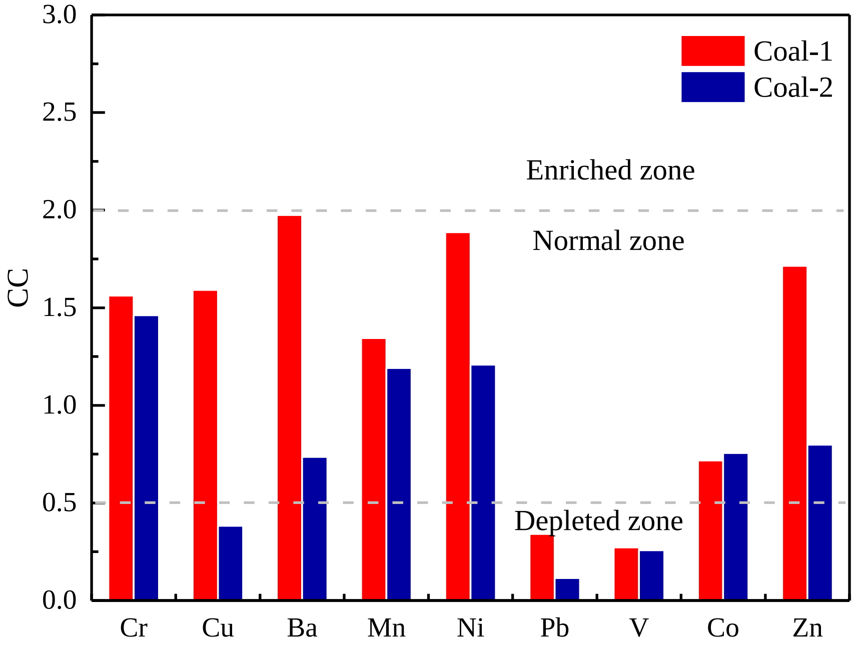

Figure 6. 4 Concentration coefficient of trace elements in feeding coals

6.3 Enrichment characteristics of heavy metals

To evaluate the enrichment behaviours, a relative enrichment (RE) index was employed, which is expressed as Eq.(6.1) [155].

$$\mathrm{RE} = \frac{C_{slag}}{C_{coal}} \times \frac{A_{coal,ad}}{A_{slag,ad}} \tag{6.1}$$

where C_{slag} and C_{coal} are concentration of heavy metals in gasification slags and coal samples, respectively, mg/kg. $A_{coal,ad}$ and $A_{slag,ad}$ represent the ash contents in the feeding coal and gasification slags on air-dried basis, wt%.

Figure 6.7 shows the RE of heavy metals for the gasification slags for different plants. As can be observed from this figure that each figure was divided into four units by the crossing lines of RE=1. For Plant -1, the elements of Mn, V and Co are located in the upper-right portion of Figure 6.7 (a), indicating that these metals are stable and enriched in the slags with RE>1. Ba, Ni and Cu are neither rich in CS nor FS since they are in the lower-left section with RE<1.

Besides, Zn and Pb are largely captured by fine particles after gasification, while the element of Cr is partitioned preferably to the coarse slag. However, Ba, Cu and Ni are shifted to the stable area in Plant -2 owing to that both of RE for FS and CS are greater than 1, indicating those elements are captured by the gasification slags. The enrichment behaviours of other heavy metals, such as Cr, Zn, Pb, Mn, V and Co in Plant -2, are the same as the corresponding elements in Plant-1. Generally, migration behaviour of heavy metals during gasification has a strong correlation with the modes of occurrence of the elements, properties of raw materials and operating conditions [154, 311], the latter two factors are similar for the two plants. Hence, to understand the migration behaviour of heavy metals, it is necessary to investigate the occurrence of the elements, which is discussed in Section 6.4.

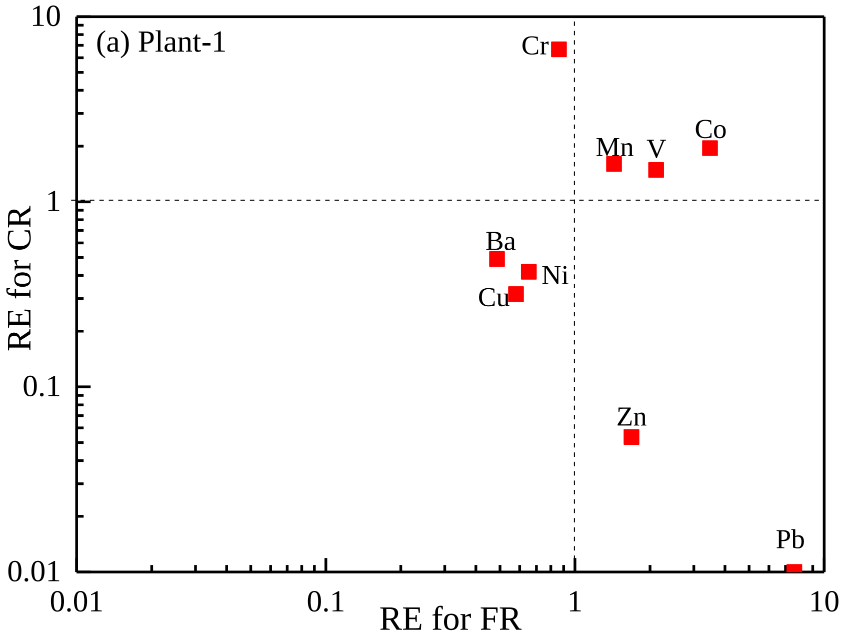

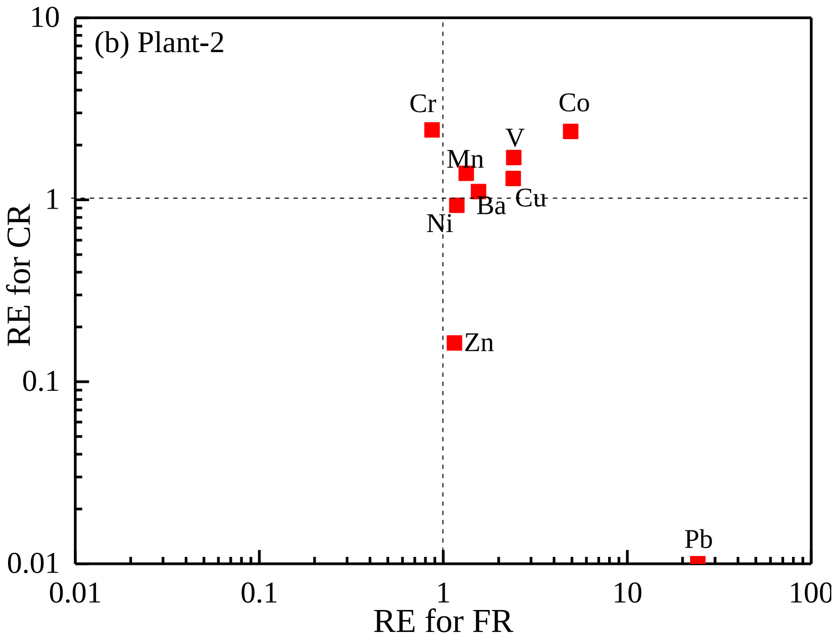

Figure 6. 5 Enrichment characteristics of heavy metals in gasification slags. (a) Plant -1 and (b) Plant – 2

6.4 Chemical speciation analysis of heavy metals

The sequential results of heavy metals in the feeding coals are shown in Table 6.4. The recovery of all the heavy metals varies from 71.0 to 125.9%, which fall in a reasonable range. Figure 6.8 shows the extraction percentage for the heavy metals. As can be noticed from this figure, the sequential extraction fractions of heavy metals in Coal-1 are similar to Coal-2 except for Barium. Most of Ba exists in the reducible fraction (55.6 wt%) and the residual fraction (31.9 wt%) in Coal-1, while the acid soluble and exchangeable fraction of Ba (49.0 wt%) is dominant, followed by the residual fraction of 24.9% in Coal-2. Normally, Ba occurred in multiple forms in coals, such as barite, barytocalcite, alsonite, Ba-felspars and in organic association in low rank coals [312], and the extraction ratio could be reached in the range of 30 to 90% using a sequential leaching solutions of CH_3COONH_4, HCl, HF, and HNO_3. Therefore, the extraction fractions of Ba in this work are consistent with reported data [312]. For cobalt, the share of oxidizable fraction is noticeably high in both coal samples, 73.4 and 82.7% for Coal-1 and Coal-2, respectively. This indicates that Co is bonded to organic matter and sulphides. The results of this study agree well with the findings that cobalt was mainly associated with sulfides and could also be found in organic matter [313].

About 78.7 and 20.5 wt% of Chromium exist in residual and oxidizable forms for Coal-1, respectively. In the case of Coal-2, the residual and oxidizable fractions of Chromium are 82.6 and 17.2 wt%, respectively. No acid soluble fraction is obtained and the reducible fractions are less than 1wt% in both coal samples. It was reported that Cr presented as trivalent in the coal and Cr was mainly associated with oxide, carbonate and monosulfide group in [313, 314]. As for copper, it is almost evenly distributed in the oxidizable and residual fractions, which occupy about 96.2-100 wt% of the total extraction fractions. Copper was normally in the oxide, carbonate, monosulfide group, pyrite and silicates as indicated in [315]. The results released by Riley et al. [314] also reflected that copper in Tar was principally embedded in oxide, monosulfide and silicate. Compared with other heavy metals, manganese has a large proportional of acid soluble fraction about 66.3 and 53.7 wt% in Coal-1 and Coal-2, respectively. About 12.5 wt% of the Mn is associated with the reducible fraction, with 14.4% in oxidizable form and 6.8% in residual in the Coal-1. Similarly, the reducible, oxidizable and residual fractions are 23.4, 17.0 and 5.9 wt% in Coal-2, respectively. Mn was primarily found in carbonates, hence it was leached out using CH_3COOH [313]. In addition, Mn was presented in linked with the silicates and sulphides [314], which are then extracted in F2, F3 and F4 steps.

It is found that Ni is majorly distributed in residual fractions with values of 70.3 and 76.4 wt% for Coal -1 and Coal -2, respectively. A lesser proportion (27.7 wt% in Coal-1 and 23.0 wt% in Coal-2) is associated with the oxidizable fraction. Research by Riley et al. [314] also indicated that nickel was presented in silicates and residual matters with a lesser relation with sulphide in BA coal. For both samples, about 98-100 wt% of lead is associated Fe and Mn oxyhydroxides. During the sequential extraction, only small amount of vanadium (less than 5%) is leached out by CH_3COOH. The reducible, oxidizable and residual fractions of vanadium show an increasing trend with the corresponding values of 11.9, 34.1, 49.1 wt% in Coal-1 and 13.9, 37.3 and 48.8 wt% in Coal -2. Vanadium in coal was associated with clays, organic matter and over 50 wt% of vanadium was associated with silicates, which was the result for the large part of residual fraction [312]. The sequential extraction experiments reflect that zinc in both coal samples predominantly presents as residual fractions accounting for 55.4 wt% in Coal-1 and 59.1 wt% in Coal-2, followed by reducible fraction (30.1%) and oxidizable fraction (12.1%) for Coal-1, while the oxidizable fraction and reducible fraction are 23.7 and 12.4 wt% in Coal-2. In addition, little zinc (< 5 wt%) is extracted by CH_3COOH. Riley et al. [314] that the Zn in coal was primarily occurred as sphalerite and also a lesser proportion of pyrite and organically bound. The heavy residual fraction of Zn could be attributed to the silicates association, which was hard to remove by the F1-F3 solutions. This findings is also supported by the a previous investigation [312].

Table 6. 4 Sequential extraction results of heavy metals in feeding coals (mg/kg)

Elements	Step	Ba	Co	Cr	Cu	Mn	Ni	Pb	V	Zn
Coal-1	F1	22.3	0	0	0	111.70	0	0	0.59	1.25
	F2	137.7	0.26	0.16	0.79	21.00	0.38	3.89	1.44	15.20
	F3	8.85	4.55	3.73	9.81	24.2	5.12	0.08	4.10	6.1
	F4	79	1.39	14.35	9.9	11.5	13	0	5.90	27.95
	Recovery/wt%	78.9	121.9	75.8	73.5	106.5	71.5	76.9	125.9	71.1
Coal-2	F1	54.6	0	0	0	71	0	0	0	1.15
	F2	27.7	0.12	0.04	0	31	0.10	1.31	1.56	2.93
	F3	15.45	4.73	3.53	2.50	22.5	3.6	0	4.20	5.6
	F4	13.7	0.87	16.95	2.26	7.80	11.95	0	5.5	13.97
	Recovery/wt%	95.3	106.7	91.2	71	94.5	94.5	75.2	124.4	71.5

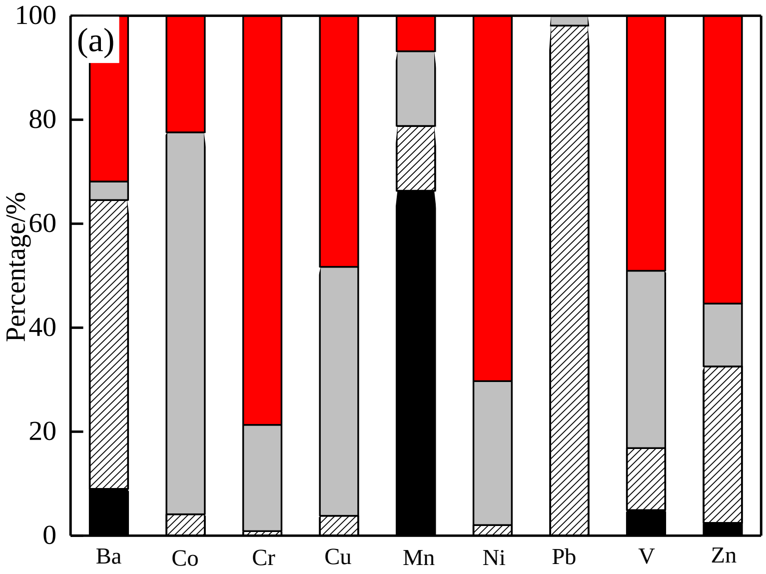

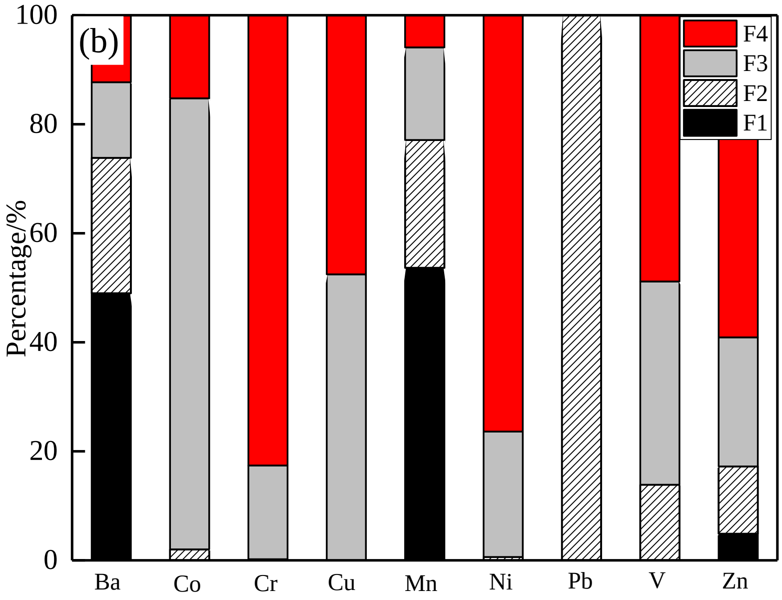

Figure 6. 6 Percentage distribution of heavy metals from sequential extraction for: (a) Coal-1 and (b) Coal-2

The sequential extraction results for the coarse residual samples are shown in Table 6.5. The percentage of each extracted elements are illustrated in Figure 6.9. As can be noticed from Table 6.5 that the recovery percentage is varied from 70.3 to 106.3%, indicating the high reliability of the experiment. Due to the high volatility of lead, near all the lead during gasification are concentrated in the fine particles. It is therefore that the fractions of lead are blank in both Table 6.5 and Figure 6.9. The distribution of each fraction of barium and cobalt are similar, both of them are mainly in residual form ranging from 76.8 to 79.6 wt%. The acid soluble fractions of Ba and Co are in the range of 10.5 to 15.6 wt% and 10.6 and 12.5 wt%, respectively. Besides, about 5.3 to 6.1 wt% and 8.9 to 9.0 wt% of Ba and Co are associated with reducible fraction. Only less than 4 wt% Ba and Co are presented in oxidizable status. Ba in the feeding coals is mainly occurred as barite, barytocalcite, witherite and organic associations as demonstrated in Table 6.4, during gasification, the solid barium compounds decomposed at 800 to 1450 ºC and reacted with silicate minerals to form complex and stable barium ortho-silicate [148]. For Co, the major association was sulphides and at high gasification temperature, it reacted with silicate and transited to a solid cobalt orthosilicate species ($(CoO)_2(SiO_2)$) according to the study by Bunt et al.[148]. As a result, the residual contents of Ba and Co are predominant. The proportion of chromium in residual association is identified over 94.8 wt% in the both coarse samples, which is consistent with the occurrence of Cr in feeding coals showing the largest share of residual contents as depicted in Figure 6.8. During gasification, the carcinogenic hexavalent form of Cr_2O_3 was obtained at reducing conditions [316, 317]. After the reactions with hematite, the stable chromite species were produced, which contributed to the increase of residual fractions in slag particles.

Copper in residual form occupies 72.2 wt% and 87.6 wt% in CS-1 and CS-2, respectively. About 19.8 wt% and 6.0 wt% of copper in CS-1 and CS-2 exist in oxidizable format, the left speciation is acid solubility accounting for 8.0 wt% in CS-1 and 6.4 wt% in CS -2. Compared with the corresponding mode of occurrence of Cu in Figure 6.8, the silicate-bound Cu increases while organically and sulfide bound Cu decreases. Cu exhibited an increasing trend in volatility as the increase of temperature and it showed 75 wt% volatilization ratio at 1125 ºC [147]. Cu vapour could be adsorbed by silicates and combined with sulphides or organic in the liquid slag [155], leading to a high content of Cu in residual fraction. Manganese and nickel display high percentage of residual contents, which are 68.0 -71.4 wt% and 72.5 -76.5 wt%, respectively. A smaller portion of Mn and Ni, 18-19.4 wt% and 10.5-11.6 wt%, respectively, is found to be acid-soluble and exchange form. About 6.8 -10.2 wt% of Mn and

8.1-11.2 wt% of Ni are leached out using hydroxylammonium chloride. The dominant mode of occurrence of Mn is carbonate, i.e. $MnCO_3$, in the gasification process, the solid $MnCO_3$ was unstable and it decomposed and reacted with silicate and Al_2O_3 minerals to form spessartite ($Mn_3Al_2Si_3O_{12}$), which further reacted and formed the stable Mn-cordierite ($Mn_2Al_4Si_5O_{18}$) and MnO slag [148]. The above transformation processes of Mn are described using the following (6.2-6.4). The MnO and Mn-cordierite species are considered to be reducible and residual fractions, respectively.

$$\mathrm{MnCO_3} \rightarrow \mathrm{MnO}+\mathrm{CO_2(g)} \tag{6.2}$$

$$3\mathrm{MnO} + \mathrm{Al_2O_3} + 3\mathrm{SiO_2} \rightarrow \mathrm{Mn_3Al_2Si_3O_{12}} \tag{6.3}$$

$$\mathrm{Mn_3Al_2Si_3O_{12}} + \mathrm{Al_2O_3} + 2\ \mathrm{SiO_2} \rightarrow \mathrm{Mn_2Al_4Si_5O_{18}} + \mathrm{MnO} \tag{6.4}$$

Compared with the speciation percentages of Ni in the feeding coal, the residual fractions of Ni in coarse slags change slightly. The operating temperature for the gasifier was 1250 °C, which suggested that a small part of Ni might escape into gas phase [317]. The evaporated Ni could be adsorbed in the slag and extracted as acid-soluble and reducible forms.

In the gasification coarse slags, vanadium is principally in residual fraction occupied 80.6 and 84.6 wt% in CS-1 and CS-2, respectively. The oxidizable form is reduced to less than 1 wt% in comparison with about 35 wt% in feeding coals. About 7.2 and 7.6 wt% percentages of vanadium in CS-1 and CS-2 are leached out in a reducible condition. Acetic acid removes about 11.6 and 6.8 wt% vanadium in CS-1 and CS-2, respectively. During gasification process, vanadium is partially transformed into gas phase above 1225 °C [318], it might be captured by the liquid slag and blocked in the amorphous and crystalline phase [155], leading to a large amount of residual form. Approximately 42.3 and 68.0 wt% of the zinc from CS-1 and CS-2 are in the residual forms, which was close to the results showing more than 50 wt% of the Zn was in the silicates of GSP-FS revealed by Tang et al. [155]. This might be the case that the Zn vapour was captured by liquid slags and combined with other chemical species such as carbonates, iron and manganese oxide as well as silicates [155].

Table 6. 5 Sequential extraction results of heavy metals in coarse slags (mg/kg)

Elements	Step	Ba	Co	Cr	Cu	Mn	Ni	Pb	V	Zn
CS-1	F1	139.45	7.15	12.95	3.98	277.75	7.3	0	10.2	7.45
	F2	47.75	5.1	9.45	0	96.5	5.1	0	6.35	3.98
	F3	20.85	0.79	24.9	9.9	34.85	2.31	0	0.58	2.06
	F4	688	44.05	863.5	36.05	1019.5	48	0	71	9.9
	Recovery/wt%	72.3	71.8	70.8	70.3	70.4	72.1	-	77.3	76.4
CS-2	F1	89.35	10	3.31	2.97	236.75	8.6	0	8.35	3.99
	F2	52.45	8.55	4.11	0	134.3	9.15	0	9.4	5.03
	F3	33	2.45	7.75	2.8	50.05	4.7	0	1.29	0.65
	F4	680	73.5	282	40.85	895.5	59.2	0	104.25	20.5
	Recovery/wt%	87.5	98.9	72.5	70.6	89.5	70.4	-	106.3	74.3

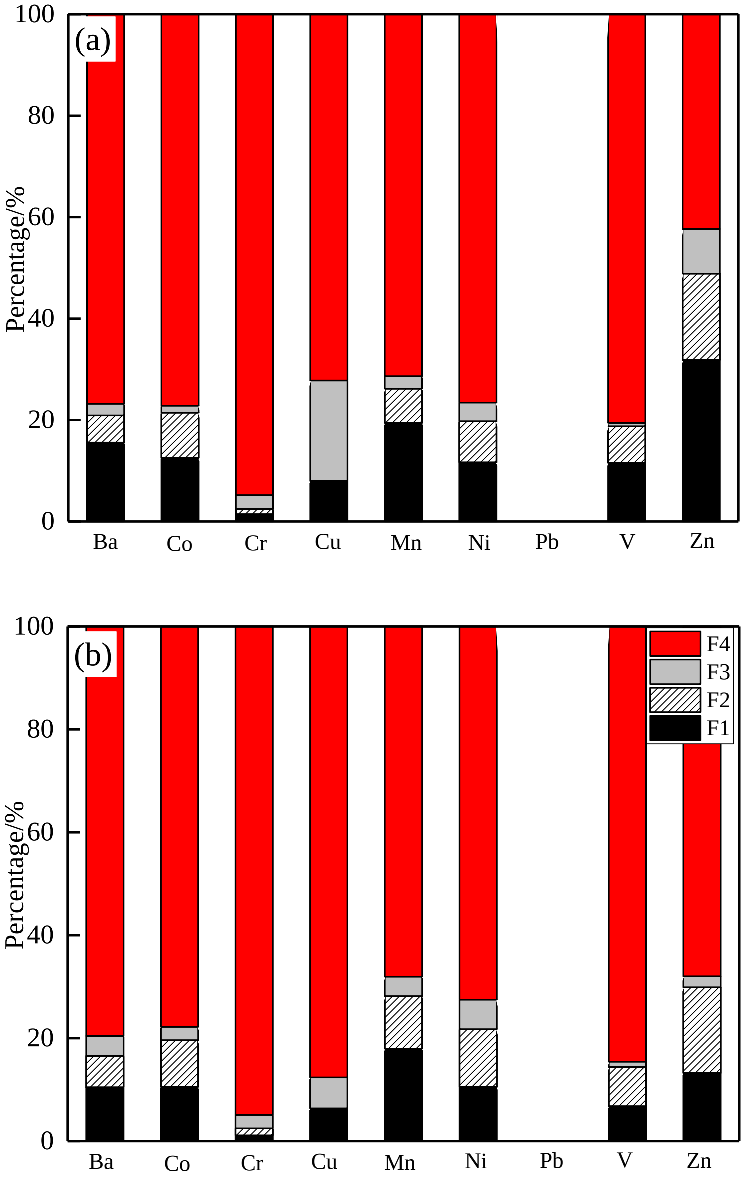

Figure 6. 7 Percentage distribution of heavy metals from sequential extraction for: (a) CS-1 and (b) CS-2

Table 6.6 presents the heavy metal concentration of the fine residual samples. Clearly the recovery percentage of the selected heavy metals is between 70.1 and 108.4 wt%, which were within the normal range. Figure 6.10 displays the sequential extraction results. Apart from zinc, the other heavy metals are dominated by residual content as the following order: 87.9 – 88.8 wt% (Cr), 83.4 – 83.7 wt% (V), 67.7 – 75.8 wt% (Pb), 54.2 - 66.5 wt% (Co), 59.6 – 64.4 wt% (Ba), 58.8 – 64.0 wt% (Mn), 57.6 – 61.7 wt% (Cu), 42.0 - 42.8 wt% (Ni).

Compared with the residual fractions of heavy metals in coarse slags, as shown in Figure 9, the residual content of corresponding elements in fine slags show a downward trend, suggesting the heavy metals are more unstable in finer residuals. Lead (Pb) only presents in FS due to its extremely high volatility. The residual fraction of Pb has the highest percentage, followed by a decreasing fraction in the oxidizable, reducible and acid-soluble forms. The original state of Pb in coal was mainly associated with galena and pyrite [312], which could decompose and vaporize to gas phase in the form of PbS, $PbSO_4$ and $PbCl_2$ [319, 320] during gasification. The former two compounds could be extracted as the oxidizable fraction, while the last compound could react with Al_2O_3 and SiO_2 and fixed in the aluminosilicate lattice [321], which is leached out as a residual fraction. As for zinc, the acid solution fraction has the highest proportion with the values 55.9 wt% and 50.5 wt% in FS-1 and FS-2, respectively. The residual fraction accounts for 26.0 wt% and 27.8 wt% of the total zinc in FS-1 and FS-2. The reducible fraction and oxidizible fraction are about 12 wt% and 6.0 wt% in both samples. Zinc was principally occurred as sphalerite (50 wt%), pyrite (15 wt%) and silicates (15 wt%) in coal samples [312]. During gasification, the evaporated Zn species from sphalerite and pyrite could be adsorbed on the surface of fine particles more easily, resulting in leaching out with acetic acid. On the other hand, part of Zn in the silicate reacted with Al_2O_3 and SiO_2 to form $ZnAl_2O_4$ and Zn_2SiO_4 at high temperature [322], which are the source of residual fractions.

Table 6. 6 Sequential extraction results of heavy metals in fine slags (mg/kg)

Elements	Step	Ba	Co	Cr	Cu	Mn	Ni	Pb	V	Zn
FS-1	F1	81.4	15.75	0.88	28.85	321	37.5	7.95	5.1	517.5

	F2	186.5	9.3	2.22	0	147.05	9.95	20.25	16.2	112
	F3	117.9	7.65	10.15	8.45	133.65	6.65	38.25	2.58	55.5
	F4	570	65	96.55	50.7	859.5	39.15	139.55	119.6	241
	Recovery/wt%	83.1	73.4	70.4	72.4	85.7	73.4	70.1	94.4	102.8
FS-2	F1	82.3	31	1.46	23.8	240.75	22.2	1.325	7.5	131.5
	F2	230	21.95	1.46	0	100.95	19.5	17.75	16.7	39.2
	F3	107.05	17.9	8.15	9.6	104.2	15.05	31.45	3.24	17.3
	F4	759.5	84	88.15	53.8	793.5	42.5	158.3	140.7	72.5
	Recovery/wt%	91.6	83.1	71.6	76.5	93.6	71.4	70.3	108.4	96.7

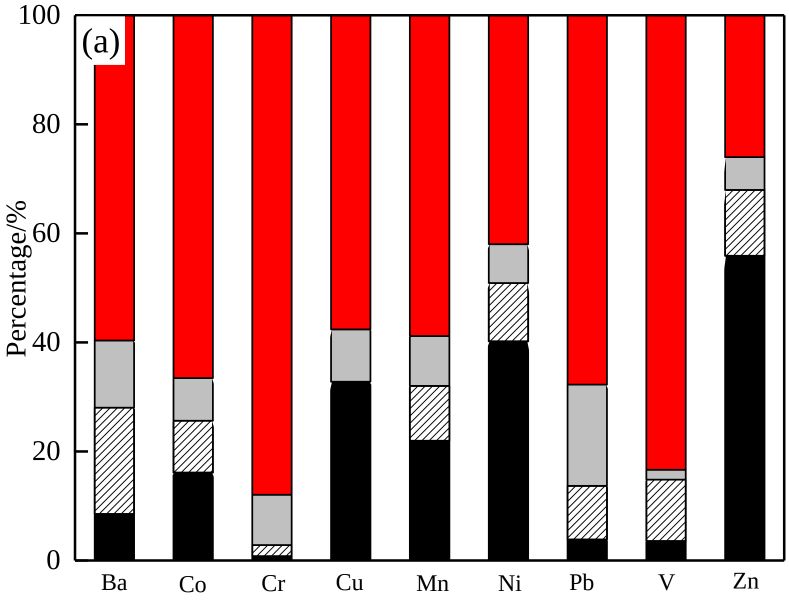

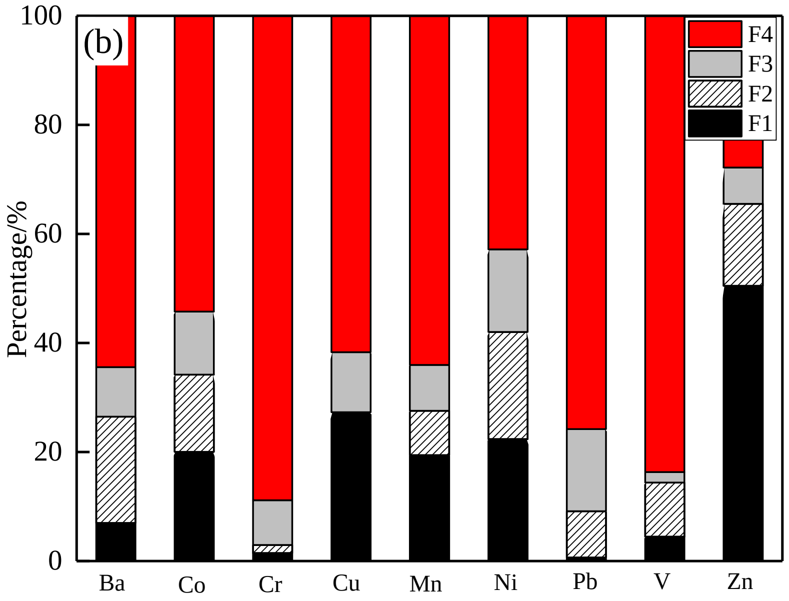

Figure 6. 8 Percentage distribution of heavy metals from sequential extraction for: (a) FS-1 and (b) FS-2

6.5 Change in mobility of heavy metals

The mobility behaviours of heavy metals are defined as the sum of the acid-soluble fraction (F1), reducible and oxidizable factions (F2 and F3), which might present as a threat to the environment [323]. Figure 6.11 the mean values of mobile fractions of heavy metals for the feeding coals, CS and FS. The mobile contents in feeding coals occurs as: Pb (100 wt%) > Mn (93.6 wt%) > Co (81.2wt%) > Ba (77.9 wt%) > Cu (53.1 wt%) > V (51.8wt%) > Zn (42.1 wt%) > Ni (26.7wt%) > Cr (19.4 wt%). In the CS, the mobile fractions of HMs are lower than that of HMs in feeding samples, especially for the Mn (30.3 wt%), Co (22.5 wt%), Ba (21.8 wt%), Cu (20.1 wt%) and V (17.4 wt%), which are only 1/3 of the HMs fractions. For the case of FS, the order of mobile fraction becomes: Zn (73.1 wt%) > Ni (57.6 wt%) > Co (40.9 wt%) > Mn (38.6 wt%) > Ba (37.9 wt%) > Pb (28.2 wt%) > V (16.5 wt%) > Cr (11.6 wt%), which are relatively abundant compared with the corresponding mobile fractions of HMs in CS except for the element of V. This characteristic indicates that the FS is more prone to be potentially toxic for the environment. Because chemical determined trace elements increased with the decreasing particles size in volatilization-condensation [320], a weaker bond for the HMs-fine slags could be expected than that for the HMs-coarse slags bonding in Al-Si glasses in the gasification. It can also be noted from this figure that the mobile fractions of Co, Cu, Mn and Ba in CS and FS have similar percentages about 20-30 wt% and 40 wt%, respectively, which are in accordance with their enrichment behaviours as shown in Figure 6.7.

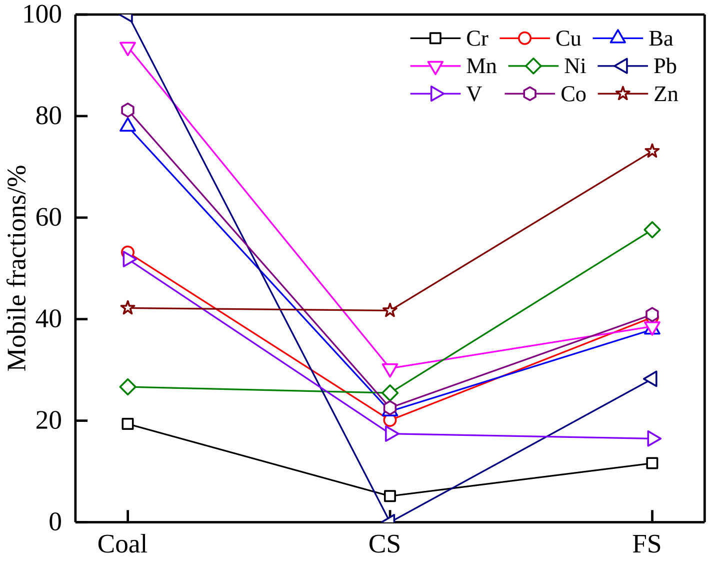

Figure 6. 9 Change in mobility of heavy metals

6.6 Leaching ability of trace element

The acid extractable fraction (F1) is easy to migrate and has the greatest potential to impact human health and ecological environment. The leaching ability was therefore calculated and compared with the Standard for Pollution Control on the Landfill Site of Municipal Solid Waste (GB 16889-2008), the results are illustrated in Figu.12. It should be noted that the leaching ability is calculated using the percentage of F1 fraction multiplied by the corresponding absolute concentration of a heavy metal [320]. The national standard indicating the maximum permissible concentration of some heavy metals are also marked in the right side of this figure. Zn shows a highest leaching ability of 502.9 mg/kg in FS-1, followed by Mn (257-394 mg/kg), Ba (89-192 mg/kg) and Ni (12-51 mg/kg), while the leaching amounts of other elements are lower than 39 mg/kg. Compared to the above standard, except Cu, none of the leaching concentrations of heavy metals in the gasification slags satisfy the standards. Among them, nickel exceeds the limited concentration by 20-102 times and lead by 7 to 45 times. Besides, the leachable Cr in coarse slags is slightly over the limiting value, but the concentration in the fine slags is lower than the standard. The case of Zn is another scenario, it meets the standard in coarse slags, while it exceeds about 1 to 5 times of the standard in the fine slags. According to the results, both of the coarse and fine slags requires treatment before disposal. Methods such as acid extractions and curing processing of the slags should be implemented to reduce the leaching ability and fulfil the standard of landfill.

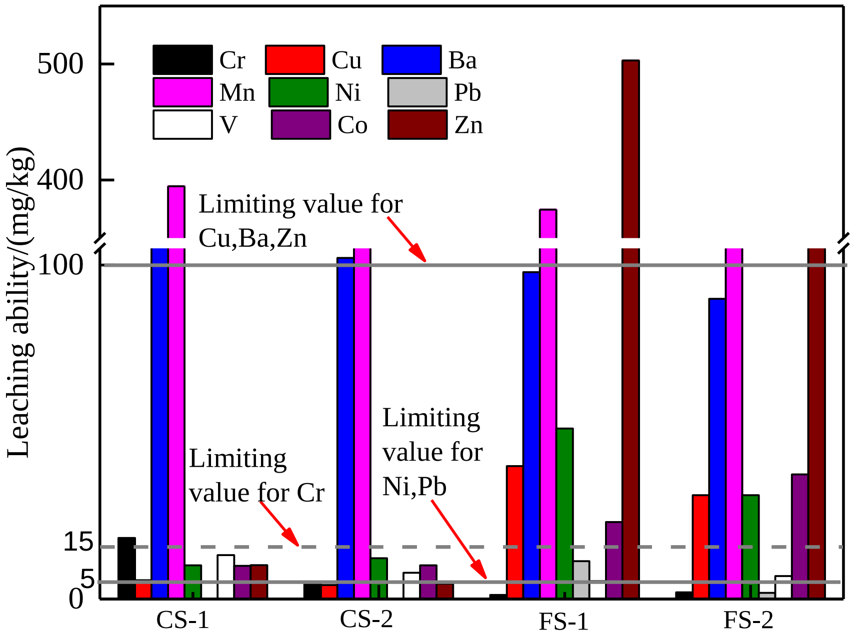

Figure 6. 10 Leaching ability of trace elements

6.7 Conclusions

In this work, the characteristics of coal and gasification slags (coarse and fine slags) derived from ECUST OMB's gasifiers were investigated. Besides, the concentrations, enrichment behaviours, modes of occurrence, mobility and leaching ability of heavy metals including Ba, Co, Cr, Cu, Mn, Ni, Pb, V and Zn in coal and gasification slags were quantified. The following conclusions can be obtained:

(1) The morphology of fine slags appeared fragmentized, small spheres and covered with fine floccules, whilst coarse slags were vitreous, angular and less porous than that of fine slags. Elements of Ba and Mn were the most abundant in all selected samples. Majority of heavy metals were more concentrated in fine slags than coarse slags. Lead was largely retained in fine particles. According to the relative enrichment index, Mn, V and Co were stablized in the gasification slags. Besides, Cr was

enriched in coarse slags, while Pb and Zn were accumulated in fine slags.

(2) For the coal samples, the elements of Cr, Cu, Ni, V and Zn were principally bonded with residual fractions (48.8 -82.6 wt%), while Co, Mn and Pb were dominated by oxidizable (78.1 wt%), acid soluble (60.0 wt%) and reducible fractions (99.2 wt%), respectively. However, Ba had higher reducible fraction (55.6 wt%) in Coal -1 and acid soluble fraction (49.0 wt%) in Coal -2, respectively.

(3) Except for Zn in fine slag, the other heavy metals were mianly in residual fractions with values of 42.3 to 94.8 wt% in both slags. The mobile fractions of heavy metals in coal samples were highest (19.4-93.6 wt%), followed by fine slags (11.6 – 73.1 wt%) and coarse slags (5.1 -41.0 wt%). Except cupper, the other metals in all slags did not meet the standard, suggesting the further treatments such as acid extractions and curing processing of slags are required before disposal.

Chapter 7 Influence of oil shale blending on the combustion of coal and ash fusion behaviour*

7.1 Introduction

As a dominant energy, coal can also be used to blend with other low-grade energies to assist their effective utilizations. Oil shale and its retorting residue (noted as semi-coke) are such low heating value fuels with high ash content. Mono-combustion or mono-gasification of oil shale and semi-coke is difficult on a large scale since their low reactivities. Hence, co-processing of oil shale (or semi-coke) and coal provide a new alternative to utilize oil shales. On the other hand, oil shale has high H/C ratio and carbonates, co-processing coal and oil shale helps to increase combustion performances and also reduce environmental pollution through sulphur fixation. A knowledge of the co-processing characteristics is crucial to achieve effective design and operation of the processes. In this thesis, investigations on the co-combustion and co-gasification performances of coal and oil shale are performed in this chapter and next chapter, respectively.

Nowadays, only few studies have been reported the co-combustion behaviours of coal and oil shale and these investigations concentrated on kinetic parameters with model-fitting method and sodium migration. Previous results may not be

---

* This chapter is currently under first-round revision in the Energy.

completely appropriate for kinetics and the ash fusion and mineral transformations in co-combustion are not performed. Hence, there is a need to perform studies on co-combustion of the coal and oil shale comprehensively.

In this chapter, the combustion characteristics of the coal, Fushun oil shale and their four blends using TGA at three heating rates were quantified and possible interactions during co-combustion were also assessed. The apparent activation energies for all the samples were estimated with both Flynn–Wall–Ozawa (FWO) and Kissinger–Akahira–Sunose (KAS) methods. Besides, the most probable combustion mechanism function and the pre-exponential factor were determined by master-plots method. Moreover, the slagging and fouling indices were theoretically calculated and the ash fusion behaviours and mineralogical compositions were predicted using FactSage 6.3 software.

7.2 Combustion process of the pure materials

The proximate and ultimate analyses of coal and oil shale are presented in Table 7.1. Simultaneously, the ash composition obtained from XRF is tabulated in Table 7.2. Figure 7.1 shows the TG/DTG curves of QH and FS under a heating rate of 10 ºC/min within a temperature range from 100 to 850 ºC. As noticed from Figure 7.1 (a), the whole combustion process for QH coal can be divided into three stages including (i) small weight loss of moisture evaporation step from 100 to 230 ºC accounting for near 2% of the total mass; (ii) volatile release and fixed carbon combustion significantly from 280 to 530 ºC taking up about 90% of the total mass; and (iii) burnout stage as the temperature increasing from 530 to 850 ºC. However, only one broad peak is observed within the temperatures ranging from 240 to 705 ºC for the FS sample, with about 21%

total weight loss. The significant mass loss for this peak was mainly due to the decomposition of a small amount of bitumen and kerogen, together with the char combustion. It can also be observed from Figure 7.1 that the first weight loss temperature of FS is lower than that of QH and the burnout temperature of FS is higher than that of QH. This was due to the high H/C ratio of FS sample, and the pyrolytic volatiles was more prone to be decomposed than that of QH coal. Meanwhile, owing to the high containment of ash (over 75 wt%) in the FS sample, the total weight loss is less than that of QH, while the combustion time is longer due to the weak oxygen diffusion and heat transfer efficiency in comparison with the combustion of QH coal. In addition, a shoulder is observed in the DTG curve with the temperature of about 360 ºC, which could be attributed to the kerogen deposition to pyrolytic bitumen [183]. Moreover, the maximum weight loss rates in the DTG curves of QH and FS are -7.8 and -1.1 %/min respectively, and the corresponding peak temperatures are approximately 425 ºC and 480 ºC, suggesting that QH coal has a stronger release of volatiles than that of FS oil shale.

Table 7. 1 Proximate and ultimate analyses of QH and FS samples

	QH	FS
Proximate analysis wt.% (air dry)		
Moisture	2.23	1.33
Fixed carbon	57.71	1.22
Volatiles	28.68	18.79
Ash	11.38	78.66
Ultimate analysis wt.% (dry)		

C	71.37	9.45
H	3.74	1.21
N	0.71	1.36
S	0.95	0.79
Cl	-	-
O (by difference)	9.61	7.19
LHV (MJ/kg dry)	24.07	4.12

Table 7. 2 XRF results of the ash composition analysis (wt%)

Ash composition	QH	FS
SiO_2	23.12	60.38
Al_2O_3	12.50	21.98
CaO	21.57	0.89
Na_2O	1.15	0.91
MgO	3.43	1.21
K_2O	0.08	1.69
Fe_2O_3	27.83	10.35
MnO	0.25	0.15
SO_3	8.09	0.70
TiO_2	1.13	1.47
P_2O_5	0.29	0.22

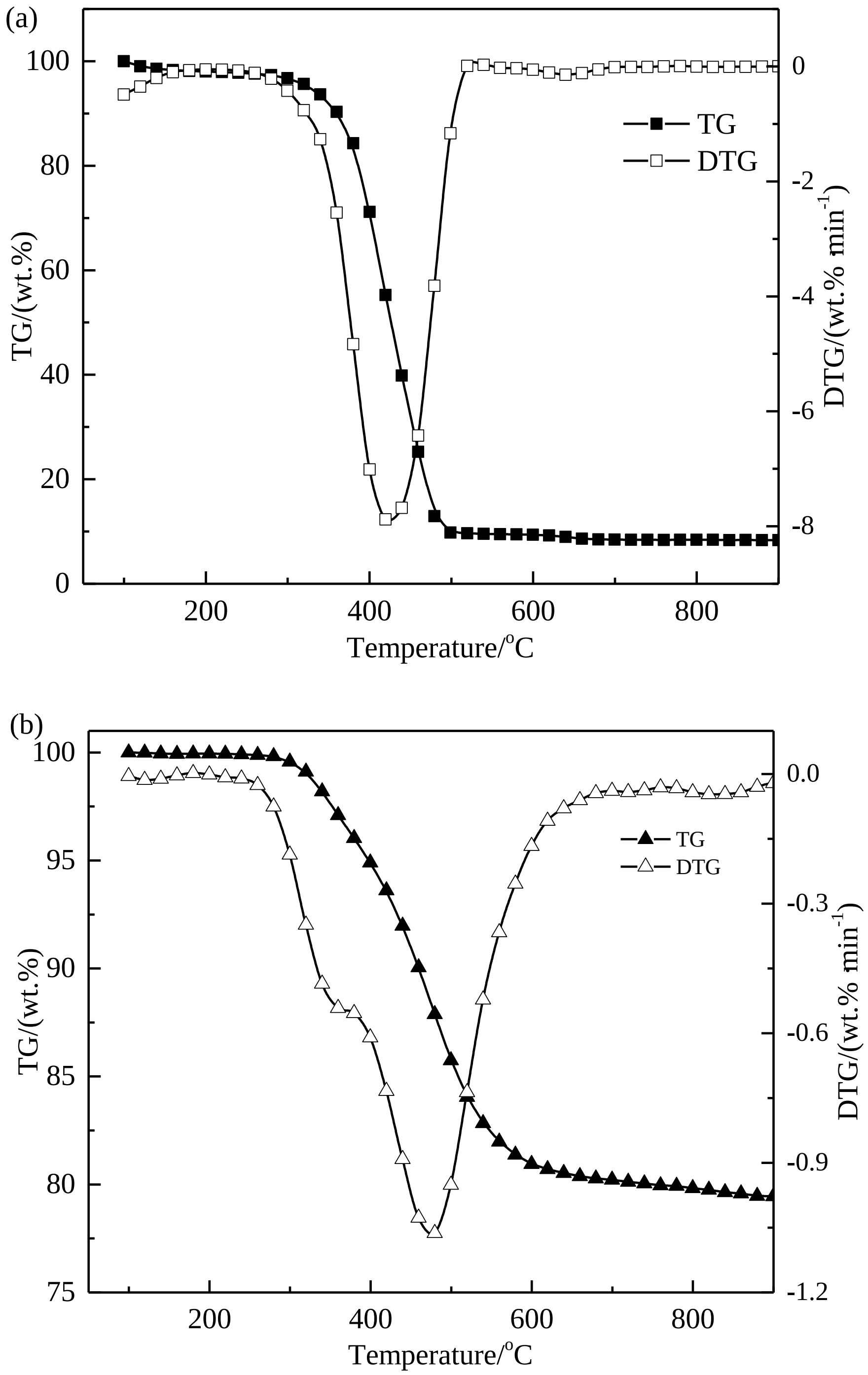

Figure 7. 1 TG-DTG profiles of (a) QH and (b) FS at 10 ºC/min

7.3 Co-Combustion of QH-FS blends

Combustion of the blended samples was performed at a heating ratio of 10 ºC/min, and the TG and DTG profiles are shown in Figure 7.2. As can be seen in Figure 7.2 (a), with the addition of FS, TG curves of FS is gradually shifted to the QH side, and the weight loss percentage decreases from 90 to 20% due to the high ash content in oil shale. However, the fastest mass loss is found to be 90QH10FS sample followed by 80QH20FS and QH, implying that the mixture of FS has an impact to the combustion behaviours of coal, while the FS sample has the slowest combustion ratio. From Figure 7.2 (b), the blends have similar DTG curves as QH, and all of them exhibit a single peak, indicating continuous combustion of volatile and char. The maximum mass-loss rates of the blended samples increase progressively from 1.1 to 9.8 %/min as the addition of FS, while the peak temperatures underwent an opposite direction.

The combustion characteristic parameters of the blends at the heating rate of 10 °C/min are presented in Table 7.3. As indicated, the ignition temperatures (T_{i}) of blends has almost the same value around 375 °C, which also has a small gap about 12 °C in comparison with that of the pure samples. The reason might be attributed to the similar devolatilization temperature between QH and FS as presented in Figure 7.1. Analogously, the peak temperatures (T_{max}) of the blends fluctuate around that of QH (420.1 °C) with a maximum change within 2 °C. Those facts suggest that the addition of FS may have little impact on the ignition and peak temperature performances of QH coal. However, the burnout temperature (T_{b}) of the blends increases significantly from 514.5 to 552.4 °C, implying that the addition of FS hinders the burnout of the blends. It can also be noticed that the burnout temperature of 90QH10FS sample is close to that of QH coal, indicating that the marginal impact of burnout temperature of QH is detected when the mass fraction of FS is less than 10. At the same time, when FS increases from 10 to 40%, the maximum weight loss rate ($(\mathrm{d}w/\mathrm{d}t)_{\mathrm{max}}$) and mean weight loss rate ($(\mathrm{d}w/\mathrm{d}t)_{\mathrm{mean}}$) drop from 9.8 and 1.9 to 5.6 %/min and 1.3 %/min, respectively. The reasons could be attributed to the increased combustion time caused by the addition of ash content in the blends, which prolonged the oxygen penetration process. It can also be observed that both of the samples of 90QH10FS and 80QH20FS have higher maximum weight loss rate than that of QH coal, indicating the enhancement of combustion intensity.

As the increase of FS percentages from 10% to 40%, the ignition index (C_i), burnout index (C_b) and the comprehensive index (*CCI*) of the blends decrease gradually from 1.12×10^{-2} to 0.64×10^{-2} %/min^3, 0.99×10^{-3} to 0.42×10^{-3} %/min^4 and from 2.55×10^{-7} to 0.97×10^{-7} %^{2}/(°C^{3}min^2), respectively, which are also reflected clearly in Figure 6.3. It is worth noting that the C_i and C_b reach respective maximum values at 90QH10FS. In particular, the C_i and C_b are enhanced by 21.7% and 76.7% respectively at the mass percentage of 10% FS, compared with those of QH coal. This could be explained by the increment of relative volatile content in the blends, leading to better ignition and burnout behaviours at a low mixing ratio (less than 20%). On the other side, when the mixing ratio was beyond 20%, the added ash gradually dominated the combustion process, leading to inferior ignition and burnout performances. The *CCI* of all the blends is smaller than QH coal, indicating that the addition of FS oil shale decreases overall combustion performance. However, when a small amount of FS (10%) is added into the QH coal, the comprehensive combustion index of S decreased slightly (less than 5%). These results indicate that the improved benefits of co-combustion are obtained at the FS mixing ratio of 10%, which is consistent with the findings reported elsewhere [324].

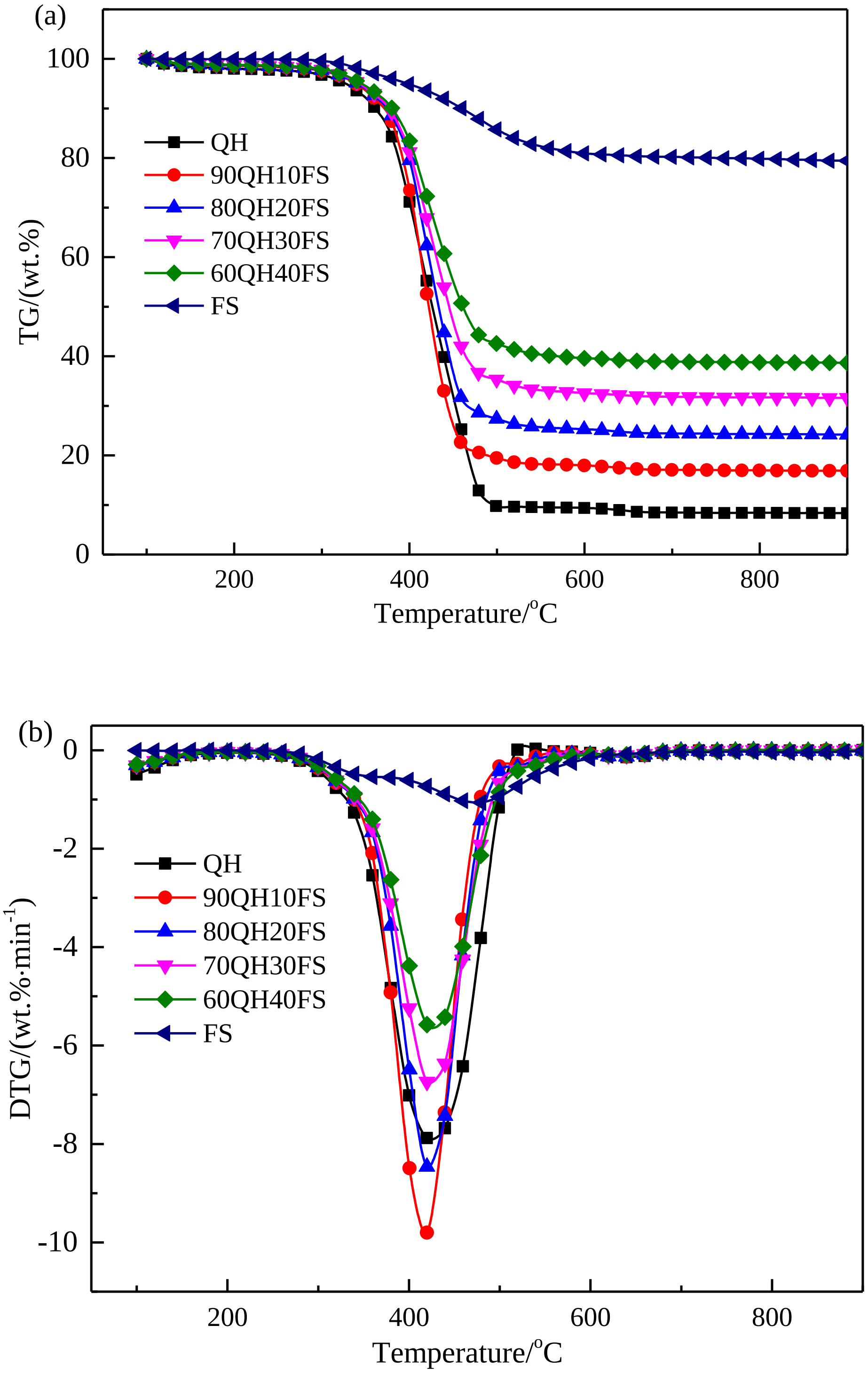

Figure 7. 2 TG/DTG profiles of all samples at 10 ^{o}C/min

Table 7. 3 Combustion characteristic parameters of all samples at a heating rate of 10 °C/min

Sample	T_i (°C)	T_{max} (°C)	T_b (°C)	$(dw/dt)_{max}$ (%/min)	$(dw/dt)_{mean}$ (%/min)	$C_i\times10^2$ %/min^3	$C_b\times10^3$ %/min^4	$CCI\times10^7$ %^{2}/(°C^{3}min^2)
QH	363.6	420.1	504.4	7.9	2.3	0.92	0.56	2.68
90QH10FS	373.5	421.1	514.5	9.8	1.9	1.12	0.99	2.55
80QH20FS	378.3	419.5	522.8	8.5	1.7	0.96	0.76	1.90
70QH30FS	375.1	418.1	540.4	6.7	1.5	0.77	0.56	1.35
60QH40FS	373.4	421.2	552.4	5.6	1.3	0.64	0.42	0.97
FS	362.1	480.2	723.1	1.1	0.3	0.11	0.02	0.04

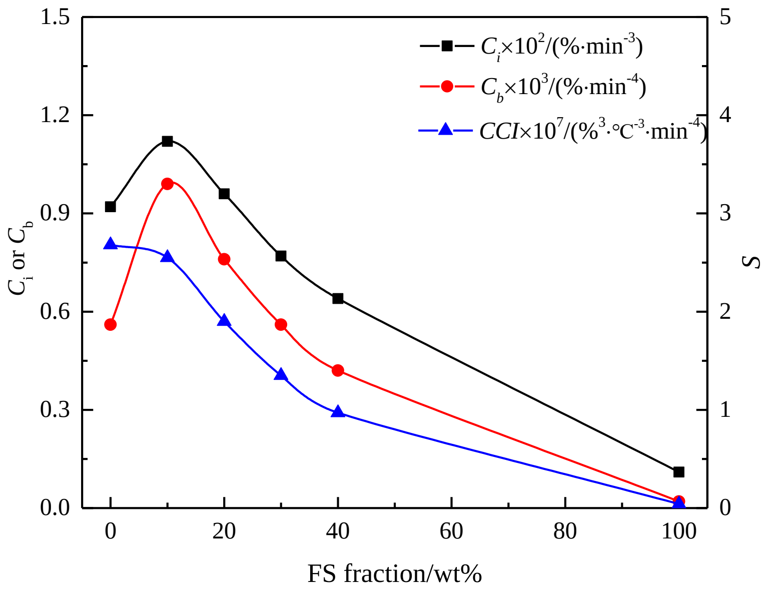

Figure 7. 3 Relationship between C_i, C_b, CCI and FS fractions

7.4 Synergistic effects during co-combustion

Figure 7.4 depicts the theoretical and experimental TG curves and derivation TG curves versus temperature of the blends at the heating rate of 10 °C/min. As presented in Figure 7.4(a) and Figure 7.4(b), when the temperature is below 320

°C, the theoretical and experimental curves are almost identical, and the corresponding values of △W are zero, suggesting that there is no synergy during volatile release. However, the experimental TG curves lag behind the theoretical TG curves at the temperature between 320 and 410 °C, in which can also be observed from the Figure 7.4 (b) that the △W value for all the blends is positive. Besides, the peak value of △W is found to be 3.74% at the temperature of 380 to 400 °C, implying that the mixing of QH and FS leads to an inhibitory interaction at a lower temperature close to the ignition point. This result also confirms that the ignition temperatures of blends are slightly higher than the QH coal as presented in Table 7.3. The reason for the inhibition could be attributed to the part of released and sticky kerogen or tar from FS oil shale, which hindered the volatiles diffusion from QH coal [169]. At the temperature range of 410 to 480 °C, the theoretical TG curves gradually hide behind the experimental curves. The maximum weight loss of the experimental value is 11.9% lower than that of the theoretical value at 439 °C under the 10% FS blend ratio. Nevertheless, such promoting synergy is firmly related to the blending ratio as it slows down with the increase of mixing ratio as illustrated in the Figure 7.4(b) that the maximum weight loss deviations shift to be 6.5, 2.7 and 0.33 at the 20%, 30% and 40% mixing ratios, respectively. On the other hand, the corresponding temperatures at the maximum weight loss deviations (△W) increase gradually from 439 to 460 °C within the blending range from 10 to 40%. The enhancements of weight loss were owing to two reasons: one was the increase of K brought by FS blends, which acted as an attractive catalyst for combustion; the other was the exiting of numerous small free radicals generated by the bond-breaking reaction of light organic matter such as bitumen at lower temperature [244, 325], which might contribute to the deposition of cross-linked aromatics in coal [326]. Besides, the light organic matters were easily to burn, and much heat was generated to accelerate the combustion reaction, leading to additional weight loss. Similarly, the increase of mixing ratio contributed to the less oxygen contacting with char due to the consumption of oxygen with the volatiles at the solid surface, resulting in the restraint of char combustion and marginal less promoting effect.

When the temperature is beyond than 480 °C, slight inhibitory interactions are observed as a tiny positive increase of 2.5% of △W and then it shows a declining trend till the temperature of 550 °C. Subsequently, the △W turns to a stable value of 1.4% at above 550 °C. The result reflects that a weakened inhibition is accompanied until the co-combustion completion. This was mainly because a large amount of ash produced during the combustion influenced heat transfer and oxygen diffusion, contributing to a weakened combustion rate.

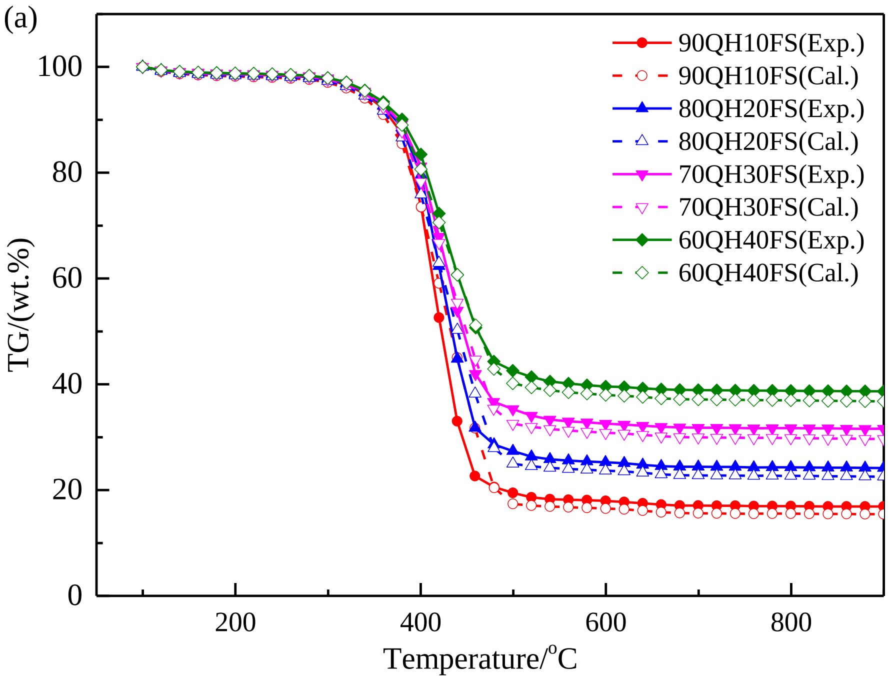

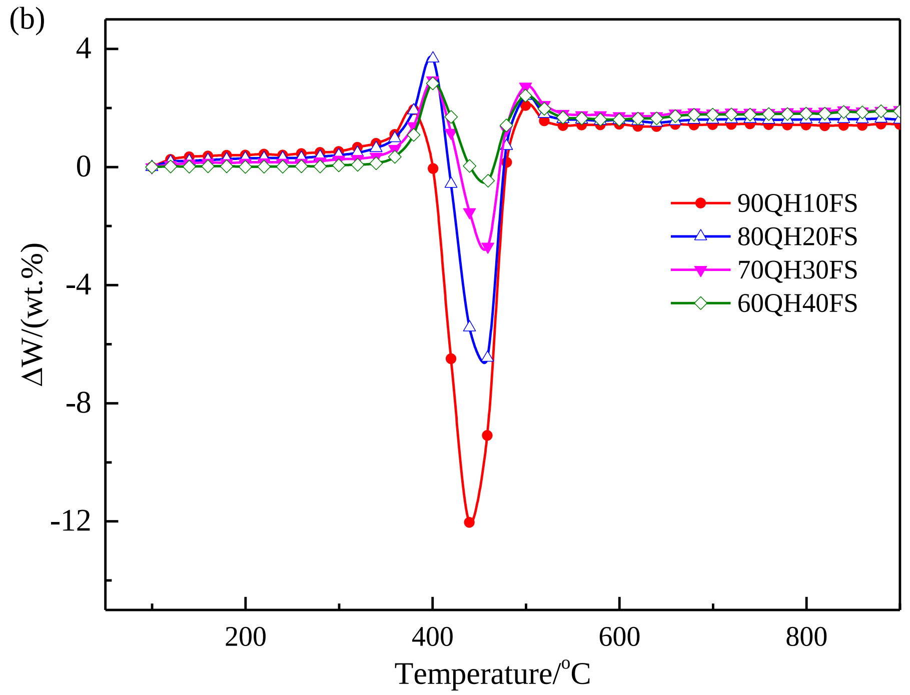

Figure 7. 4 Plotting of: (a) comparison of the calculated versus experimental TG curves and (b) variations in profiles of △W at four blending ratios

7.5 Effect of heating rate

The TG and DTG curves at β = 10, 20 and 30 °C/min for the blending ratio of 10% are presented in Figure 7.5. As shown in Figure 7.5(a), with the increase of heating rates, the TG curves are transferred to a higher temperature at the range of 335 to 670 °C. Besides, the weight losses are 81.94% at the β of 10 and 30 °C/min, which is very close to that value of 83.81% at β =20 °C/min, indicating that the impact of residue yield is unobvious. Clearly, in Figure 7.5(b), a wider combustion temperature range is observed as the increase of heating ratio. The DTG curves are also detected to shift to a higher temperature zone. The combustion performances are quantitatively reflected in Table 7.4.

From Table 7.4, as β is enhanced to 30 °C/min, the ignition temperatures vary slightly while the peak temperatures and burnout temperatures are shifted from

421.1 to 440.2 °C and from 524.5 to 657.8 °C respectively, implying that the addition of heating rate is unfavourable to the burnout. In addition, the comprehensive combustibility index is observed to increase from 2.55×10^{-7} to 4.36×10^{-7} $\%^2/$ ($°C^3min^2$), suggesting that the combustion performance is improved significantly. At a higher heating rate, the heat transfer and temperature difference between the particle surface and the core were prone to be larger, so the residence time at a designated temperature became shorter, resulting in a low degree of char oxidation. Hence, both the peak and burnout temperature are shifted to a higher temperature zone. Meanwhile, the overall burnout time was shortened due to a higher heating rate. Therefore, the average combustion rate was increased, and subsequently, the CCI is enhanced.

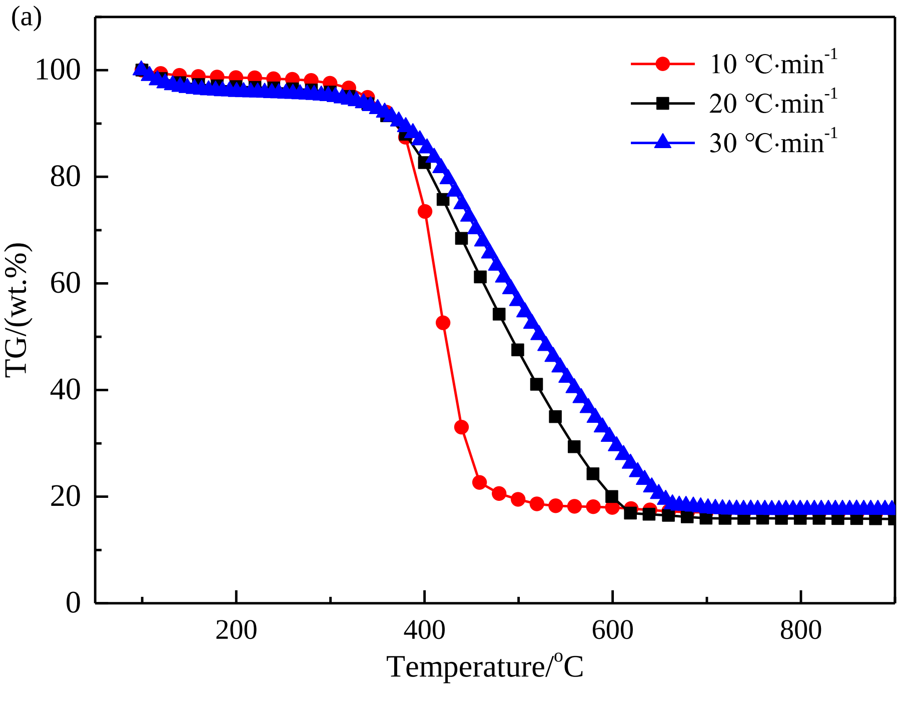

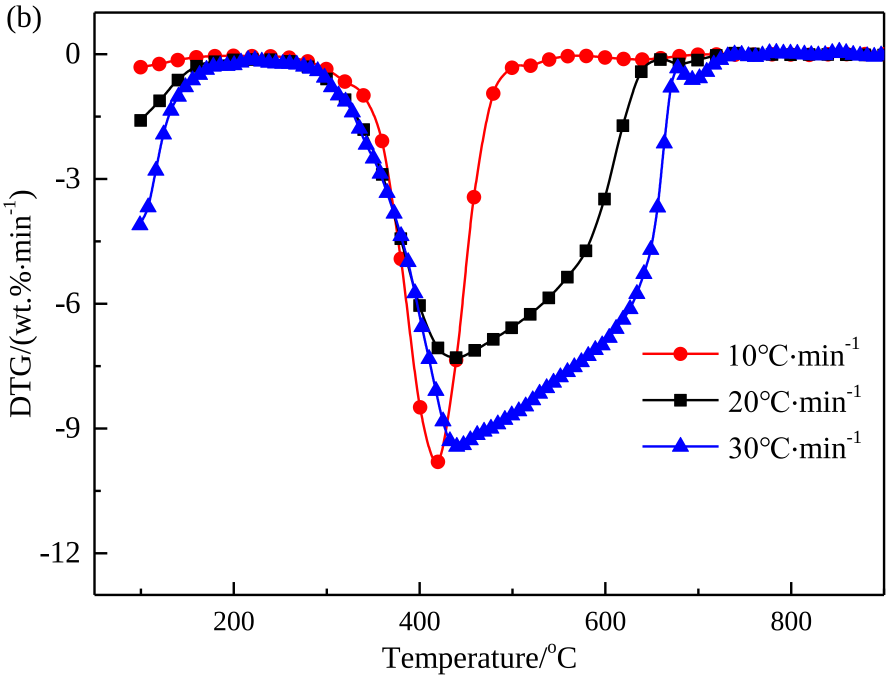

Figure 7. 5 Plotting of (a) TG and (b) DTG profiles of 90QH10FS at different heating rates

Table 7. 4 Combustion characteristic indexes of 90QH10FS at different heating rates

Heating rate (°C/min)	T_i (°C)	T_{max} (°C)	T_b (°C)	CCI ×10^7 (%^{2}/°C^{3}min^2)
10	373.5	421.1	524.5	2.55
20	362.7	438.5	614.9	2.91
30	376.6	440.2	657.8	4.36

7.6 Kinetic analysis

The activation energies (E_a) at different conversions (α) for the investigated samples were obtained according to the slopes of the FWO and KAS methods as displayed in Eqs. (3.25) and (3.26) respectively under the heating rates of 10, 20 and 30 °C/min. The conversion considered in this study was from 0.2 to 0.9 for the outer scope had a weak correlation. Figure 7.6 shows the representative regression lines proposed by FWO and KAS for the sample of QH, respectively. The variation of calculated E_a versus conversion for QH, FS and their blends is illustrated in Figure 7.7.

As can be noticed from Figure 7.7, the E_a for all the samples is varied as the enhancement of conversion, indicating the combustions are not a single reaction stage. Then E_a of FS increases with conversion, and when $\alpha \geq 0.3$, the E_a of FS is obviously higher than that values of QH and the blends. It suggests that the QH and blends are burned more easily than FS. This was mainly due to the lower carbon content and a higher ash content of FS. However, at $\alpha = 0.2$, the E_a of FS is observed to be about 138 kJ/mol, which is lower than that value of the other samples, implying a better ignition performance of FS. The finding is in accordance with the result shown in Table 7.3 that the T_i of FS was slightly lower than that of the other sample. Except for FS, E_a values of the other samples exhibit a decreasing trend with the increase of α from 0.2 to 0.9. Besides, the E_a values calculated by KAS model are slightly lower than the ones obtained from FWO model, while a consistent shape of the curves derived from the two methods is observed. For example, the E_a value of QH is determined to be 73.5 and 64.9 kJ/mol by FWO and KAS, respectively. The reason for decreasing E_a with α was mainly attributed to the fact that a large amount of energy was required in order to ignite the considerable volatile hydrocarbons at the initial combustion stage. Subsequently, the generated voids in the char (less stable compounds) after devolatilization provided a beneficial place for the combustion between char surfaces and air, and hence, less heat supply was needed [249], and the combustion of char became more easily.

Figure 7.8 depicts the effect of FS fraction on the average activation energy (E_a) calculated by both of the FWO and KAS methods. Clearly, in this figure, with the increase of blending ratio, E_a exhibits a general uptrend. Besides, the values of E_a determined by FWO are slightly higher than the ones obtained from KAS, while they have similar variation trends. This difference was due to the impact of samples' heterogeneity [327], and it is also in agreement with the previous studies [328, 329]. In addition, the minimum activation energy is determined at FS fraction of 10% with a value of 68.4 kJ/mol by FWO and 59.8 kJ/mol by KAS, respectively. This phenomenon is also supported by the studies from Yu et al. [28] and Yan et al. [29] who found that the combustion activation energy decreased by the addition of a small amount of oil shale. Hence, the 10 wt.% FS blending ratio might be potentially applied in the co-firing process. Besides, the findings also support the improved ignition and burnout indexes as presented in Figure 6.3.

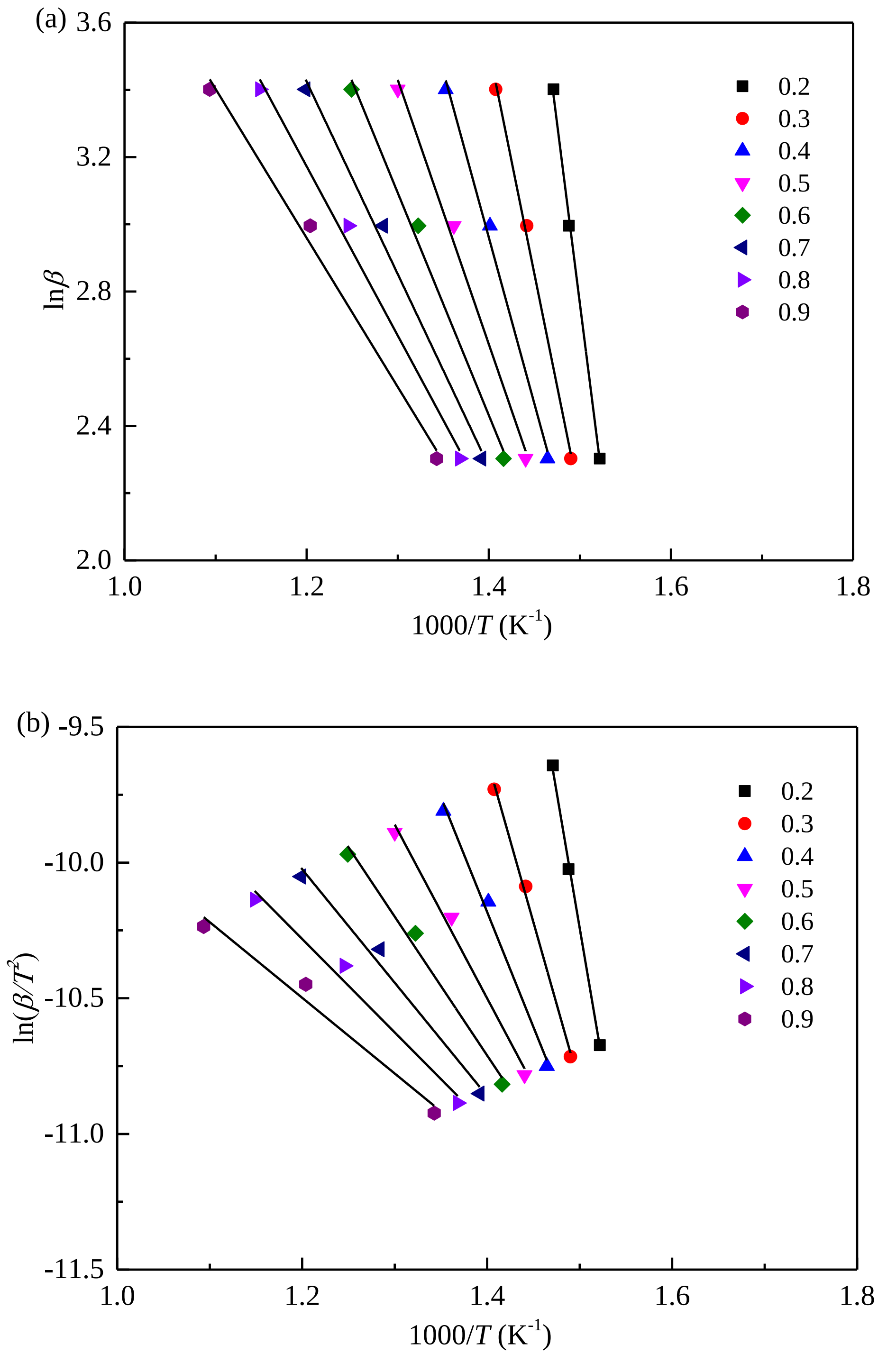

Figure 7. 6 Regression lines of E_a proposed by (a) FWO and (b) KAS methods for the sample of QH

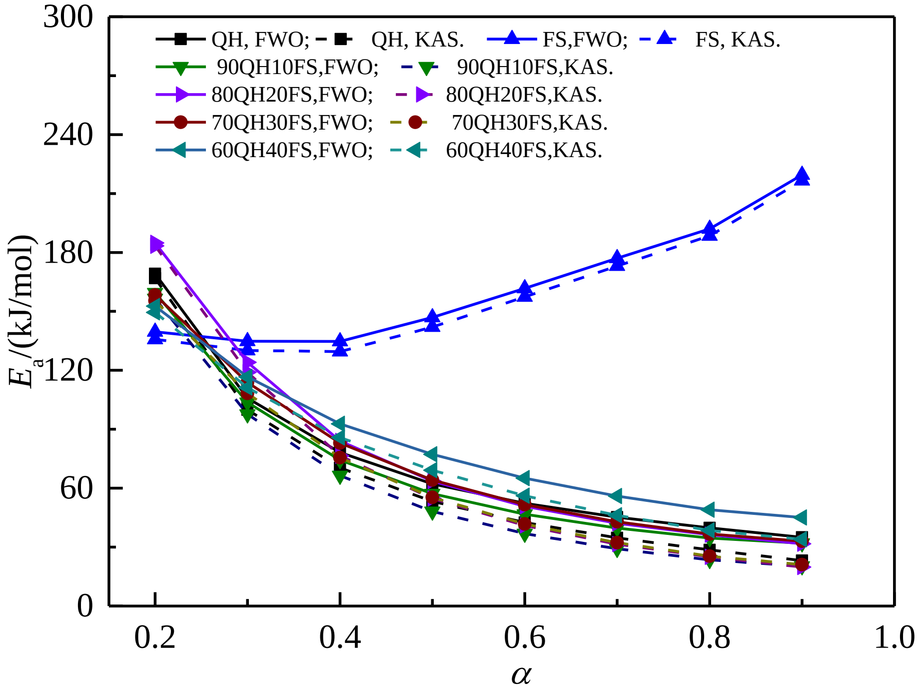

Figure 7. 7 Relationship between E_a and α for QH, FS and their blends obtained from FWO and KAS methods

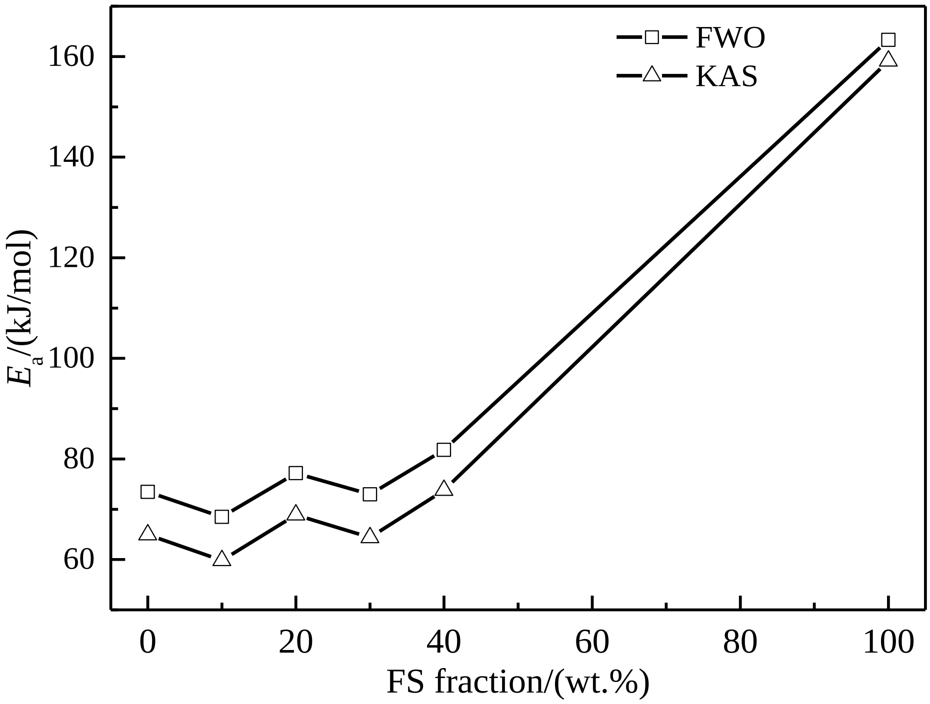

Figure 7. 8 Relationship between E_a and FS mass fractions

The activation energy used in the master-plots method for each sample was calculated based on the average E_a value from the corresponding FWO and KAS methods. Subsequently, together with the conversion data, the theoretical master plots of G(α)/G(0.5) using various mechanism functions (as referred in [245, 249]) and the experimental master plots of P(u)/P($u_{0.5}$) against α at three heating rates could be obtained accordingly. Figure 7.9 shows the theoretical and experimental master plots for the sample of 90QH10FS as can be seen from this figure that the experimental master plots at the heating rates of 10 and 30 ^{o}C/min fit well with the theoretical models of A2 and D2, respectively. However, there is no existing mechanism model closing the experimental master plot at β = 20 ^{o}C/min for it locates in the middle of F1 and F2 curves. Therefore, an F_n model was adopted to match the experimental master plot [329]. It is found that when the reaction order n =1.3, the best fitting theoretical master plot curve is obtained, and the corresponding G(α) is expressed as G(α)=10[(1-α)$^{-0.3}$-1]/3. Based on the determined reaction mechanism models at different heating rates, the pre-exponential factor A can be estimated from the slope by plotting $G(\alpha)$ against $\frac{E_a}{\beta R}P(u)$ as displayed in Figure 7.10. The pre-exponential factors are calculated to be 29137.9, 6904.9, and 4788.4 min^{-1} at the heating rate of 10, 20 and 30 ^{o}C/min, respectively.

Table 7.5 summarizes the kinetics parameters including E_a, A and f(α) of QH, FS and their blends under different heating rates by master-plots method. As can be noticed from this table that the combustion mechanism functions and pre-exponential factors are inconsistent with each other. The dominant co-combustion mechanisms are described by the F_n model with f(α)= (1-α)^{n} ($1.2 \leq n \leq 3$), followed by the R3 and D1 models. In addition, it is observed that there is no linear correlation of the kinetic parameters between the blends and single species because of the interaction between the coal and oil shale.

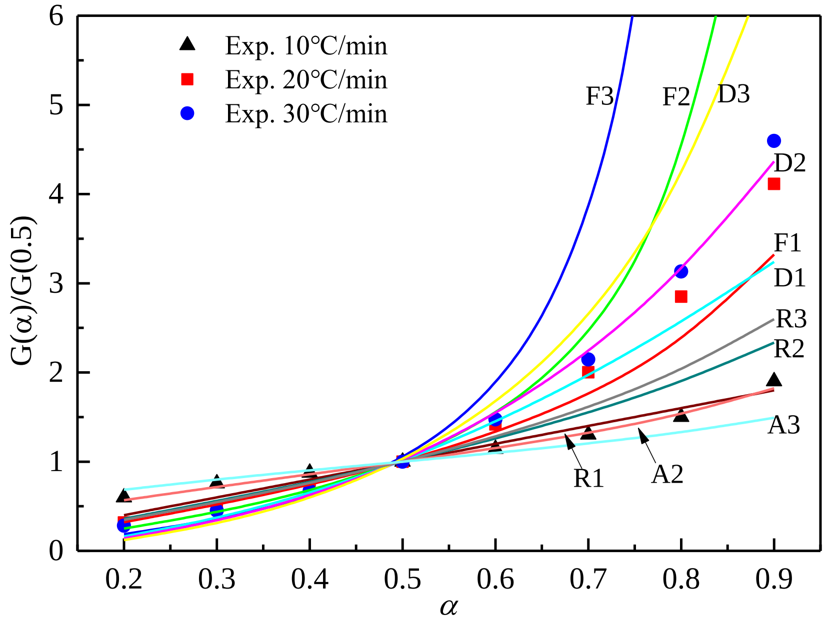

Figure 7. 9 Plotting G(α)/G(0.5) against α for variation reaction models and $P(u)/P(u_{0.5})$ against α from experimental data at different heating rates for the sample of 90QH10FS.

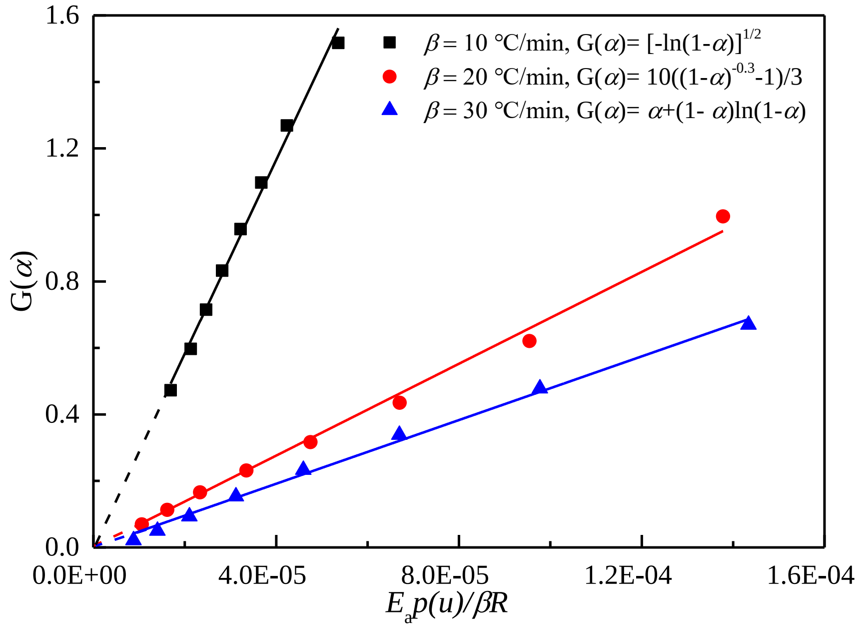

Figure 7. 10 Plotting G(α) versus $E_aP(u)/\beta R$ and linear-fitting drawing (solid line) for the sample of 90QH10FS

Table 7. 5 Kinetics parameters of QH, FS and their blends at different heating rates by master-plots method

Sample	E_a(kJ/mol)	10 °C/min		20 °C/min		30 °C/min	
		f(α)	A (min^{-1})	f(α)	A (min^{-1})	f(α)	A (min^{-1})
QH	69.2	$2(1-\alpha)^{1/2}$	21500.7	$(1-\alpha)^{1.2}$	53340.7	$1.5(1-\alpha)^{2/3}[1-(1-\alpha)^{1/3}]^{-1}$	3013.6
90QH10FS	64.1	$2(1-\alpha)\ [-\ln(1-\alpha)]^{1/2}$	29137.9	$(1-\alpha)^{1.3}$	6904.9	$[-\ln(1-\alpha)]^{-1}$	4788.4
80QH20FS	73.0	1	68113.0	$3(1-\alpha)^{2/3}$	32935.5	$1.5(1-\alpha)^{2/3}[1-(1-\alpha)^{1/3}]^{-1}$	5497.4
70QH30FS	70.6	$2(1-\alpha)\ [-\ln(1-\alpha)]^{1/2}$	67032.1	$3(1-\alpha)^{2/3}$	34201.3	$(1-\alpha)^{1.7}$	49911.1
60QH40FS	77.8	$3(1-\alpha)^{2/3}$	60327.9	$(1-\alpha)$	283749.8	$(1-\alpha)^{1.7}$	176046.5
FS	161.2	$(1-\alpha)^{3}$	1.44E11	$(1-\alpha)^{2.9}$	1.57E11	$(1-\alpha)^{2.8}$	8.95E10

7.7 Ash slagging and fusion characteristics

Based on the slagging and fouling indexes as listed in Eqs. (3.33) and (3.34), the results for all the samples are exhibited in Figure 7.11. As shown in this figure, the QH coal had the highest $R_{B/A}$ and F_U values of 1.46 and 1.79 respectively, while FS oil shale had the lowest $R_{B/A}$ and F_U values accounting for 0.18 and 0.46 respectively, suggesting that QH coal has the most considerable tendency for slagging and fouling. Besides, the increasing FS blending ratio simultaneously decreased both of the two indices. When the FS blending ration varied from 10% to 40%, the $R_{B/A}$ and F_U dropped slightly from 0.49 to 0.27 and from 1.01 to 0.46, respectively. In particular, the $R_{B/A}$ and F_U of the 90QH10FS decreased about 66% and 38% in comparison with those values in pure QH coal, indicating that by addition of 10% FS oil shale in the QH coal, the slagging propensity changes from a high to a low slagging tendency and the fouling inclination shifts from a high to a medium trend.

Figure 7.12 presents the predicted slag liquid fraction as a function of combustion temperature for the pure and mixture samples. Besides, the initial deformation temperature (IDT), hemispherical temperature (HT) and flow temperature (FT) line accounting for 62.9%, 80.1% and 86.0% of the slag fractions respectively, which based on the findings proposed by Thulasi et al. [330], are also presented in this figure. As depicted, the FS oil shale had the highest characteristic temperatures, which were about 94 to 124 °C larger than those values of QH coal due to higher SiO_2 and Al_2O_3 contents in the FS ash. Besides, the liquid slag fraction curves of the blending sample were located between the QH and FS curves when the combustion temperature is beyond 1100 °C, which showed a good agreement with the findings in Figure 7.11. The results suggest the addition of FS decreases the slagging propensity considerably. However, it was interesting to see that all the blending samples had an identical IDT, while the 10% of the FS additive had the more significant HT and FT values, indicating that the addition of 10% FS to QH is better than other blending ratios with regard to slagging resistance.

Based on previous test, it is clear that the 10% FS blending had the highest ignition and burnout indexes, nearly identical comprehensive combustion index with QH coal, lowest activation energy, and better slagging and fouling resistance. Nevertheless, the heating value of a blending sample should also be higher than 20 MJ/kg to ensure the auto-thermal combustion [258]. The LHV of the blends could be usually speculated by the mass-weighted calculation from the single QH and FS samples [331], and it was found that the 90QH10FS sample had an LHV of 22.07 MJ/kg. Accordingly, the addition of 10% of FS was determined to be the optimum blend ratio for co-firing.

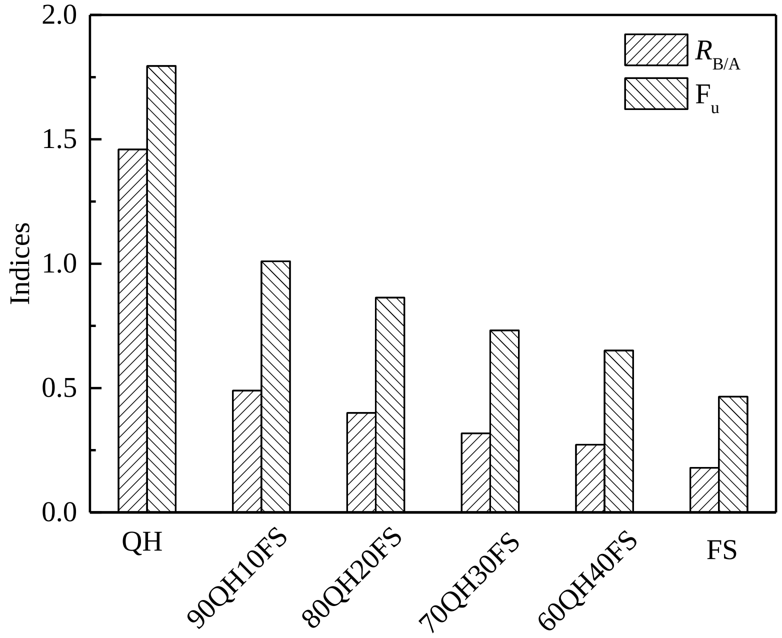

Figure 7. 11 Calculated indices under different coal and oil shale blending ratio

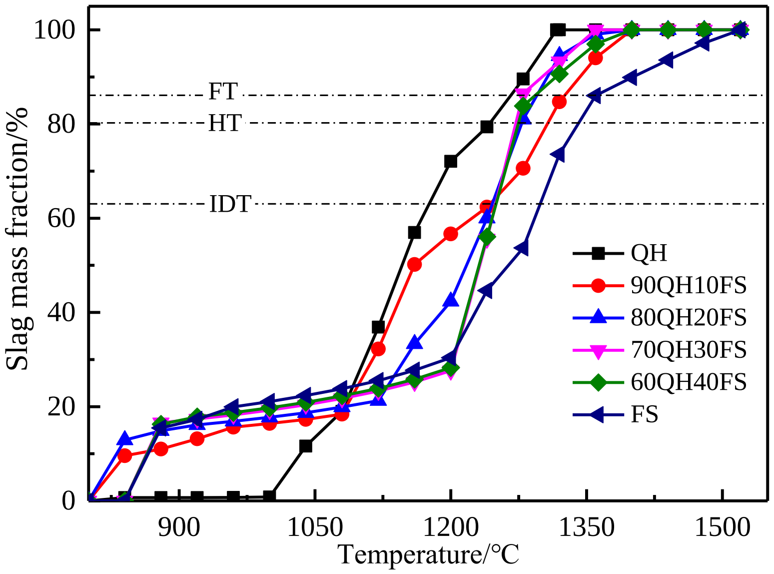

Figure 7. 12 Predicted ash slag mass fraction for the mixture of coal and oil shale

In order to test the mineral phase transformation and quantify its relationship with slag formation during co-combustion, FactSage was first employed to predict the sample of 90QH10FS from 800 to 1500 ºC. The result is depicted in Figure 7.13. As can be observed from this figure that there were mainly six compounds including anorthite, hematite, diopside, quartz, albite and titanite, with a mass fraction of about 40%, 20%, 10%, 10%, 10% and 5% of the total minerals respectively at the initial temperature of 800 ºC. As the temperature shifted from 800 to 950 ºC, the contents of albite and titanite decreased gradually, while slag liquid and diopside showed an increasing trend. These changes were due to the solid deposition to slag and the formation of diopside, which could be described by the following reactions [332]:

$$NaAlSi_3O_8\text{ (solid)} \rightarrow SiO_2\text{(slag)} + Al_2O_3\text{(slag)} + NaAlO_2\text{ (slag)} \qquad (7.1)$$

$$CaSiTiO_5\text{ (solid)} \rightarrow CaO\text{ (slag)} + TiO_2\text{(slag)} + SiO_2\text{ (slag)} \qquad (7.2)$$

$$CaSO_4\text{ (solid)} + MgSiO_3\text{ (solid)} \rightarrow CaMgSi_2O_6\text{ (solid)} + SO_2\text{ (gas)} \qquad (7.3)$$

Increasing the temperature from 950 to 1100 ºC, all the minerals presented a constant state, which was consistent with the findings in [333]. After 1100 ºC, anorthite, diopside and quartz started to melt, and at about 1200 ºC, both of the diopside and quartz disappeared completely. Subsequently, anorthite and hematite transferred from the solid phase into slagging phase totally at 1360 and 1390 ºC, respectively. The reasons for decreasing diopside and anorthite contents were mainly attributed to the mineral deposition via the following reactions [332]:

$$CaMgSi_2O_6\text{ (solid)} \rightarrow SiO_2\text{(slag)} + CaO\text{(slag)} + MgO\text{ (slag)} \qquad (7.4)$$

$$CaAl_2Si_2O_8\text{ (solid)} \rightarrow SiO_2\text{(slag)} + Al_2O_3\text{(slag)} + CaO\text{ (slag)} \qquad (7.5)$$

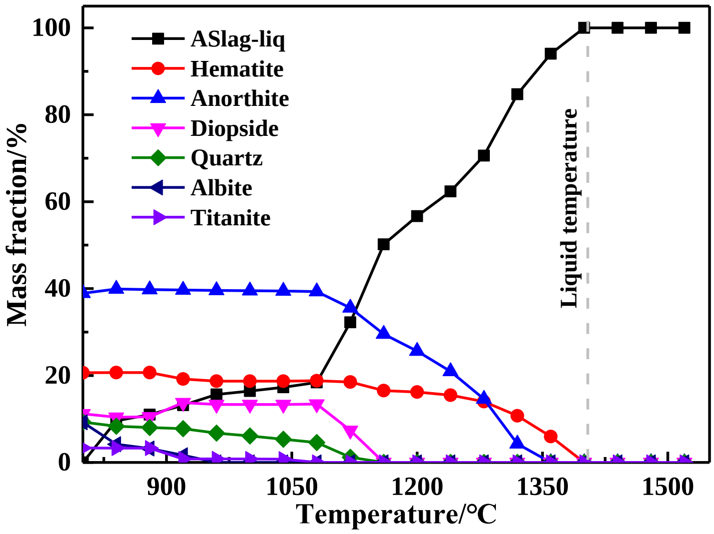

Figure 7. 13 Mineral transformation behaviour of the 90QH10FS by FactSage

7.8 Conclusions

The feasibility of co-utilization of coal and Fusion oil shale (FS) was evaluated through a few key performance indices, such as combustion characteristics and kinetics, and ash fusion behaviours. It was found that the highest ignition and burnout indexes, smallest activation energy and better ash fusion performance were obtained at FS fraction of 10 wt%, while the comprehensive combustibility index showed nearly unchanged at FS=10% compared with that of the individual coal combustion. The most substantial positive interaction during co-combustion was also observed at the 10% FS blending. Meanwhile, the increase of heating rates promoted the comprehensive combustibility index for all samples. In addition, the anorthite, hematite, diopside and quartz were identified as the main crystalline phases at high temperature at the blending ratio of 10% FS, and the major molten phase was exhibited to be anorthite, which provided a significant information about slagging properties. These findings can provide references for the justification of optimal blending ratio and reliable operation of the co-firing of coal and Fusion oil shale.

Chapter 8 Utilization of an inert oil shale semi-coke in the coal gasification under CO_2 atmosphere: thermal, kinetics and artificial neutral network investigations

8.1 Introduction

Compared with combustion, gasification can convert the solid fuels into syngas, which is subsequently used for chemical productions. As indicated previously, co-gasification of coal and oil shale semi-coke increases energy density of semi-coke as well as benefits environmental protections. It is imperative to investigate the thermal behaviours and kinetics of co-gasification of coal and oil shale semi-coke since they have significant influences on the modelling of gasification at industrial scale, whilst there is little study focusing on it based on the previous literature review.

In this chapter, co-gasification of coal, oil shale semi-coke and their blends were conducted by non-isothermal thermogravimetric analysis (TGA) under CO_2 atmosphere. The effect of heating rates and the blending ratios on the gasification characteristics were also addressed. Besides, interactions between the coal and semi-coke, and kinetics parameters using volume reaction model and shrinking core model were quantified. Moreover, the GA integrated with BPNN model (GA-BPNN) was proposed to predict the co-gasification TGA curves and a comparison of prediction accuracy between the GA-BPNN with BPNN model was presented.

8.2 TGA analysis of co-gasification

Table 8.1 shows the basic analyses results including proximate, ultimate and ash composition of the Qinghai coal (QH) and oil shale- semi-coke (SC) samples. Figure 8.2 shows the comparison of mass loss TG and DTG curves of QL, SC and their blends at 10 K/min. As can be observed from Figure 8.2, the weight losses of QH and SC are 85.7% and 19.7%, respectively. The TG curves of the blended samples are located in between the two individual lines and closer to the QH side with a similar shape as QH sample. Meanwhile, the final weight losses are 76.4% of 10 wt% SC mixing ratio and 64.8% of 30% SC mixing ratio. Besides, it is noted that TG line of SC decreases slightly after 1000 °C, demonstrating that the gasification has not been completed due to the large containment of ash. However, the TG curves for all the blends are presented to a plateau after 1000°C, indicating that coal mixture can contribute to the gasification of SC and can help to realize the full conversion of semi-coke from oil shale retorting. Clearly in Figure 8.2 (b), there are two obvious stages for all the samples. The first stage corresponds to the release of volatiles under the temperature range of 280 to 600 °C. The second stage demonstrates the CO_2 gasification of char from 620 to 1050 °C. Visually, the weight loss rate of the second stage is higher than that in the first stage, especially for the case of QH. This presents that the reactivity of QH and its blends is better than that of SC sample, which mass loss rate is less than 1 wt%/min. Besides, the DTG shapes of blends are also homologous with QH, while due to lower carbon contents, their maximum weight loss rates are observed to be less than that of QH.

Table 8. 1 Proximate, ultimate and ash composition analyses of QH and FS samples

Sample	Proximate analysis (wt.%, ar)				Ultimate analysis (wt.%, ar)						LHV (MJ/kg)
	Moisture	Fixed carbon	Volatiles	Ash	C	H	N	S	Cl	O	
QH	2.23	57.71	28.68	11.38	71.37	3.74	0.71	0.95	-	9.61	24.07
SC	0.89	12.52	7.88	78.71	18.08	1.26	0.44	0.12	-	0.5	6.06
Sample	SiO_2	Al_2O_3	CaO	Na_2O	MgO	K_2O	Fe_2O_3	MnO	SO_3	TiO_2	P_2O_5
(b) Chemical composition of ashes (wt.%)											
QH	23.12	12.5	21.57	1.15	3.43	0.08	27.83	0.25	8.09	1.13	0.29
SC	56.14	35.15	1.29	0.31	0.18	1.63	2.68	-	2.01	0.62	-

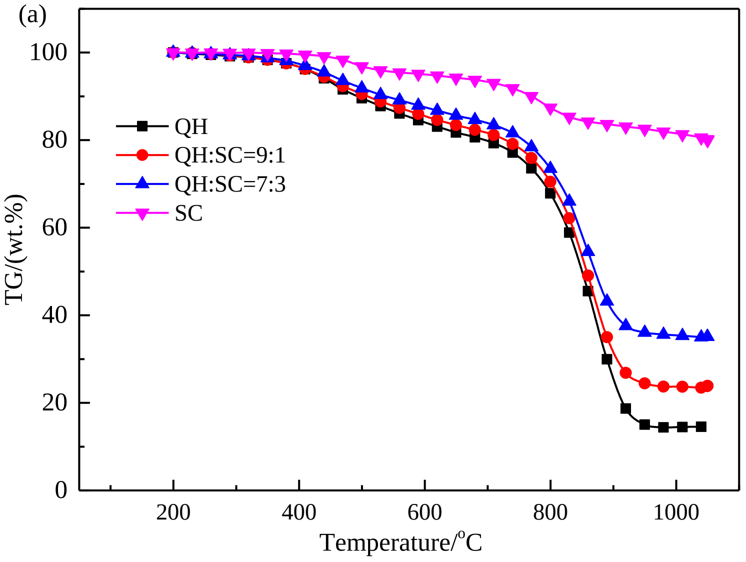

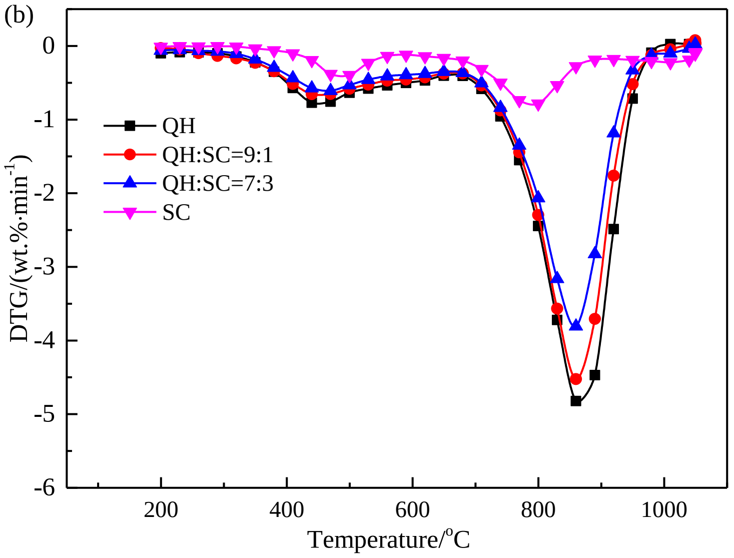

Figure 8. 1 TG and DTG curves of all the blends at 10°C/min

The gasification characteristics including maximum weight loss and its corresponding temperatures, ignition temperature, burnout temperature and comprehensive gasification index are revealed quantitatively in Table 8.2. As indicated, the starting temperatures of S1 and S2 for the SC and the blended samples are lower than that of QH, indicating that the SC is more easily to volatize and gasify. This was mainly due to the following two facts: i) the SC sample had more developed pore structure after retorting, resulting in a better volatiles emission; ii) SC sample had more content of K_2O than others based on the XRF analysis of Table 8.1. Besides, K_2O was regard as the strongest catalyst for gasification than other alkali metal oxides such as Na_2O [334], thus the starting temperature of S2 and the maximum temperature ($T_{\max}$) of SC was lower than those of other samples. However, due to the heavy containment of ash in SC, which caused a higher corresponding T_b than others, indicating that the blending is helpful for the complete conversion of SC. With the addition of

SC content, the increase of T_{i} was mainly attributed to the existence of increased ash which hindered the evaporation of volatiles. As the SC content varies from 0 to 100%, the indexes of $(\mathrm{dw/dt})_{\mathrm{max}}$, $(\mathrm{dw/dt})_{\mathrm{mean}}$, and S of samples decrease from 4.85 to 0.78 %/min, 1.12 to 0.24 %/min, and 4.48×10^{-8} to 0.11 $\times10^{-8}$ $\%^2/(°C^3 min^2)$, respectively. Although the increase of alkali metal oxide (mainly K_2O) was beneficial to the gasification as the rise of SC content, its effect could be offset or weakened by the additive SC ash, which caused the decrease of organic content in samples, leading to the decrease of $(\mathrm{dw/dt})_{\mathrm{max}}$. On the other hand, the decreased total weight loss was responsible for the $(\mathrm{dw/dt})_{\mathrm{mean}}$ reduction. It is therefore that the S value is shown to decrease.

Table 8. 2 Characteristic parameters obtained from gasification thermo gravimetric for all samples at 10 °C/min

Sample	Blending ratio	Temperature range		Weight loss		T_{i}	T_{max}	T_{b}	$(\mathrm{dw/dt})_{\mathrm{ma}}$	$(\mathrm{dw/dt})_{\mathrm{me}}$	S×10^8
		S1	S2	S1	S2	(°C)	(°C)	(°C)	(%/min)	(%/min)	$\%^2/(°C^3$ $min^2)$
QH:SC	1:0	301-589	709-1004	19.3	66.1	347.9	858.8	923.3	4.85	1.12	4.86
	9:1	288-590	677-994	17.5	58.9	360.1	860.4	918.5	4.52	0.95	3.61
	7:3	288-591	680-1017	15.6	49.2	367.6	860.9	913.5	3.78	0.8	2.45
	1:0	288-560	620-1018	4.9	14.8	418.7	797.2	1008.5	0.78	0.24	0.11

8.3 Interactions of co-gasification

The synergistic interaction during co-gasification is demonstrated by comparison of the experimental TG curves with the additively calculated TG curves based on Eq. (3.17) at different mixing ratios are stated in Figure 8.3. Besides, the $\triangle W$ variation with gasification temperature is also presented in Figure 8.3. It can be noticed that the theoretical TG curves lag slightly behind the experimental TG curves at the volatile stage as the temperature ranging from 280 to 470 °C, in which the $\triangle W$ of the blends is found to be negatively up to 0.31%, suggesting the existence of slightly positive synergetic effects. This was mainly because that SC sample contained light molecules and had relatively large pore structures, which was not only beneficial for the volatile cracking for QH sample, but also provided less resistance for the gas diffusion, leading to the enhancement of decomposition reactions. This characteristic also explains the previous narrower temperature range of stage 1 for the blends and SC than that of QH.

When the temperature is beyond 470 °C, the experimental TG curves slightly fall behind the TG_{cal} firstly, as the $0 < \triangle W < 0.6\%$ in the Figure 8.3(b), indicating slight inhibitory interactions. However, at the temperature from 850 to 890 °C for SC = 10% and 710 to 930 °C for SC = 30%, the TG_{exp} curves excess the TG_{cal} curves as demonstrated that the value of $\triangle W$ is less than zero. The maximum positive synergetic effects take place at the temperature near 870 °C with the $\triangle W$ values of -0.36% and -2.96% at the SC = 10% and 30% respectively. This temperature is approximately equivalent to the peak temperature in the above DTG curves, suggesting that the strong enhancement interactions occurred between the SC and QH at the char gasification stage. This was mainly contributed to the catalytic effect on gasification induced by alkali metals mainly K_2O contained in the SC sample, which could accelerate the carbon oxidation at this temperature region [335]. Besides, the synergetic interaction is connected with the SC content as illustrated that the ⊿W becomes smaller as the addition of SC content [199].

The TG_{exp} curves lag behind TG_{cal} curves when the temperatures are higher than 890 and 930 °C for blends of SC=10% and 30%, respectively. Meanwhile, the deviations of ⊿W are observed to be negative. The result reflects that a weakened inhibition is accompanied until the co-gasification completion. Such a phenomenon could be interpreted as the accumulation of ash hindering the CO_2 diffusion to the char surface, thus suppressive interaction was detected.

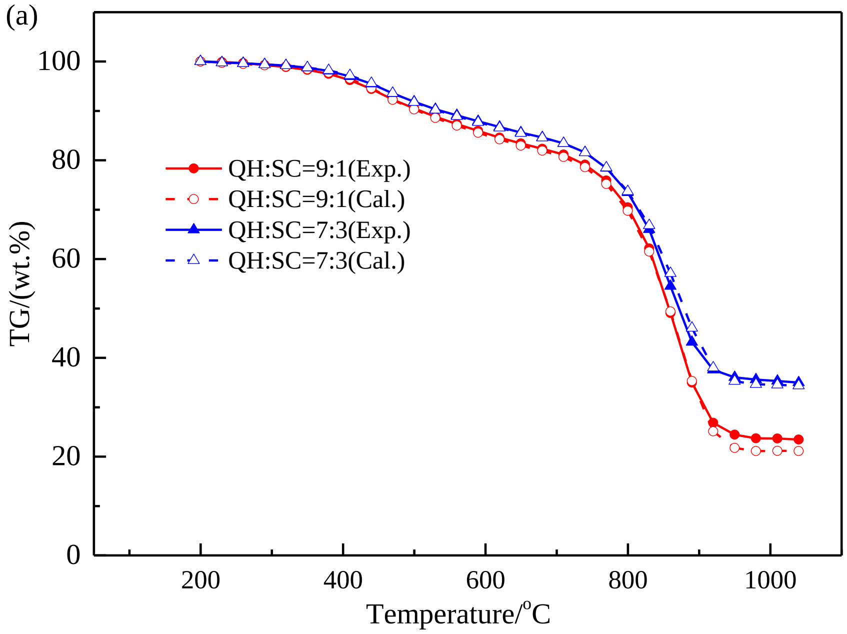

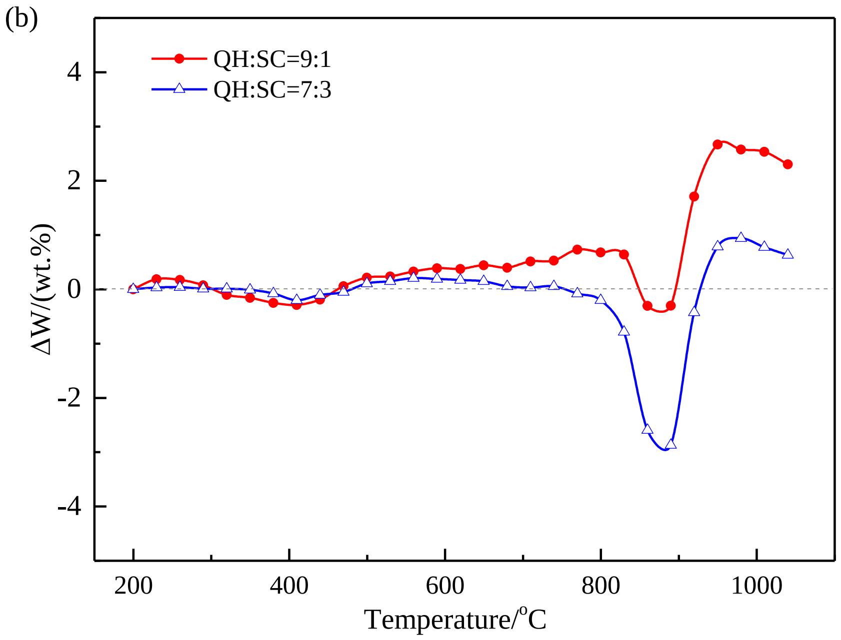

Figure 8. 2 Comparison of experimental data and calculating data for the TG curves (a) and weight difference between the experimental and theoretical values (b) for the blends of QH and SC

8.4 Effect of heating rate

The effect of heating rate of 5, 10, 15 °C/min on TG and DTG curves for the SC blending ratio of 10% sample are exhibited in Figure 8.4. Obviously, the TG profile is gradually lagged behind as the increase of heating rates. Besides, the DTG profiles are shifted to higher temperatures and temperature ranges for both stages of devolatilization and gasification are found to be wider as the increase of heating ratios based on the DTG curves. In addition, the values $(\mathrm{dw/dt})_{\mathrm{max}}$ are observed to be 2.5, 4.5 and 5.7 %/min under the corresponding the peak temperatures of 829.6, 860.4 and 877.7 °C respectively for heating rates of 5, 10, 15 °C/min. Table 8.3 details the gasification indexes for different heating rates. Both of the initial and burnout temperatures become higher impressively. Meanwhile, the comprehensive gasification characteristic indexes are calculated to increase from 1.32×10^{-8} to 6.74×10^{-8} $\%^2/(^\circ C^3 min^2)$, which reveals that the gasification performances are improved significantly. The reasons were mainly attributed to the followings: (1) at high heating rate, there was no enough time for the completion of gasification reactions, resulting in TG curves shifting to a higher temperature; (2) as the temperature gradient between the sample inner and ambient also becoming larger, a wider temperature movement was obtained in the DTG curves; (3) owing to the endothermic property of Boudouard reaction, high heating rate was able to accelerate the gasification reaction and hence higher $(\mathrm{dw/dt})_{\mathrm{max}}$ was achieved. On the other hand, the reduction of gasification time was beneficial for the improvement of$(\mathrm{dw/dt})_{\mathrm{mean}}$. Consequently, a larger *S* could be expected at a higher heating rate.

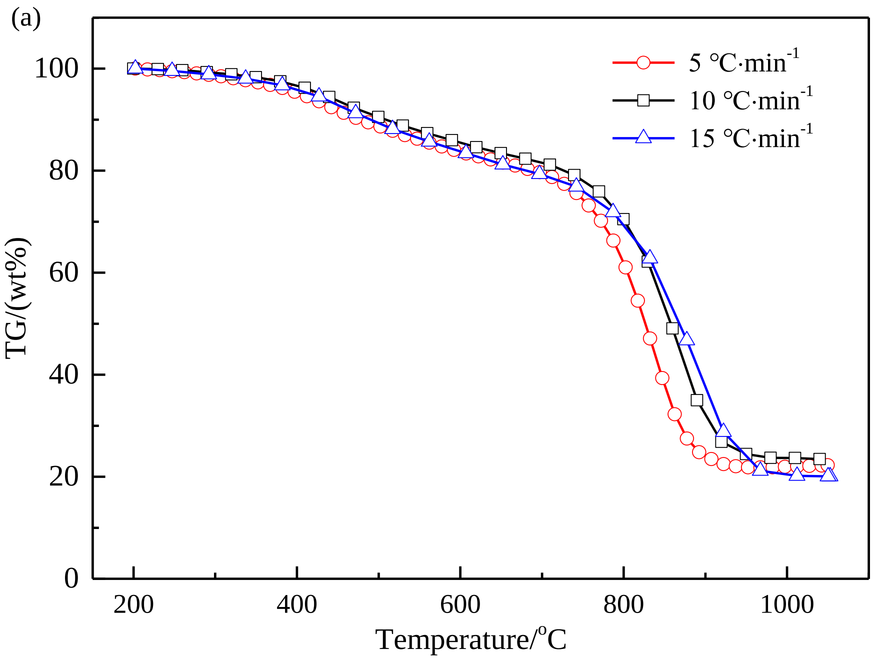

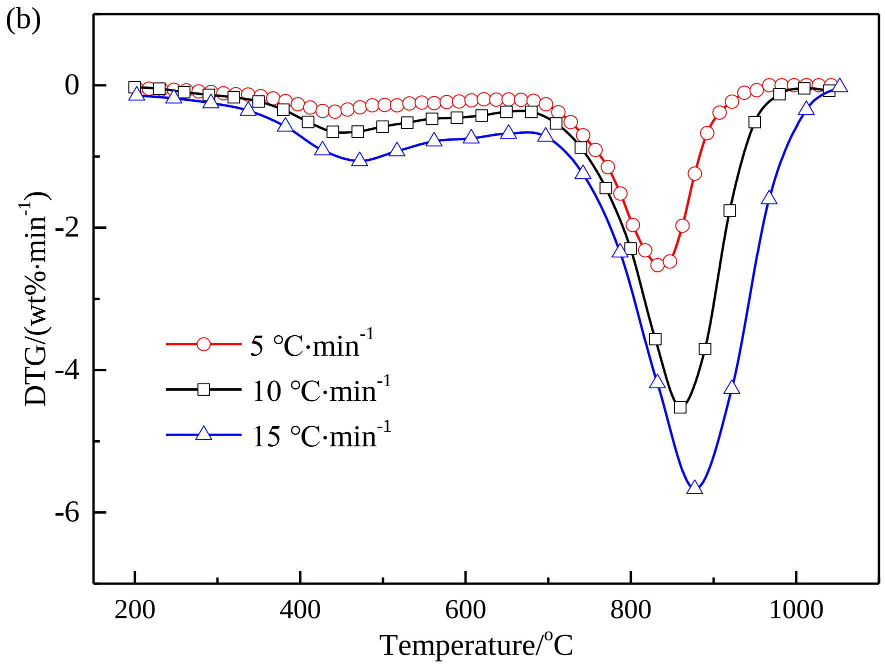

Figure 8. 3 TG and DTG profiles for the blending fraction of 10% at 5, 10, 15°C/min heating rates

Table 8. 3 Gasification characteristic indexes of sample at 5, 10, 15°C/min heating rates

Heating rate (°C/min)	T_i (°C)	T_{max} (°C)	T_b (°C)	$S\times10^8$ (%^{2}/°C^{3}min^2)
5	337.3	829.6	887.3	1.32
10	360.1	860.4	918.5	3.61
15	362.3	877.7	944.1	6.74

8.5 Artificial neutral network modelling

The effect of number of hidden neuros on the model performance indices including MSE, RMSE, MAE and MAPE is illustrated in Figure 8.5. As indicated, with hidden layer neuros increases from 2 to 9, all indices initially decrease sharply before the neuros of 4, and then decline slightly within the neuros number from 4 to 6. When the neuro number is beyond 6, all the indices are nearly unchanged under their smallest values closing zero, indicating that the ANN model presents good accuracy. Hence, the number of hidden neuron is set to be 6. The determined BPNN structure is 3-6-1 topology and is clearly presented in Figure 8.1. The modelling results and error distributions are displayed in Figure 8.6.

Figure 8.6 (a) presents the comparison of the measured data and the predicted data based on BPNN and GA-BPNN models using the test data sets. It is observed from this figure that both of the BPNN and GA-BPNN models are well agreement with the experimental values. Nevertheless, the MSE, RMSE and MAPE of BPNN model are 1.61, 1.21 and 2.23, which are higher than those of GA-BPNN model with 0.61, 0.77 and 1.44, respectively. The results indicate that the GA-BPNN model is more robust and reliable in predicting of TG loss curves than the BPNN model. Figure 8.6 (b) shows the variation of fitness along with the genetic iterations based on GA-BPNN model. The fitness is the sum of the errors between the numerical outputs and experimental outputs during the ANN training process. It is noticed that the fitness value decrease with the increase of genetic iterations and at the iteration of 47, the fitness reaches the minimum value, which suggest that the weights and biases of ANN are optimized. The fitting results of the BPNN for the TG curves at different heating rates are illustrated in Figure 8.6(c). Error histogram of the previous predicted TG curves at various heating ratios is presented in Figure 8.6 (d). The errors are distributed around zero with the mean value of 0.13. Therefore, the proposed GA-BPNN has a smaller error and is more suitable for the prediction of TG curves.

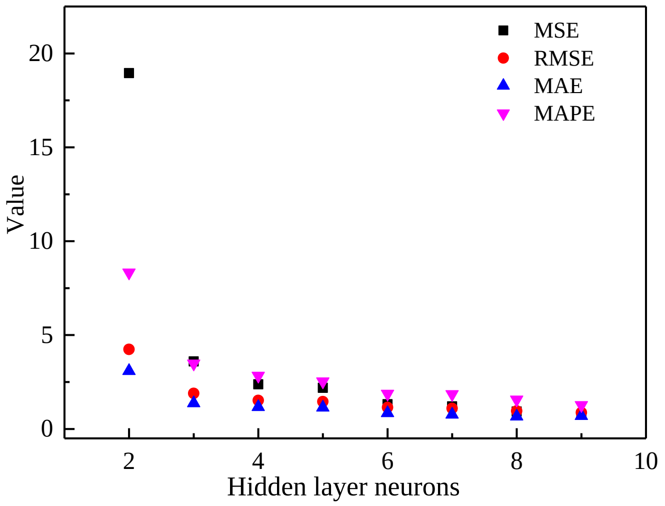

Figure 8. 4 Variation of MSE, RMSE, MAE and MAPE with the hidden layer neurons

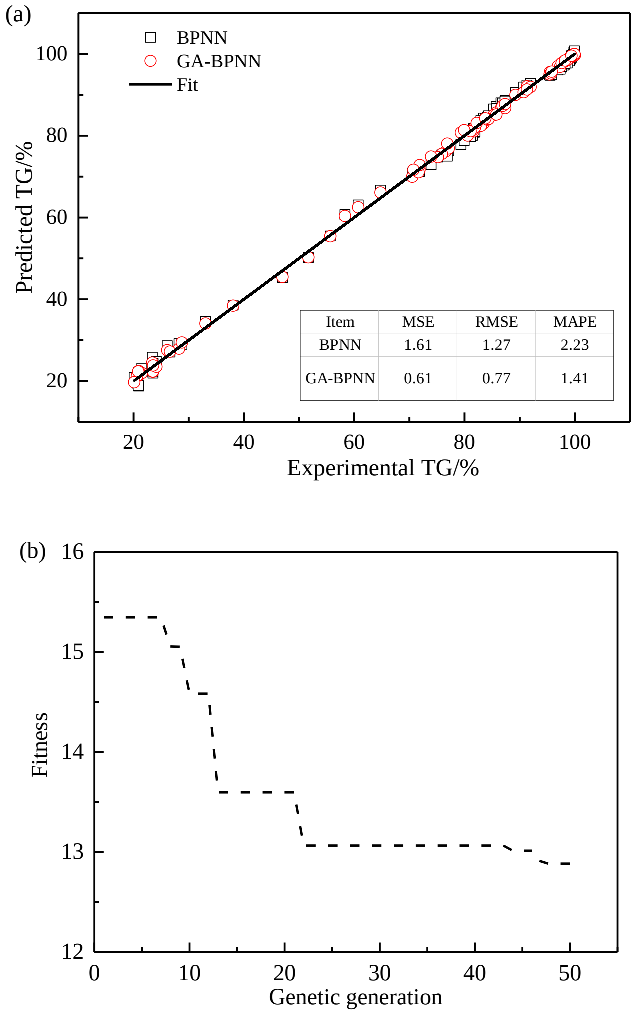

Item	MSE	RMSE	MAPE
BPNN	1.61	1.27	2.23
GA-BPNN	0.61	0.77	1.41

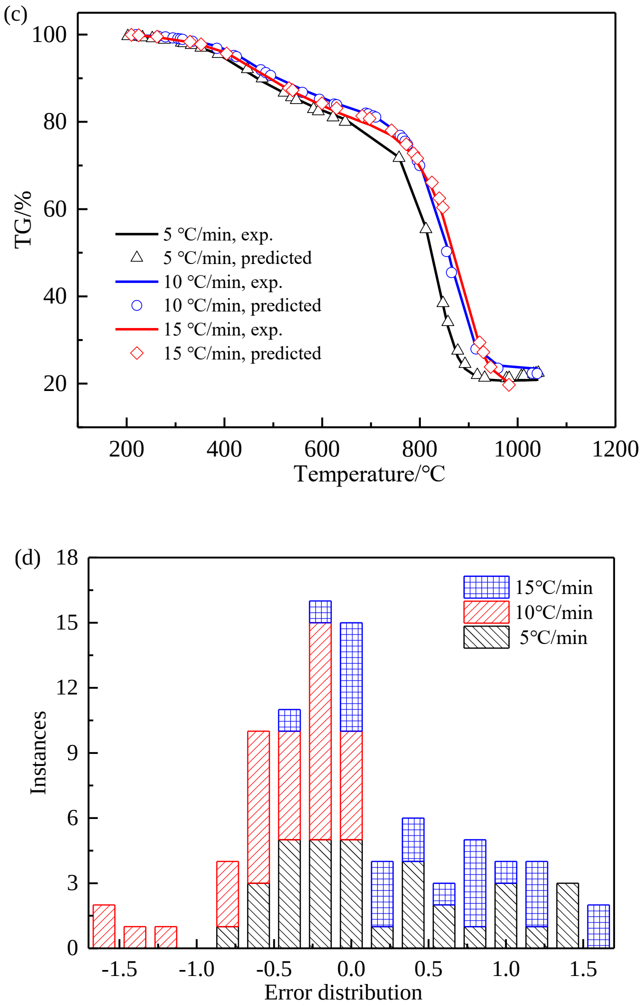

Figure 8. 5 (a) Comparison between the experimental TG data with the predicted TG data using BPNN and GA-BPNN models respectively; (b) Fitness curve as a function of genetic iteration; (c) TG curves as a function of temperature using experiment and GA-BPNN methods for different heating rates; (d) Error histogram plot for the test data based on the GA-BPNN model

8.6 Kinetic analysis

The evaluation of kinetic parameters can be obtained by the reciprocal relationship between the $\ln[g(x)/T^2]$ and the $1/T$ of each gasification stage using the VM and SCM models for all the samples at the heating rate of 10 K/min, the plots are presented in Figure 8.7. As can be observed from this figure, the lines of the VM and SCM models of stage 1 are nearly parallel for each sample and the coefficient of determinations (R^2) of stage 1 by each model are the same with their values being beyond 0.97, indicating that the fittings are well matched and their activation energy values from the two models are approximately equivalent. On the other side, for stage 2, the slopes obtained from the VM model are slightly higher than those from the SCM model. Nevertheless, the SCM model fits better than the VM model, especially for the case of QH, because it has the highest R^2 value. Hence, the activation energy (E_a) and pre-exponential factor (A) can be computed for all the samples on the basis of the SCM using the fitted slopes and intersection values, and are listed in Table 8.4.

From Table 8.4, it can be seen that the activation energy for the QH coal at the first stage is 32.96 kJ/mol, which is much smaller than that of the SC with its activation energy reached 67.36 kJ/mol. However, in respect to mixtures, at the blending ratios of 10 wt% and 30 w% SC sample, their activation energies are around 31.95 and 32.55 kJ/mol respectively, slightly lower than that of the QH coal. As shown in Figure 8.3, there is a promoting interaction within the temperature range of stage 1, resulting in the accelerative impact on the volatiles decomposition. With regard to the char gasification stage, the QH coal has largest activation energy, followed by the QH/SC blends at the ratios of 9:1 and 7:3, the least activation energy belongs to the SC sample of 38.04 kJ/mol. This was due to the catalytic contributions originated from the alkali oxides in the SC sample, the promoting interactions were occurred and hence the activation energy decreased as the addition of SC. On the other side, the activation energies of stage 1 are lower than those of stage 2 except for the SC case. This was mainly attributed to the light volatiles which are more easily to decompose. The above findings suggest that the blending of SC is beneficial for the coal gasification and it has considerable potential as a fuel.

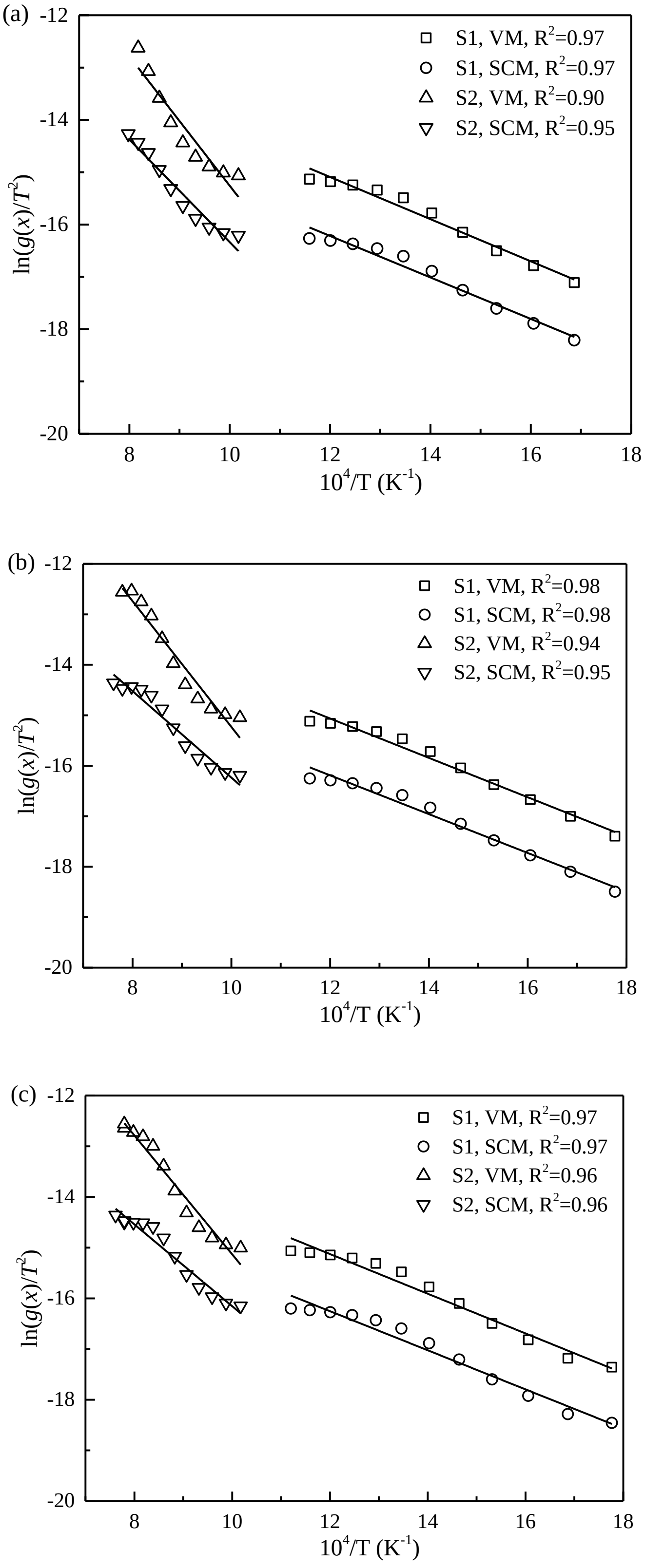

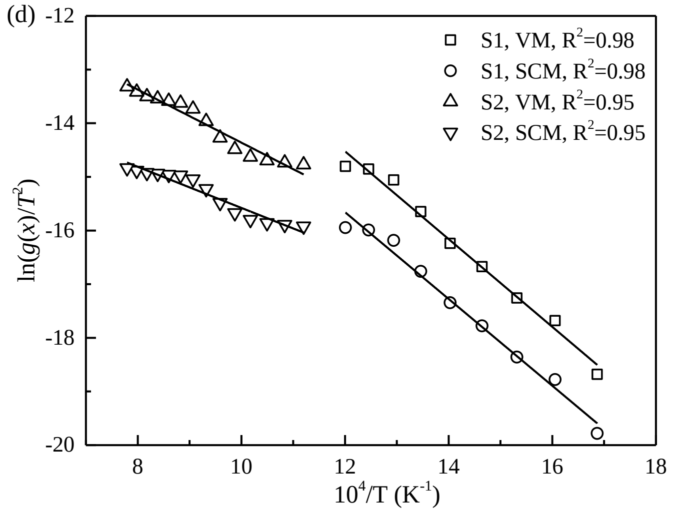

Figure 8. 6 Plots of ln[g(x)/T^2] against 1/T with two different models of VM and SCM at the heating rates of 10K/min for the samples of (a) QH; (b) 10% SC mixture; (c)30% SC and (d) SC

Table 8. 4 Summary of kinetic parameters for the all blending samples based on SCM model at heating rate of 10 °C/min

Blending ratio	S1		S2	
	E(kJ/mol)	*A*(min^{-1})	*E*(kJ/mol)	*A*(min^{-1})
1:0	32.96	0.67	81.54	186.1
9:1	31.95	0.57	71.24	54.6
7:3	32.55	1.15	67.07	34.33
1:0	67.36	283.4	38.04	1.56

It can also be noticed from Table 8.4 that the E_a and the pre-exponential factor *A* vary toward the same direction, which is recognized as “compensation effect”. This compensational behaviour can be described quantitatively using a linear correlation derived from Arrhenius equation as:

$$lnA = -\frac{E_a}{RT} + \ln(k) = a \times E_a + b \tag{8.1}$$

Figure 8.8 shows the relationship between ln$A$ and E_a using the values from Table 8.4. Clearly, well satisfactory fittings for the respective stages were achieved. The following expressions are derived for the S1 and S2 respectively:

$$lnA = 0.17E_a - 5.8, R^2 = 0.99 \tag{8.2}$$

$$lnA = 0.11E_a - 3.7, R^2 = 1 \tag{8.3}$$

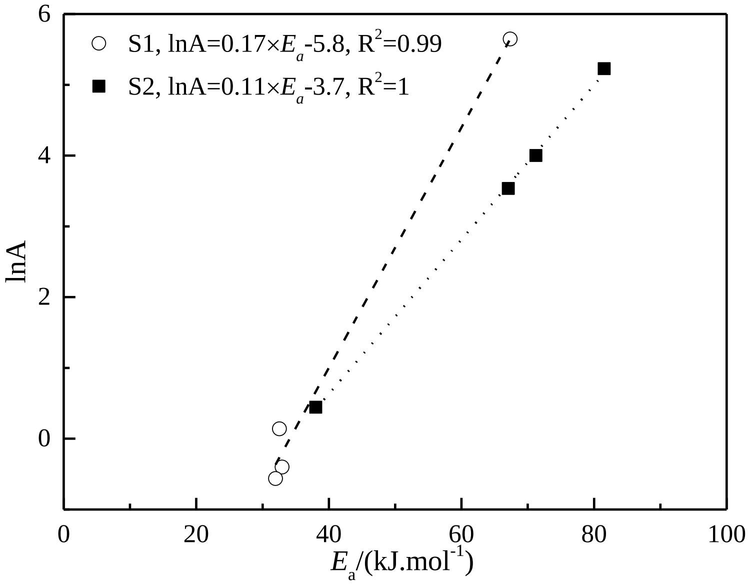

Figure 8. 7 Plot of ln$A$ versus E_a for the demonstration of compensation effect

Although the addition of semi coke is beneficial for the gasification performances, the impact on ash fusion and cannot be ignored. Using the empirical indices such as base to acid ratio ($R_{B/A}$) and fouling index (F_u) referred in [30, 256, 257], the slag and fouling propensities can be determined. Figure 8.9 shows the calculated slagging and fouling indexes based on the metal oxide contents as displayed in Table 8.1. As shown in this figure, the $R_{B/A}$ and F_u values for QH sample are 1.47 and 1.81, which are classified into the high slagging and fouling inclinations, while for the SC case, their index values are calculated to be 0.07 and 0.13 respectively, suggesting the least slagging and fouling propensities. The blending of SC into the QH coal help to reduce the $R_{B/A}$ and F_u, as their values decrease separately about 63% and 53% at the 10 wt% SC blending ratio and approximately 84% and 77% for the case of 30 wt% SC sample. These results reflect that the mixture of SC can solve the severely ash-related slagging and fouling problems and the blending fuels are more suitable for gasification.

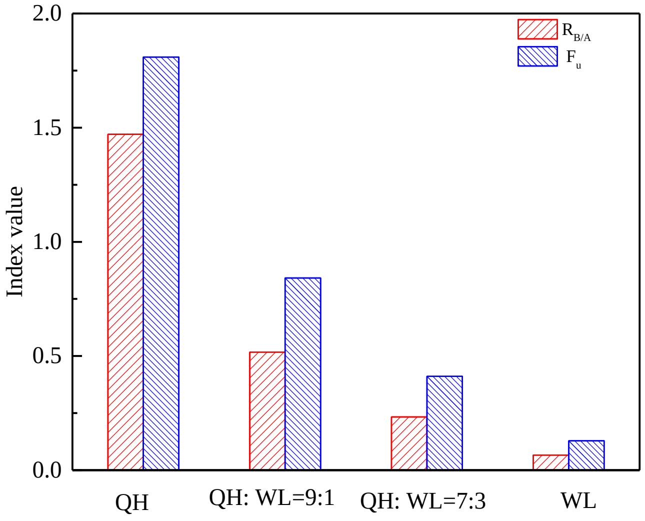

Figure 8. 8 Variation of $R_{B/A}$ and F_u for different samples

8.7 Conclusions

In this work, co-gasification of QH and SC from shale oil was investigated using TGA and GA-BPNN model. The main conclusions are shown as follows.

(1) The gasification for all samples experienced two distinct stages: volatile release at the temperature < 590 °C and the char gasification when temperature >620 °C. The mixture of SC content in coal decreased the comprehensive gasification characteristic index (S), while the addition of heating rate was beneficial for the improvement of gasification

performances.

(2) The promoting interactions were existed in the both pyrolysis stage and char gasification stages. However, the inhibitory interaction was detected at the end of char gasification stage due to the increase of ash content.

(3) The best layer topology was determined to be 3×6×1 for the ANN model. The GA-BPNN model had a better performance to predict the thermogravimetric experimental data than BPNN model because the GA-BPNN model had less MSE and RMSE closing to zero.

(4) Both VM and SCM models were employed to calculate the activation energies of all samples under the heating rate of 10K/min. The SCM model were detected to be more excellent in fitting the experimental points for both pyrolysis and char gasification stages based on the R^2 values of beyond 0.95. The activation energies of blend were smaller than the pure QH coal.

Chapter 9 Exergetic, economic and carbon emission studies of bio-olefin production via indirect steam gasification process*

9.1 Introduction

To realize the goal of the Paris Agreement on climate change that the increase of global temperature is within 2 ºC by the end of this century, and reach the pledges of China that the carbon intensity decreases by 60 to 65% and the non-fossil energy increases to 20% by the same time, development of carbon-negative process is required [336]. Biomass is a carbon-neutral organic material principally deriving from plants, and the introduction of biomass to partial or complete replacement of coal in power generation is a most promising carbon mitigation option since the large availability of biomass. Hence, in this thesis, the use of biomass as the feedstock for gasification is also carried out.

Considering the increasing demand of light olefins, design a biomass gasification to olefins process can contribute to the decarbonisation of traditional olefins production through steam cracking of naphtha. Several investigations have employed a O_2/steam-blown biomass fluidized-bed gasifier to generate syngas and

---

* This chapter has been published in the Energy.

subsequently used for methanol and olefins productions. Another biomass gasification scheme, i.e., indirect biomass steam gasification, can be potentially used for syngas production with high hydrogen to carbon monoxide ratio, which is more suitable for methanol and olefins synthesis. Nevertheless, the systematic energy, economic and environmental investigations of indirect biomass steam gasification have not been reported.

In this chapter, a biomass indirect steam gasification to olefins via methanol with CO_2 utilization (IDBTO) process was proposed and developed using Aspen Plus^{TM}. Besides, the performance of the proposed route has been evaluated in terms of olefins yield, energy and exergy efficiencies and later systematically compared with the direct oxygen-steam based biomass gasification to olefins (DBTO) process. In addition, the effects of some important parameters, such as unreacted gas recycle ratio and CO_2 to dry biomass mass ratio, on thermodynamic performance were also discussed. Moreover, life cycle CO_2 emission and economic evaluations of these two cases were performed in this work.

9.2 Process description and simulation

The schematic diagrams of direct oxygen-steam based biomass gasification (DBTO) and biomass indirect steam gasification to olefins process (IDBTO) are shown in Figure 9.1 (a) and Figure 9.1 (b), respectively. As seen in Figure 9.1, the production of olefins process using biomass as feedstock mainly consists of three parts, namely, bio-syngas generation, methanol synthesis and purification, olefins synthesis and separation. The major difference between the two processes lies in the syngas generation strategy. It can be seen in Figure 9.1, the DBTO process uses steam and O_2 as the gasifying agents and biomass is gasified under pressurized fluidized-bed reactor combined with a catalytic reforming unit to convert the long carbon chain hydrocarbon into syngas, while the IDBTO process comprises a biomass steam gasifier interconnected with a combustor providing heat that is required by the gasification. The main beneficial features of IDBTO process are the avoidance of energy-intensive and high-priced air separation unit (ASU) and water gas shift (WGS) unit [337]. The outlet gas composition from the biomass steam gasifier contains less heavy hydrocarbons due to the use of steam [338]. Besides, the suitable H_2/CO ratio for methanol synthesis is desired by the consideration of CO_2, which is readily from AGR unit, as the gasifying agent. Methanol is produced and purified (99.5w%) in the methanol synthesis and purification subsystem. Olefins synthesis and separation subsystem utilizes methanol to produce olefins in the DMTO reactor and separate the olefins mixture into polymer-grade ethylene and propylene. The detailed subsystem descriptions and simulations are illustrated in the following sections.

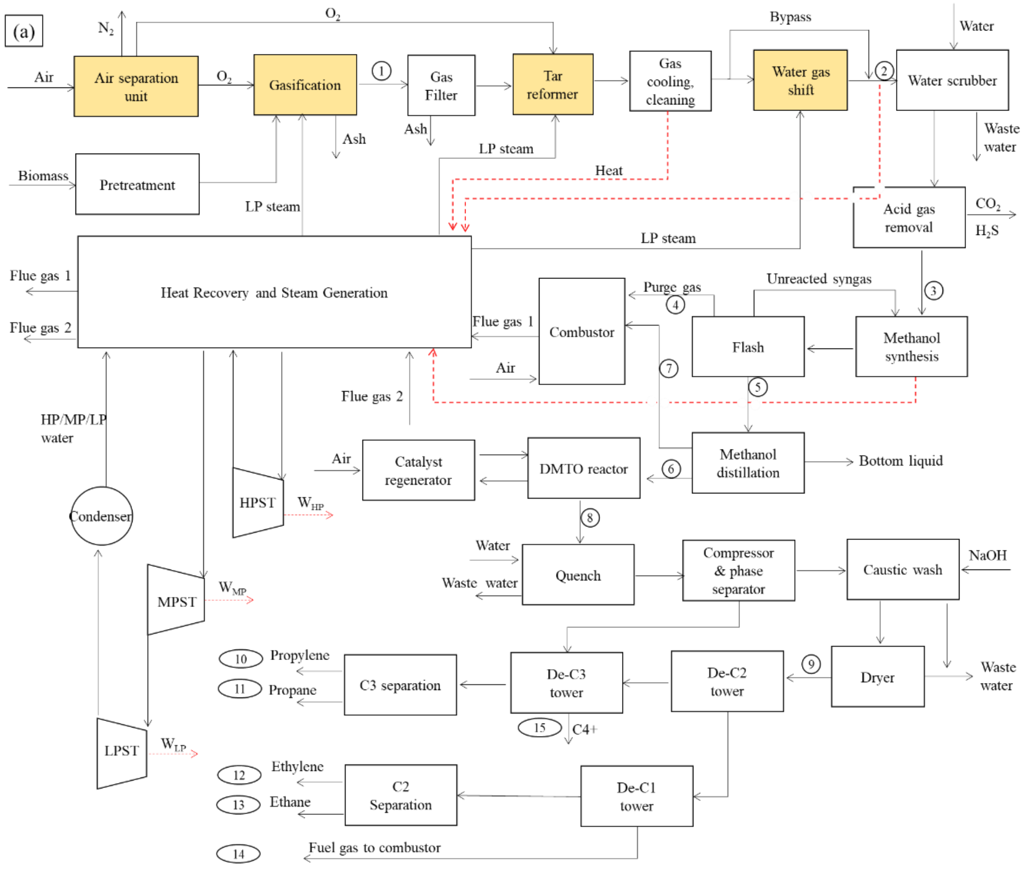

(a)
N_2
O_2
Bypass
Water
Air
Air separation unit
O_2
Gasification
①
Gas Filter
Tar reformer
Gas cooling, cleaning
Water gas shift
②
Water scrubber
Ash
Ash
LP steam
Waste water
Biomass
Pretreatment
Heat
LP steam
Acid gas removal
CO_2
H_2S
LP steam
Flue gas 1
Heat Recovery and Steam Generation
Flue gas 2
Purge gas
④
Unreacted syngas
③
Flue gas 1
Combustor
Flash
Methanol synthesis
Air
⑦
⑤
Flue gas 2
HP/MP/LP water
Air
Catalyst regenerator
DMTO reactor
⑥
Methanol distillation
Bottom liquid
HPST
W_{HP}
Condenser
⑧
Water
Quench
Compressor & phase separator
Caustic wash
NaOH
Waste water
MPST
W_{MP}
10
Propylene
11
Propane
C3 separation
De-C3 tower
De-C2 tower
⑨
Dryer
Waste water
15
C4+
LPST
W_{LP}
12
Ethylene
13
Ethane
C2 Separation
De-C1 tower
14
Fuel gas to combustor

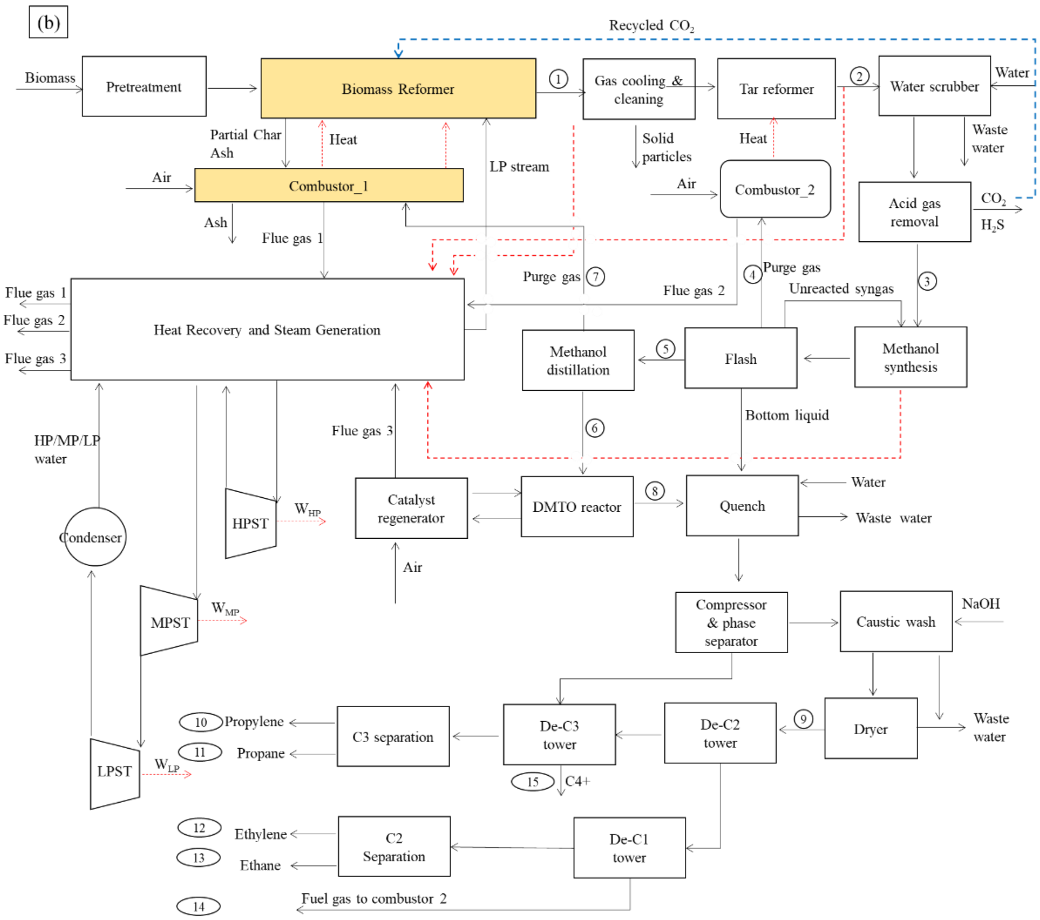

Figure 9. 1 Schematic diagram of the biomass to olefins process based on: (a) DBTO; (b) IDBTO

9.2.1 Bio-syngas generation

The feedstock considered in this study was wood chip. The ultimate and proximate analysis data are listed in Table 9.1 [339]. In DBTO process, the dried wood chips were fed into the fluidized-bed gasifier at an elevated pressure of 0.5 MPa via lock-hoppers. The gasification medium (mixture of steam and oxygen) was injected to realize the conversion of fuel into CO, H_2, CO_2, CH_4, and small portion of heavier hydrocarbons and tars. The use of oxygen made it possible to the avoidance of nitrogen dilution and also had the advantage of auto-thermal operation [340]. The requirement of oxygen for gasification was from air separation unit where the separated oxygen had the purity of 99%. The raw syngas generated from gasifier after the fly ash separation in a hot gas filter was sent to an autothermal tar reforming unit where most of tar and high hydrocarbons were catalytically cracked into CO and H_2 accompanied by oxygen and steam at a temperature of approximately 860 °C [341, 342]. After that, the syngas was cooled and fed into a wet scrubber and a sulfur guard bed (ZnO bed) to eliminate other particles and Sulphur. The clean syngas had the H_2/CO molar ratio about 1.44. To reach the desired H_2/CO ratio (equal 2.05-2.1) of methanol synthesis, the cooling syngas was partly directed to the adiabatic water gas shift reactor (WGSR), where CO and H_2O were converted into H_2 and CO_2, while the remaining syngas was bypassed [48, 343]. The waste heat generated in the gasification and cooling units was recovered in the heat recovery and steam generation (HRSG) unit as shown in Figure 9.1.

Table 9. 1 Ultimate and proximate analysis of the wood chip

Ultimate analysis (wt%, dry basis)		Proximate analysis (wt%)	
C	50.7	Moisture	6.9
H	6.2	Volatile	83.3
N	0.1	Fixed carbon	16.5
S	0.01	Ash	0.2
O (by difference)	42.8	HHV(MJ/kg)	20.6

The simulation strategy for the biomass direct gasification unit was adopted from the concept detailed elsewhere [339, 344]. The RYield and RGibbs modules were employed to simulate biomass decomposition and gasification, respectively [345]. Tar (*i.e.*, $C_{10}H_8$) catalytic reforming unit was modelled using a RGibbs module which converted tar and high hydrocarbons into CO and H_2. However, complete accomplishment of the chemical equilibrium in the tar reformer could not be achieved. To address the problem, conversions of hydrocarbon were adjusted according to the work in [346, 347], and these correlations were embedded into Aspen Plus^{TM} as a Fortran subroutine. For the simulation of WGS reaction, the REquil model was considered with a temperature approach of 10 ºC [348]. The simulated wet syngas compositions from gasifier in comparison with the experimental data are presented in Figure 9.2 (a). It is confirmed that the simulation values agreed well with the experimental data, indicating the accuracy of the built model.

However, for the proposed scheme in Figure 9.1(b), the biomass steam gasification took place in a fluidized bed reactor. The heat for endothermic gasification reactions was supplied by the combustion of char and the purge gas from methanol distillation. Sand was circulated as the heat carrier between the biomass reformer and combustor via a loop seal [349]. The biomass steam reforming could produce hydrogen-rich syngas without being diluted by nitrogen [350]. In addition, the biomass reformer and combustor operated at near-atmospheric pressure and eventually achieved a higher carbon conversion efficiency, higher mass and heat transfer and low tar level [338, 351]. Typically, at the gasification temperature of about 850 °C and steam to biomass mass ratio (STBR) of 0.75, the syngas from the gasifier produced a H_2/CO ratio of 2.3. However, by adding CO_2 as the gasification agent, the H_2/CO ratio at the outlet of tar reformer could be adjusted close to 2.05-2.1 and the methane content of raw syngas from gasifier decreased as well, which was suitable for methanol synthesis [352]. This aspect would be discussed extensively in Section 9.3. The raw sygas from the cyclone in the gasifier was routed to a catalytic tar cracker, which comprised a reformer and a catalyst regenerator. In the reformer, hydrocarbons and tars were reacted with steam and reformed to syngas in the presence of catalyst (Ni/Mg/K supported by Al_2O_3) in a circulating fluidized bed reactor [353]. Then, the spent catalyst was regenerated in the tar catalyst regenerator. The heat for the tar reformer was provided by combusting the purge gas from methanol flash unit along with fuel gas from De-C1 tower in the regenerator. As can be seen from Figure 9.1, compared with DBTO process, the WGS and ASU systems were avoided in IDBTO that would reduce total cost and shorten process route.

The simulation of the biomass indirect steam gasification was carried out by the Ryield and RGibbs modules. Char (*i.e.*, carbon) combustion was simulated using RGibbs block. The biomass steam gasifier temperature was kept lower than the combustion temperature by 50°C to ensure efficient heat transfer. The carbon conversion in the biomass gasifier was assumed to be 70% [354], the residual char was directed to combustor. Both the methane steam reforming and water gas shift reactions in the biomass gasifier were restricted by inputting temperature approaches of -265 °C and -90 °C, respectively [293, 355]. The biomass steam gasification model was validated by comparing the outlet syngas composition between literature values and simulation values, as shown in Figure 9.2(b). As indicated, the deviation is less than 2 %, which proves the validity of model [356].

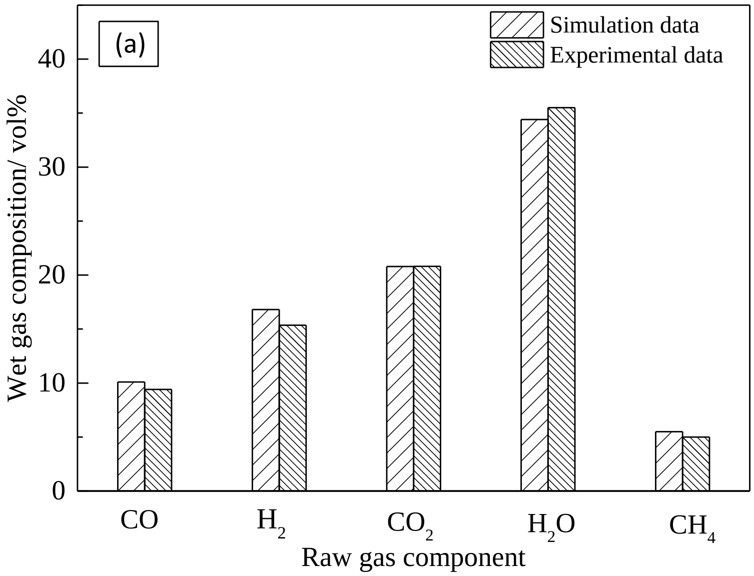

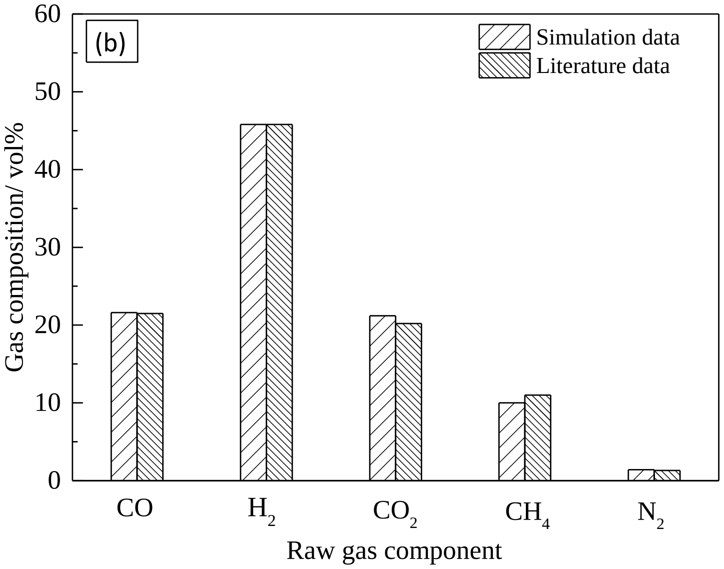

Figure 9. 2 Comparison of the outlet syngas composition between simulation data and the experimental/literature data. (a) DBTO process, $T_{Gasifier}$=823 °C, STBR=0.5, and oxygen to fuel ratio of 0.31 [339]. (b) IDBTO process, $T_{Gasifier}$=850 °C and STBR=0.75 [356]

9.2.2 Methanol synthesis and purification

The readily syngas from WGSR or tar reformer was cooled down and scrubbed with water to remove particulates, ammonia and halides, etc. The clean syngas was then compressed to 2.0 MPa in a three-stage centrifugal compressor before it was decarbonized in the Rectisol-based unit using methanol solvent. Approximately 90% CO_2 in the feed gas was removed to achieve the molar ratio of $(H_2\text{-}CO_2)/(CO_2+CO) = 2.03$ and $H_2/(2CO+3CO_2) = 1$ in the purified syngas [357, 358]. For the IDBTO process, a stream of captured CO_2 was recycled to the biomass reformer as a gasifying agent to realize the CO_2 utilization. After the CO_2 removal, the pure syngas was compressed to the desired operating pressure (8.0 MPa) and introduced to methanol reactor, where methanol was synthetized over a commercial catalyst of $Cu/ZnO/Al_2O_3$. The main reactions for methanol are presented as below [359]:

$$CO+2H_2 \rightarrow CH_3OH,\ \triangle H_{25\,^{o}C}=-90.9kJ/mol \tag{9.1}$$

$$CO_2+3H_2 \rightarrow CH_3OH+H_2O,\ \triangle H_{25\,^{o}C}=-50.1kJ/mol \tag{9.2}$$

As seen from Eqs.(9.1) and (9.2) that the methanol reactions are exothermic, so heat must be removed from the reactors simultaneously to maintain the operating temperature at 260 ºC [39]. The product gas was cooled down and the unreacted gas was separated from the raw methanol in the flash unit. Then, a large portion of unreacted gas was recompressed to 8.0 MPa and recycled to the methanol reactor to enhance the methanol yield and the remaining was purged to combustors. Here, the Lurgi synthesis reactor was used and simulated using REquil block with a temperature approach of 10 ºC [360]. Raw methanol from the flash tank was transferred to a stripper and followed by a distillation column to purify the methanol to an extent of 99.5 wt% purity [361]. Both the methanol stripper and distillation column were simulated using RadFrac block and the methanol recovery was specified to 99.8%. To validate the methanol unit, the inlet syngas composition, temperature and pressure a methanol reactor was taken as the reference [362]. The comparison of the outlet gas from methanol reactor between the predicted value and literature value as shown in Table 9.2. It is clear that the model value agrees well with the literature data, demonstrating that the built model was reliable and could be employed for the simulation.

Table 9. 2 Comparison between the simulation value and literature value

Composition (mole frac)	CO	H_2	CO_2	H_2O	CH_4O
Model predicted value	0.075	0.472	0.101	0.009	0.344
Literature value [362]	0.073	0.473	0.102	0.007	0.343

9.2.3 Olefins synthesis and separation

The methanol product from the top of methanol distillation tower was pumped and superheated before it was sent to the turbulent fluidized bed MTO reactor. DMTO technology developed by Dalian Institute of Chemical Physics was considered in olefins production unit due to its high methanol conversion (99.8%) and high ethane and propene selectivity (80%) [44]. Besides, the ethane to propene ratio could be adjusted in the range of 0.8 to 1.2 by varying operating conditions [44]. SAPO-34 catalyst was used as the catalytic medium for the olefins production owing to its excellent catalytic performance and high thermal stability [363]. Coked catalyst was burned in the regenerator at a temperature of 600 °C and recycled to DMTO reactor, while the flue gas was routed to HRSG to recover heat. The main reactions that occurred in the reactor are shown as below [364, 365]:

$$2CH_3OH \rightarrow C_2H_4+2H_2O,\ \triangle H_{25\ ^oC}=-23.1\ kJ/mol \quad (9.3)$$

$$3CH_3OH \rightarrow C_3H_6+3H_2O,\ \triangle H_{25\ ^oC}=-92.9\ kJ/mol \quad (9.4)$$

$$4CH_3OH \rightarrow C_4H_8+4H_2O,\ \triangle H_{25\ ^oC}=-150.0\ kJ/mol \quad (9.5)$$

The DMTO reactor effluent was cooled down and entered to the water-quench column. Afterwards, the vapor gas from the quench tower was compressed to 2.5 MPa and directed to the caustic wash tower for CO_2 removal. The remaining gas was fed to a molecular sieve dryer before it was sent to the olefins separation units. The water-free gas was firstly fed into de-ethaniser (De-C2) to separate methane, ethylene, ethane and other light gases from propylene and other heavier components. The overhead light components were then injected into de-methaniser (De-C1) column where methane-rich fuel gas was separated from the mixture of ethane and ethylene. Subsequently, the overhead fuel gas was directly sent to combustion chamber followed by heat recovery in HRSG. The bottom product from De-C1 was further distillated in the C2 separation column, in which polymer-grade ethylene component with a molar purity of 99.9% was obtained at the overhead stream [366]. The bottom stream from De-C2 was directed to the de-propaniser (De-C3) to split propylene and propane from heavy hydrocarbons such as butylene and pentane (C4+). To obtain polymer-grade propylene (molar purity of 99% [366]), the overhead product from De-C3 was sent to the C3 separation column to recover the propylene at the top. In this study, the desire olefins were ethylene and propylene.

For the modelling of DMTO reactor, the RYield module in Aspen Plus with a specified mass yield of each component was utilized [39]. The catalytic regenerator was simulated using a RStoic reactor [39]. The mass yield distributions of the DMTO reactor at the temperature of 490 ºC and 0.22 MPa were calculated according to [367] and tabulated as Table 9.3. Water quench tower and olefins separation columns were simulated using the RadFrac block. Table 9.4 shows the main design parameters and assumptions during the simulation of the above two processes [296, 364, 366, 368].

Table 9. 3 Mass yield of each component from the DMTO reactor

Component	wt%
H_2+CH_4	0.84
CO_x	0.12
H_2O	56.2
CH_3OH	0.1
DME	0.08
C_2H_6	0.34
C_2H_4	17.26
C_3H_8	1.12
C_3H_6	16.76
C_4H_{10}	0.18

C_4H_8	4.09
C_5H_{10}	1.21
Coke	1.36

Table 9. 4 Simulation assumption and operation conditions for the main components

Item	Operation conditions
Fuel	Wood chip Mass rate: 5 kg/s
Air separation unit	Oxygen purity: 99 vol% power consumption: 325kWh/ton O_2 delivery pressure: 0.55 MPa
Pressurized steam /O_2 gasifier	Gasification pressure: 0.5 MPa Oxygen to fuel mass ratio: 0.42 Steam to fuel mass ratio (STBR): 0.54 Heat loss: 1% HHV of feed fuel
Biomass steam reformer and combustor	Steam to fuel mass ratio (STBR): 0.75 CO_2 to fuel mass ratio: 0.143 Operation pressure: 0.15 MPa Air molar excess ratio in combustor: 1.2
Tar reformer	For DBTO: autothermal reforming using oxygen and steam. Mole conversion: CH_4=0.2247T-127.36%; C_2H_2

	= 0.8439T-634.66%; C_2H_4=0.3818T-237.31%; C_2H_6 = 0.2753T-143.5%; C_3H_8=100%; C_6H_6 = 0.1875T-76.532%; $C_{10}H_8$=94.6%; NH_3 = 1.0679T-899.25%; T = reformer outlet temperature [°C] For IDBTO: steam reforming in a circulating fluidized bed Mole conversion: CH_4 = 80%; C_2H_6 = 99%; C_2H_4 = 90%; $C_{10}H_8$ = 99.9%; C_6H_6 = 99%; NH_3 = 90%
Water gas shift reactor	Adiabatic reactor Steam to CO molar ratio: 2 Equilibrium temperature approach: 10 °C Split ratio for the WGS: adjust the split ratio using Fortran code in the calculator to reach the H_2/CO molar ratio of 2.1 in mixture gas at the outlet of WGSR Operation pressure: 0.4 MPa
Acid gas removal	Rectisol CO_2 removal technology CO_2 molar fraction after absorption: 3% Refrigeration work: 0.55 kWh/kmol CO_2 removed Utility electricity: 0.53 kWh/kmol CO_2 removed
Methanol synthesis reactor	Temperature: 260 °C Pressure: 8.0 MPa

Methanol separation	Stripper model: RadFrac, 10 stages, partial vapor condenser, reflux ratio: 1.6, B/F=0.91, operation pressure: 0.45 MPa Methanol distillation column: 30 stages, total condenser, reflux ratio:0.73, D/F=0.964, operation pressure: 0.4 MPa, methanol purity: > 99.5% (wt)
MTO reactor	DMTO technology Operation temperature: 490 °C Operation pressure: 0.22 MPa
Olefins separation	Ethylene molar purity: 99.9% Propylene molar purity: 99% Cooling work consumption: 62 kJ/kg methanol
Purge gas/Fuel gas combustor	Combustion temperature 950 °C
Heat recovery steam generation	High pressure steam: 12.0 MPa Medium pressure steam: 3.4 MPa Low pressure steam: 0.6 MPa Condenser pressure: 0.005 MPa Reheated temperature: 540 °C
Compressors and steam turbines	Isotropic efficiency: 0.88 Mechanical efficiency: 0.99

9.3 Process evaluation

9.3.1 Thermodynamic evaluation

The thermodynamic evaluation of both olefins production processes was mainly based on energy and exergy analyses. Energy efficiency tracks the efficiency of converting biomass to olefins and power, which is defined as:

$$\eta_{en} = \frac{W_{net} + LHV_{olefins} \times \sum m_{olefins}}{m_{bio} \times LHV_{bio}} \tag{9.6}$$

where $m_{olefins}$ and m_{bio} represent the mass flow rate of the olefins products and the biomass feedstock, respectively. Here, $LHV_{olefins}$ and LHV_{bio} represent the lower heating value of the olefins and biomass, respectively. W_{net} is the net power output.

Exergy follows the conservation of Second Law of Thermodynamics and for a system, it can be expressed by [369]:

$$\sum E_{x,in} = \sum E_{x,out} + \sum E_{x,des/loss} \tag{9.7}$$

where $\sum E_{x,in}$ and $\sum E_{x,out}$ are the total exergy input into a system and output from a system including the material stream and heat stream. $\sum E_{x,des/loss}$ is the combination term of exergy destruction and loss owing to the irreversibility of a system and streams exited to the environment from a system without further utilization, respectively [369].

The exergy efficiency of the overall system is defined as the product exergy output as well as the power output divided by biomass exergy input to the system.

$$\eta_{ex} = \frac{W_{net} + \sum E_{x,olefins}}{E_{x,bio}} \qquad (9.8)$$

where $\sum E_{x,olefins}$ is the olefins exergy output and $E_{x,bio}$ stands for the chemical exergy of biomass.

$E_{x,bio}$ can be deduced according to the common exergy formula (O/C mass ratio ≤2) as follows [370]:

$$E_{x,bio} = \beta m_{\mathrm{bio}} \cdot \mathrm{LHV}_{\mathrm{bio}} \qquad (9.9)$$

$$\beta = \frac{1.044 + 0.016\frac{h}{c} - 0.3496\frac{o}{c}\left(1 + 0.0531\frac{h}{c}\right) + 0.0493\frac{n}{c}}{1 - 0.4124\frac{o}{c}} \qquad (9.10)$$

where h, c, o, n stand for the mass fraction of H, C, O, N in the ultimate analysis of biomass, respectively.

9.3.2 Environmental evaluation

Life cycle analysis enables the identification and evaluation of environmental burdens of the biomass to olefins production from cradle-to-gate perspective [47]. The conduction of LCA analysis usually involves four components, namely, objective and boundary definition, inventory data collection, environmental assessment, and interpretation of the results. Figure 9.3 shows the boundary of the studied biomass to olefins processes. It can be seen from Figure 9.3 that the main units inside the boundary are biomass production, collection and transportation, pretreatment, syngas production either using the direct gasification or indirect gasification subsystem, methanol synthesis and rectification, olefins synthesis and separation, combustion of char, purge gas and fuel gas, HRSG and steam turbines.

The major emissions were CO_2, NO_x, SO_2, waste water and waste solids, which were associated with a series of environmental effects, such as abiotic depletion, acidification, human toxicity, eutrophication and photochemical oxidation. In this study, CO_2 emission equivalent was used to compare environmental behaviors of these two processes ([371].

The CO_2 emissions included two major sources, direct emission and indirect emission. Indirect CO_2 emission consisted of the CO_2 emission from biomass production, transportation and pretreatment. On the contrary, direct CO_2 emission originated from the combustion system fueled by purge gas, char and fuel gas. The CO_2 emission from biomass production was calculated to be 133.03 kg equivalent CO_2 per ton while for biomass pretreatment, the value was 7.46 kg CO_2 eq./ ton [372]. The CO_2 emission from biomass transport was assumed to be 1504 kg CO_2/km, which was a typical CO_2 emission rate for a diesel-fueled heavy vehicle (capacity: 10 t) [373]. In addition, landfill of ash and uncovered carbon was also considered. The biomass transportation distance was calculated from the Eq.(9.14) and waste solid disposal distance were assumed to 10 km, respectively [296]. Generally, the CO_2 emissions from plant construction, manufactured materials, maintenance and plant dismantling should be considered. However, due to their less significant contribution [371], they were not included in this study. The direct CO_2 emissions were counted directly from the simulation results.

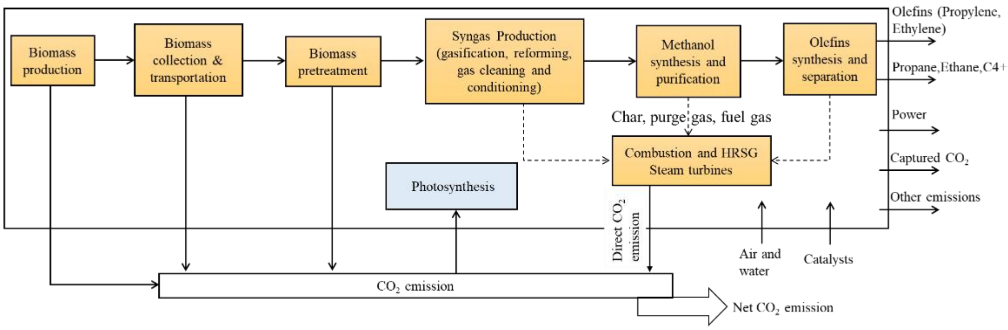

Figure 9. 3 System boundary considered for life cycle evaluation

9.3.3 Economic evaluation

This work employed the total capital costs, net present value (NPV) and internal rate of return (IRR) to justify the economic feasibility of the proposed process. The total capital cost was estimated by direct and indirect capital costs based on the ratio factor method outlined in [374, 375]. The estimation of individual equipment is determined by the base equipment cost and size [376].

$$C_{eqB} = C_{eqA}\left(\frac{Q_B}{Q_A}\right)^{SF} \tag{9.11}$$

where *SF* is scaling factor ranging from 0.5 to 1. Here, C_{eqB} and Q_B are the predicted equipment cost and size, respectively. The terms of C_{eqA} and Q_A are the reference equipment cost and size which are obtained from Refs. [230, 364, 374, 377-380], and summarized in Table 9.5. It is worth noting that the capital costs of all equipment have been updated to the price level of 2016 in accordance with Chemical Engineering’s Plant Cost Index (CEPCI). Typically, the uncertainty of equipment cost estimation is ±30% [381]. In addition, other components included in the total capital cost such as installation and control, construction phase, land, site preparation, plant start-up and contingency were further calculated based on the ratio factors of the total equipment cost referred in [374, 375].

Table 9. 5 Investment costs estimates for the main components

Units	C_{eqA}	Q_A(M$,2016)	SF	Reference
Biomass pretreatment	17.9 kg/s as received biomass	4.29	0.77	[377]
Air separation unit	6.67 kg-O_2/s	21.9	0.75	[374]
Direct gasification island (incl. auto-thermal tar reforming and scrubbing)	17.9 kg/s dry biomass	54.34	0.77	[230]
Indirect gasification island (incl. steam tar reforming and scrubbing)	23.1 kg/s dry biomass	33.58	0.77	[378]
Water gas shift unit	150 kg/s feed gas	3.47	0.67	[379]
Acid gas removal	2064.4 mol/s CO_2 captured	30.39	0.67	[364]
Methanol synthesis and separation	35.647 kg/s feed	7.61	0.65	[379]
MTO	62.5 kg methanol /s	206.7	1	[364]
Heat recovery and steam reforming	355 MW_{th} boiler duty	53.61	1	[380]
Steam cycle and power generation	275 MW_e ST gross power	68.77	0.67	[380]

The operating cost consists of fixed operating cost and variable operating cost. The former was estimated based on percentages of total indirect cost (TIC) or personnel cost as listed in [375]. The number of operators and costs of personnel are estimated by the following equations [374, 378]:

$$N_{OL} = \left(6.29 + 31.7P^2 + 0.23N_{np}\right)^{0.5} \tag{9.12}$$

$$C_{Personnel} = 0.67M\$/100MW_{LHV} \tag{9.13}$$

where N_{OL} is the number of operators per shift; P is the number of processing steps for the particulate solid; N_{np} is the number of processing steps for non-particulate.Here, $C_{Personnel}$ is the personnel cost estimation based on the LHV of feedstock.

Variable operating costs such as biomass, water and catalyst and ash disposals were calculated based on their prices and consumable rates. It is useful to inform that the total cost of biomass was estimated by the consideration of production, collecting, storage and road transportation cost. According to the work of [382, 383], the biomass production, collecting and storage costs were fixed at 22.1, 11.7, 3.7$/tonne dry biomass respectively. The currency exchange rate of US dollar to Chinese Yuan was assumed to be 6.8 in 2016. The road transportation cost depends on distance which is determined by the plant size further. The average distance is calculated by the following correlation [384]:

$$r_b = \frac{1}{6}\tau\sqrt{\frac{P\times 330}{(1-\omega)\times 100\times m\times l_c}} \times \left(\sqrt{2} + ln\left(1+\sqrt{2}\right)\right) \tag{9.14}$$

where r_b is the collection distance (km, one way); τ is the tortuosity factor (for rural road, $\tau = 1.5$). Here, P is the processing capacity for dry biomass tonnes per day and a total of 330 operating days per year is assumed. ω represents the moisture content of feeding biomass, while l_c is biomass land coverage, l_c=90%. Here, m stands for biomass productivity and its value equals 10 green tonnes per hectare per year. The formula for biomass transportation cost (C_{tran}) is estimated using the following correlation [383]:

$$C_{tran} = \begin{cases} 3.67\,\$/ton \quad , \quad 0 < r_b < 15 \ km \\ 7.35 \ \$/ton\,, \ 15 < r_b < 25 \ km \\ 10.3\sim 14.7 \ \$/ton\,, \quad r_b > 25km \end{cases} \tag{9.15}$$

Once the total and variable costs were estimated, the economic evaluating factors could be calculated accordingly. The NPV is used to identify the present sum of net cash flow over an entire plant life. To calculate NPV, the net earnings at years *t* should be discounted to year zero with a Marginal Rate of Return [385]. The expression for NPV is presented as [386]:

$$\mathrm{NPV} = \sum_{t=-1}^{n} \frac{CF_t}{(1+i)^t} \tag{9.16}$$

where CF_t represents the cash flow in year *t*. The range of *t* is from -1 to 20, which stands for the construction time of 2 years and plant life span of 20 years. Table 9.6 shows the main parameters and assumptions for the economic evaluation [381, 387, 388].

The cash flow at year t is given by:

$$CF_t = GF_t(1 - \varphi) + DC_t \tag{9.17}$$

where GF_t, DC_t and φ are gross profit flow, depreciation cost at year t respectively, while φ represents tax rate. The depreciation period is assumed to be 10 years with a straight line depreciation method.

The expression for GF_t is given as [389]:

$$GF_t = R_t - F_t - V_t - DC_t \tag{9.18}$$

where R_t ,F_t and V_t represent the revenue, fixed cost and variable cost at year t, respectively.

The IRR is another parameter to measure the profitability of a potential project [390]. It discounts all the cash flow back into year zero and leads to the *NPV* equaling to zero. When IRR≥i, the project is profitable and a higher IRR means a better economy performance. The calculation of IRR is implemented as [359] :

$$NPV = \sum_{t=-1}^{n} \frac{CF_t}{(1+IRR)^t} = 0 \tag{9.19}$$

Table 9. 6 Main parameters and assumption for economic evaluation [381, 387, 388]

Parameters	Value
Biomass price, \$/ tonne dry	41.2
Water cost, \$/ tonne	0.05
Electricity, \$/ kWh	0.07
Catalyst and ash disposal cost, % of variable cost	2
Discount rate, %	8
Construction time, yr	2 (25%, 75%)
Operating labor	Calculated based on Eq.(9.12)
Personnel	Calculated based on Eq.(9.13)
Depreciation	Plant life: 20 years, salvage value: 5% of

	equipment costs
Tax rate (φ), %	20
Annual operation time, hr	8000
Ethylene, \$/tonne	1300
Propylene, \$/tonne	1400
Light paraffin (C1-C3), \$/tonne	543
Mixture of C4+, \$/tonne	672

9.4 Results and Discussion

In the biomass to olefins processes, the unreacted syngas recycle flow rate in the methanol synthesis unit was a crucial parameter to determine the overall performances, for insufficient unreacted syngas recycle flow rate leads to a low yield of intermediate (methanol), significantly affecting the performances (such as olefins yield, energy and exergy efficiencies as well as profitability) of the downstream process. The unreacted gas recycle fraction (RU), as a key decisive factor, is defined as the ratio of the recycled gas molar flow to the total molar flow of vapor stream from the flash unit, and is shown as Eq.(9. 20).

$$\mathrm{RU} = \frac{\text{unreacted syngas back to the methanol reactor (molar basis)}}{\text{vapor flow rate from the flash unit after the methonal reactor (molar basis)}} \tag{9.20}$$

On the other hand, the crude syngas from biomass steam reformer in IDBTO had an H_2/CO molar ratio of 2.3, which was very close to the desired H_2/CO for methanol synthesis. The employment of readily CO_2 from AGR unit as a gasifying agent could reinforce the gasification of biomass (especially the Boudouard reaction: $C+CO_2 \rightarrow 2CO$) so as to offer a carbon source to enhance the CO fraction in the output syngas, leading to a possibility to reach the suitable syngas production for downstream methanol application. Therefore, the injection of CO_2 into gasifier had also influence on the methanol and olefins yield, resulting in different thermodynamic and economic performances of the IDBTO process. The variable of CO_2/B, representing the ratio of mass flow of CO_2 to mass flow of biomass can be expressed as follows:

$$\mathrm{CO_2/B} = \frac{mass\ flow\ of\ CO_2\ recycled\ to\ gasifier\ section}{\text{mass flow of feed biomass (dry basis)}} \tag{9.21}$$

This section presented the mass balance as well as energy and exergy balances firstly. Then a sensitivity analysis for the variation of the unreacted gas recycle fraction (RU) and CO_2 to biomass mass ratio (CO_2/B) on the thermodynamic performances were demonstrated. After that, environmental impact evaluation regarding net CO_2 emission were reported. In the end of this section, the economic performances were illustrated using total investment cost, NPV and IRR. Besides, the effect of RU, CO_2/B and plant scale on the IRR were also discussed.

9.4.1 Mass balance

According to the assumptions and operating conditions shown in Table 9.4, the simulation results, such as temperature, pressure, mass flow and mole fraction of the key nodes in DBTO and IDBTO processes, are presented in Table 9.7 and Table 9.8 respectively. Figure 9.4 shows the methanol, ethylene and propylene yields of the DBTO and IDBTO processes. It is found that the mass yield of methanol in DBTO is 51.1 wt%, while that of IDBTO is 57.5 wt%. With respect to ethylene and propylene yield, for the IDBTO, it is 9.6 wt% and 9.5 wt% while those for the DBTO are 8.5 wt% and 8.4 wt%, respectively. Clearly in Table 9.7, the readily syngas for methanol synthesis in DBTO was smaller than that in IDBTO (12186.6 kg/h, seeing Node3 in Table 9.8) mainly due to the combustion of partial syngas with oxygen in both autothermal gasifier and tar reformer in DBTO. As a consequence, the methanol production of higher quality in IDBTO was expected, leading to a better performance of olefins yield for IDBTO process.

In addition, owing to a similar process configuration of biomass to olefins between DBTO and the previously published works in [39, 368], comparisons of the methanol and olefins yields were conducted. It was found that both the calculated methanol and olefins yields of DBTO were consistent with the respective methanol and light olefins yields of 51.08% and 16.93% reported by Hannula [39]. Meanwhile, Johansson also demonstrated that the methanol yield was 51.5% and the olefins yield was between 17.6 and 18.2% [368], suggesting that the proposed IDBTO process with an olefins yield of 19.1% was an attractive approach for bio-olefins production.

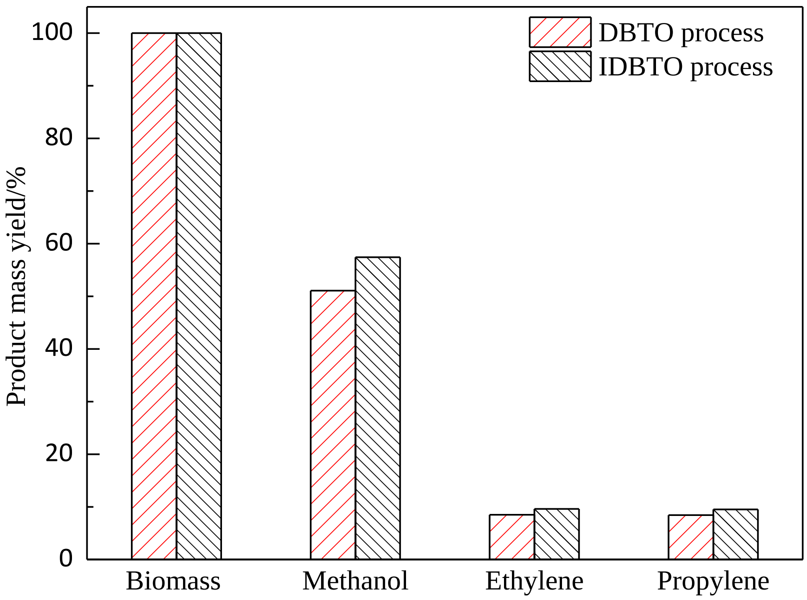

Figure 9. 4 Comparison of mass yield of product between the DBTO and the IDBTO

Table 9. 7 Simulation results for the main nodes shown in the DBTO process

Node	T/^{o}C	P/bar	Mass flow/(kg/h)	Mole fraction											
				CO	CO_2	H_2	H_2O	CH_4	C_2H_4	C_2H_6	C_3H_6	C_3H_8	C_4H_8	C_5H_{10}	Methanol
1	846.1	0.5	30368.2	0.14	0.23	0.20	0.35	0.06	0.02	0.01					
2	60	0.48	40958.2	0.13	0.21	0.28	0.38	0.01							
3	196	8	10374.7	0.30	0.04	0.64	0.00	0.02							
4	29.2	7.5	656.2	0.14	0.14	0.26		0.41							0.01
5	29.2	7.5	9713.3		0.06		0.05	0.02							0.88
6	87.5	0.3	8561.4												0.996
7	24.9	0.15	893.6	0.01	0.67	0.01		0.2							0.1
8	111	0.22	8445.7			0.06	0.68	0.01	0.13		0.09	0.01	0.02		
9	15	2.5	3563.5			0.2		0.02	0.42	0.01	0.27	0.02	0.05	0.01	
10	46.9	2	1415.5						0.01		0.99				
11	56	2	103.3								0.11	0.87	0.02		
12	-13.6	3	1425.2						0.999						
13	-5.5	3	61.18						0.58	0.42					
14	-91	3.05	95.6	0.01		0.91		0.07	0.01						
15	110.8	2.1	507.8								0.04	0.01	0.76	0.16	

Table 9. 8 Simulation results for the main nodes shown in the IDBTO process

Node	T/^{o}C	P/bar	Mass flow/(kg/h)	Mole fraction											
				CO	CO_2	H_2	H_2O	CH_4	C_2H_4	C_2H_6	C_3H_6	C_3H_8	C_4H_8	C_5H_{10}	Methanol
1	831.8	0.15	26348.1	0.18	0.15	0.36	0.27	0.04							
2	760.7	0.15	26348.1	0.21	0.13	0.43	0.22	0.01							
3	196	8	12186.6	0.31	0.03	0.65	0.00	0.01							
4	50	7.5	1446.9	0.18	0.12	0.57		0.10							0.01
5	50	7.5	10739.7	0.00	0.05		0.02	0.01							0.92
6	94	0.3	9628.0												1
7	41.7	0.12	998.8	0.02	0.58	0.03	0.00	0.06							0.297
8	109.4	0.22	9498.2			0.06	0.68	0.01	0.13		0.09	0.01	0.02		
9	10	2.48	3848.3			0.21		0.02	0.43	0.01	0.27	0.02	0.05	0.01	
10	50.3	2.1	1563.9								0.99	0.01			
11	55.7	2.1	150.4								0.36	0.63	0.01		
12	-13	3.05	1612.2						0.999						
13	-0.3	3.05	46.7						0.38	0.62					
14	-90.1	3.05	124.8	0.01		0.89		0.07	0.03						
15	114.3	2.1	562.6				0.04				0.01		0.76	0.16	

The carbon distributions (as percentage of total input carbon) of the DBTO and IDBTO processes are depicted in Figure 9.5. From Figure 9.5(a), it can be seen that the maximum carbon flow is the captured CO_2, accounting for about 54% of the total carbon in the biomass feedstock. This was mainly because the combustion of syngas took place in the gasification and tar reforming units, leading to the generation of large amount of CO_2. The carbon contained in ethylene and propylene accounts for 29%. While, only 8% carbon goes to the atmosphere from boiler and MTO regenerator. For the IDBTO process, the carbon to combustor contributes to the largest share of 30% of the total carbon input from Figure 9.5 (b). The total carbon emission to the atmosphere from the combustor and regenerators is about 42%. Similar with the DBTO process, the second largest carbon share is presented in olefins product, which accounts for 32%. Nevertheless, only 18% carbon is separated from syngas.

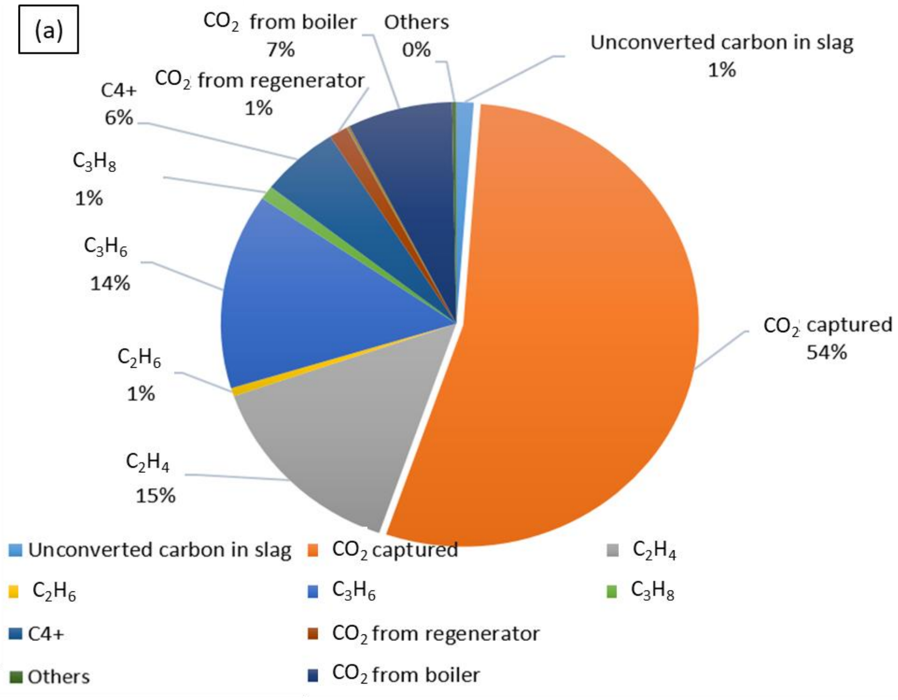

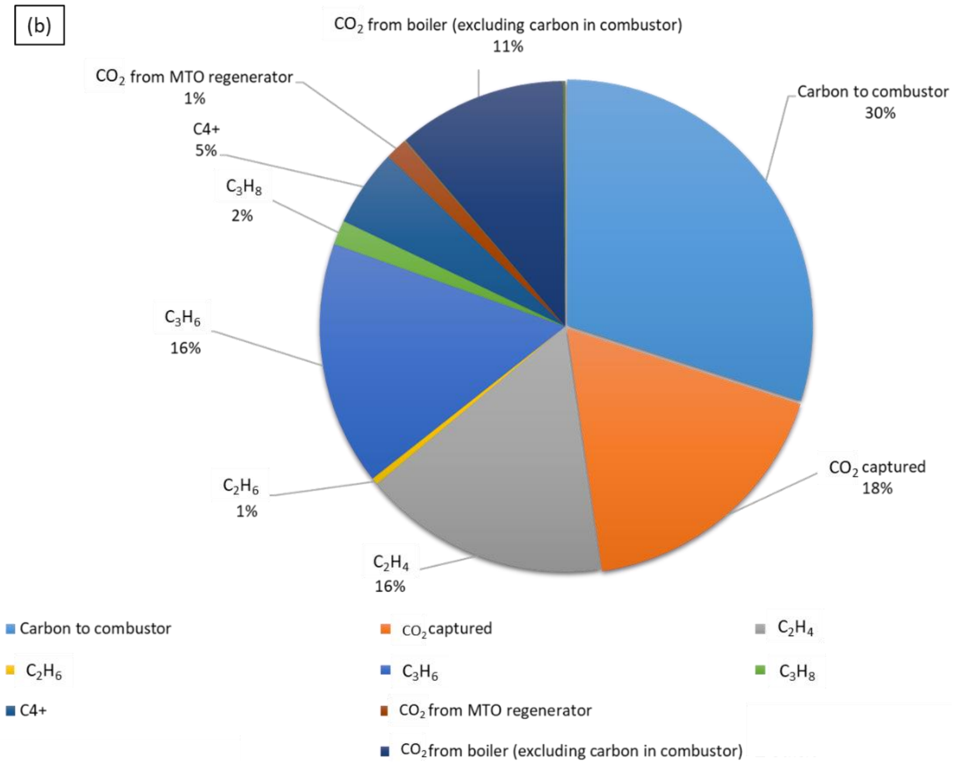

Figure 9. 5 Carbon distributions: (a) DBTO; (b) IDBTO

9.4.2 Energy and exergy balance

Table 9.9 compares the energy balance of the two cases based on energy input, energy output and power consumption of each subsystem. Besides, net power efficiency and overall energy efficiency are also given in this table. It can be observed that the net power outputs of both the DBTO and the IDBTO processes are positive, indicating that the power generation in the plants can cover the plant power requirements, and their values are 327.1 kW and 2612.5 kW, respectively. The reason for the larger net power generation of the IDBTO was mainly attributed to the absence of air separation unit. With respect to energy output of olefins, the DBTO process is about 5% lower than that of the IDBTO process. This was because of higher olefins production yield (Figure 9.4) of the IDBTO process. As for the overall energy efficiency, it is 41.3% for the DBTO process, which is lower than that of IDBTO process (49.2%). The maximum power consumption took place in the syngas compression units for both two processes with values of 3381.7 kW and 5139.1kW for DBTO and IDBTO process, respectively. This was mainly due to the flow rate of effective syngas of the IDBTO was higher than that of the DBTO process (seeing Node 3 in Table 9.7 and 9.8), which resulted in additional compression power inputs.

Table 9. 9 Energy balance of the two processes

Item/kW	DBTO	IDBTO
Biomass input to gasifier (LHV basis)	89456.3	89456.3
Ethylene output (LHV basis)	18666.1	21112.8
Propylene output (LHV basis)	17986.3	20286.4
Power consumption		
Air separation unit	2954.9	-
O_2 compression	528.4	-
Air compression for gasification	-	401.5
Feeding and handling	575	575
Acid gas removal	413.6	194.2
CO_2 compression	640.7	195.8
Syngas compression	3381.7	5139.1
Recompression of methanol recycle gas	371.6	47.7
MTO unit	328.3	369.5
Olefins separation	157.5	178.8

Air compression for combustion	260.3	141.6
Air compression for regenerator	87.2	76.9
Pump consumption	130.1	109.1
Power generation		
High pressure steam turbine	2607.9	1818.2
Medium pressure steam turbine	3795.1	4340.9
Low pressure steam turbine	3753.4	3882.6
Net power output	327.1	2612.5
Net power efficiency/%	0.4	2.9
Overall energy efficiency/%	41.3	49.2

Exergy efficiencies of both the DBTO and the IDBTO processes in terms of total exergy input, output, destruction and loss, and exergy efficiency are presented in Table 9.10. The exergy output items consider the exergy of olefins and the net power value. As shown in Table 9.10, the total exergy destruction and the loss rate are more in the DBTO as compared with the IDBTO, primarily due to the ASU (2954.9 kW) and CO_2 separation and compression unit (5059.3 kW) in the DBTO process. Besides, the exergy destruction rate of methanol synthesis unit is higher in the DBTO than that in IDBTO. This was because of the higher recycle ratio (99%) of methanol reactor in the DBTO, leading to higher exergy destruction compared with that of IDBTO (89%). The exergy efficiency of DBTO is presented to be 37.4%, which is around 7% lower than that of the IDBTO.

Figure 9.6 depicts exergy destruction and loss of different units against the total exergy loss for each process. It is obvious that the largest exergy destruction and loss occur in the gasification and reforming unit, which account for 48.3% and 55.6% of the total exergy loss of the DBTO and IDBTO processes, respectively. This phenomenon was mainly caused by the high irreversibility of gasification, combustion and tar reforming processes. The second largest exergy destruction and loss exists in olefins separation unit, which accounts for 10.9% and 13.3% of the total exergy loss of the DBTO and IDBTO processes, respectively. This was mainly associated with the huge amount of material losses, such as ethane, propane and C4+. At the same time, the separation of olefins via five distillation columns also led to the increase in exergy destruction due to the increase of entropy. The sum of purge gas combustion, HRSG and steam turbines subunits was responsible for a total of 9.58% and 9.91% of the total exergy loss for the DBTO and IDBTO processes, respectively. For those subunits, irreversible chemical conversion of purge gas was the primary reason for the loss. Another reason of exergy destruction was the temperature difference in HRSG. The inefficiencies of the CO_2 separation and compression unit was occupying to 7.86% and 5.02% of the total for DBTO and IDBTO processes, respectively. Exergy destruction of the MTO reactor was 5.34% for the DBTO process while it was 7.34% for the IDBTO process.

Table 9. 10 Exergy balance for the proposed processes

Item/kW	DBTO	IDBTO
Exergy input	102788.7	102788.7
Exergy output		

Olefins	38101.6	43061.7
Power	327.1	2612.5
Exergy destruction and loss		
Air separation unit	2954.9	-
Gasification and tar reforming	31053.4	-
Gasification and steam reforming	-	31767.4
Gas cooling	1360.5	178.7
Water gas shift and water scrubber	2422.6	-
Water scrubber	-	377.3
CO_2 separation and compression	5059.3	2866.7
Methanol synthesis	2165.4	1015.4
Methanol purification	1332.3	1970.5
Methanol to olefins synthesis	3440.2	4190.2
Olefins water quench and caustic wash	1370.2	1487.5
Olefins separation	7030.7	7599.9
Purge gas combustion, HRSG, and steam turbines	6172.2	5661.2
Exergy efficiency/%	37.4	44.3

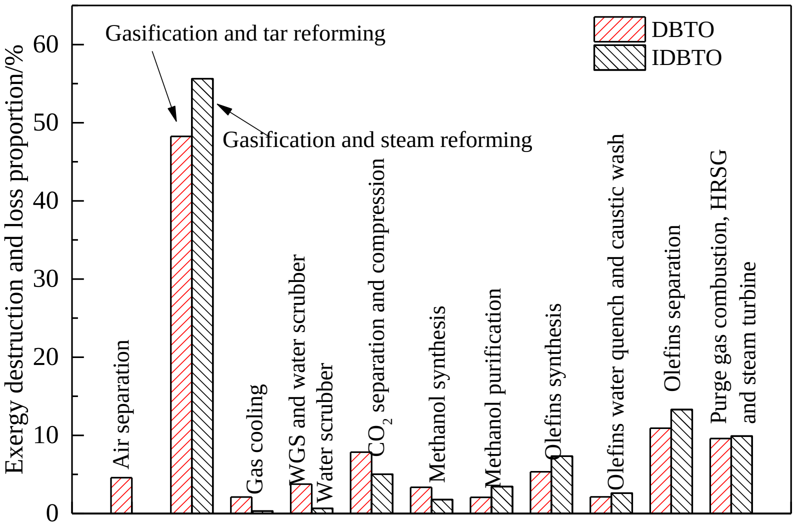

Figure 9. 6 Exergy destruction and loss of different units in the DBTO and IDBTO processes

9.4.3 Sensitivity analysis

9.4.3.1 Effect of unreacted gas recycle fraction

The unreacted gas recycle fraction (RU) was varied by changing the unreacted syngas recycle flow rate from the methanol flash tank to methanol synthesis reactor. The influence of RU on thermodynamic performances of the DBTO process is depicted in Figure 9.7. As shown in Figure 9.7 (a), an increase of RU leads to the simultaneous increment of olefins production while the net power output decreases gently. When the RU was beyond 0.95, the net power output drops dramatically. At RU=0.99, the olefins output reaches the maximum value of 2840.2 kg/h, whereas net power output is shown to be the minimum value of 321.2 kW. The changes of olefins and net power output were expected since more methanol was produced as the addition of RU, and more power was consumed to recompress the unreacted syngas. This eventually resulted in the addition of olefin yield and the reduction of net power.

However, the effect of RU on the overall energy and exergy efficiencies exhibit another scenario. As seen in Figure 9.7(b), when RU changes in the range of 0.2 to 0.99, the energy efficiency obviously rises from 32.5 to 41.3% and similarly, the exergy efficiencies increase from 29.2 to 37.4%. It is worth noting that small increases of both efficiencies are observed when RU exceeds 0.95. The reason of increasing system efficiencies was dominantly attributed to the addition of olefins output as seen in Figure 9.7 (a). However, the rapidly drop of net power output slowed down the total energy or exergy output, leading to a small increment of both efficiencies when RU > 0.95. In addition, the energy efficiency is higher than exergy efficiency at the same RU, owing to the higher exergy input mainly brought by biomass.

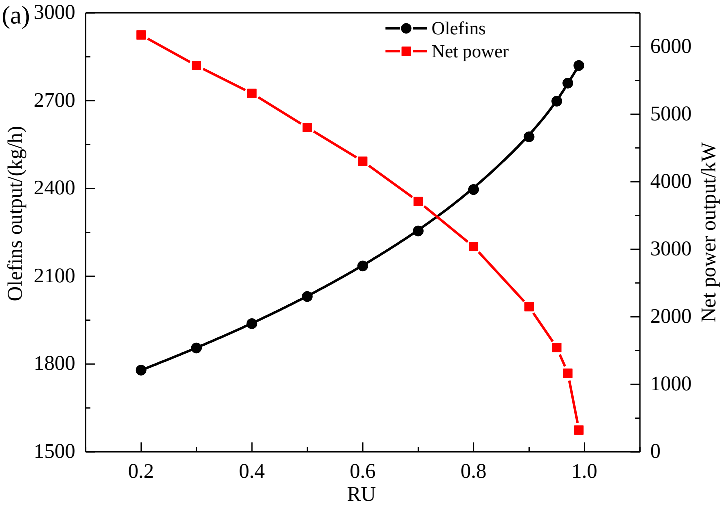

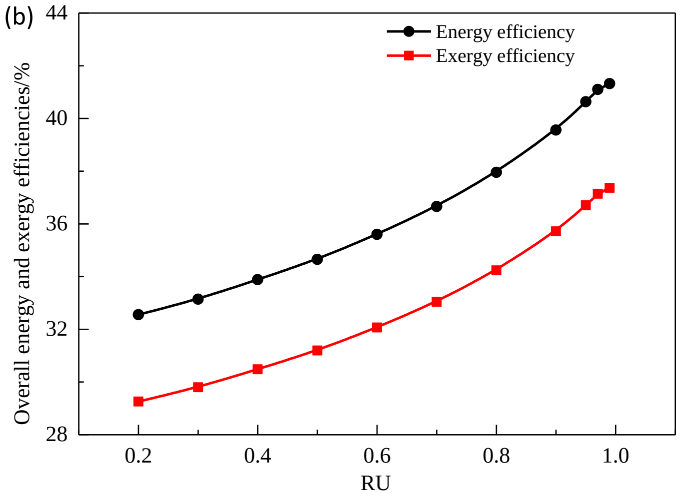

Figure 9. 7 Effect of RU on the thermodynamic performances of DBTO process

The effect of RU on the thermodynamic performances of IDBTO is illustrated in Figure 9.8. As presented in Figure 9.8 (a), the olefins output increases with the increase of RU while the net power output decreased when RU is below 0.89, and levels off thereafter. The variation of overall energy and exergy efficiencies with RU is shown in Figure 9.8(b). From this plot, both the energy and exergy efficiencies increase with the RU initially and then reach their maximum values (49.2% of energy efficiency and 43.3% of exergy efficiency) and drop thereafter. The initial improvement was largely because of the enhanced olefins output. As stated previously, the purge gas from methanol synthesis unit was sent to combustion to provide the energy requirement of tar reformer operating at an elevated temperature of about 760 °C. When the RU was greater than 0.89, the burning of purge gas in the tar catalyst regenerator failed to satisfy the heat demand. Thus, external fuel (such as biomass) input was required to maintain the heat balance in the tar reformer, leading to the drop of energy and exergy efficiencies significantly.

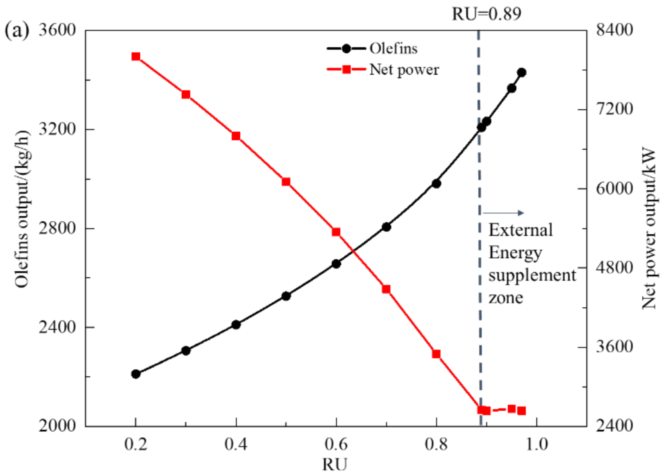

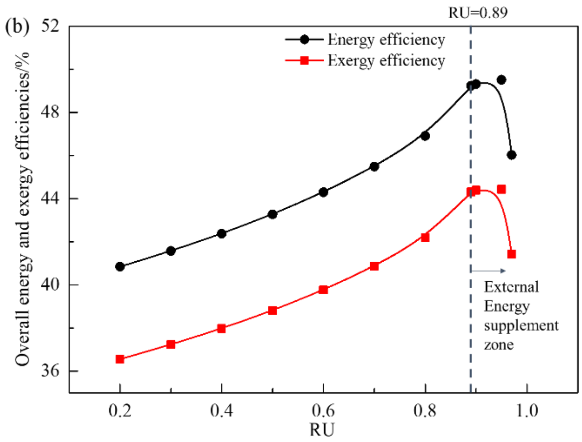

Figure 9. 8 Effect of RU on thermodynamic performances of IDBTO process

9.4.3.2 Effect of CO_2 in gasification

The effect of CO_2 in gasification, denoted as CO_2 to dry biomass ratio (CO_2/B), on the thermodynamic performances of the IDBTO, is shown in Figure 9.9. Clearly in Figure 9.9 (a), when CO_2/B increases from 0 to 0.185, the gasification temperature decreases promptly from 918 to 821 °C and H_2 concentration drops slightly from 66.8 to 63.9% while CO concentration gradually increases from 28.9 to 30.0%. Besides, the H_2/CO molar ratio also decreases progressively from 2.31 to 2.03. The addition of CO_2 promoted the endothermic Boudouard reaction ($C+CO_2 \rightarrow 2CO$, $\varDelta H=172$ kJ/mol), which led to the decrease of temperature, H_2 fraction and H_2/CO molar ratio while simultaneously increased CO molar fraction. When the CO_2/B was over 0.143, external energy supplement was required. It also can be observed that the H_2/CO molar ratio of 2.1, which suits methanol synthesis, is achieved at a CO_2/B of 0.143.

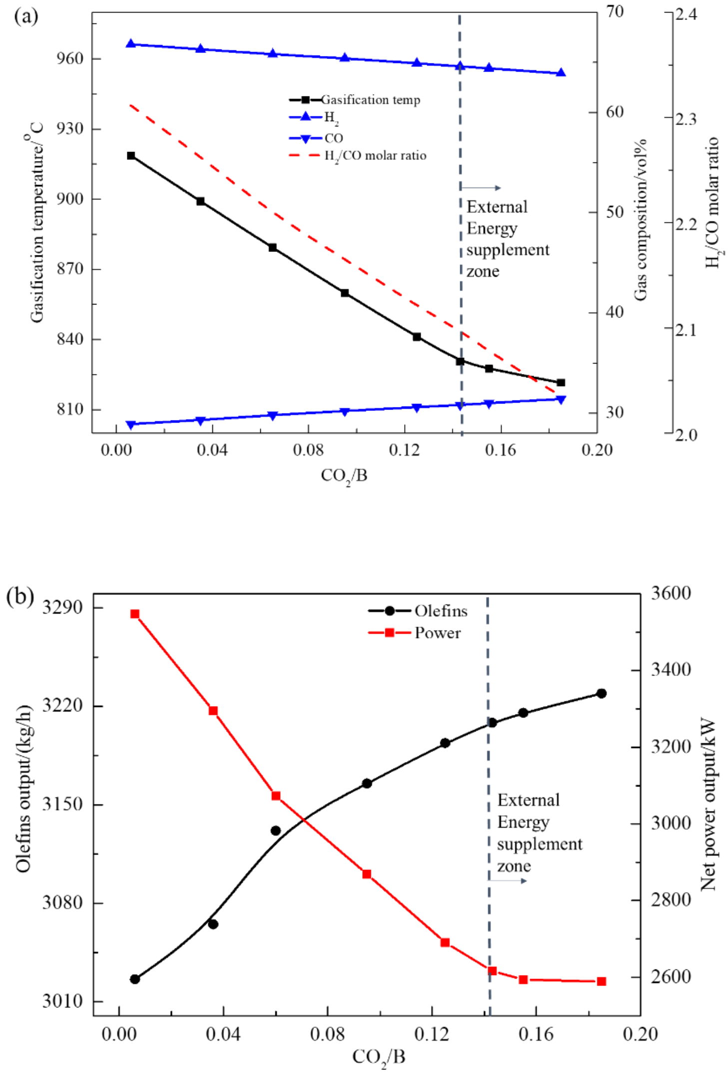

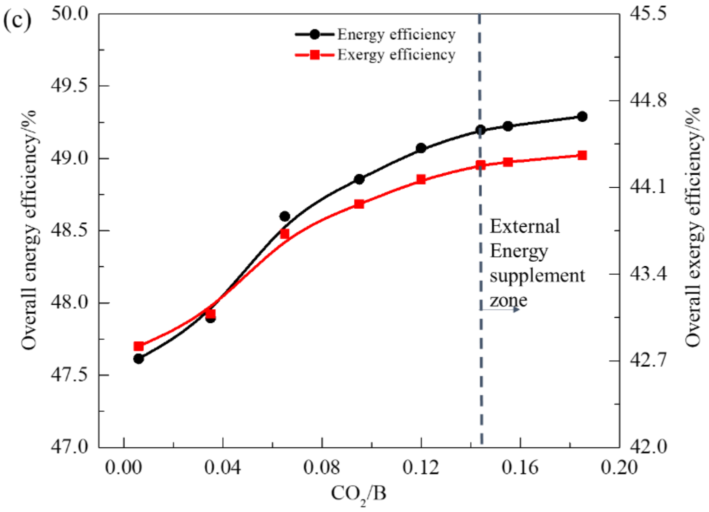

Figure 9. 9 Effect of CO_2/B on the thermodynamic performances of IDBTO process

The variation of olefins output and net power out with the CO_2/B is shown in Figure 9.9(b). The olefins output reaches to 3229.2 kg/h, increased by 6.3% as compared with the process without CO_2 addition, whereas there is a reduction of 27% in net power output. The figure also exhibited that both of the upward trend of olefins and downward trend of net power are significant at the range of 0 to 0.143 and afterwards, their trends became slow or even steady. Because when the CO_2/B was beyond 0.143, the H_2/CO molar ratio was deviated the optimal ratio for the methanol synthesis gradually. As a result, although the syngas flow rate into the methanol increased, it did not have significant impact towards methanol yield, which determined olefins directly. In the meantime, the effect of CO_2/B on the overall energy and exergy efficiencies is depicted in Figure 9.9(c). It can be seen that the overall energy and exergy efficiencies increase from 47.6 to 49.2% and from 42.7 to 44.3% respectively within the CO_2/B interval 0-0.143, and a slight increase is observed after that range. This was because more olefins were produced when the $CO_2/B < 0.143$ (shown in Figure 9.9(b)), and consequently the energy and exergy efficiencies were enhanced. Nevertheless, when CO_2/B was higher than 0.143, the supplemental energy fuel was required in the combustor and it showed an increase with the addition of CO_2 input due to the endothermic Boudouard reaction. Besides, the olefins yield was shown to rise slightly as seen in Figure 9.9(b). As a result of those combined influences, the energy and exergy efficiencies remaining steady.

In summary, the thermodynamic performances of both processes, such as olefins yield, energy and exergy efficiencies, could improve significantly by selecting appropriate RU. Besides, the adjustment of the CO_2/B could achieve the desirable H_2/CO molar ratio for methanol synthesis and consequently, both the energy and exergy efficiencies increased by 1.6% in comparison with CO_2 unemployment (CO_2/B=0).

9.4.4 Environmental impact evaluation

Moreover, the environmental impact evaluation was carried out to provide the quantitative information of CO_2 emission via the DBTO and IDBTO routes. The results are presented in Figure 9.10. As can be noticed from this figure, with respect to DBTO process, the biggest CO_2 emission takes place in the biomass production phase accounting for 58% of the total CO_2 positive emission, followed by the direct CO_2 emission occupying approximately 35% of the total positive CO_2 emission. However, the main contributions to CO_2 emission in the IDBTO process are direct emission and biomass production phases, with a value of 3.99 and 1.15 kg CO_2 eq./ kg olefins occupying about 76% and 22% of the total positive CO_2 emission, respectively.

The net CO_2 emissions for both processes in the entire life cycle are found to be negative. Specifically, the net CO_2 emission value of IDBTO process is -4.44

kg CO_2 eq./ kg olefins and is -8.74 kg CO_2 eq./ kg olefins for the DBTO. It was mainly attributed to the facts that large proportion (approx.30%, seeing Figure 9.5(b) of residual char was forwarded to combustor for combustion to provide the heat requirement of biomass gasifier, and the resulted flue gas was emitted to the atmosphere. However, the CO_2 generated during gasification, tar reforming and WGS was captured in the DBTO process. Besides, the unreacted syngas recycle ratio of the IDBTO process was 89% which was 10% less than that in DBTO process. Consequently, the CO_2 emission from the combustion of purge gas for the IDBTO process was higher than that of the DBTO process. Thus, the direct and net emissions of CO_2 of IDBTO were greater than those in DBTO.

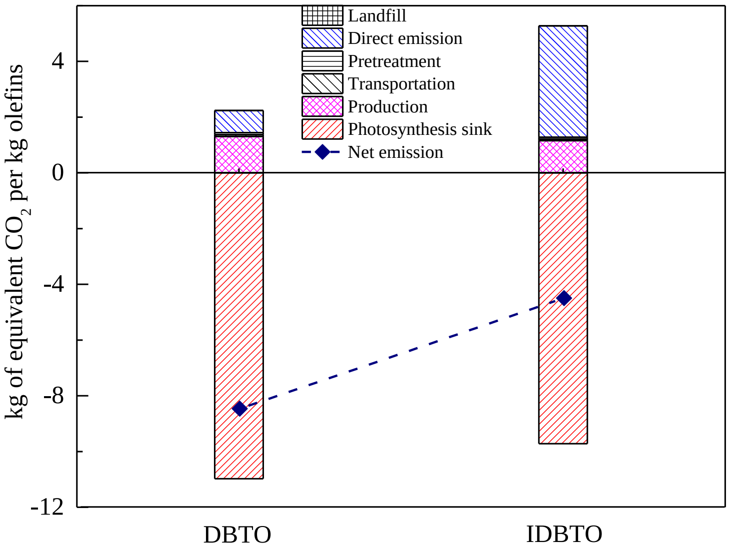

Figure 9. 10 LCA results in CO_2 emission mass flow per kg olefins

9.4.5 Economic analysis

The economic performances of the DBTO and IDBTO routes are shown in Table 9.11. The total capital cost of IDBTO is 74.22 M$, which is 22% lower than that of the DBTO process. This was mainly attributed to the investment elimination of a pressurized direct oxygen-steam biomass gasifier and an air separation unit in IDBTO route. Besides, the increment of equipment capital costs of MTO and methanol synthesis for IDBTO process due to higher methanol rate and syngas rate was relatively small. As a result, the total capital cost for DBTO was higher than that of IDBTO. On the other hand, as listed in the table that the annual operating cost of DBTO is determined to 17.96 M$, which is higher than that of IDBTO about 10%. Because both of the processes had similar variable cost, while the fixed operating cost was calculated from proportions of total indirect capital cost, the DBTO held a higher total indirect capital cost, which led to a larger operating cost eventually.

However, the annual gross sale revenues brought by the valuable products and by-products of IDBTO system equaled to 39.62 M$$\cdot$yr^{-1} and that of DBTO was calculated to be 34.30 M$$\cdot$yr^{-1}. This was because more olefins and electricity were generated in the case of IDBTO. Thus, the cumulative cash flow within the plant life of IDBTO was 116.67 M$ higher than that of DBTO of 50.09 M$, demonstrating that the IDBTO system was economically competitive. In Table 9.11, it also can be found that the IRR of the DBTO were 13.1%, which is inferior to that of IDBTO with 23.5%. Consequently, the IDBTO is more advantageous than the DBTO system in the view of economic performances.

Table 9. 11 Economic performance of the biomass gasification to olefins processes

Item	DBTO	IDBTO
Total capital cost, M$	96.14	74.22
Annual total operating and maintenance	17.96	16.01

cost, M$/yr		
Gross sale revenue, M$/yr	34.30	39.62
NPV, M$	50.09	116.67
IRR,%	13.1	23.5

As demonstrated in the previous section, as the unreacted gas recycle ratio increased, the molar flow rate of the synthesis methanol increased. As a result, the investment cost of MTO unit became higher due to the requirement of larger equipment. By contrast, the equipment cost for HRSG and ST decreased simultaneously because less heat generated by the combustion of purge gas from methanol reactor was extracted from the system. Therefore, to justify the impact of unreacted gas recycle ratio on IRR quantitatively, an economic investigation should be performed.

Variation of internal rate of return with unreacted gas recycle ratio for the both DBTO and IDBTO processes is presented in Figure 9.11. The minimum acceptable rate of return (MARR) line of 8% is also shown in this figure. Clearly in this figure, in the DBTO case, increasing RU from 0.2 to 0.99 greatly contributes to IRR from of 2.5 to 14.1%, while for the case of IDBTO, as RU enhances from 0.2 to 0.89, the IRR increases from 13.5 to 23.5% remarkably. The reason was explained as followings: increase of RU benefited olefins yield as shown in Figure 9.7 and Figure 9.8, with simultaneous promotion of gross revenues. Besides, the total capital cost decreased slightly. Consequently, the cash flow in each year was taken advantages from rising RU. The figure also implies that the RU of DBTO process should exceed to 0.65 to meet the feasibility criteria adequately.

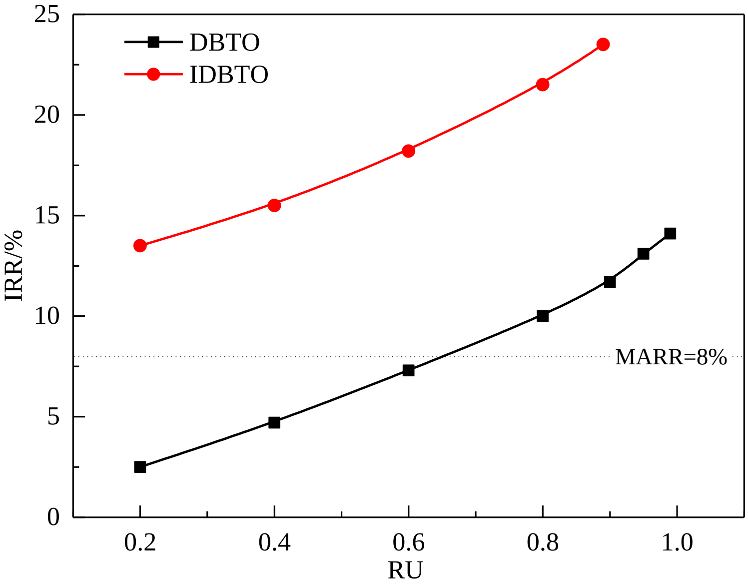

Figure 9. 11 Effect of RU on IRR of the biomass to olefins processes

In addition, to demonstrate the economic advantages of CO_2 recycle for the IDBTO case, the effect of CO_2/B on total capital cost, gross revenue and IRR is depicted in Figure 9.12. As it can be observed from this figure that the IRR exhibits increasing tendency with CO_2/B, as it rises from 22.1 to 23.5%, which reveals that the economic performance is promoted to be more profitable. The reason of increasing IRR was mainly attributed to the addition of gross revenue introduced by the increase of olefins product (as explained previously). Clearly in Figure 9.12, although the total capital cost is also seen in a slight rise, its increment rate is smaller than the gross revenue, resulting from positive cash flow increase is expected. Thus, the addition of CO_2 recycle in the IDBTO system is not only beneficial for energy and exergy efficiencies, but also it is favored financially.

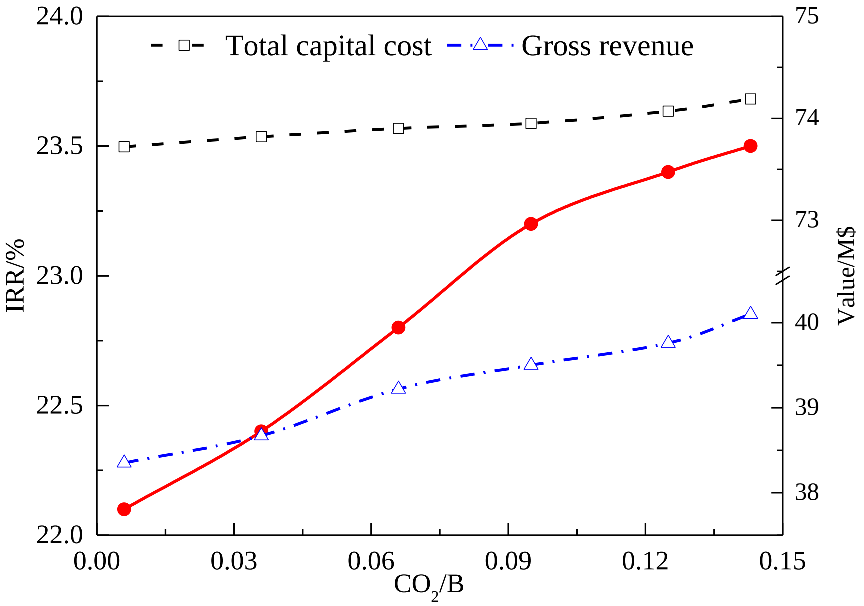

Figure 9. 12 Effect of CO_2/B on IRR of the biomass to olefins processes

The plant capacity is another significant factor for economic assessment. In this study, the variation of plant size on specific total capital cost and IRR for both processes are displayed in Figure 9.13 (a) and (b). As indicated in this figure that with the increase of biomass feed rate to 9 kg/s, the specific total capacity cost drops about 39% for DBTO and 51% for IDBTO comparing with a 1kg/s plant, respectively. This was expected since the total equipment cost had a power law relationship with the base scale by means of Eq.(9.11) [391]. Besides, the other parts in total capital cost such as buildings, site preparation, contingency, etc., were calculated from the total equipment cost. Therefore, the specific total capital cost reduced drastically followed by gradual decrease at feedstock rate of 5 kg/s. In addition, since the total capital cost of IDBTO was smaller than DBTO, the effect of economy was considerably low [364]. Hence, the change in value of specific total capital cost of DBTO was less than IDBTO. However, IRR exhibits increasing tendency with plant size, as it rises from 4.3 to 16.1% for DBTO and from 9.5 to 29.1% for IDBTO, which suggests enhanced the economic performances. Similarly, when the plant capacity is beyond 5kg/s of feedstock rate, the IRR increasing rate slows down. It can also be noticed that the minimum profitable feedstock rate is 2.42 kg/s regarding DBTO process because the IRR exceeds 8% over that plant capacity. In contrast, the IDBTO process is profitable in the range of the studied plant size.

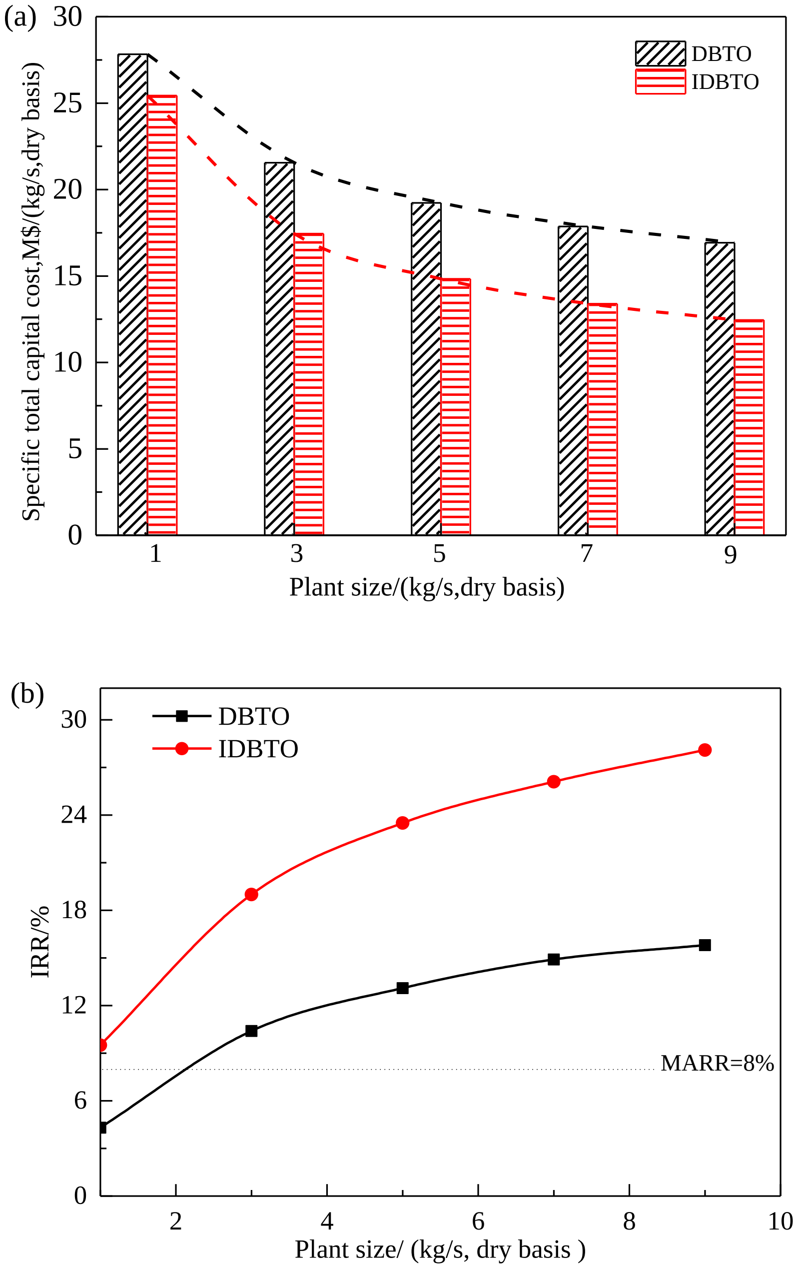

Figure 9. 13 Effect of plant size on: (a) specific total capital cost and (b) IRR (internal rate of return)

9.5 Conclusions

The biomass indirect steam gasification to olefins via methanol as the intermediate with CO_2 utilization process was proposed and compared with direct oxygen-steam based biomass gasification to olefins process. The main findings of this study are as follows:

(1) The mass yield of olefins in DBTO was 16.9 wt%, while that of IDBTO was shown to be 19.1 wt%. The overall energy and exergy efficiencies of the IDBTO process were around 49 and 44%, respectively, compared to respective 41% and 37% in the DBTO process. The major exergy destruction and loss occurred in gasification and tar reforming units followed by olefins separation and purge gas combustion subsystem.

(2) The increase of unreacted gas recycle ratio resulted in the improvement of overall energy and exergy efficiencies of both processes. However, when RU > 0.95, the increment of efficiency was not obvious for the case of the DBTO. Besides, energy and exergy efficiencies started to reduce when RU > 0.89 for the IDBTO. The energy and exergy efficiencies of IDBTO process could be further enhanced (around 1.6%) by the addition of CO_2 into the gasification unit. Nevertheless, extra energy input was demanded after CO_2/B was beyond 0.143, resulting almost constant trend for efficiencies.

(3) The negative CO_2 emission was achieved for both processes. The IDBTO route was predicted to be -4.4 kg CO_2 eq./ kg olefins, which

was higher 4.3 kg CO_2 eq./ kg olefins than that of the DBTO process.

(4) The economic evaluation indicated that the IDBTO process significantly improved economic performances as demonstrated by high NPV (116.67 M$) and IRR (23.5%).

Chapter 10 Conclusions and future work

10.1 Conclusions

10.1.1 Coal pyrolysis and gasification

The microwave-induced char had the largest C/H mass ratio and most ordered carbon structure, but the smallest gasification reactivity. Kinetic analysis indicated that the RPM was better for describing both gasification conversion and reaction rates of the studied chars, and the activation energies and pre-exponential factors varied in the range of 78.45 - 194.72 kJ/mol and 3.15 - 102231.99 s^{-1}, respectively. In addition, a compensation effect was noted during gasification. Finally, the microwave-derived char exhibited better thermodynamic performance than the conventional chars, with the highest CGE and CO molar concentration of 1.3 and 86.18%, respectively. Increasing the pyrolysis temperature, gasification temperature, and CO_2-to-carbon molar ratio improved the CGE.

For the macerals gasification, the parent coal and its macerals exhibited different gasification behaviours at the same operating conditions, such as the SOC and SCC decreased in the order of inertinite > vitrinite > liptinite, whereas CGE changed in the order of liptinite > vitrinite > inertinite. The synergistic coefficients of SOC and SCC for the simulated coals were in the range of 0.94 to 0.97, whereas the synergistic coefficient of CGE was from 1.05 to 1.13. Moreover, the relationships between synergistic coefficients of gasification indicators were correlated well with maceral contents. In addition, the increase of temperature was found promoting the synergistic coefficients slightly, whilst at an oxygen to coal (OTC) mass ratio of 0.8 and a steam to coal (STC) mass ratio of 0.8, the highest synergistic coefficients were obtained.

After coal gasification, fine slags had a higher carbon content than that of the coarse slags and were fragmentized, smaller spheres, and more porous. Majority of heavy metals were more concentrated in fine slags than coarse slags. Some heavy metals, such as Cu, Ni, Pb, V, Co and Zn, were enriched in the fine slags. Cr was enriched in coarse slags, while Pb and Zn were accumulated in fine slags based on the relative enrichment index. The sequential extraction demonstrated HMs of Cr, Cu, Ni, V and Zn were principally associated with residual fractions (48.8 -82.6 wt%), while Co, Mn and Pb were dominated by oxidizable (78.1 wt%), acid soluble (60.0 wt%) and reducible fractions (99.2 wt%), respectively, in the coal samples. Except for Zn in fine slag, the other HMs were mianly distributed in residual fractions with values of 42.3 to 94.8 wt% in fine and coarse slags. The mobile fractions of heavy metals in coal samples were highest (19.4 - 93.6 wt%), followed by fine slags (11.6 – 73.1 wt%) and coarse slags (5.1 -41.0 wt%). Based on the leaching ability, except cupper, the contents other HMs in all slags were above the standard for landfill disposal.

10.1.2 Thermal co-processing of coal and oil shale

The co-combustion of coal and oil shale suggested that ignition index and burnout index of the blends reached maximum for 10% of FS, while the comprehensive combustibility index remained nearly unchanged for the blend with 10% FS when compared with the pure coal sample. With the increase in heating rates, combustion performances of the samples improved significantly. Besides, there are noticeable deviations between the experimental combustion curves and theoretical burning curves of the blends, which occur mainly in the temperature range of 410-480 °C. This indicates the existence of significant synergistic interactions. Moreover, the average activation energy was determined using two model-free integral methods, *i.e.*, Flynn–Wall–Ozawa (FWO) and Kissinger–Akahira–Sunose (KAS), which agreed well with each other. The lowest apparent activation energy was found to be 64.1kJ/mol for the blend with an FS fraction of 10%. Pre-exponential factors and reaction mechanism functions of samples at different heating rates were also calculated using the integral master-plots method. Furthermore, the addition of FS was found to improve the slagging and fouling tendency of the QH coal combustion. The slag formation and mineral transformation of different samples were calculated by FactSage 6.3. At the blending ratio of 10 wt% of FS, the anorthite, hematite, diopside and quartz were found to be the main crystalline phases at high temperatures.

As for the co-gasification of coal and oil shale semi-coke, the increase of SC contents and heating rates had a significant impact on the gasification performances. The positive interactions between the blends occurred in both pyrolysis and char gasification stages. The GA-BPNN model was validated effectively by the comparison with experimental data, and it outperformed BPNN model as indicted by the lower mean square error (MSE) magnitudes of 0.61 in GA-BPNN than that of 1.61 in BPNN. The employment of SCM model were determined to be more excellent in fitting the experimental points for both pyrolysis and char gasification stages ($R^2 > 0.95$). The activation energies of blends were smaller than that of the pure QH coal.

10.1.3 Olefins production from biomass gasification: process design and systematic evaluations

The simulation and evaluation of the proposed biomass gasification based olefins production indicated that the yields of olefins of DBTO and IDBTO were 17 wt% and 19 wt%, respectively, the overall energy and exergy efficiencies of the IDBTO were around 49% and 44%, which were 8% and 7% higher than those of the DBTO process, respectively. A higher RU was found favor higher energy and exergy efficiencies for both routes. Besides, for the IDBTO process, it is found that the addition of CO_2 to gasification system led to an improvement in both energy efficiency and exergy efficiency by around 1.6%. Moreover, life-cycle net CO_2 emission was predicted to be -4.4 kg CO_2 eq./ kg olefins for IDBTO, while for DBTO, it was -8.7 kg CO_2 eq./ kg. However, the quantitative economic performance of IDBTO was superior to that of the DBTO process.

10.2 Future work

Future work could be carried out through the following aspects:

- Effect of different types of microwave absorbers and loadings on the characteristics of produced coal char needs further investigations since absorbers also act as catalysts adjusting the properties of pyrolysis products.
- Experimental studies of synergy in maceral blends under gasification conditions deserve further research.

- Mesoporous silica preparation from wasteful slags for heavy metals removal application is preferred in order to achieve “zero emission” goal in gasification.
- Gaseous emissions and syngas compositions from the co-combustion and co-gasification of coal and oil shale need to be detected. Meanwhile, a bench scale or pilot scale test of blends using a fixed bed or fluidized bed is required by adopting different oxidants.
- Compared with conventional exergy analysis, the advanced exergy analysis allows to provide comprehensive information regarding the interactions among components in a process and hence the potential improvements of the components’ exergy destructions can be determined. Therefore, advanced exergy analysis is recommended to investigate the gasification for olefins process.

Bibliography

[1] Wang Z, Liu M, Guo H. A strategic path for the goal of clean and low-carbon energy in China. Natural Gas Industry B. 2016;3(4):305-11.

[2] Lan C, Lyu Q, Qie Y, Jiang M, Liu X, Zhang S. Thermodynamic and kinetic behaviors of coal gasification. Thermochimica Acta. 2018;666:174-80.

[3] Zhu T, Wang R, Yi N, Niu W, Wang L, Xue Z. CO_2 and SO_2 emission characteristics of the whole process industry chain of coal processing and utilization in China. International Journal of Coal Science & Technology. 2020:1-7.

[4] BP. BP energy oulook 2018. London. 2018.

[5] Attwood T, Fung V, Clark WW. Market opportunities for coal gasification in China. Journal of Cleaner Production. 2003;11(4):473-9.

[6] Li C, Bai H, Lu Y, Bian J, Dong Y, Xu H. Life-cycle assessment for coal-based methanol production in China. Journal of Cleaner Production. 2018;188:1004-17.

[7] Gao M, Yang Z, Wang Y, Bai Y, Li F, Xie K. Impact of calcium on the synergistic effect for the reactivity of coal char gasification in H_2O/CO_2 mixtures. Fuel. 2017;189:312-21.

[8] Wang Q, Zhang R, Luo Z, Fang M, Cen K. Effects of pyrolysis atmosphere and temperature on coal char characteristics and gasification reactivity. Energy Technology. 2016;4(4):543-50.

[9] Parvez AM, Wu T, Hong Y, Chen W, Lester EH, Mareta S, et al. Gasification reactivity and synergistic effect of conventional and microwave pyrolysis derived algae chars in CO_2 atmosphere. Journal of the Energy Institute. 2019;92(3):730-40.

[10] Joseph J, Fisher R, Masin C, Dyrkacz G, Bloomquist C, Winans R. Coal maceral chemistry. 1. Liquefaction behavior. Energy & Fuels. 1991;5(5):724-9.

[11] Scott AC. Coal petrology and the origin of coal macerals: a way ahead? International Journal of Coal Geology. 2002;50(1-4):119-34.

[12] Zhao Y, Hu H, Jin L, He X, Wu B. Pyrolysis behavior of vitrinite and inertinite from Chinese Pingshuo coal by TG–MS and in a fixed bed reactor. Fuel Processing Technology. 2011;92(4):780-6.

[13] Gräbner M, Meyer B. Performance and exergy analysis of the current developments in coal gasification technology. Fuel. 2014;116:910-20.

[14] Matjie RH, Li Z, Ward CR, French D. Chemical composition of glass and crystalline phases in coarse coal gasification ash. Fuel. 2008;87(6):857-69.

[15] Wu T, Gong M, Lester E, Wang F, Zhou Z, Yu Z. Characterisation of residual carbon from entrained-bed coal water slurry gasifiers. Fuel. 2007;86(7):972-82.

[16] Price CE, Barnwell WL, Groppo Jr JG. Method and system for beneficiating gasification slag. Google Patents; 2008.

[17] Wu X, Guo Q, Gong Y, Cheng C, Ding L, Wang F, et al. Visualization study on particle flow behaviors during atomization in an impinging entrained-flow gasifier. Chemical Engineering Science. 2020;225:115834.

[18] Torres M, Castiglioni J, Yermán L, Suescun L, Conti B, Demarco MM, et al. Assessment of Uruguayan oil shales: physicochemical, thermal and morphological characterization. Fuel. 2018;234:347-57.

[19] Lin Y, Liao Y, Yu Z, Fang S, Ma X. The investigation of co-combustion of sewage sludge and oil shale using thermogravimetric analysis. Thermochimica Acta. 2017;653:71-8.

[20] Bai F, Sun Y, Liu Y, Li Q, Guo M. Thermal and kinetic characteristics of pyrolysis and combustion of three oil shales. Energy Conversion and Management. 2015;97:374-81.

[21] Yang Y, Lu X, Wang Q. Investigation on the co-combustion of low calorific oil shale and its semi-coke by using thermogravimetric analysis. Energy Conversion and Management. 2017;136:99-107.

[22] Jiang X, Han X, Cui Z. New technology for the comprehensive utilization of Chinese oil shale resources. Energy. 2007;32(5):772-7.

[23] Yang Q, Qian Y, Zhou H, Yang S. Conceptual design and techno-economic evaluation of efficient oil shale refinery processes ingratiated with oil and gas products upgradation. Energy Conversion and Management. 2016;126:898-908.

[24] Peng X, Ma X, Xu Z. Thermogravimetric analysis of co-combustion between microalgae and textile dyeing sludge. Bioresource Technology. 2015;180:288-95.

[25] Knoist A, Loo L, Valtsev V, Maaten B, Siirde A, Neshumayev D, et al. Calculation of the amount of estonian oil shale products from combustion in regular and oxy-fuel mode in a CFB boiler. Oil Shale. 2014;31(3):211-24.

[26] Hotta A, Parkkonen R, Hiltunen M, Arro H, Loosaar J, Parve T, et al. Experience of Estonian oil shale combustion based on CFB technology at Narva power plants. Oil Shale. 2005;22(4):381-97.

[27] You CF, Xu XC. Coal combustion and its pollution control in China. Energy. 2010;35(11):4467-72.

[28] Yu HL, Jiang XM, Zhao X, Zhou JH, Cen KF. Study on combustion property of mixture of oil shale and heshan coal. Journal of Fuel Chemistry and Technology. 2014;32(3):274-7.

[29] Yan JB, Wang HR, Liang D, Li XX. Combustion and emission performance of oil shale mixed with coal. Journal of Combustion Science and Technology. 2014;20(2):159-63.

[30] Rizvi T, Xing P, Pourkashanian M, Darvell L, Jones J, Nimmo W. Prediction of biomass ash fusion behaviour by the use of detailed characterisation methods coupled with thermodynamic analysis. Fuel. 2015;141:275-84.

[31] Guo L, Zhai M, Wang Z, Zhang Y, Dong P. Comparison of bituminous coal and lignite during combustion: Combustion performance, coking and slagging characteristics. Journal of the Energy Institute. 2019;92(3):802-12.

[32] Raukas A, Punning J-M. Environmental problems in the Estonian oil shale industry. Energy & Environmental Science. 2009;2(7):723-8.

[33] Liu H, Gong S, Jia C, Wang Q. TG-FTIR analysis of co-combustion characteristics of oil shale semi-coke and corn straw. Journal of Thermal Analysis and Calorimetry. 2017;127(3):2531-44.

[34] Sun B-Z, Wang Q, Shen P-Y, Qin H, Li S-H. Kinetic analysis of co-combustion of oil shale semi-coke with bituminous coal. Oil Shale. 2012;29(1):63-75.

[35] Sun B, Wang Q, Shen P, Liu H, Qin H, Li S. Experimental investigation on combustion characteristics of oil shale semi-coke and bituminous coal blends. Journal of China Coal Society. 2010;35(3):476-80.

[36] Wang P, Yuan M, Wang C, Zhang J, Du Y, Tao Z, et al. Experimental evaluation on co-combustion characteristics of semi-coke and coal under enhanced high-temperature and strong-reducing atmosphere. Applied Energy. 2020;260:114203.

[37] Chen W-H, Chen C-J, Hung C-I. Taguchi approach for co-gasification optimization of torrefied biomass and coal. Bioresource Technology. 2013;144:615-22.

[38] Mei C, Wen P, Liu Z, Liu H, Wang Y, Yang W, et al. Selective production of propylene from methanol: Mesoporosity development in high silica HZSM-5. Journal of Catalysis. 2008;258(1):243-9.

[39] Hannula I, Arpiainen V. Light olefins and transport fuels from biomass residues via synthetic methanol: performance and cost analysis. Biomass Conversion and Biorefinery. 2015;5(1):63-74.

[40] Xiang D, Qian Y, Man Y, Yang S. Techno-economic analysis of the coal-to-olefins process in comparison with the oil-to-olefins process. Applied Energy. 2014;113:639-47.

[41] Chen JQ, Bozzano A, Glover B, Fuglerud T, Kvisle S. Recent

advancements in ethylene and propylene production using the UOP/Hydro MTO process. Catalysis Today. 2005;106(1):103-7.

[42] Xu X, Liu Y, Zhang F, Di W, Zhang Y. Clean coal technologies in China based on methanol platform. Catalysis Today. 2017;298:61-8.

[43] Zhao Z, Liu Y, Wang F, Li X, Deng S, Xu J, et al. Life cycle assessment of primary energy demand and greenhouse gas (GHG) emissions of four propylene production pathways in China. Journal of Cleaner Production. 2017;163:285-92.

[44] Tian P, Wei Y, Ye M, Liu Z. Methanol to olefins (MTO): from fundamentals to commercialization. ACS Catalysis. 2015;5(3):1922-38.

[45] Yi Q, Zhao Y, Huang Y, Wei G, Hao Y, Feng J, et al. Life cycle energy-economic-CO_2 emissions evaluation of biomass/coal, with and without CO_2 capture and storage, in a pulverized fuel combustion power plant in the United Kingdom. Applied Energy. 2018;225:258-72.

[46] Heyne S, Thunman H, Harvey S. Exergy-based comparison of indirect and direct biomass gasification technologies within the framework of bio-SNG production. Biomass Conversion and Biorefinery. 2013;3(4):337-52.

[47] Liptow C, Tillman A-M, Janssen M. Life cycle assessment of biomass-based ethylene production in Sweden—is gasification or fermentation the environmentally preferable route? The International Journal of Life Cycle Assessment. 2015;20(5):632-44.

[48] Xiang Y, Zhou J, Lin B, Xue X, Tian X, Luo Z. Exergetic evaluation of renewable light olefins production from biomass via synthetic methanol.

Applied Energy. 2015;157:499-507.

[49] Arvidsson M, Haro P, Morandin M, Harvey S. Comparative thermodynamic analysis of biomass gasification-based light olefin production using methanol or DME as the platform chemical. Chemical Engineering Research and Design. 2016;115:182-94.

[50] Xie K-C. Coal gasification. Structure and Reactivity of Coal: Springer; 2015. p. 181-241.

[51] Speight JG. The chemistry and technology of petroleum: CRC press, 2014.

[52] Falcon RMS, Snyman CP. An introduction to coal petrography: atlas of petrographic constituents in the bituminous coals of Southern Africa. Johannesburg: Geological Society of South Africa, 1986.

[53] Teichmüller M. The genesis of coal from the viewpoint of coal petrology. International Journal of Coal Geology. 1989;12(1-4):1-87.

[54] Pickel W, Kus J, Flores D, Kalaitzidis S, Christanis K, Cardott B, et al. Classification of liptinite–ICCP System 1994. International Journal of Coal Geology. 2017;169:40-61.

[55] Suárez-Ruiz I, Crelling JC. Applied coal petrology: the role of petrology in coal utilization: Academic Press, 2008.

[56] Tomeczek J, Palugniok H. Kinetics of mineral matter transformation during coal combustion. Fuel. 2002;81(10):1251-8.

[57] Matjie RH, French D, Ward CR, Pistorius PC, Li Z. Behaviour of coal mineral matter in sintering and slagging of ash during the gasification process. Fuel Processing Technology. 2011;92(8):1426-33.

[58] Pike S, Dewison MG, Spears DA. Sources of error in low temperature plasma ashing procedures for quantitative mineral analysis of coal ash. Fuel. 1989;68(5):664-8.

[59] Ward CR. Analysis and significance of mineral matter in coal seams. International Journal of Coal Geology. 2002;50(1-4):135-68.

[60] Fuchs W, Sandhoff A. Theory of coal pyrolysis. Industrial & Engineering Chemistry. 1942;34(5):567-71.

[61] Solomon P, Fletcher T, Pugmire R. Progress in coal pyrolysis. Fuel. 1993;72(5):587-97.

[62] Xie K-C. Structure and reactivity of coal. Science, Beijing(In Chinese). 2002.

[63] Solomon PR, Serio MA, Suuberg EM. Coal pyrolysis: experiments, kinetic rates and mechanisms. Progress in Energy and Combustion Science. 1992;18(2):133-220.

[64] Molina A, Mondragon F. Reactivity of coal gasification with steam and CO2. Fuel. 1998;77(15):1831-9.

[65] Gadsby J, Long F, Sleightholm P, Sykes K. The mechanism of the carbon dioxide-carbon reaction. Proceedings of the Royal Society of London Series A Mathematical and Physical Sciences. 1948;193(1034):357-76.

[66] Hurt R. Development plan for CBK/gasification. Preliminary Report for Niksa Energy Associates, Belmont, CA. 2002.

[67] Laurendeau NM. Heterogeneous kinetics of coal char gasification and combustion. Progress in Energy and Combustion Science. 1978;4(4):221-70.

[68] Ergun S. Kinetics of the reaction of carbon with carbon dioxide. The Journal of Physical Chemistry. 1956;60(4):480-5.

[69] Kristiansen A. Understanding coal gasification. United Kingdom: N. p., 1996.

[70] Roberts DG, Hodge EM, Harris DJ, Stubington JF. Kinetics of char gasification with CO_2 under regime II conditions: effects of temperature, reactant, and total pressure. Energy & Fuels. 2010;24(10):5300-8.

[71] Radović LaR, Walker Jr PL, Jenkins RG. Effect of lignite pyrolysis conditions on calcium oxide dispersion and subsequent char reactivity. Fuel. 1983;62(2):209-12.

[72] Mathews JP, Eser S, Hatcher PG, Scaroni AW. The shape of pulverized bituminous vitrinite coal particles. KONA Powder and Particle Journal. 2007;25:145-52.

[73] Ye D, Agnew J, Zhang D. Gasification of a South Australian low-rank coal with carbon dioxide and steam: kinetics and reactivity studies. Fuel. 1998;77(11):1209-19.

[74] Beamish BB, Shaw KJ, Rodgers K, Newman J. Thermogravimetric determination of the carbon dioxide reactivity of char from some New Zealand coals and its association with the inorganic geochemistry of the parent coal. Fuel Processing Technology. 1998;53(3):243-53.

[75] Takarada T, Tamai Y, Tomita A. Reactivities of 34 coals under steam gasification. Fuel. 1985;64(10):1438-42.

[76] Miura K, Hashimoto K, Silveston PL. Factors affecting the reactivity of

coal chars during gasification, and indices representing reactivity. Fuel. 1989;68(11):1461-75.

[77] Huang Y-H, Yamashita H, Tomita A. Gasification reactivities of coal macerals. Fuel Processing Technology. 1991;29(1-2):75-84.

[78] Megaritis A, Messenböck R, Chatzakis I, Dugwell D, Kandiyoti R. High-pressure pyrolysis and CO_2-gasification of coal maceral concentrates: conversions and char combustion reactivities. Fuel. 1999;78(8):871-82.

[79] Sun Q, Li W, Chen H, Li B. The CO_2-gasification and kinetics of Shenmu maceral chars with and without catalyst. Fuel. 2004;83(13):1787-93.

[80] Wang J-H, Chang L-P. Pyrolysis and gasification reactivity of several typical Chinese coals and their macerals. Energy Sources, Part A: Recovery, Utilization, and Environmental Effects. 2015;37(6):670-8.

[81] Yu J, Lucas JA, Wall TF. Formation of the structure of chars during devolatilization of pulverized coal and its thermoproperties: A review. Progress in Energy and Combustion Science. 2007;33(2):135-70.

[82] Roberts MJ, Everson RC, Neomagus HW, Okolo GN, Van Niekerk D, Mathews JP. The characterisation of slow-heated inertinite-and vitrinite-rich coals from the South African coalfields. Fuel. 2015;158:591-601.

[83] Ochoa J, Cassanello M, Bonelli P, Cukierman A. CO_2 gasification of Argentinean coal chars: a kinetic characterization. Fuel Processing Technology. 2001;74(3):161-76.

[84] Kovacik G, Chambers A, Özüm B. CO_2 gasification kinetics of two Alberta coal chars. The Canadian Journal of Chemical Engineering. 1991;69(3):811-5.

[85] Kajitani S, Suzuki N, Ashizawa M, Hara S. CO_2 gasification rate analysis of coal char in entrained flow coal gasifier. Fuel. 2006;85(2):163-9.

[86] Chin G, Kimura S, Tone S, Otake T. Gasification of coal char with steam. Part 1: analysis of reaction rate. Int Chem Eng;(United States). 1983;23.

[87] Hanson S, Patrick JW, Walker A. The effect of coal particle size on pyrolysis and steam gasification. Fuel. 2002;81(5):531-7.

[88] Jayaraman K, Gokalp I. Effect of char generation method on steam, CO_2 and blended mixture gasification of high ash Turkish coals. Fuel. 2015;153:320-7.

[89] Xu W-C, Tomita A. Effect of coal type on the flash pyrolysis of various coals. Fuel. 1987;66(5):627-31.

[90] Furimsky E, Vancea L, Belanger R. Effect of coal rank on structure of tars from low-temperature pyrolysis of Canadian coals. Industrial & Engineering Chemistry Product Research and Development. 1984;23(1):134-40.

[91] Cheng L, Zhang R, Bi J. Pyrolysis of a low-rank coal in sub-and supercritical water. Fuel Processing Technology. 2004;85(8-10):921-32.

[92] Liu H, Xu L, Jin Y, Fan B, Qiao X, Yang Y. Effect of coal rank on structure and dielectric properties of chars. Fuel. 2015;153:249-56.

[93] Zhu W, Song W, Lin W. Effect of the coal particle size on pyrolysis and char reactivity for two types of coal and demineralized coal. Energy & Fuels. 2008;22(4):2482-7.

[94] Ludvig MM, Gard GL, Emmett PH. Use of controlled oxidation to increase the surface area of coal: application to a bituminous and a semi-anthracite coal.

Fuel. 1983;62(12):1393-6.

[95] Qiu J. The change of specific surface areas and porous structure in the coal particle thermal decomposition process: J. Fuel Chemistry Journals. 1994;22(3):316-9.

[96] Xiao J, Li F, Zhong Q, Huang J, Wang B, Zhang Y. Effect of high-temperature pyrolysis on the structure and properties of coal and petroleum coke. Journal of Analytical and Applied Pyrolysis. 2016;117:64-71.

[97] Cai H-Y, Güell A, Chatzakis IN, Lim J-Y, Dugwell D, Kandiyoti R. Combustion reactivity and morphological change in coal chars: effect of pyrolysis temperature, heating rate and pressure. Fuel. 1996;75(1):15-24.

[98] Wu C, Budarin VL, Wang M, Sharifi V, Gronnow MJ, Wu Y, et al. CO_2 gasification of bio-char derived from conventional and microwave pyrolysis. Applied Energy. 2015;157:533-9.

[99] Chen P, Xie Q, Addy M, Zhou W, Liu Y, Wang Y, et al. Utilization of municipal solid and liquid wastes for bioenergy and bioproducts production. Bioresource Technology. 2016;215:163-72.

[100] Mushtaq F, Mat R, Ani FN. A review on microwave assisted pyrolysis of coal and biomass for fuel production. Renewable and Sustainable Energy Reviews. 2014;39:555-74.

[101] Peng Z, Hwang J-Y, Kim B-G, Mouris J, Hutcheon R. Microwave absorption capability of high volatile bituminous coal during pyrolysis. Energy & Fuels. 2012;26(8):5146-51.

[102] Marland S, Han B, Merchant A, Rowson N. The effect of microwave

radiation on coal grindability. Fuel. 2000;79(11):1283-8.

[103] Lester E, Kingman S, Dodds C. Increased coal grindability as a result of microwave pretreatment at economic energy inputs. Fuel. 2005;84(4):423-7.

[104] Ge L, Zhang Y, Wang Z, Zhou J, Cen K. Effects of microwave irradiation treatment on physicochemical characteristics of Chinese low-rank coals. Energy Conversion and Management. 2013;71:84-91.

[105] Monsef-Mirzai P, Ravindran M, McWhinnie WR, Burchill P. Rapid microwave pyrolysis of coal: Methodology and examination of the residual and volatile phases. Fuel. 1995;74(1):20-7.

[106] Liu H-P, Chen T-P, Li Y, Song Z-Y, Wang S-W, Wu S-H. Temperature rise characteristics of ZhunDong coal during microwave pyrolysis. Fuel Processing Technology. 2016;148:317-23.

[107] Peng Z, Lin X, Li Z, Hwang J-Y, Kim B-G, Zhang Y, et al. Dielectric characterization of Indonesian low-rank coal for microwave processing. Fuel Processing Technology. 2017;156:171-7.

[108] Abdelsayed V, Shekhawat D, Smith MW, Link D, Stiegman AE. Microwave-assisted pyrolysis of Mississippi coal: A comparative study with conventional pyrolysis. Fuel. 2018;217:656-67.

[109] Reddy BR, Vinu R. Microwave assisted pyrolysis of Indian and Indonesian coals and product characterization. Fuel Processing Technology. 2016;154:96-103.

[110] Reddy BR, Shravani B, Das B, Dash PS, Vinu R. Microwave-assisted and analytical pyrolysis of coking and non-coking coals: Comparison of tar and char

compositions. Journal of Analytical and Applied Pyrolysis. 2019;142:104614.

[111] Binner E, Lester E, Kingman S, Dodds C, Robinson J, Wu T, et al. A review of microwave coal processing. Journal of Microwave Power and Electromagnetic Energy. 2014;48(1):35-60.

[112] Salema AA, Ani FN. Pyrolysis of oil palm empty fruit bunch biomass pellets using multimode microwave irradiation. Bioresource Technology. 2012;125:102-7.

[113] Liu T-f, Fang Y-t, Wang Y. An experimental investigation into the gasification reactivity of chars prepared at high temperatures. Fuel. 2008;87(4-5):460-6.

[114] Everson RC, Neomagus HW, Kaitano R, Falcon R, Du Cann VM. Properties of high ash coal-char particles derived from inertinite-rich coal: II. Gasification kinetics with carbon dioxide. Fuel. 2008;87(15-16):3403-8.

[115] Schmal M, Monteiro JLF, Toscani H. Gasification of high ash content coals with steam in a semibatch fluidized bed reactor. Industrial & Engineering Chemistry Process Design and Development. 1983;22(4):563-70.

[116] Adánez J, Miranda J, Gavilán J. Kinetics of a lignite-char gasification by CO_2. Fuel. 1985;64(6):801-4.

[117] Sha X-Z, Chen Y-G, Cao J, Yang Y-M, Ren D-Q. Effects of operating pressure on coal gasification. Fuel. 1990;69(5):656-9.

[118] Wang G, Zhang J, Shao J, Li K, Zuo H. Investigation of non-isothermal and isothermal gasification process of coal char using different kinetic model. International Journal of Mining Science and Technology. 2015;25(1):15-21.

[119] Jayaraman K, Gokalp I, Bonifaci E, Merlo N. Kinetics of steam and CO_2 gasification of high ash coal–char produced under various heating rates. Fuel. 2015;154:370-9.

[120] Wang F, Zeng X, Wang Y, Su H, Yu J, Xu G. Non-isothermal coal char gasification with CO_2 in a micro fluidized bed reaction analyzer and a thermogravimetric analyzer. Fuel. 2016;164:403-9.

[121] Huo W, Zhou Z, Wang F, Yu G. Mechanism analysis and experimental verification of pore diffusion on coke and coal char gasification with CO_2. Chemical Engineering Journal. 2014;244:227-33.

[122] Tanner J, Bhattacharya S. Kinetics of CO2 and steam gasification of Victorian brown coal chars. Chemical Engineering Journal. 2016;285:331-40.

[123] Hecht ES, Shaddix CR, Geier M, Molina A, Haynes BS. Effect of CO_2 and steam gasification reactions on the oxy-combustion of pulverized coal char. Combustion and Flame. 2012;159(11):3437-47.

[124] Mühlen H-J, van Heek KH, Jüntgen H. Kinetic studies of steam gasification of char in the presence of H_2, CO_2 and CO. Fuel. 1985;64(7):944-9.

[125] Roberts D, Harris D. Char gasification with O_2, CO_2, and H_2O: effects of pressure on intrinsic reaction kinetics. Energy & Fuels. 2000;14(2):483-9.

[126] Zhang L, Huang J, Fang Y, Wang Y. Gasification reactivity and kinetics of typical Chinese anthracite chars with steam and CO_2. Energy & Fuels. 2006;20(3):1201-10.

[127] Umemoto S, Kajitani S, Hara S. Modeling of coal char gasification in

coexistence of CO_2 and H_2O considering sharing of active sites. Fuel. 2013;103:14-21.

[128] Zhang R, Wang QH, Luo ZY, Fang MX, Cen KF. Competition and inhibition effects during coal char gasification in the mixture of H_2O and CO_2. Energy & Fuels. 2013;27(9):5107-15.

[129] Minchener AJ. Coal gasification for advanced power generation. Fuel. 2005;84(17):2222-35.

[130] Chmielniak T, Sciazko M. Co-gasification of biomass and coal for methanol synthesis. Applied Energy. 2003;74(3):393-403.

[131] Wang P, Massoudi M. Effect of coal properties and operation conditions on flow behavior of coal slag in entrained flow gasifiers: A brief review. National Energy Technology Lab.(NETL), Pittsburgh, PA, and Morgantown, WV; 2011.

[132] Huang Z, Zhang J, Yue G. Status of domestic gasification technology in China. Frontiers of Energy and Power Engineering in China. 2009;3(3):330-6.

[133] Gong Y, Yu G, Guo Q, Wang Y, Chen X, Wang F. Progress on opposed multi-burner (OMB) coal-water slurry gasification technology and its industrial applications. Energy Procedia. 2017;142:1089-94.

[134] Gong Y, Guo Q, Zhu H, Yu G. Refractory failure in entrained-flow gasifier: Investigation of partitioned erosion characteristics in an industrial opposed multi-burner gasifier. Chemical Engineering Science. 2019;210:115227.

[135] Doering E, Cremer G. Advances in the Shell coal gasification process. Preprints of Papers, American Chemical Society, Division of Fuel Chemistry.

1995;40(CONF-950402-).

[136] Ju Y, Lee C-H. Evaluation of the energy efficiency of the shell coal gasification process by coal type. Energy Conversion and Management. 2017;143:123-36.

[137] Wang F, Yu G, Gong X, Liu H, Wang Y, Liang Q. Research and development of large-scale coal gasification technology. Chemical Industry and Engineering Progress. 2009;268:77-82.

[138] Phillips J. Different types of gasifiers and their integration with gas turbines. The Gas Turbine Handbook. 2006;1:67-76.

[139] Krishnamoorthy V, Pisupati SV. A critical review of mineral matter related issues during gasification of coal in fixed, fluidized, and entrained flow gasifiers. Energies. 2015;8(9):10430-63.

[140] Wall TF, Liu G-s, Wu H-w, Roberts DG, Benfell KE, Gupta S, et al. The effects of pressure on coal reactions during pulverised coal combustion and gasification. Progress in Energy and Combustion Science. 2002;28(5):405-33.

[141] Zhao X, Zeng C, Mao Y, Li W, Peng Y, Wang T, et al. The surface characteristics and reactivity of residual carbon in coal gasification slag. Energy & Fuels. 2010;24(1):91-4.

[142] Xu S, Zhou Z, Gao X, Yu G, Gong X. The gasification reactivity of unburned carbon present in gasification slag from entrained-flow gasifier. Fuel Processing Technology. 2009;90(9):1062-70.

[143] Pan C, Liang Q, Guo X, Dai Z, Liu H, Gong X. Characteristics of different sized slag particles from entrained-flow coal gasification. Energy & Fuels.

2016;30(2):1487-95.

[144] Wu S, Huang S, Ji L, Wu Y, Gao J. Structure characteristics and gasification activity of residual carbon from entrained-flow coal gasification slag. Fuel. 2014;122:67-75.

[145] Dai G, Zheng S, Wang X, Bai Y, Dong Y, Du J, et al. Combustibility analysis of high-carbon fine slags from an entrained flow gasifier. Journal of Environmental Management. 2020;271:111009.

[146] Bunt J, Waanders F. Trace element behaviour in the Sasol–Lurgi MK IV FBDB gasifier. Part 1–the volatile elements: Hg, As, Se, Cd and Pb. Fuel. 2008;87(12):2374-87.

[147] Bunt J, Waanders F. Trace element behaviour in the Sasol–Lurgi MK IV FBDB gasifier. Part 2–The semi-volatile elements: Cu, Mo, Ni and Zn. Fuel. 2009;88(6):961-9.

[148] Bunt JR, Waanders FB. Trace element behaviour in the Sasol-Lurgi fixed-bed dry-bottom gasifier. Part 3–The non-volatile elements: Ba, Co, Cr, Mn, and V. Fuel. 2010;89(3):537-48.

[149] Chen G, Sun Y, Yan B, Yang R, Liu B, Cheng Z, et al. Distribution of trace elements during coal gasification: the effect of upgrading method. Journal of Cleaner Production. 2018;190:193-9.

[150] Kapusta K, Stańczyk K. Pollution of water during underground coal gasification of hard coal and lignite. Fuel. 2011;90(5):1927-34.

[151] Strugała-Wilczek A, Stańczyk K. Comparison of metal elution from cavern residue after underground coal gasification and from ash obtained during

coal combustion. Fuel. 2015;158:733-43.

[152] Strugała-Wilczek A, Stańczyk K. Leaching behaviour of metals from post-underground coal gasification cavity residues in water differing in mineralization. Fuel. 2016;173:106-14.

[153] Tang Y, Wang Y, Huan B, Guo X, Finkelman RB. Leachability of hazardous trace elements from entrained-flow coal gasification residues in Ningdong, China. Energy & Fuels. 2017;31(9):9703-16.

[154] Wang Y, Tang Y, Guo X, Xie Q, Finkelman RB, Li P, et al. Fate of potentially hazardous trace elements during the entrained-flow coal gasification processes in China. Science of The Total Environment. 2019;668:854-66.

[155] Tang Y, Guo X, Pan X, Finkelman RB, Wang Y, Huan B, et al. Changes and distribution of modes of occurrence of seventeen potentially-hazardous trace elements during entrained flow gasification of coals from Ningdong, China. Minerals. 2018;8(5):202.

[156] Zhao X, Zhang X, Liu Z, Lu Z, Liu Q. Organic matter in Yilan oil shale: characterization and pyrolysis with or without inorganic minerals. Energy & Fuels. 2017;31(4):3784-92.

[157] Ru X, Cheng Z, Song L, Wang H, Li J. Experimental and computational studies on the average molecular structure of Chinese Huadian oil shale kerogen. Journal of Molecular Structure. 2012;1030:10-8.

[158] R NRCPo, Coal DNiRo, Liquids S, Research USE, Administration D. Refining synthetic liquids from coal and shale: final report of the Panel on R&D Needs in Refining of Coal and Shale Liquids, Energy Engineering Board,

Assembly of Engineering: National Academy Press, 1980.

[159] Liu X, Cui P, Ling Q, Zhao Z, Xie R. A review on co-pyrolysis of coal and oil shale to produce coke. Frontiers of Chemical Science and Engineering. 2020;14(4):504-12.

[160] Kang Z, Zhao Y, Yang D. Review of oil shale in-situ conversion technology. Applied Energy. 2020;269:115121.

[161] Külaots I, Goldfarb JL, Suuberg EM. Characterization of Chinese, American and Estonian oil shale semicokes and their sorptive potential. Fuel. 2010;89(11):3300-6.

[162] Vyas A, Xue J, Goldfarb JL. Improving the environmental and economic viability of US oil shale via waste-to-byproduct conversion of semicoke to sorbents. Energy & Fuels. 2016;30(1):188-95.

[163] Kikas V. Application of shale ash in the building materials industry: Polytechnic Institute, 1968.

[164] Kikas V. Mineral matter of kukersite oil shale and its utilization. Oil Shale. 1988;5(1):15-27.

[165] Yan J, Jiang X, Han X. Study on the Characteristics of the Oil Shale and Shale Char Mixture Pyrolysis. Energy & Fuels. 2009;23(12):5792-7.

[166] Jiang H, Zhang M, Chen J, Li S, Shao Y, Yang J, et al. Characteristics of bio-oil produced by the pyrolysis of mixed oil shale semi-coke and spent mushroom substrate. Fuel. 2017;200:218-24.

[167] Han X, Jiang X, Cui Z. Study of the combustion mechanism of oil shale semicoke in a thermogravimetric analyzer. Journal of Thermal Analysis and

Calorimetry. 2008;92(2):595-600.

[168] Yang Y, Lu X, Wang Q, Mei L, Song D, Hong Y. Experimental study on combustion of low calorific oil shale semicoke in fluidized bed system. Energy & Fuels. 2016;30(11):9882-90.

[169] Wang Q, Wang H, Sun B, Bai J, Guan X. Interactions between oil shale and its semi-coke during co-combustion. Fuel. 2009;88(8):1520-9.

[170] Liu H, Feng S, Zhang S, Xuan H, Jia C, Wang Q. Analysis of the pore structure of Longkou oil shale semicoke during fluidized bed combustion. Oil Shale. 2020;37(2):89-103.

[171] Liu H-p, Liang W-x, Wu M-h, Wang Q. Co-combustion of oil shale retorting solid waste with cornstalk particles in a circulating fluidized bed. Energy & Fuels. 2015;29(10):6832-8.

[172] Trikkel A, Kuusik R, Martins A, Pihu T, Stencel JM. Utilization of Estonian oil shale semicoke. Fuel Processing Technology. 2008;89(8):756-63.

[173] Al-Asheh S, Banat F, Masad A. Physical and chemical activation of pyrolyzed oil shale residue for the adsorption of phenol from aqueous solutions. Environmental Geology. 2003;44(3):333-42.

[174] Han X, Kulaots I, Jiang X, Suuberg EM. Review of oil shale semicoke and its combustion utilization. Fuel. 2014;126:143-61.

[175] Kaljuvee T, Prikk A, Trikkel A, Arroc H. Fluidized-bed combustion of oil shale retorting solid waste. Oil Shale. 2004;21(3):237.

[176] Han X, Jiang X, Cui Z. Thermal analysis studies on combustion mechanism of oil shale. Journal of Thermal Analysis and Calorimetry.

2006;84(3):631-6.

[177] Kök M, Pamir M. ASTM kinetics of oil shales. Journal of Thermal Analysis and Calorimetry. 1998;53(2):567-75.

[178] Brendow K. Global oil shale issues and perspectives (Synthesis of the Symposium on Oil Shale held in Tallinn (Estonia) on 18 and 19 November 2002). Oil Shale. 2003;20(1):81-92.

[179] Oja V, Suuberg EM. Oil Shale Processing, Chemistry, and Technology. Fossil Energy. 2020:47-83.

[180] Hotta A, Parkkonen R, Hiltunen M, Arro H, Loosaar J, Parve T, et al. Experience of estonian oil shale combustion based on CFB technology at Narva power plants. Oil Shale. 2005;22(4):381-97.

[181] Jiang X, Han X, Cui Z. Progress and recent utilization trends in combustion of Chinese oil shale. Progress in Energy and Combustion Science. 2007;33(6):552-79.

[182] Jiang X, Cui Z, Han X, Yu H. Thermogravimetric investigation on combustion characteristics of oil shale and high sulphur coal mixture. Journal of Thermal Analysis and Calorimetry. 2006;85(3):761-4.

[183] Wang Q, Zhao W, Liu H, Jia C, Li S. Interactions and kinetic analysis of oil shale semi-coke with cornstalk during co-combustion. Applied Energy. 2011;88(6):2080-7.

[184] Özgür E, Miller SF, Miller BG, Kök MV. Thermal analysis of co-firing of oil shale and biomass fuels. Oil Shale. 2012;29(2):190-201.

[185] Torres M, Portugau P, Cuña A, Castiglioni J, Yermán L. Pollutant gas

emissions during the co-combustion of oil shales from Uruguay with biomass wastes. Proceedings of the 4th World Congress on Momentum, Heat and Mass Transfer (MHMT'19). 2019.

[186] Yao Z, Ma X, Wang Z, Chen L. Characteristics of co-combustion and kinetic study on hydrochar with oil shale: A thermogravimetric analysis. Applied Thermal Engineering. 2017;110:1420-7.

[187] Fan Y, Yu Z, Fang S, Lin Y, Lin Y, Liao Y, et al. Investigation on the co-combustion of oil shale and municipal solid waste by using thermogravimetric analysis. Energy Conversion and Management. 2016;117:367-74.

[188] Yu H-l, Jiang X-m, Zhao X, Zhou J-h, Cen K-f. Study on combustion property of mixture of oil shale and Heshan coal. Journal of Fuel Chemistry and Technology. 2004;32(3):274-7.

[189] Gai C, Liu Z, Han G, Peng N, Fan A. Combustion behavior and kinetics of low-lipid microalgae via thermogravimetric analysis. Bioresource Technology. 2015;181:148-54.

[190] Lu Y, Wang Y, Zhao Y, Wei Z, Li Y, Hao W, et al. The characteristics of mineralogy, morphology and sintering during co-combustion of Zhundong coal and oil shale. RSC Advances. 2017;7(81):51036-45.

[191] García G, Arauzo J, Gonzalo A, Sánchez JL, Ábrego J. Influence of feedstock composition in fluidised bed co-gasification of mixtures of lignite, bituminous coal and sewage sludge. Chemical Engineering Journal. 2013;222:345-52.

[192] Aznar MP, Caballero MA, Sancho JA, Francés E. Plastic waste

elimination by co-gasification with coal and biomass in fluidized bed with air in pilot plant. Fuel Processing Technology. 2006;87(5):409-20.

[193] Masnadi MS, Grace JR, Bi XT, Lim CJ, Ellis N. From fossil fuels towards renewables: Inhibitory and catalytic effects on carbon thermochemical conversion during co-gasification of biomass with fossil fuels. Applied Energy. 2015;140:196-209.

[194] Beagle E, Wang Y, Bell D, Belmont E. Co-gasification of pine and oak biochar with sub-bituminous coal in carbon dioxide. Bioresource Technology. 2018;251:31-9.

[195] Fermoso J, Arias B, Plaza M, Pevida C, Rubiera F, Pis J, et al. High-pressure co-gasification of coal with biomass and petroleum coke. Fuel Processing Technology. 2009;90(7-8):926-32.

[196] Ren L, Wei R, Gao Y. Co-gasification reactivity of petcoke and coal at high temperature. Fuel. 2017;190:245-52.

[197] Azargohar R, Gerspacher R, Dalai AK, Peng D-Y. Co-gasification of petroleum coke with lignite coal using fluidized bed gasifier. Fuel Processing Technology. 2015;134:310-6.

[198] Fan J, Hong H, Jin H. Biomass and coal co-feed power and SNG polygeneration with chemical looping combustion to reduce carbon footprint for sustainable energy development: Process simulation and thermodynamic assessment. Renewable Energy. 2018;125:260-9.

[199] Li S, Ma X. CO_2 gasification characteristics of nascent pyrolyzed particles from coals and oil shale. International Journal of Energy Research.

2017;41(11):1612-25.

[200] Zamaniyan A, Joda F, Behroozsarand A, Ebrahimi H. Application of artificial neural networks (ANN) for modeling of industrial hydrogen plant. International Journal of Hydrogen Energy. 2013;38(15):6289-97.

[201] Patil-Shinde V, Kulkarni T, Kulkarni R, Chavan PD, Sharma T, Sharma BK, et al. Artificial intelligence-based modeling of high ash coal Gasification in a pilot plant scale fluidized bed gasifier. Industrial & Engineering Chemistry Research. 2014;53(49):18678-89.

[202] Pandey DS, Das S, Pan I, Leahy JJ, Kwapinski W. Artificial neural network based modelling approach for municipal solid waste gasification in a fluidized bed reactor. Waste Management. 2016;58:202-13.

[203] Puig-Arnavat M, Hernández JA, Bruno JC, Coronas A. Artificial neural network models for biomass gasification in fluidized bed gasifiers. Biomass and Bioenergy. 2013;49:279-89.

[204] Ozonoh M, Oboirien B, Higginson A, Daramola M. Performance evaluation of gasification system efficiency using artificial neural network. Renewable Energy. 2020;145:2253-70.

[205] Chavan P, Sharma T, Mall B, Rajurkar B, Tambe S, Sharma B, et al. Development of data-driven models for fluidized-bed coal gasification process. Fuel. 2012;93:44-51.

[206] Xie C, Liu J, Zhang X, Xie W, Sun J, Chang K, et al. Co-combustion thermal conversion characteristics of textile dyeing sludge and pomelo peel using TGA and artificial neural networks. Applied Energy. 2018;212:786-95.

[207] Buyukada M. Co-combustion of peanut hull and coal blends: Artificial neural networks modeling, particle swarm optimization and Monte Carlo simulation. Bioresource Technology. 2016;216:280-6.

[208] Buyukada M, Aydogmus E. Utilization of apricot seed in (co-) combustion of lignite coal blends: Numeric optimization, empirical modeling and uncertainty estimation. Fuel. 2018;216:190-8.

[209] Buyukada M. Investigation of thermal conversion characteristics and performance evaluation of co-combustion of pine sawdust and lignite coal using TGA, artificial neural network modeling and likelihood method. Bioresource Technology. 2019;287:121461.

[210] Chen J, Liu J, He Y, Huang L, Sun S, Sun J, et al. Investigation of co-combustion characteristics of sewage sludge and coffee grounds mixtures using thermogravimetric analysis coupled to artificial neural networks modeling. Bioresource Technology. 2017;225:234-45.

[211] Huang H-X, Li J-C, Xiao C-L. A proposed iteration optimization approach integrating backpropagation neural network with genetic algorithm. Expert Systems with Applications. 2015;42(1):146-55.

[212] Zeng Y-R, Zeng Y, Choi B, Wang L. Multifactor-influenced energy consumption forecasting using enhanced back-propagation neural network. Energy. 2017;127:381-96.

[213] Kundu P, Paul V, Kumar V, Mishra IM. Formulation development, modeling and optimization of emulsification process using evolving RSM coupled hybrid ANN-GA framework. Chemical Engineering Research and Design. 2015;104:773-90.

[214] Ptasinski KJ, Prins MJ, Pierik A. Exergetic evaluation of biomass gasification. Energy. 2007;32(4):568-74.

[215] Lin Y, Tanaka S. Ethanol fermentation from biomass resources: current state and prospects. Applied Microbiology and Biotechnology. 2006;69(6):627-42.

[216] Caputo AC, Palumbo M, Pelagagge PM, Scacchia F. Economics of biomass energy utilization in combustion and gasification plants: effects of logistic variables. Biomass and Bioenergy. 2005;28(1):35-51.

[217] Van der Drift A, Boerrigter H, Coda B, Cieplik M, Hemmes K. Entrained flow gasification of biomass ash behaviour, feeding issues, system analyses: Petten: ECN, 2004.

[218] Basu P. Biomass gasification, pyrolysis and torrefaction: practical design and theory: Academic Press, 2018.

[219] Zhang Y, Xiao J, Shen L. Simulation of methanol production from biomass gasification in interconnected fluidized beds. Industrial & Engineering Chemistry Research. 2009;48(11):5351-9.

[220] Rauch R, Hofbauer H, Bosch K, Siefert I, Aichernig C, Voigtlaender K, et al. Steam gasification of biomass at CHP plant Guessing-Status of the demonstration plant: Citeseer, 2004.

[221] Katikaneni SP, Adjaye JD, Idem RO, Bakhshi NN. Catalytic conversion of canola oil over Potassium-impregnated HZSM-5 Catalysts: C2− C4 olefin production and model reaction studies. Industrial & Engineering Chemistry Research. 1996;35(10):3332-46.

[222] Masudi A, Jusoh NWC, Muraza O. Opportunities for less-explored zeolitic materials in the syngas-to-olefins pathway over nanoarchitectured catalysts: a mini review. Catalysis Science & Technology. 2020;10(6):1582-96.

[223] Ren T, Patel M, Blok K. Olefins from conventional and heavy feedstocks: Energy use in steam cracking and alternative processes. Energy. 2006;31(4):425-51.

[224] Funk GA, Myers D, Vora B. A different game plan. Hydrocarbon Engineering. 2013;18(12):25-8.

[225] Pyl SP, Schietekat CM, Reyniers M-F, Abhari R, Marin GB, Van Geem KM. Biomass to olefins: Cracking of renewable naphtha. Chemical Engineering Journal. 2011;176-177:178-87.

[226] Andersson J, Lundgren J, Marklund M. Methanol production via pressurized entrained flow biomass gasification – Techno-economic comparison of integrated vs. stand-alone production. Biomass and Bioenergy. 2014;64:256-68.

[227] Holmgren KM, Andersson E, Berntsson T, Rydberg T. Gasification-based methanol production from biomass in industrial clusters: Characterisation of energy balances and greenhouse gas emissions. Energy. 2014;69:622-37.

[228] Kumabe K, Fujimoto S, Yanagida T, Ogata M, Fukuda T, Yabe A, et al. Environmental and economic analysis of methanol production process via biomass gasification. Fuel. 2008;87(7):1422-7.

[229] Johansson E. Process integration study of biomass-tomethanol (via gasification) and methanol-toolefins (MTO) processes in an existing steam

cracker plant. Chalmers University of Technology, Göteborg (Sweden). 2013.

[230] Onel O, Niziolek AM, Elia JA, Baliban RC, Floudas CA. Biomass and natural gas to liquid transportation fuels and olefins (BGTL+ C2_C4): process synthesis and global optimization. Industrial & Engineering Chemistry Research. 2015;54(1):359-85.

[231] Zhang S, Dai Z, Xu J, Liu H, Wang F. Sensitivity and safety boundary analysis of opposed multi-burner coal water slurry gasification system. International Journal of Energy Research. 2020;44(3):2278-88.

[232] Shi K, Yan J, Luo X, Lester E, Wu T. Microwave-assisted pyrolysis of bamboo coupled with reforming by activated carbon for the production of hydrogen-rich syngas. Energy Procedia. 2017;142:1640-6.

[233] Marland S, Merchant A, Rowson N. Dielectric properties of coal. Fuel. 2001;80(13):1839-49.

[234] Atwater J, Wheeler R. Temperature dependent complex permittivities of graphitized carbon blacks at microwave frequencies between 0.2 and 26 GHz. Journal of Materials Science. 2004;39(1):151-7.

[235] Coats A, Redfern J. Thermogravimetric analysis. A review. Analyst. 1963;88(1053):906-24.

[236] Dwivedi KK, Chatterjee P, Karmakar M, Pramanick A. Pyrolysis characteristics and kinetics of Indian low rank coal using thermogravimetric analysis. International Journal of Coal Science & Technology. 2019;6(1):102-12.

[237] Wang G, Zhang J, Shao J, Liu Z, Wang H, Li X, et al. Experimental and

modeling studies on CO2 gasification of biomass chars. Energy. 2016;114:143-54.

[238] Xu C, Hu S, Xiang J, Zhang L, Sun L, Shuai C, et al. Interaction and kinetic analysis for coal and biomass co-gasification by TG–FTIR. Bioresource Technology. 2014;154:313-21.

[239] Edreis EMA, Luo G, Li A, Xu C, Yao H. Synergistic effects and kinetics thermal behaviour of petroleum coke/biomass blends during H_2O co-gasification. Energy Conversion and Management. 2014;79:355-66.

[240] Zhong Q, Zhang J, Yang Y, Jiang T, Li Q, Xu B. Combustion behavior of coals in rotary kiln and their interaction on co-combustion. Energy & Fuels. 2018;32(3):3833-41.

[241] Cong K, Han F, Zhang Y, Li Q. The investigation of co-combustion characteristics of tobacco stalk and low rank coal using a macro-TGA. Fuel. 2019;237:126-32.

[242] Wu T, Gong M, Lester E, Hall P. Characteristics and synergistic effects of co-firing of coal and carbonaceous wastes. Fuel. 2013;104:194-200.

[243] Xie W, Wen S, Liu J, Xie W, Kuo J, Lu X, et al. Comparative thermogravimetric analyses of co-combustion of textile dyeing sludge and sugarcane bagasse in carbon dioxide/oxygen and nitrogen/oxygen atmospheres: thermal conversion characteristics, kinetics, and thermodynamics. Bioresource Technology. 2018;255:88-95.

[244] Wang Z, Hong C, Xing Y, Li Y, Feng L, Jia M. Combustion behaviors and kinetics of sewage sludge blended with pulverized coal: With and without

catalysts. Waste Management. 2018;74:288-96.

[245] Liu C, Liu J, Sun G, Xie W, Kuo J, Li S, et al. Thermogravimetric analysis of (co-) combustion of oily sludge and litchi peels: combustion characterization, interactions and kinetics. Thermochimica Acta. 2018;667:207-18.

[246] Vyazovkin S, Burnham AK, Criado JM, Pérez-Maqueda LA, Popescu C, Sbirrazzuoli N. ICTAC Kinetics Committee recommendations for performing kinetic computations on thermal analysis data. Thermochimica Acta. 2011;520(1-2):1-19.

[247] Chen C, Lu Z, Ma X, Long J, Peng Y, Hu L, et al. Oxy-fuel combustion characteristics and kinetics of microalgae Chlorella vulgaris by thermogravimetric analysis. Bioresource Technology. 2013;144:563-71.

[248] Coats AW, Redfern J. Kinetic parameters from thermogravimetric data. Nature. 1964;201(4914):68.

[249] Vuppaladadiyam AK, Memon MZ, Ji G, Raheem A, Jia TZ, Dupont V, et al. Thermal characteristics and kinetic analysis of woody biomass pyrolysis in the presence of bifunctional alkali metal ceramics. ACS Sustainable Chemistry & Engineering. 2018;7(1):238-48.

[250] Long Q, Xia Y, Liao S, Li Y, Wu W, Huang Y. Facile synthesis of hydrotalcite and its thermal decomposition kinetics mechanism study with masterplots method. Thermochimica Acta. 2014;579:50-5.

[251] Zhu Q. Coal sampling and analysis standards. IEA Clean Coal Centre, London, United Kingdom. 2014.

[252] Huo W, Zhou Z, Chen X, Dai Z, Yu G. Study on CO_2 gasification

reactivity and physical characteristics of biomass, petroleum coke and coal chars. Bioresource Technology. 2014;159:143-9.

[253] Ure A, Quevauviller P, Muntau H, Griepink B. Speciation of heavy metals in soils and sediments. An account of the improvement and harmonization of extraction techniques undertaken under the auspices of the BCR of the Commission of the European Communities. International Journal of Environmental Analytical Chemistry. 1993;51(1-4):135-51.

[254] Reid MK, Spencer KL, Shotbolt L. An appraisal of microwave-assisted Tessier and BCR sequential extraction methods for the analysis of metals in sediments and soils. Journal of Soils and Sediments. 2011;11(3):518-28.

[255] Nemati K, Bakar NKA, Abas MR, Sobhanzadeh E. Speciation of heavy metals by modified BCR sequential extraction procedure in different depths of sediments from Sungai Buloh, Selangor, Malaysia. Journal of Hazardous Materials. 2011;192(1):402-10.

[256] Akdağ AS, Atak O, Atimtay AT, Sanin FD. Co-combustion of sewage sludge from different treatment processes and a lignite coal in a laboratory scale combustor. Energy. 2018;158:417-26.

[257] Pronobis M. Evaluation of the influence of biomass co-combustion on boiler furnace slagging by means of fusibility correlations. Biomass and Bioenergy. 2005;28(4):375-83.

[258] Teixeira P, Lopes H, Gulyurtlu I, Lapa N, Abelha P. Evaluation of slagging and fouling tendency during biomass co-firing with coal in a fluidized bed. Biomass and Bioenergy. 2012;39:192-203.

[259] Dirbeba MJ, Brink A, Zevenhoven M, DeMartini N, Lindberg D, Hupa L, et al. Characterization of vinasse for thermochemical conversion—fuel fractionation, release of inorganics, and ash-melting behavior. Energy & Fuels. 2019.

[260] Xiong Q-a, Li J, Guo S, Li G, Zhao J, Fang Y. Ash fusion characteristics during co-gasification of biomass and petroleum coke. Bioresource Technology. 2018;257:1-6.

[261] Reinmöller M, Klinger M, Schreiner M, Gutte H. Relationship between ash fusion temperatures of ashes from hard coal, brown coal, and biomass and mineral phases under different atmospheres: a combined FactSage™ computational and network theoretical approach. Fuel. 2015;151:118-23.

[262] Song WJ, Tang LH, Zhu XD, Wu YQ, Zhu ZB, Koyama S. Prediction of Chinese coal ash fusion temperatures in Ar and H_2 atmospheres. Energy & Fuels. 2009;23(4):1990-7.

[263] Yıldız Z, Uzun H, Ceylan S, Topcu Y. Application of artificial neural networks to co-combustion of hazelnut husk–lignite coal blends. Bioresource Technology. 2016;200:42-7.

[264] Sunphorka S, Chalermsinsuwan B, Piumsomboon P. Artificial neural network model for the prediction of kinetic parameters of biomass pyrolysis from its constituents. Fuel. 2017;193:142-58.

[265] Hornik K, Stinchcombe M, White H. Multilayer feedforward networks are universal approximators. Neural Networks. 1989;2(5):359-66.

[266] Rong Y, Zhang Z, Zhang G, Yue C, Gu Y, Huang Y, et al. Parameters

optimization of laser brazing in crimping butt using Taguchi and BPNN-GA. Optics and Lasers in Engineering. 2015;67:94-104.

[267] Dupont C, Nocquet T, Da Costa Jr JA, Verne-Tournon C. Kinetic modelling of steam gasification of various woody biomass chars: influence of inorganic elements. Bioresource Technology. 2011;102(20):9743-8.

[268] Fan J, Hong H, Zhu L, Wang Z, Jin H. Thermodynamic evaluation of chemical looping combustion for combined cooling heating and power production driven by coal. Energy Conversion and Management. 2017;135:200-11.

[269] Zhang Y, Hara S, Kajitani S, Ashizawa M. Modeling of catalytic gasification kinetics of coal char and carbon. Fuel. 2010;89(1):152-7.

[270] Renganathan T, Yadav M, Pushpavanam S, Voolapalli R, Cho Y. CO_2 utilization for gasification of carbonaceous feedstocks: a thermodynamic analysis. Chemical Engineering Science. 2012;83:159-70.

[271] Sadhwani N, Li P, Eden MR, Adhikari S. Process modeling of fluidized bed biomass-CO_2 gasification using ASPEN Plus. In: Espuña A, Graells M, Puigjaner L, editors. Computer Aided Chemical Engineering: Elsevier; 2017. p. 2509-14.

[272] Guizani C, Louisnard O, Sanz FJE, Salvador S. Gasification of woody biomass under high heating rate conditions in pure CO_2: experiments and modelling. Biomass and Bioenergy. 2015;83:169-82.

[273] Cheng Y, Thow Z, Wang C-H. Biomass gasification with CO_2 in a fluidized bed. Powder Technology. 2016;296:87-101.

[274] Liu Q, He H, Li H, Jia J, Huang G, Xing B, et al. Characteristics and kinetics of coal char steam gasification under microwave heating. Fuel. 2019;256:115899.

[275] Liu H, Chen T, Fang L. Evolution of char structure during non-isothermal low temperature pyrolysis of ZhunDong coal by microwave heating: A comparative study with conventional heating. Journal of the Energy Institute. 2020;93(3):1195-206.

[276] Xu J, Zuo H, Wang G, Zhang J, Guo K, Liang W. Gasification mechanism and kinetics analysis of coke using distributed activation energy model (DAEM). Applied Thermal Engineering. 2019;152:605-14.

[277] Li H, Yu Y, Han M, Lei Z. Simulation of coal char gasification using O_2/CO_2. International Journal of Coal Science & Technology. 2014;1(1):81-7.

[278] Jiang P, Parvez AM, Meng Y, Xu M-x, Shui T-c, Sun C-g, et al. Exergetic, economic and carbon emission studies of bio-olefin production via indirect steam gasification process. Energy. 2019;187:115933.

[279] Jiang P, Guo D, Luo X, Xu M, Wu T. Comparative study of the gasification of coal and its macerals and prediction of the synergistic effects under typical entrained-bed pulverized coal gasification conditions. Journal of Energy Resources Technology. 2020;142(3).

[280] Sun Q, Li W, Chen H, Li B. The variation of structural characteristics of macerals during pyrolysis☆. Fuel. 2003;82(6):669-76.

[281] Sun Q, Li W, Li B. The synergistic effect between macerals during pyrolysis. Fuel. 2002;81(7):973-4.

[282] Chang H, Deng H, Yang Q, Du S, Hu F, Jia C. Interaction of vitrinite and inertinite of Bulianta coal in pyrolysis. Fuel. 2017;207:643-9.

[283] Sun Q, Li W, Chen H, Li B. The synergistic effect between coal macerals during hydropyrolysis. Energy Sources, Part A. 2007;29(2):125-32.

[284] Zubkova V, Kosewska M, Wrobelska K, Prezhdo V. Synergetic effects during carbonisation of Polish orthocoking coals. Fuel Processing Technology. 2005;86(8):899-912.

[285] Xiangdong K, Zhong W, Wenli D, Feng Q. Three stage equilibrium model for coal gasification in entrained flow gasifiers based on aspen plus. Chinese Journal of Chemical Engineering. 2013;21(1):79-84.

[286] Zhao Y, Yu B, Wang B, Zhang S, Xiao Y. Heat integration and optimization of direct-fired supercritical CO_2 power cycle coupled to coal gasification process. Applied Thermal Engineering. 2018;130:1022-32.

[287] Mallick D, Buragohain B, Mahanta P, Moholkar VS. Gasification of mixed biomass: analysis using equilibrium, semi-equilibrium, and kinetic models. Coal and Biomass Gasification: Springer; 2018. p. 223-41.

[288] Becker WL, Penev M, Braun RJ. Production of synthetic natural gas from carbon dioxide and renewably generated hydrogen: a techno-economic analysis of a power-to-gas strategy. Journal of Energy Resources Technology. 2019;141(2):021901.

[289] Martelli E, Kreutz T, Carbo M, Consonni S, Jansen D. Shell coal IGCCS with carbon capture: conventional gas quench vs. innovative configurations. Applied Energy. 2011;88(11):3978-89.

[290] Maurstad O. An overview of coal based integrated gasification combined cycle (IGCC). Technology; MIT LFEE 2005-002 WP; Laboratory for Energy and the Environment, Massachusetts Institute of Technology.

[291] Higman C, van der Burgt M. Gasification. 2nd. 2008.

[292] Collot A-G. Matching gasification technologies to coal properties. International Journal of Coal Geology. 2006;65(3-4):191-212.

[293] Fernandez-Lopez M, Pedroche J, Valverde J, Sanchez-Silva L. Simulation of the gasification of animal wastes in a dual gasifier using Aspen Plus®. Energy Conversion and Management. 2017;140:211-7.

[294] Zhu L, Jiang P, Fan J. Comparison of carbon capture IGCC with chemical-looping combustion and with calcium-looping process driven by coal for power generation. Chemical Engineering Research and Design. 2015;104:110-24.

[295] Al-Zareer M, Dincer I, Rosen MA. Influence of Selected Gasification Parameters on Syngas Composition From Biomass Gasification. Journal of Energy Resources Technology. 2018;140(4):041803.

[296] Fan J, Hong H, Zhu L, Jiang Q, Jin H. Thermodynamic and environmental evaluation of biomass and coal co-fuelled gasification chemical looping combustion with CO_2 capture for combined cooling, heating and power production. Applied Energy. 2017;195:861-76.

[297] Ogidiama OV, Zahra MA, Shamim T. Techno-economic analysis of a carbon capture chemical looping combustion power plant. Journal of Energy Resources Technology. 2018;140(11):112004.

[298] Xie K-C. Structure and reactivity of coal: a survey of selected Chinese

coals. Heidelberg: Springer, 2015.

[299] JIAO S. Choice of gasifier's pattern for IGCC power plant. Gas Turbine Technology. 2002;15(2):5-14.

[300] Li S, Jin H, Gao L. Cogeneration of substitute natural gas and power from coal by moderate recycle of the chemical unconverted gas. Energy. 2013;55:658-67.

[301] Duan W, Yu Q, Zuo Z, Qin Q, Li P, Liu J. The technological calculation for synergistic system of BF slag waste heat recovery and carbon resources reduction. Energy Conversion and Management. 2014;87:185-90.

[302] Seo H-K, Park S, Lee J, Kim M, Chung S-W, Chung J-H, et al. Effects of operating factors in the coal gasification reaction. Korean Journal of Chemical Engineering. 2011;28(9):1851.

[303] Channiwala S, Parikh P. A unified correlation for estimating HHV of solid, liquid and gaseous fuels. Fuel. 2002;81(8):1051-63.

[304] Bilgen S, Kaygusuz K, Sari A. Second law analysis of various types of coal and woody biomass in Turkey. Energy Sources. 2004;26(11):1083-94.

[305] Elliott MA. Chemistry of coal utilization. Second Supplementary Volume. 1981.

[306] Edreis EMA, Luo G, Li A, Chao C, Hu H, Zhang S, et al. CO_2 co-gasification of lower sulphur petroleum coke and sugar cane bagasse via TG–FTIR analysis technique. Bioresource Technology. 2013;136:595-603.

[307] Wu S, Huang S, Wu Y, Gao J. Characteristics and catalytic actions of inorganic constituents from entrained-flow coal gasification slag. Journal of the

Energy Institute. 2015;88(1):93-103.

[308] Tang Y, Guo X, Xie Q, Finkelman RB, Han S, Huan B, et al. Petrological characteristics and trace element partitioning of gasification residues from slagging entrained-flow gasifiers in Ningdong, China. Energy & Fuels. 2018;32(3):3052-67.

[309] Dai S, Seredin VV, Ward CR, Hower JC, Xing Y, Zhang W, et al. Enrichment of U–Se–Mo–Re–V in coals preserved within marine carbonate successions: geochemical and mineralogical data from the Late Permian Guiding Coalfield, Guizhou, China. Mineralium Deposita. 2015;50(2):159-86.

[310] Dai S, Ren D, Chou C-L, Finkelman RB, Seredin VV, Zhou Y. Geochemistry of trace elements in Chinese coals: a review of abundances, genetic types, impacts on human health, and industrial utilization. International Journal of Coal Geology. 2012;94:3-21.

[311] Hu G, Liu G, Wu D, Fu B. Geochemical behavior of hazardous volatile elements in coals with different geological origin during combustion. Fuel. 2018;233:361-76.

[312] Finkelman RB, Palmer CA, Wang P. Quantification of the modes of occurrence of 42 elements in coal. International Journal of Coal Geology. 2018;185:138-60.

[313] Finkelman RB. Modes of occurrence of potentially hazardous elements in coal: levels of confidence. Fuel Processing Technology. 1994;39(1-3):21-34.

[314] Riley K, French D, Farrell O, Wood R, Huggins F. Modes of occurrence of trace and minor elements in some Australian coals. International Journal of

Coal Geology. 2012;94:214-24.

[315] Dale L, Chapman J, Buchanan S. Mechanisms for trace element partitioning in Australian coals: University of Newcastle, 1999.

[316] Sheps S, Finkelman R, Councell T, Cohen H. Leaching of hexavalent chromium from fly ash. Conference Leaching of Hexavalent Chromium from Fly Ash. p. 1883-6.

[317] Frandsen F, Dam-Johansen K, Rasmussen P. Trace elements from combustion and gasification of coal—an equilibrium approach. Progress in Energy and Combustion Science. 1994;20(2):115-38.

[318] Lee JD. Concise inorganic chemistry: John Wiley & Sons, 2008.

[319] Bunt JR, Waanders FB. Trace element behaviour in the Sasol–Lurgi MK IV FBDB gasifier. Part 1 – The volatile elements: Hg, As, Se, Cd and Pb. Fuel. 2008;87(12):2374-87.

[320] Wang L, Zheng C, Zhang Y, Yue T, Weng W, Zhao H, et al. Speciation characteristics and mobility of trace elements across ultralow emission air pollution control devices. Energy & Fuels. 2017;31(12):13963-71.

[321] Linak WP, Wendt JO. Trace metal transformation mechanisms during coal combustion. Fuel Processing Technology. 1994;39(1-3):173-98.

[322] Zhang S, Jiang X, Liu B, Lv G, Jin Y, Yan J. Co-combustion of bituminous coal and pickling sludge in a drop-tube furnace: thermodynamic study and experimental data on the distribution of Cr, Ni, Mn, As, Cu, Sb, Pb, Cd, Zn, and Sn. Energy & Fuels. 2017;31(3):3019-28.

[323] Quispe D, Pérez-López R, Silva LF, Nieto JM. Changes in mobility of

hazardous elements during coal combustion in Santa Catarina power plant (Brazil). Fuel. 2012;94:495-503.

[324] Qi X, Song G, Song W, Yang S, Lu Q. Combustion performance and slagging characteristics during co-combustion of Zhundong coal and sludge. Journal of the Energy Institute. 2018;91(3):397-410.

[325] Sun Y, Bai F, Lü X, Jia C, Wang Q, Guo M, et al. Kinetic study of Huadian oil shale combustion using a multi-stage parallel reaction model. Energy. 2015;82:705-13.

[326] Lin Y, Ma X, Ning X, Yu Z. TGA–FTIR analysis of co-combustion characteristics of paper sludge and oil-palm solid wastes. Energy Conversion and Management. 2015;89:727-34.

[327] Kok MV, Özgür E. Thermal analysis and kinetics of biomass samples. Fuel Processing Technology. 2013;106:739-43.

[328] Xiao H-m, Ma X-q, Lai Z-y. Isoconversional kinetic analysis of co-combustion of sewage sludge with straw and coal. Applied Energy. 2009;86(9):1741-5.

[329] Shuping Z, Yulong W, Mingde Y, Chun L, Junmao T. Pyrolysis characteristics and kinetics of the marine microalgae Dunaliella tertiolecta using thermogravimetric analyzer. Bioresource Technology. 2010;101(1):359-65.

[330] Sasi T, Mighani M, Örs E, Tawani R, Gräbner M. Prediction of ash fusion behavior from coal ash composition for entrained-flow gasification. Fuel Processing Technology. 2018;176:64-75.

[331] Wang Ca, Liu Y, Zhang X, Che D. A study on coal properties and

combustion characteristics of blended coals in northwestern China. Energy & Fuels. 2011;25(8):3634-45.

[332] Xing P, Darvell L, Jones J, Ma L, Pourkashanian M, Szuhánszki J, et al. The use of equilibrium thermodynamic models for the prediction of inorganic phase changes in the co-firing of wheat straw with El Cerrejon coal. Journal of the Energy Institute. 2019;92(3):813-23.

[333] Zhang Y, Ren Q, Deng H, Lyu Q. Ash fusion properties and mineral transformation behavior of gasified semichar at high temperature under oxidizing atmosphere. Energy & Fuels. 2017;31(12):14228-36.

[334] Wang G, Zhang J, Zhang G, Ning X, Li X, Liu Z, et al. Experimental and kinetic studies on co-gasification of petroleum coke and biomass char blends. Energy. 2017;131:27-40.

[335] Skodras G. Catalysis and compensation effect of K_2CO_3 in low-rank coal—CO_2 gasification. Open Chemistry. 2013;11(7):1187-200.

[336] Lu X, Cao L, Wang H, Peng W, Xing J, Wang S, et al. Gasification of coal and biomass as a net carbon-negative power source for environment-friendly electricity generation in China. Proceedings of the National Academy of Sciences. 2019;116(17):8206-13.

[337] Parvez AM, Mujtaba IM, Wu T. Energy, exergy and environmental analyses of conventional, steam and CO_2-enhanced rice straw gasification. Energy. 2016;94:579-88.

[338] Zaini IN, Nurdiawati A, Aziz M. Cogeneration of power and H_2 by steam gasification and syngas chemical looping of macroalgae. Applied Energy.

2017;207:134-45.

[339] Hannula I, Kurkela E. A parametric modelling study for pressurised steam/O2-blown fluidised-bed gasification of wood with catalytic reforming. Biomass and Bioenergy. 2012;38:58-67.

[340] Zhou C, Rosén C, Engvall K. Biomass oxygen/steam gasification in a pressurized bubbling fluidized bed: Agglomeration behavior. Applied Energy. 2016;172:230-50.

[341] Mertzis D, Koufodimos G, Kavvadas I, Samaras Z. Applying modern automotive technology on small scale gasification systems for CHP production: A compact hot gas filtration system. Biomass and Bioenergy. 2017;101:9-20.

[342] Tuomi S, Kurkela E, Simell P, Reinikainen M. Behaviour of tars on the filter in high temperature filtration of biomass-based gasification gas. Fuel. 2015;139:220-31.

[343] Hsieh T-L, Zhang Y, Xu D, Wang C, Pickarts M, Chung C, et al. Chemical looping gasification (CLG) for producing high purity, H_2-rich syngas in a co-current moving bed reducer with coal and methane co-feeds. Industrial & Engineering Chemistry Research. 2018;57(7):2461-75.

[344] Hannula I, Kurkela E. A semi-empirical model for pressurised air-blown fluidised-bed gasification of biomass. Bioresource Technology. 2010;101(12):4608-15.

[345] Dhanavath KN, Shah K, Bhargava SK, Bankupalli S, Parthasarathy R. Oxygen–steam gasification of karanja press seed cake: fixed bed experiments, Aspen plus process model development and benchmarking with saw dust, rice

husk and sunflower husk. Journal of Environmental Chemical Engineering. 2018;6(2):3061-9.

[346] He J, Zhang W. Techno-economic evaluation of thermo-chemical biomass-to-ethanol. Applied Energy. 2011;88(4):1224-32.

[347] Valle CR, Perales AV, Vidal-Barrero F, Gómez-Barea A. Techno-economic assessment of biomass-to-ethanol by indirect fluidized bed gasification: impact of reforming technologies and comparison with entrained flow gasification. Applied Energy. 2013;109:254-66.

[348] Hannula I. Synthetic fuels and light olefins from biomass residues, carbon dioxide and electricity. Espoo: VTT Julkaisu: VTT Science. 2015;107.

[349] Azadi P, Brownbridge G, Mosbach S, Inderwildi O, Kraft M. Simulation and life cycle assessment of algae gasification process in dual fluidized bed gasifiers. Green Chemistry. 2015;17(3):1793-801.

[350] Abdelouahed L, Authier O, Mauviel G, Corriou J-P, Verdier G, Dufour A. Detailed modeling of biomass gasification in dual fluidized bed reactors under Aspen Plus. Energy & Fuels. 2012;26(6):3840-55.

[351] Myöhänen K, Palonen J, Hyppänen T. Modelling of indirect steam gasification in circulating fluidized bed reactors. Fuel Processing Technology. 2018;171:10-9.

[352] Chaiwatanodom P, Vivanpatarakij S, Assabumrungrat S. Thermodynamic analysis of biomass gasification with CO_2 recycle for synthesis gas production. Applied Energy. 2014;114:10-7.

[353] Dutta A, Talmadge M, Hensley J, Worley M, Dudgeon D, Barton D, et al.

Techno-economics for conversion of lignocellulosic biomass to ethanol by indirect gasification and mixed alcohol synthesis. Environmental Progress & Sustainable Energy. 2012;31(2):182-90.

[354] Shen L, Gao Y, Xiao J. Simulation of hydrogen production from biomass gasification in interconnected fluidized beds. Biomass and Bioenergy. 2008;32(2):120-7.

[355] Doherty W, Reynolds A, Kennedy D. Aspen plus simulation of biomass gasification in a steam blown dual fluidised bed. A. Méndez-Vilas (Ed.), Formatex Research Centre.2013;212-20.

[356] Proell T, Rauch R, Aichernig C, Hofbauer H. Coupling of biomass steam gasification and an SOFC-gas turbine hybrid system for highly efficient electricity generation. Conference Coupling of biomass steam gasification and an SOFC-gas turbine hybrid system for highly efficient electricity generation. American Society of Mechanical Engineers, p. 103-12.

[357] Olah GA, Goeppert A, Prakash GS. Beyond oil and gas: the methanol economy: John Wiley & Sons, 2011.

[358] Phillips SD, Tarud JK, Biddy MJ, Dutta A. Gasoline from woody biomass via thermochemical gasification, methanol synthesis, and methanol-to-gasoline technologies: A technoeconomic analysis. Industrial & Engineering Chemistry Research. 2011;50(20):11734-45.

[359] Gong M-h, Yi Q, Huang Y, Wu G-s, Hao Y-h, Feng J, et al. Coke oven gas to methanol process integrated with CO_2 recycle for high energy efficiency, economic benefits and low emissions. Energy Conversion and Management. 2017;133:318-31.

[360] Liu X, Liang J, Xiang D, Yang S, Qian Y. A proposed coal-to-methanol process with CO_2 capture combined Organic Rankine Cycle (ORC) for waste heat recovery. Journal of Cleaner Production. 2016;129:53-64.

[361] Isaksson J, Pettersson K, Mahmoudkhani M, Åsblad A, Berntsson T. Integration of biomass gasification with a Scandinavian mechanical pulp and paper mill–Consequences for mass and energy balances and global CO_2 emissions. Energy. 2012;44(1):420-8.

[362] Ng KS, Sadhukhan J. Process integration and economic analysis of bio-oil platform for the production of methanol and combined heat and power. Biomass and Bioenergy. 2011;35(3):1153-69.

[363] Liang J, Li H, Zhao S, Guo W, Wang R, Ying M. Characteristics and performance of SAPO-34 catalyst for methanol-to-olefin conversion. Applied Catalysis. 1990;64:31-40.

[364] Xiang D, Yang S, Liu X, Mai Z, Qian Y. Techno-economic performance of the coal-to-olefins process with CCS. Chemical Engineering Journal. 2014;240:45-54.

[365] Qin Xin JX. Modern Catalysis Chemistry (in Chinese). Beijing: Science China Press, 2016.

[366] Salkuyeh YK, II TAA. Co-production of olefins, fuels, and electricity from conventional pipeline gas and shale gas with near-zero CO_2 emissions. Part I: Process Development and Technical Performance. Energies. 2015;8(5):3739-61.

[367] Operation condtions and products composition of DMTO. 2011.

[368] JOHANSSON E. Process integration study of biomass-to-methanol (via gasification) and methanol-to-olefins (MTO) processes in an existing steam cracker plant: Master's thesis. Chalmers University of Technology: Gothenburg, Sweden, 2013.

[369] Parvez AM, Wu T, Li S, Miles N, Mujtaba IM. Bio-DME production based on conventional and CO_2-enhanced gasification of biomass: A comparative study on exergy and environmental impacts. Biomass and Bioenergy. 2018;110:105-13.

[370] Zhang X, Li H, Liu L, Bai C, Wang S, Song Q, et al. Exergetic and exergoeconomic assessment of a novel CHP system integrating biomass partial gasification with ground source heat pump. Energy Conversion and Management. 2018;156:666-79.

[371] Corti A, Lombardi L. Biomass integrated gasification combined cycle with reduced CO_2 emissions: Performance analysis and life cycle assessment (LCA). Energy. 2004;29(12-15):2109-24.

[372] Larson ED, Fiorese G, Liu G, Williams RH, Kreutz TG, Consonni S. Co-production of decarbonized synfuels and electricity from coal+ biomass with CO_2 capture and storage: an Illinois case study. Energy & Environmental Science. 2010;3(1):28-42.

[373] Beer T, Grant T, Williams D, Watson H. Fuel-cycle greenhouse gas emissions from alternative fuels in Australian heavy vehicles. Atmospheric Environment. 2002;36(4):753-63.

[374] Ng KS, Sadhukhan J. Techno-economic performance analysis of bio-oil based Fischer-Tropsch and CHP synthesis platform. Biomass and Bioenergy.

2011;35(7):3218-34.

[375] Im-orb K, Simasatitkul L, Arpornwichanop A. Techno-economic analysis of the biomass gasification and Fischer–Tropsch integrated process with off-gas recirculation. Energy. 2016;94:483-96.

[376] Albrecht FG, König DH, Baucks N, Dietrich R-U. A standardized methodology for the techno-economic evaluation of alternative fuels–A case study. Fuel. 2017;194:511-26.

[377] Kreutz TG, Larson ED, Liu G, Williams RH. Fischer-Tropsch fuels from coal and biomass. 25th Annual International Pittsburgh Coal Conference.2008;29(2):1-86.

[378] Spath P, Aden A, Eggeman T, Ringer M, Wallace B, Jechura J. Biomass to hydrogen production detailed design and economics utilizing the Battelle Columbus Laboratory indirectly-heated gasifier. National Renewable Energy Lab., Golden, CO (US); 2005.

[379] Phillips SD, Tarud JK, Biddy MJ, Dutta A. Gasoline from wood via integrated gasification, synthesis, and methanol-to-gasoline technologies. National Renewable Energy Lab.(NREL), Golden, CO (United States); 2011.

[380] Liu G, Larson ED, Williams RH, Kreutz TG, Guo X. Making Fischer−Tropsch fuels and electricity from coal and biomass: performance and cost analysis. Energy & Fuels. 2010;25(1):415-37.

[381] Haro P, Johnsson F, Thunman H. Improved syngas processing for enhanced Bio-SNG production: A techno-economic assessment. Energy. 2016;101:380-9.

[382] Guangzhou Institute of Energy Conversion. Consultation on biomass power technology improvement. Chinese Academy of Sciences, 2011.

[383] Huang Y, Zhao Y-j, Hao Y-h, Wei G-q, Feng J, Li W-y, et al. A feasibility analysis of distributed power plants from agricultural residues resources gasification in rural China. Biomass and Bioenergy. 2019;121:1-12.

[384] Wu H, Yu Y, Yip K. Bioslurry as a fuel. 1. Viability of a bioslurry-based bioenergy supply chain for mallee biomass in Western Australia. Energy & Fuels. 2010;24(10):5652-9.

[385] Malek AA, Hasanuzzaman M, Rahim NA, Al Turki YA. Techno-economic analysis and environmental impact assessment of a 10 MW biomass-based power plant in Malaysia. Journal of Cleaner Production. 2017;141:502-13.

[386] Zhang Q, Hu S, Chen D. A comparison between coal-to-olefins and oil-based ethylene in China: an economic and environmental prospective. Journal of Cleaner Production. 2017;165:1351-60.

[387] Jana K, De S. Sustainable polygeneration design and assessment through combined thermodynamic, economic and environmental analysis. Energy. 2015;91:540-55.

[388] Xiang D, Yang S, Qian Y. Techno-economic analysis and comparison of coal based olefins processes. Energy Conversion and Management. 2016;110:33-41.

[389] Do TX, Lim Y-i, Yeo H, Choi Y-t, Song J-h. Techno-economic analysis of power plant via circulating fluidized-bed gasification from woodchips. Energy.

2014;70:547-60.

[390] Ozonoh M, Aniokete T, Oboirien B, Daramola M. Techno-economic analysis of electricity and heat production by co-gasification of coal, biomass and waste tyre in South Africa. Journal of Cleaner Production. 2018;201:192-206.

[391] Leboreiro J, Hilaly AK. Biomass transportation model and optimum plant size for the production of ethanol. Bioresource Technology. 2011;102(3):2712-23.